THÈSE

UNIVERSITE DE PAU ET DES PAYS DE L'ADOUR
École doctorale Science Exactes et Leurs Applications (ED211)

Soutenue le 12 Novembre 2015
par **Alberto GREGORI**

pour obtenir le grade de docteur
de l'Université de Pau et des Pays de l'Adour
Spécialité : Physico-Chimie de Polymères

Synthesis of Conjugated Polymers and Adhesive Properties of Thin Films in OPV Devices

MEMBRES DU JURY

RAPPORTEURS
• Mme. Natalie STINGELIN   Professeur, Imperial College London
• M. Markus C. SCHARBER   Professeur, Johannes Kepler University Linz

EXAMINATEURS
• M. Paul D. TOPHAM   Maitre de Conférence, Aston University Birmingham
• M. Patrice RANNOU   Directeur de Recherche, CEA, CNRS, Université de Grenoble Alpes

DIRECTEURS
• Mme. Christine DAGRON-LARTIGAU   Maitre de Conférence, HDR (superviseur), Université de Pau et des Pays de l'Adour
• M. Ahmed ALLAL   Professeur (co-superviseur), Université de Pau et des Pays de l'Adour
• M. Roger C. HIORNS   Chargé de Recherche, HDR (co-encadrant), CNRS, IPREM/EPCP, Pau

UNIVERSITÉ
DE PAU ET DES
PAYS DE L'ADOUR

"It is sometimes a mistake to climb; it is always a mistake never even to make the attempt.
If you do not climb you will not fall. This is true. But is it that bad to fail, that hard to fall?
Sometimes you wake and, yes, sometimes you die.
But there is a third alternative.
(…) sometimes when you fall, you fly"

Fear of Falling - The Sandman, N. Gaiman

Acknowledgement

During these three years, I had the chance to meet and work many valuable researchers and wonderfull human beings.

I would like to start thanking my family for having supported me all along my academic studies. Then I have to thank my supervisor Christine, Ahmed and Roger, for entrusting me with the freedom to conduct the experiment in my own way, without never let me miss their support and their guidance in times of need.

Hussein, Hasina, Bruna, Hongyao, Edilene, Tonimar, Sebastien, Coralie, Julien, Mohamed, Oscar, Rayane and all the other students at the IPREM for their help in the lab and their friendship, which gave me the strength to overcome the darkest moments of these three years.

To all the Establis fellows a special thanks for the great scientifique exchanges and the partying during our meeting. Hasina, Stefan, Simon, Isabel, Auré, Jenia, Jojo and Meera, I hope our friendships will last for a long time.

To Mirella, Andi, Sebastian, Tobi, Sambatra, Bas, Bart, Mario, Christian, Michi, Hugo, Heike, Kata and all the others I met at Belectric OPV go all my gratitude for the useful experience I had in Nuremberg and I hope to see you all the next months.

Dani, Lorenzo and Juan meeting you was one of the best fluke of these past three years. Pau would have not been the same without you. I'll really miss you and it won't be easy to find such great friends as you.

Mask, Dani, Carla, Riccà, Lori, Ale, Fede, Luciano and Mauro thanks for making me feel less homesick through your constant presence and friendship.

Last but not least, my deepest thankfulness goes to Mélanie and his family. For her support in facing french administration, but mostly for having been such a precious friend and counselor from the very first till the very end of my french chapter.

Contents

List of Figures

List of Figures

List of Figures

List of Figures

List of Figures

List of Figures

List of Schemes

List of Tables

Glossary

AFM   Atomic Force Microscopy

AL   Active Layer

BHJ   BulkheteroJunction Solar Cell

CV   Cyclic Voltammetry

DIO   diiodooctane

DPP   diketopyrrolopyrrole

DSC   Differential Scanning Calorimetry

DTP   dithienylthienopyrazine

DTS   dithienosilole

E_g Energy Gap

EPR   Electron Paramagnetic Resonance

EQE   External Quantum Efficiency

ETL   Electron Transporting Layer

FF   Fill Factor

HOMO   Highest Occupied Molecular Orbital

HTL   Hole Transporting Layer

ITO   Indium Tin Oxide

J_{SC} Short-Circuit Current Density

LBGs   Low BandGap Polymers

LUMO   Lowest Unoccupied Molecular Orbital

NBS   N-bromosuccinimide

NMR   Nuclear Magnetic Resonance

OPV   organic photovoltaic

P3HT   poly(3-hexylthiophene)

$PC_{61}BM$ phenyl-C_{61}-butyric acid methyl ester

PCE   Power Conversion Efficiency

PEDOT:PSS   poly(3,4-ethylenedioxythiophene)-*compl*-poly(styrene sulfonate)

PL   PhotoLuminescence Spectroscopy

Glossary

RHC   Rapid Heat-Cool Calorimetry

R_S series resistance

R_{SH} shunt resistance

TAS   Transient Absorption Spectroscopy

TGA   Thermal Gravimetric Analysis

UV-vis Ultraviolet-visible absorption spectroscopy

V_{OC} Open-Circuit Voltage

XPS   X-Ray Photoelectron Spectroscopy

XRD   X-Ray Diffraction

Abstract

Organic photovoltaic (OPV) devices are one of the most promising applications of organic semiconductors due to their compatibility with flexible plastic substrates resulting in light weight, inexpensive and decorative products. For a long time poly(3-hexylthiophene) (P3HT) has been the polymer of choice in organic photovoltaic devices in combination with [6,6]-phenyl-C_{61}-butyric acid methylester ($PC_{61}BM$) as acceptor. However, recent research has focused on polymers with improved absorbance and processability that can ensure higher efficiencies and longer lifetimes (Low BandGap polymers (LBGs)). This has been fully demonstrated with a power conversion efficiency (PCE) above 11%.

This thesis reports synthesis and characterization of two series of so-called "push-pull" (or donor-acceptor) LBGs based on the donor unit 4,4'-bis(2-ethylhexyl)-5,5'-dithieno[3,2-b:2',3'-d]silole (DTS) and either 3,6-dithiophen-2-yl-2, 5-dihydropyrrolo[3,4-c]pyrrole-1,4-dione (DPP) or 5,7-di(thienyl)thieno[3,4-*b*]pyrazines (DTP), as acceptor unit. All π-conjugated D-A molecules and polymers were characterized by chemical investigation and their optical, electrochemical, morphological, and photovoltaic properties are reported. The DTS-DPP series was chosen because it is representative of a large number of donor-acceptor LBG polymers and provided an easily accessible and useful template to discover the importance of the type of side-chain used on the polymer optoelectronic and thermal properties. First studies on DTS-DPP:$PC_{61}BM$ devices have been conducted, in order to investigate any effect on their photovoltaic properties. The best device obtained had a PCE of 1.7% with J_{SC} of 5.9 mA·cm^{-2}, V_{OC} of 0.54 V and FF of 0.58. The DTS-DTP series was chosen for the high stability of the two units and the for the ease of substitution of the side-groups. The synthesis was partially successful and only oligomers were obtained. Nonetheless, chemical characterization was performed but their application in OPV was not explored.

In terms of device stability, the electrical failure mechanisms in OPV devices have been thoroughly investigated, while little is known about their mechanical stability, which is as important and critical to ensure long term reliability. The characteristic thin film stresses of each layer present in organic solar cells, in combination with other possible fabrication, handling and operational stresses, provide the mechanical driving force for delamination of weak interfaces or even their de-cohesion, leading to a loss of device integrity and performance.

In the second part of this thesis, a technique to probe weak layers or interfaces in inverted polymer:fullerene solar cells is presented. It was developed by establishing a new set-up for the pull-off test, which ensure an improved control on the test parameters. The technique was developed using inverted device, with the structure glass/ITO/ZnO/P3HT:PC$_{61}$BM/PEDOT:PSS/Ag. The delaminated devices showed that the weakest point was localized at the active layer/hole transporting layer interface, in good agreement with the literature. The technique was extended varying both sensitive layers, using different p-type low bandgap (co)polymers for the active layer (PSBTBT and PDTSTzTz) in combination with two different PEDOT:PSS formulations, the water based Clevios^{TM} HTL Solar and a new organic solvent based HTL Solar 2. The half-devices produced upon destructive testing have been characterized by contact angle measurement, AFM and XPS to locate the fracture point. A difference in the stress at break for devices made with different combinations of active and hole transporting layers is visible, suggesting different fracture paths, as confirmed by surface characterization and could be correlated to the different behavior of the active layer with the two PEDOT:PSS formulations. A second solution adopted, it had been the introduction of amphiphilic block-copolymer interlayer in order to enhance the compatibility of the two layers. This strategy was not successful and the new architecture showed reduced adhesion strength. Further development of device processing could make this new architecture a viable alternative.

Résumé

La production d'énergie avec des cellules photovoltaïques organiques (OPV) est une des applications les plus prometteuses des semi-conducteurs organiques, en raison de leur compatibilité avec les substrats flexibles en plastique permettant des produits légers, peu chers et décoratifs. Pendant longtemps, le poly(3-hexylthiophène) (P3HT) a été le polymère de choix dans l'OPV combine au le [6,6]-phényl-C_{61}-butanoate de méthyle ($PC_{61}BM$) comme accepteur. Toutefois, des recherches récentes ont porté sur des polymères avec de meilleures absorption et processabilité, qui peuvent assurer des rendements et des durées de vie plus élevés (polymères à faible bande interdite (LBG)). Des rendements de conversion en puissance (PCE) au-dessus de 11% ont récemment été démontrés.

Cette thèse rapporte sur la synthèse et la caractérisation de deux séries de polymères dits à faible bande interdite, LBGs "push-pull" (ou donneur-accepteur), constitués de l'unité donneuse 4,4-bis(2-ethylhexyl)-5,5'-dithieno[3,2-*b*:2',3'-*d*]silole (DTS) combinée au 3,6-dithiophén-2-yl-2,5-dihydro-pyrrolo[3,4-*c*]pyrrole-1,4-dione (DPP) ou au 5,7-di(thiényl)thiéno[3,4-*b*]pyrazines (DTP), comme unité acceptrice. Toutes les molécules et les polymères π-conjugués ont été caractérisés chimiquement et leur propriétés optiques, électrochimiques, morphologiques et photovoltaïques ont été determinées. La série DTS-DPP a été choisie parce qu'elle est représentative d'un grand nombre de polymères donneur-accepteur LBG et a fourni un modèle facilement accessible pour évaluer l'importance de la chaîne latérale utilisée sur les propriétés optoélectroniques et thermiques des polymères. Les premières études sur les dispositifs à base de DTS-DPP:$PC_{61}BM$ ont été menées, pour déterminer les propriétés photovoltaïques. Le meilleur dispositif permet d'obtenir un PCE de 1,7% avec J_{SC} de 5,9 mA cm^{-2}, V_{OC} de 0,54 V et FF de 0,58. La série DTS-DTP a été choisie pour la stabilité chimique élevée des deux unités et pour la facilité de substitution des groupes latéraux. La polymérisation a partiellement abouti, en donnant seulement des oligomères. La caractérisation chimique a pu être effectuée, mais leur application dans l'OPV n'a pas été explorée.

En termes de stabilité des dispositifs, les mécanismes de défaillance électrique de dispositifs de OPV ont été étudiés, montrant une méconnaissance de leur stabilité mécanique, alors que c'est important et même essentiel pour assurer une fiabilité à long terme. Les contraintes caractéristiques de chaque couche mince présentes dans les cellules solaires organiques, en combinaison avec d'autres contraintes possibles liées à la fabrication, à la manipulation et au fonctionnement,

constituent la force motrice à l'origine de la délamination des interfaces faibles ou même leur decohésion, causant une perte de l'intégrité et des performances du dispositif.

Dans la deuxième partie de cette thèse, une technique pour sonder les couches ou les interfaces fragiles dans les cellules solaires polymère:fullerene en géométrie inverse est présentée. Elle a été développée par l'établissement d'un nouveau set-up pour le test pull-off, qui assure un meilleur contrôle sur les paramètres du test. La technique a été développée en utilisant un dispositif à géométrie inverse, de structure verre/ITO/ZnO/P3HT:PC$_{61}$BM/PEDOT:PSS/Ag. Les dispositifs délaminés ont montré que le point le plus faible est localisé à l'interface couche active/couche de transport de trous, en bon accord avec la littérature. La technique a été étendue en variant les deux couches sensibles, en utilisant differents polymères de type *p* à faible bande interdite pour la couche active (PSBTBT et PDTSTzTz) en combinaison avec deux formulations de PEDOT:PSS, Clevios^{TM} HTL Solar à base d'eau et un nouveau HTL Solar 2 à base de solvant organique. Les demi-dispositifs obtenus après ce test destructif ont été caractérisés par mesure d'angle de contact, AFM et XPS pour localiser le point de rupture. Une différence entre la contrainte à la rupture des dispositifs avec différentes combinaisons de couches actives et de transport de trous est visible, suggérant différents chemins de fracture, tel que confirmé par la caractérisation de surface et qui pourrait être corrélée avec la différence de comportement de la couche active avec les deux formulations de PEDOT:PSS. Une autre voie adoptée, a été d'introduire une couche d'interface de copolymère à blocs amphiphile afin d'améliorer la compatibilité des deux couches. Cette stratégie n'a pas abouti et la nouvelle architecture présente une force d'adhésion réduite. La poursuite de l'amélioration des procédés de fabrication de ces dispositifs pourrait faire de cette nouvelle architecture, une alternative viable.

1   Motivation and Background

"Because past environmental destruction was the result of ignorance we can easily forgive it. Today, we are better informed. Therefore, it's essential that we make an ethical examination of what we have inherited, what we are responsible for, and what we will pass on to coming generations. Ours is clearly a pivotal generation. We have global communication and yet confrontation is more common than dialogue."

Tenzin Gyatso, XIV Dalai-Lama

1.1   Introduction

The projections of world population growth prepared by the United Nations (UN) estimate an increase in global population from the actual 7 billion to 9.5 billion by 2050 (Figure 1.1). Today, only 1.5 billion people have access to the amount of energy which allows comfortable living conditions (> 2 kWh). The increasing population and the rapid industrialisation of countries around the world have led to projections of an increase in global energy demands of between 35-55 % in the next 30 years [1]. This increase in demand will require an increase in energy production capacity.
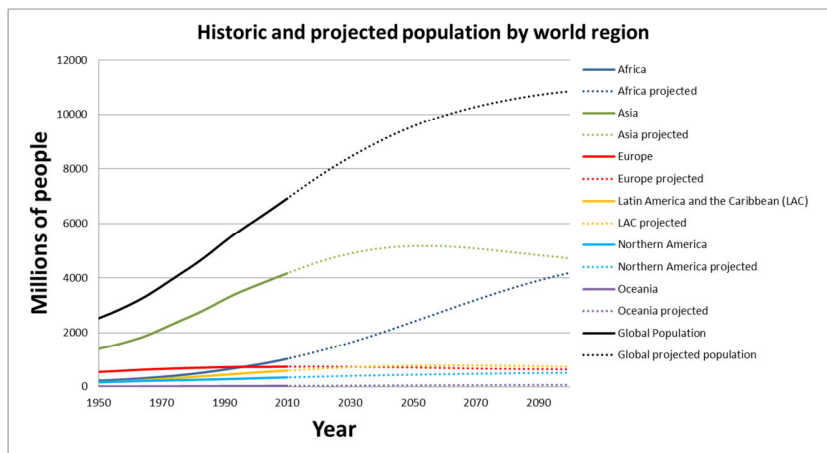
Figure 1.1 **UN world population prospects: The 2012 revision** provided by **United Nations Department of Economic and Social Affairs (UN DESA)** (Reproduced from **EEA**).

Electricity consumption can be considered as one of the most important factors that impacts the prosperity of any society, visible through both economic indices (such as GDP per capita, Figure

1.2-a) and social development indices (such as HDI[1], Figure 1.2-b) [2]. Increasing electricity consumption per capita can directly stimulate faster economic growth that indirectly promotes social development. The aforementioned value of 2 kWh can be considered the threshold for moving from a low to medium HDI economy transition (Figure 1.2-b). When this minimal amount of electricity is used for pumping water, providing light, and refrigerating food and medicines, a community can significantly improve its living conditions.
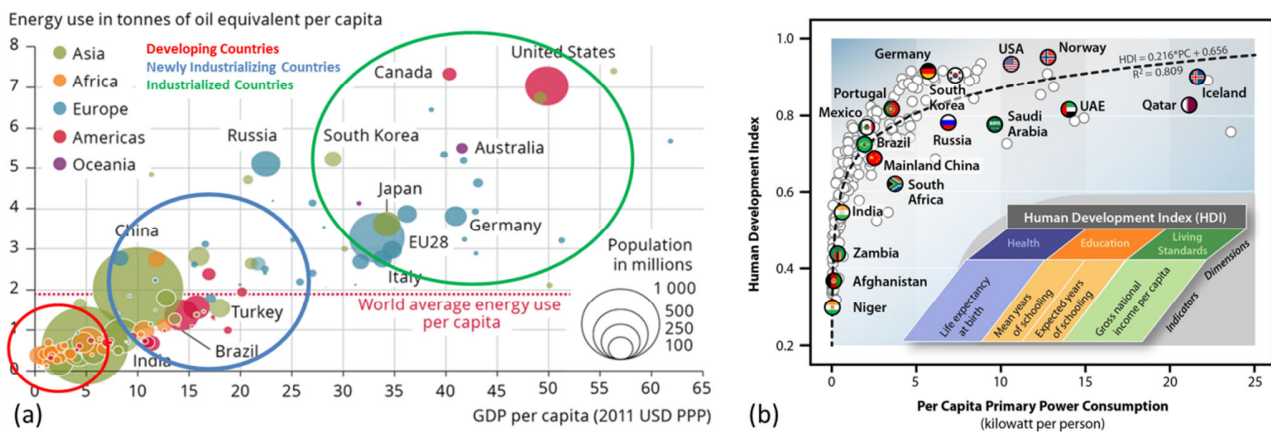
Figure 1.2 a) The relation between mean income (GDP per capita) and energy consumption (per capita demand in kWh) in 2011 for various country groups. The primary energy consumption of a country is shown – i.e. its industry and transport are also included – divided by the number of inhabitants. (b) Per capita energy consumption and Human Development Index for 1991/1992, based on data for 100 countries. Source a) EEA b) ourenergypolice.org.

Electricity plays a key role in both economic and social development and obtaining the appropriate amount of energy to support the growing population and the industrial development, in a clean as possible way is one of the toughest challenges our generation has to face.

1.1.1 Current situation and the role of renewable sources

Currently approximately 80% of the world's energy is generated by the combustion of fossil fuels (Figure 1.3-a). However, conventional fossil fuels are a finite resource. Known world reserves of oil and gas are expected to become depleted in less than 65 years, and coal in just over 100 years at 2012 consumption levels [1].

---

[1] HDI is the Human Development Index is a summary composite index used to measure a country's average achievements in three basic aspects of human development: longevity, knowledge, and a decent standard of living. (Source UNDP)
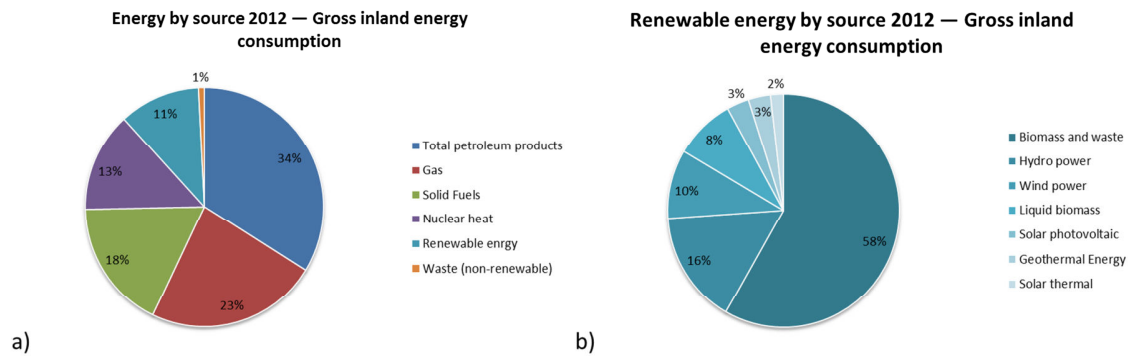
Figure 1.3 a) Gross inland energy consumption by source in EU-28 in 2012 and b) renewable energy share. EEA).

The main disadvantage in the use of fossil fuels is the emission of carbon dioxide as a by-product of the combustion process and its effect on the environment. The scientific community agrees that the concentration of CO_2 (and other so-called greenhouse gases) in the atmosphere is one of the main players in the anthropogenic climate change, together with the ozone depletion in the atmosphere. Global warming is closely associated with other climate changes and impacts, including rising sea levels, increases in intense rainfall events, decreases in snow cover and sea ice, more frequent and intense heat waves, increases in wildfires, longer growing seasons, and ocean acidification. Individually and collectively, these changes pose risks for a wide range of human and environmental systems [3]. The resulting loss of land, will reduce food production and force migration of a large part of the world population [4]. Therefore, the limitation of the severity of climate change effects should be considered a global priority. An effective long-term strategy should include both the reduction of all the anthropogenic contributions to climate change and the development of strategies for alleviating its effects. Hopefully, the Kyoto protocol will be successful in reducing CO_2 concentrations, as it has already been done with atmospheric CFC concentrations with the Montreal protocol [5].

In the 2050 Roadmap [6], the European Commission concretely assess the problem of how to reduce fossil fuel usage while maintaining the actual standards of living. The EU considers the expansion of the renewable energy sector as the most viable and important way to solve this problem. Besides the well-known environmental benefits, there is the secondary (or primary) effect that an expansion of the EU's renewable energy sector would have on its geostrategic position. Decreasing the dependence of EU from the international market of fossil fuels, will help to increase EU's position as a key global power. In fact, as the non-renewable giants of the world tend to have authoritarian governments and weak institutions [7], the EU could improve its ability to maintain a

united and tough stance against such countries, also by weakening the financial benefits they experience.

Figure 1.4 Energy security represents a viable way to improve international influence.

Energy security represents the need of an uninterrupted availability of energy sources at an affordable price (source IEA) [8]. It has both a long- and short-term dimensions. The first deals with investments oriented to support economic developments and sustainable environmental needs, the second focuses on the ability of the energy system to react changes in the supply-demand balance. Lack of energy security has negative economic and social impacts related to energy distribution or elevated and volatile prices.

1.1.2 Alternative energy and the contribution of renewable sources

Abundant and cheap electricity without high CO_2 emissions could come from the use of nuclear fission. Today, the nuclear heat production in the EU-28 accounts for 13% (Figure 1.3-a). Nuclear electricity production increased by 11% between 1990 and 2012, however, since 2005, an average decrease of 1.7%/year have been registered (Figure 1.5-a). This is mainly due to the unpopularity of nuclear energy in the public opinion, mainly related to the, real or perceived, dangers related to the disposal of nuclear waste and even more to disasters such as Chernobyl and Fukushima. This situation does not allow the government to invest in the long term, as would be necessary to assure fuel provisions and power-plant constructions in such amounts as to wholly replace fossil fuels.

1 Motivation and Background
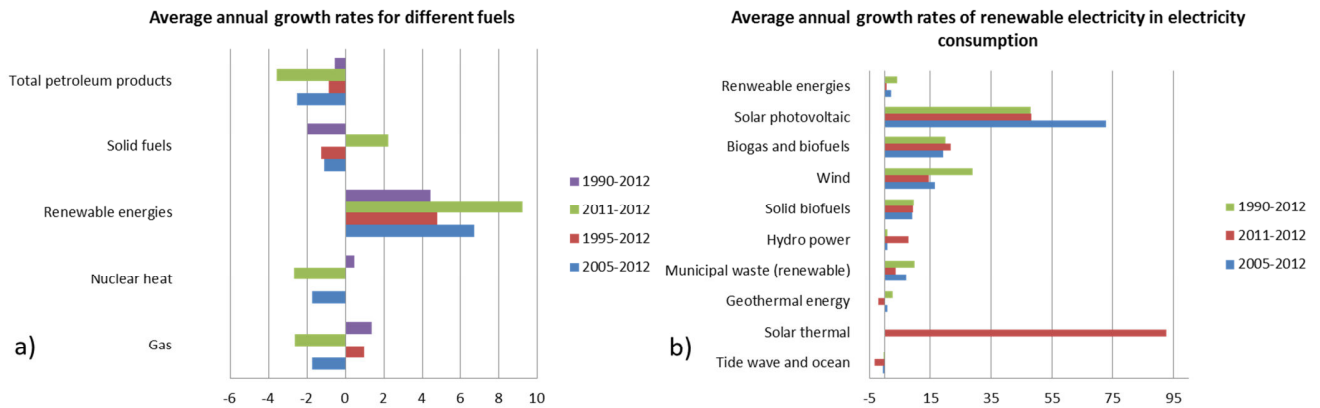
Figure 1.5 a) Average growth rates in energy consumption for different fuels and d) detailed renewable rates in EU-28 (Reproduced from a) EEA and b) EEA).

Alternative sources of energy to both nuclear and fossil fuel have existed for a long time and they are usually grouped under the term renewable energies. A renewable energy source is one that can be considered to be naturally regenerated on a reasonable timescale such that it will never be exhausted. Moreover, in order to promote the diffusion of a renewable energy source or technology, the energy generated from that source must have a price competitive with fossil fuel. Until now, the most utilised renewable sources of energy are biomass and waste, which together account for almost 60% of European renewable energy supply (Figure 1.3-b) Unfortunately, its continued expansion is not feasible due to the limited supply of bio-sourced materials. Currently the alternative competitive technologies and sources are onshore wind farms, hydroelectric facilities, and geothermal phenomena. Sadly, the geological features necessary for construction of the appropriate power plants are not common enough to replace fossil fuel. Wind power has shown some promise and construction is being undertaken all over the world and most extensively in Europe, North America and Asia. In Europe, wind energy production increased of 29%/year between 1990 and 2012 (Figure 1.5-b). However, the prospect of covering the landscape with wind farms to cover the increasing demand is not viable. Offshore wind farms have the advantage of reducing the impact on both land and landscape, but the cost of building the infrastructure make it uncompetitive. However, the costs of these technologies is predicted to come down in the future (Figure 1.6), and it is possible that they will play a key role in assuring the energy security.
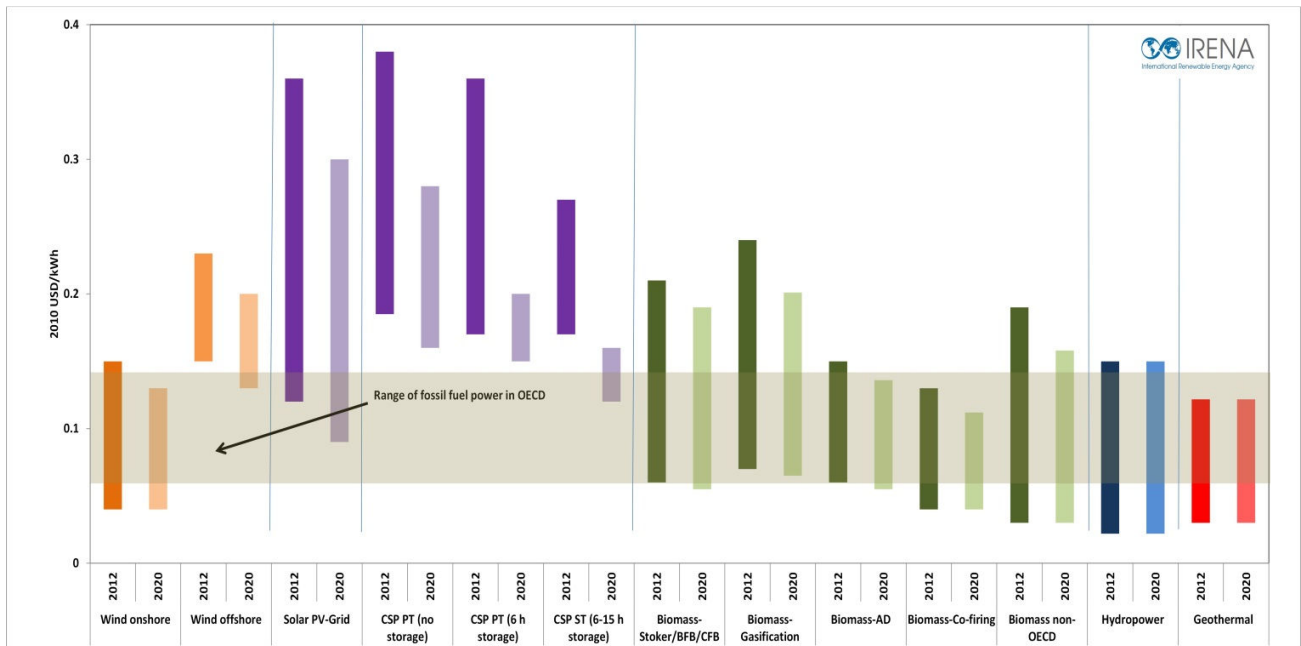
Figure 1.6 Price for kWh generated from different renewable sources in 2012 and a projection in 2020 [9].

Another option that deserves consideration is the use of solar energy. In the last 25 years, solar energy production grew at a rate of 48%/year and since 2005 even faster (70%/year) (Figure 1.5-b). This has been possible thanks to government policies, since the costs related to the actual technology (concentrated solar power CSP and photovoltaic PV) are too high and not really competitive (Figure 1.6). However, according to the IEA, solar energy potential has the greater potential (and it is abundant enough) to cover alone several times the future global energy demand.

1.1.3 Photovoltaics and Organic Photovoltaics

The earth receives more solar energy in 1 hour than is required for all human needs in a year [10]. Given the ease with which solar panels can be installed, solar energy is the most marketable and accessible energy form [10]. There is considerable interest in PV and capacity is increasing annually (Figure 1.5-b). However, the observed growth of the PV industry has been heavily supported by government incentives worldwide. This had been necessary due to the high cost of the generated energy, which is in part related to the costs associated with the fabrication of the most common silicon or cadmium telluride (CdTe) solar modules. Many improvements in the fabrication processes over the years have made available cheaper solar cells and subsequently reduced the cost of electricity. Unfortunately, the costs of 1 kWh is not competitive with fossil fuel yet (Figure 1.6).

The overall aim of all PV research is to achieve low cost and highly efficient modules that are commercially attractive. Organic photovoltaics (OPV) is an attractive alternative to Si technology, since it offers intrinsic flexibility, low cost, a low thermal budget, solution processing, and very fast methods for fabrication. The main advantage over inorganic PV is the reduced fabrication costs. On the other hand, organic photovoltaics have exhibited lower stabilities and efficiencies. Crystalline silicon modules have efficiencies of around 20% and over 25 years lifetime, while OPV are still far from these values.
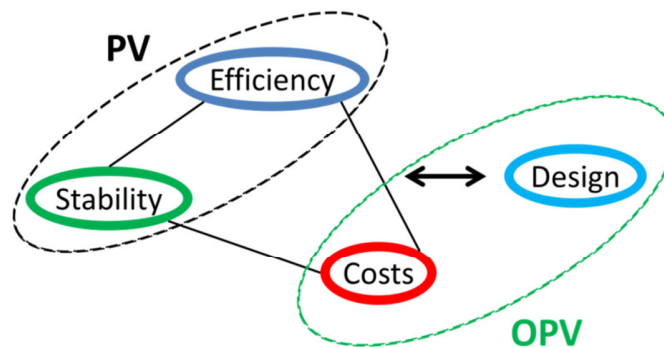
Figure 1.7 The so-called Brabec's triangle (Efficiency, Stability, Costs) and a unique advantage for OPV: design freedom.

Even if OPV is inferior to silicon photovoltaic technology, it is still worth developing this technology due to its low production costs, fast processing and environmental benefits. Moreover, secondary advantages, such as flexibility, light weight, design freedom open the way to niche market in which inorganic has not application and OPV can make the difference (Figure 1.7). A large research effort, from both academia and industry, needs to be done with respect to stability and power-conversion efficiency. A lot of work has already been done and, on a laboratory scale, solar cells with a power conversion efficiencies over 10% have already been achieved [11], while, in terms of stability, more research efforts are still required. The current challenge is the production of a low-cost organic photovoltaic modules on an industrial scale, with good stability (10-15 years) and efficiency (10-15%).

1.1.4 The ESTABLIS Project

The project, 'Ensuring stability in organic solar cells' (FP7, ESTABLIS) is an interdisciplinary and inter-sectorial research and training network, based on the complementary expertise of leading industrial and university groups. Specifically, four Experienced Researchers (ERs) and eleven Early Stage Researcher (ESRs) have been trained in areas from synthetic organic chemistry through

complementary aspects of polymer science to complete industrial scale photovoltaic device manufacture, and the interdisciplinary training was an important goal. The objective of this project was to develop materials and techniques required to give cheap organic solar cells (OSCs) with 10 years stability. OSCs are at the crossroads of the forefront chemical and physical sciences and ESTABLIS applied tested routes to develop new polymers and OSC architectures, and known characterization techniques in innovative ways.

Two different approaches have been used to improve long-term device stability. The first was the introduction of new materials, the improvement of technological processes and extensive aging studies. The second approach was adopted in order to clarify the correlations between material optoelectronic properties and charge transfer mechanisms, their photochemistry and stability.

The scientific objectives, in order to achieve the project goal, can be pooled in four groups: (i) producing materials with increased stabilities; (ii) clarifying photo(chemical) and mechanical degradation pathways; (iii) processing OSCs with reduced inter-layer contaminations and increased interfacial adhesion and (iv) modelling interrelated OSC photochemical ageing and optoelectronic properties. Researchers were consequently divided in four working groups (Figure 1.8) with specific task and wide multi-disciplinary competences.
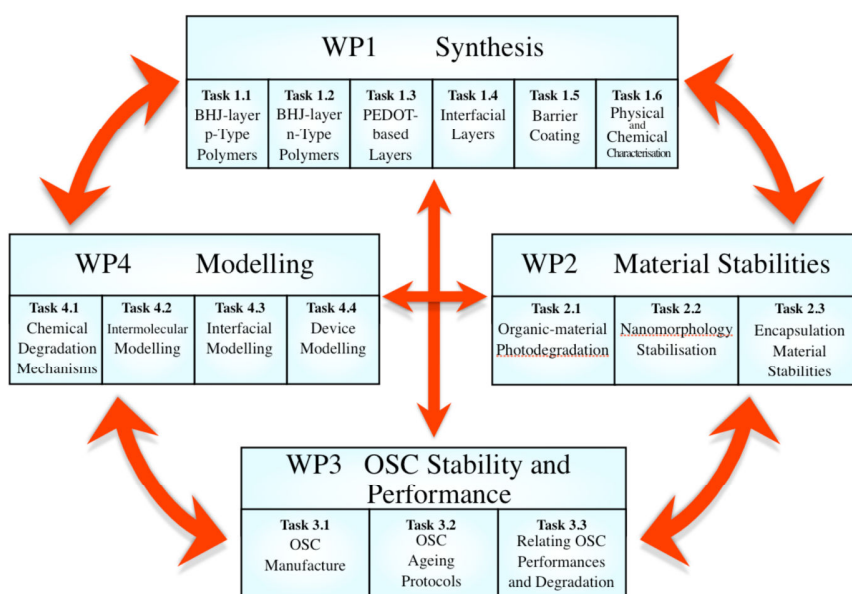
Figure 1.8 Establis work packages and relative tasks.

The different partners (P) and associated partners (AP) with the corresponding ERs and ESRs of the ESTABLIS project are reported in Table 1.1.

Table 1.1 Establis partners and involved fellows.

P1	Université de PAU et des pays de l'Adour	Hugo Santos Silva (ESR1)
		Alberto Gregori (ESR2)
P2	Belectric OPV GmbH (formerly Konarka Technologies GmbH)	Dr. Simon A. Dowland (ER1)
		Dr. Dargie Deribew (ER2)
P3	Vilniaus Universitetas	Meera Stephen (ESR3)
P4	Merck Chemicals Ltd	Dr. Grahgam Morse (ER3)
P5	Instituto Madrileno de Estudios Avanzados	Safakath Karuthedath (ESR4)
P6	Heraeus Precious Metals GmbH & Co KG	Dr. Stefan Schumann (ER4)
P7	Johannes Kepler Universität Linz	Olena Kozlova (ESR5)
P8	Aston University	Joanna Kolomanska (ESR6)
		Anna Isakova (ESR7)
P9	Institut de Chimie de Clermont-Ferrand (Centre National de Recherche Scientifique)	Isabel Fraga Dominguez (ESR8)
		Evgeniia Topolniak (ESR9)
P10	Eberhard-Karls-Universität Tibingen	Aurélien Tournebize (ESR10)
P11	Medzinarodne Laserove Centrum	Mamadou Abass Seck (ESR11)
AP1	Evonik Degussa GmbH	
AP2	Siemens Corporate Technology	
AP3	AMCOR	

1.1.5 Aim of the work

The aim of this thesis project was to synthesize new low-band gap (LBG) (co-)polymers to apply in OPV devices with improved stabilities. The synthesis and characterization of 5 new LBG polymers based on dithienosilole and diketopyrrolopyrrole or dithienyl-thienopyrazine are described, as well as their photovoltaic responses in OPV devices.

The mechanical stability of devices is fundamental for long term application and investigation in this cutting-edge research field started only recently. A new experimental set-up was developed in order to investigate adhesive strength in OPV devices and is presented, together with two possible routes to improve the adhesion at the weakest interface, either by the use of new materials and/or new architectures.

1 Motivation and Background

The work presented in the following chapters has been done in collaboration with some of the other ERs and ESRs, in the spirit of collaboration of the project. The design and synthesis of the two series of low bandgap polymers (*LBGs*) was done by myself at the University of Pau, with the advice of Dr. Graham Morse at Merck Chemicals Ltd, who also performed part of the chemical characterization. Dr. Simon A. Dowland, Dr. Mirella El Gemayel and Dr. Dargie Deribew trained me in device fabrication during my secondment at Belectric OPV GmbH and we worked together on the fabrication and characterization of devices integrating the LBGs synthesized at the Université de Pau. Safakath Karutedath at IMDEA Nanociencia was involved in the characterization of the charge carrier behaviour in the polymer:$PC_{61}BM$ blend, by Transient Absorption Spectroscopy (TAS). Isabel Fraga Domínguez investigated the stability of one series of polymer (**PSBDPP**) alone and in blend with **PCBM**, under photo- and thermo-oxidative condition. With the aim of relating the degradation rate to their physicochemical properties, she characterized the content in paramagnetic species by Electronic Paramagnetic Resonance (EPR), the crystallinity of thin films by X-Ray Diffraction (XRD) and the thermal properties by Rapid Heat-Cool Calorimetry (RHC) of this polymer series.

Dr. Stefan Schumann was involved in the set-up development during his secondment in Pau and then we collaborated by testing the adhesive properties of inverted devices integrating different **PEDOT:PSS** formulations from our partner Heraeus Deutschland GmbH & Co. KG, aiming to an improvement of the adhesive strength of the weak active layer/**PEDOT:PSS** interface. The second strategy to improve adhesive strength has been the introduction of a block-copolymer interlayer at the aformentioned interface. These block copolymers were designed and synthetized by Joanna Kolomanska at Aston University. I also participated to the synthesis of these block copolymers during my secondment at Aston University. Aurélien Tournebize at Tubingen University was also involved in the characterization of the fracture surfaces by XPS and AFM, in order to gain a better understanding about the effect of the new materials in the layer stack.

All the presented results, arise from discussion with my supervisors (Dr. Christine Dagron-Lartigau, Prof. Ahmed Allal, Dr. Roger C. Hiorns and Dr. Andreas Distler) as well as with the other researcher involved (Dr. Stefan Schumann, Aurélien Tournebize, Dr. Simon A. Dowland, Dr. Dargie Deribew, Dr. Graham Morse, Isabel Fraga Dominguez, Joanna Kolomanska, Safakath Karuthedath and Dr. Mirella El Gemayel from POCAONTAS Project). Specific acknowledgements are given when their produced data is presented as part of the discussion.

1 Motivation and Background

This thesis is structured as follows: after this first chapter which presents the actual socio-economical, environmental and political background which contextualize the scientific work, the manuscript proceeds with an introduction of the basic concepts and the evolution of OPV, presenting the principles of molecular design, polymer synthesis, thin film formation and device architecture, which led to the actual state of the art. In Chapters 3 and 4, the results in terms of synthesis, chemical characterization and device performance of the new push-pull LBGs based on dithienosilole (donor unit) and diketopyrrolopyrrole or dithienylthienopyrazine (acceptor unit) are presented. Chapter 5 describes the development of an experimental set-up to characterize adhesive strengths of thin films in real device applications. The technique has then been extended to new materials and architecture developed inside the ESTABLIS project.

1 Motivation et contexte

1 Motivation et contexte

> *"Parce que la destruction environnementale passé était le résultat de l'ignorance, nous pouvons facilement pardonner. Aujourd'hui, nous sommes mieux informés. Par conséquent, il est essentiel que nous fassions un examen éthique de ce que nous avons hérité, ce que nous sommes responsables, et ce que nous allons transmettre aux générations à venir. La nôtre est clairement une génération charnière. Nous avons la communication globale et pourtant confrontation est plus commun que le dialogue ".*
>
> *Tenzin Gyatso, XIV Dalaï Lama*

1.1 Introduction

Les projections de la croissance de la population mondiale préparées par les Nations Unies (ONU) estiment une augmentation de la population mondiale de 7 à 9,5 milliards en 2050 (Figure 1.1). Aujourd'hui, seulement 1,5 milliard de personnes ont accès à la quantité d'énergie qui permet des conditions de vie confortables (> 2 kWh). La population croissante et l'industrialisation rapide des pays à travers le monde ont conduit à des projections d'une augmentation de la demande mondiale d'énergie comprises entre 35-55% dans les 30 prochaines années [1]. Pour répondre à cette augmentation de la demande, il faudra une augmentation de la capacité de production d'énergie.
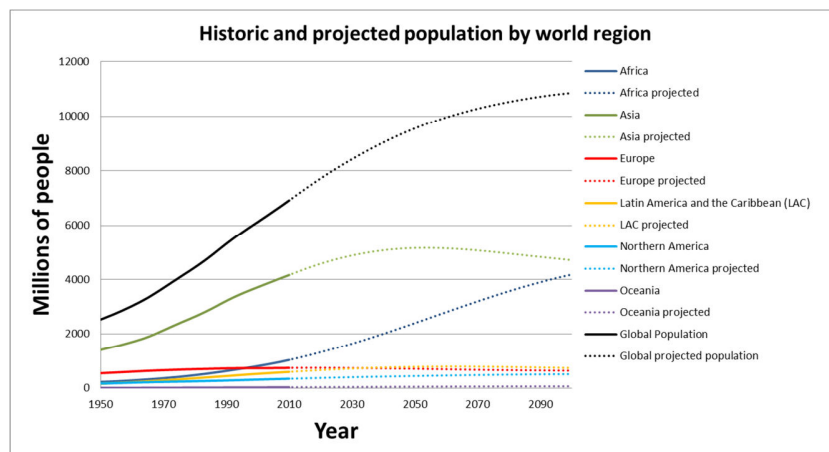
Figure 1.1 Previsions ONU de la population mondiale: La révision 2012 fournis par le ministère des Nations Unies des affaires économiques et sociales (DAES) (Reproduit de l'EEE).

1 Motivation et contexte

La consommation d'électricité peut être considérée comme l'un des facteurs les plus importants pour garantir la prospérité d'une société, visibles à travers deux indices économiques (tels que le PIB par habitant, Figure 1.2-a) et des indices de développement social (tels que l'IDH, Figure 1.2-b) [2]. L'augmentation de la consommation d'électricité par habitant peut directement stimuler une croissance économique plus rapide, qui favorise indirectement le développement social. La valeur précitée de 2 kWh peut être considérée comme le seuil de transition pour passer d'une économie à IDH basse à une moyenne (Figure 1.2-b). Lorsque cette quantité minimale d'électricité est utilisée pour le pompage de l'eau, la fourniture de lumière ou la réfrigération de nourriture et de médicaments, une communauté peut améliorer considérablement ses conditions de vie.
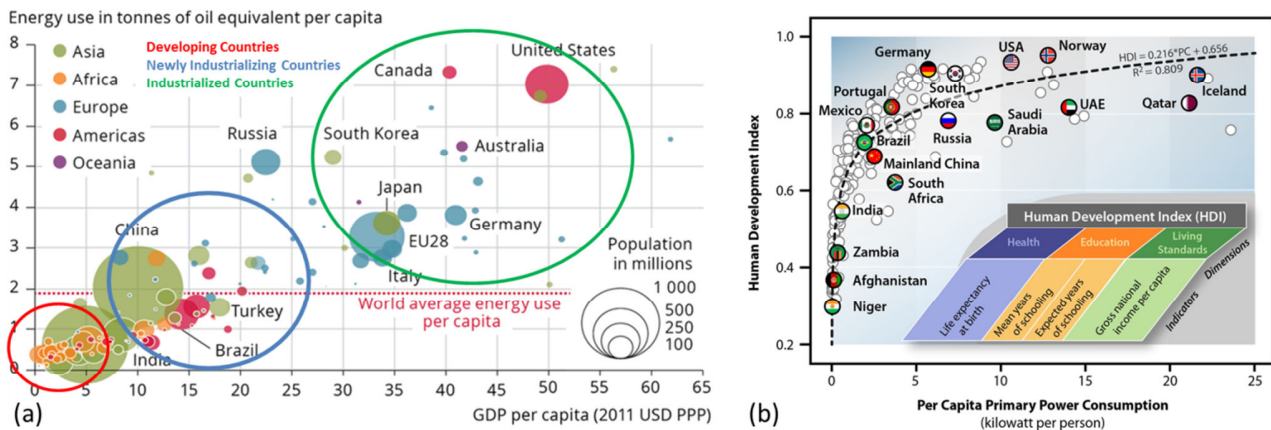
Figure 1.2 a) La relation entre le revenu moyen (GDP par habitant) et la consommation d'énergie (demande par habitant en kWh) en 2011 pour divers groupes de pays. La consommation d'énergie primaire d'un pays est représenté divisés par le nombre d'habitants. (b) consommation d'énergie par habitant et indice du développement humain pour 1991/1992, sur la base des données de 100 pays. Source a) EEA b) ourenergypolice.org.

L'électricité joue un rôle clé dans le développement économique et social. L'obtention de la quantité appropriée d'énergie propre pour soutenir la croissance de la population et le développement industriel est l'un des défis les plus difficiles auxquels notre génération doit faire face.

1.1.1 Situation actuelle et rôle des sources d'énergie renouvelables

Actuellement, environ 80% de l'énergie mondiale est produite par combustion de combustibles fossiles (Figure 1.3-a). Toutefois, ces combustibles sont une ressource finie. Les réserves mondiales connues de pétrole et de gaz s'épuiseront dans en moins de 65 ans, et celles du charbon en un peu plus de 100 ans si les niveaux du consummation restent ceux du 2012 [1].

Energy by source 2012 — Gross inland energy consumption

Renewable energy by source 2012 — Gross inland energy consumption

a)   b)
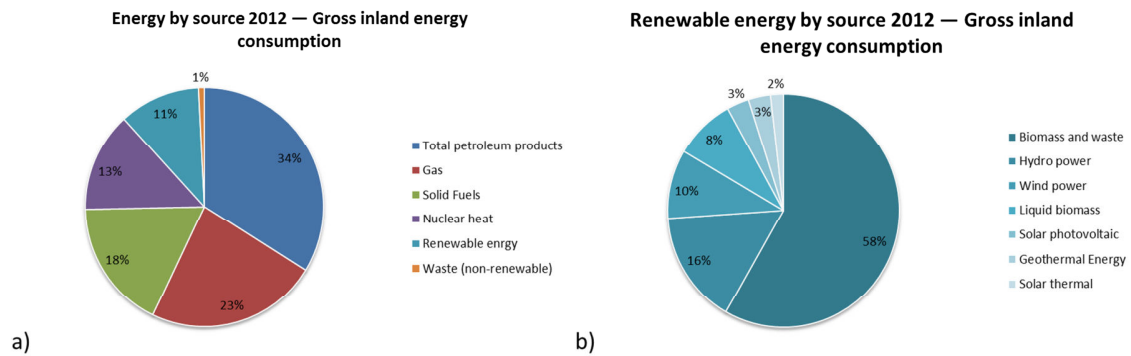
Figure 1.3 a) consomation intérieure brute d'énergie par source dans l'UE-28 en 2012 et b) la partie relative auxénergies renouvelables (EEA).

Le principal inconvénient de l'utilisation des combustibles fossiles est l'émission de dioxyde de carbone, comme sous-produit du processus de combustion, qui a un effet négatif sur l'environnement. La communauté scientifique reconnaît que la concentration de CO_2 (et autres gaz à effet de serre) dans l'atmosphère est l'un des principaux acteurs dans le changement climatique anthropique, avec l'appauvrissement de l'ozone dans l'atmosphère. Le réchauffement climatique est étroitement associé à d'autres changements et à leurs conséquences, comme la hausse du niveau des mers, l'augmentation des épisodes de précipitations intenses, la diminution de la couverture neigeuse et de la calotte glaciaire, plus fréquentes et les vagues de chaleur intenses, l'augmentation des feux de forêt, les saisons de croissance plus importantes, et l'acidification des océans. Individuellement et collectivement, ces changements posent problème pour les humains et l'environnement [3]. Ainsi, la perte de terres qui en résultera, entrainera une réduction de la production alimentaire et forcera la migration d'une grande partie de la population du monde [4]. Par conséquent, le rechauffement climatique devrait être une priorité mondiale. Une stratégie efficace à long terme devrait inclure à la fois la réduction de toutes les contributions anthropiques aux changements climatiques et le développement de stratégies pour atténuer ses effets. Espérons que le protocole de Kyoto sera couronné de succès dans la réduction des concentrations de CO_2, comme cela a déjà été fait avec des concentrations de CFC dans l'atmosphère avec le protocole de Montréal [5].

Dans sa feuille de route 2050 [6], la Commission européenne pose concrètement le problème du comment réduire l'utilisation de combustibles fossiles, tout en maintenant le niveau de vie actuel. L'UE considère que l'expansion du secteur des énergies renouvelables est le moyen viable important pour résoudre ce problème. En plus des avantages environnementaux bien connus, il offres un effet secondaire géostratégique, la diminution de dépendance aux combustibles fossils; celui permettra

d'accroître la position de l'UE en tant que puissance mondiale. En fait, comme les grandes puissances du monde ont tendance à avoir des gouvernements autoritaires et des institutions faibles [7], l'UE unie pourrait renforcer sa position vis-a-vis pays, en affaiblissant leur ressources financièrs.

Figure 1.4 La sécurité énergétique représente un moyen viable pour améliorer l'influence internationale.

La sécurité énergétique impose la nécessité de disposer des sources d'énergie permanent et à un prix abordable (source AIE) [8]. Elle a à la fois une dimension à court et à long terme. La première porte sur les investissements orientés pour soutenir les développements économiques et les besoins environnementaux durables, la deuxième se focalise sur la capacité du système énergétique à s'adapter aux changements de l'offre et de la demande. Le manque de sécurité énergétique a des conséquences socio-économiques négatives liées à la distribution d'énergie ou à des prix élevés et volatils.

1.1.2 Energies alternatives et contribution des sources renouvelables

Électricité abondante et pas chère sans forte émission de CO_2 pourrait provenir de l'utilisation de la fission nucléaire. Aujourd'hui, la production de chaleur nucléaire dans l'UE s'éléve à 13% (Figure 1.3-a). La production d'électricité nucléaire a augmenté de 11% entre 1990 et 2012, cependant, depuis 2005, une baisse moyenne de 1,7%/an a été enregistrée (Figure 1.5-a). Ceci est principalement dû à l'impopularité de l'énergie nucléaire dans l'opinion publique, liée aux dangers, réels ou perçus, en lien avec les déchets nucléaires ou à des catastrophes comme Tchernobyl et Fukushima. Cette situation ne permet pas aux gouvernements d'investir dans le long terme, comme dans la

construction de centrales électriques pour remplacer en totalité les combustibles fossiles.
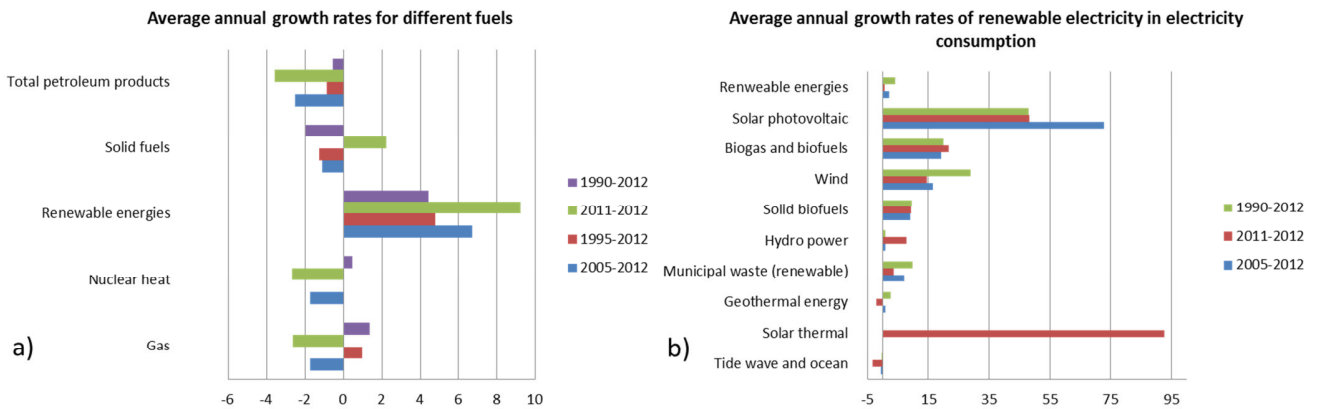
Figure 1.5 a) taux de croissance moyenne de la consommation d'énergie pour les différents sources et b) taux de croissance pour les sources renouvelables dans l'UE-28 (reproduit à partir de a) EEA et b EEA).

Les sources alternatives d'énergie capables de remplacer les combustibles nucléaires et fossiles existent depuis longtemps et ils sont généralement regroupés sous le terme d'énergies renouvelables. Une source d'énergie renouvelable est une énergie naturellement régénérée dans un délai raisonnable de sorte qu'elle ne soit jamais épuisée. En outre, afin de favoriser la diffusion d'une source d'énergie renouvelable ou de la technologie, l'énergie produite à partir de cette source doit avoir un prix compétitif vis-à-vis de ceaux des combustibles fossiles. Jusqu'à présent, les sources d'énergies renouvelables les plus utilisées sont les énergies produites à partir de biomasse et des déchets, qui représentent ensemble près de 60% de l'approvisionnement européenne en énergie renouvelable (Figure 1.3-b). Malheureusement, son expansion continue n'est pas possible en raison de la disponibilité limitée de combustibles bio-sourcés. Actuellement, les technologies et les sources alternatives concurrentielles sont les parcs éoliens terrestres, les installations hydroélectriques et la géothermie. Malheureusement, les caractéristiques géologiques nécessaires à la construction des centrales appropriées ne sont pas assez fréquentes pour remplacer les carburants fossiles. L'énergie éolienne a montré un certain intérêt ce qui a entrainé la construction de nombreux parc éoliens partout dans le monde et plus largement en Europe, Amérique du Nord et en Asie. En Europe, la production d'énergie éolienne a augmenté de 29%/an entre 1990 et 2012 (Figure 1.5-b). Cependant, la perspective défigurer les paysage avec des parcs éoliens pour couvrir la demande croissante n'est pas raisonnable. Les parcs éoliens offshore ont l'avantage de réduire l'impact à la fois sur terre et le paysage, mais le coût de construction de l'infrastructure les rend non compétitives. Cependant, le

coût de ces technologiesdevrait baisser dans l'avenir (Figure 1.6) et il est possible qu'ils joueront un rôle clé pour assurer la sécurité énergétique.

Range of fossil fuel power in OECD
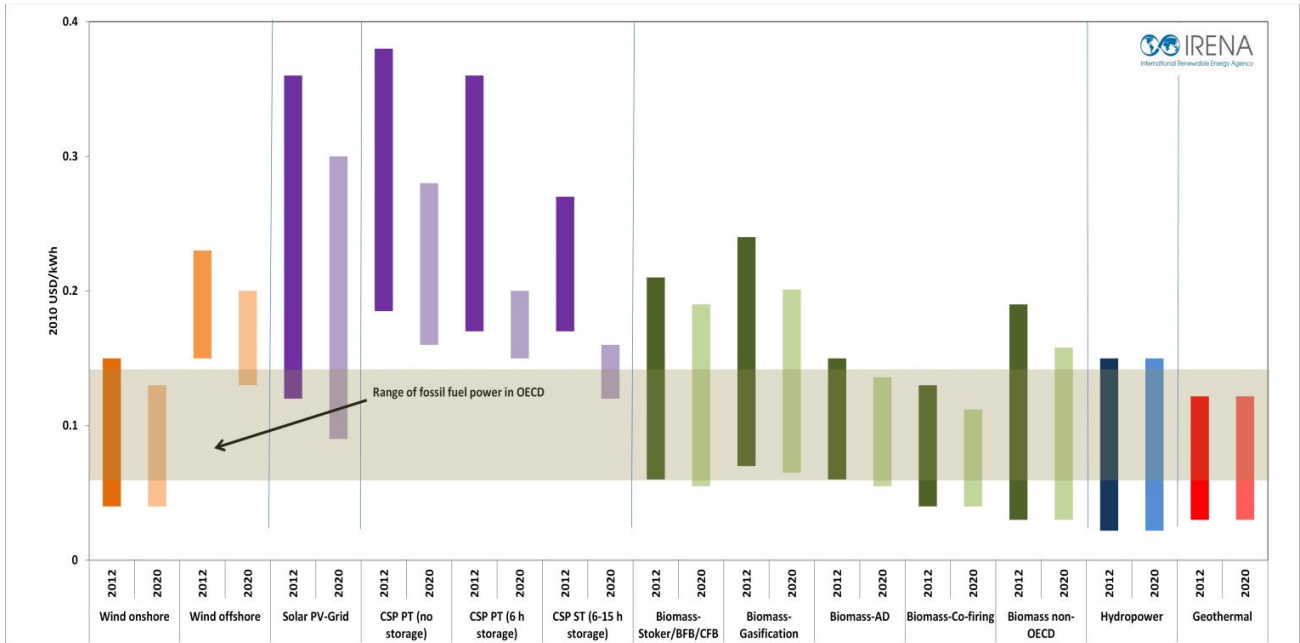
Figure 1.6 Prix pour kWh produit à partir de différentes sources d'énergie renouvelables en 2012 et une projection en 2020 [9].

Une autre option qui mérite considération est l'utilisation de l'énergie solaire. Dans les 25 dernières années, la production de l'énergie solaire a augmenté avec un taux de 48%/an et encore plus vite depuis 2005 (70%/an) (Figure 1.5-b). Cela a été possible grâce à des politiques gouvernementales, car les coûts liés à la technologie actuelle (CSP concentrée d'énergie solaire et photovoltaïque PV) sont trop élevés et pas vraiment concurrentiels (Figure 1.6). Cependant, selon l'AIE, l'énergie solaire a le plus grand potentiel (et il est assez abondante) pour couvrir toute seule et plusieurs fois la demande mondiale d'énergie à venir.

1.1.3 Photovoltaïque et photovoltaïque organique

La Terre reçoit plus d'énergie solaire en 1 heure que ce qui est nécessaire pour tous les besoins humains en un an [10]. Compte tenu de la facilité avec laquelle les panneaux solaires peuvent être installés, l'énergie solaire est la forme d'énergie la plus commercialisable et accessible [10]. Il y a un intérêt considérable dans le PV et sa capacité augmente chaque année (Figure 1.5-b). Toutefois, la croissance observée de l'industrie photovoltaïque, a été fortement subventionnée. Cela a été nécessaire en raison du coût élevé de l'énergie produite, en partie liée aux coûts associés à la fabrication des modules solaires en silicium ou en tellurure de cadmium (CdTe). Beaucoup

d'améliorations dans les processus de fabrication au cours des dernières années ont abouti à des cellules solaires moins chères, ce qui a permis de réduire le coût de l'électricité. Malheureusement, les coûts du 1 kWh n'est pas encore compétitif relativement à celui produit avec des combustibles fossiles (Figure 1.6).

L'objectif final de toutes les recherches sur le PV est de réaliser des modules commercialement attrayants (coût reduit et à haut rendement). Le photovoltaïque organique (OPV) est une alternative intéressante à la technologie silicium, car il offre une flexibilité intrinsèque, un coût réduit, un budget thermique réduit, traitement par solution, et des méthodes de fabrication très rapides. Le principal avantage par rapport aux PV inorganique est le coût de fabrication réduit. Par contre, le photovoltaïque organique a une efficacité et une stabilité inférieures au silicium. En fait, les modules de silicium cristallin ont des rendements de l'ordre de 20% et plus de 25 ans la durée de vie, tandis que le OPV sont encore loin de ces valeurs.
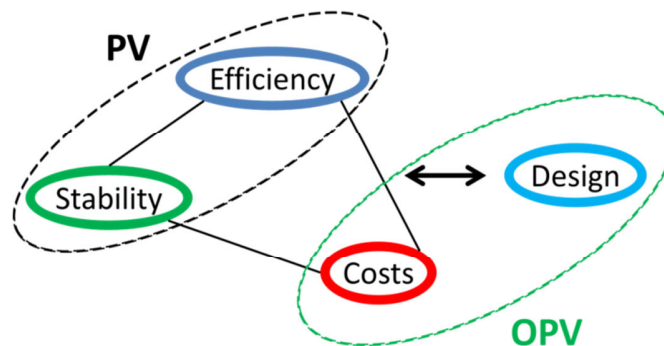
Figure 1.7 Le soit-disant triangle de Brabec (efficacité, stabilité, coûts) et un avantage unique pour l'OPV: liberté de conception.

Même si l'OPV a des performances inférieures à la technologie photovoltaïque au silicium, il est toujours utile de développer cette technologie en raison de ces faibles coûts de production, un traitement rapide et des avantages environnementaux. En outre, les avantages secondaires, tels que la flexibilité, légèreté, liberté de conception ouvrent la voie à des marchés de niche dans lequels le PV inorganique n'a pas d'application et où l'OPV peut faire la différence (Figure 1.7). Un grand effort de recherche, dans le milieu universitaire et industriel, doit être encore fait pour ce qui concerne l'efficacité et la stabilité. Beaucoup de travaux ont déjà été faits et, au niveau du laboratoire, des cellules solaires avec une efficacité de plus de 10% ont déjà été réalisées [11], alors que, en termes de stabilité, des efforts de recherche sont encore nécessaires. Le défi actuel est la production de ces

modules à l'échelle industrielle, avec une bonne stabilité (10-15 ans) et une efficacité comprise entre 10-15% et un coût reduit.

1.1.4 Le projet ESTABLIS

Le projet, 'Ensuring stability in organic solar cells' (FP7, Establis) est un réseau de recherche et de formation interdisciplinaire et inter-sectorielle, basée sur l'expertise complémentaire des grands groupes industriels et universitaires. Plus précisément, quatre "experienced researchers" (ER) et onze "early stage reaserchers" (ESR) ont été formés dans les domaines plus variés, à partir de la chimie organique à travers les aspects complémentaires de la science des polymères pour terminer avec la fabrication de dispositifs photovoltaïques à l'échelle industrielle, et cette formation interdisciplinaire a été un objectif important. L'objectif de ce projet était de développer des matériaux et des techniques nécessaires à obtenir des cellules solaires organiques (OSC) à bon marché avec 10 ans de stabilité. Les OSC sont à l'intersection des sciences physiques et chimiques et Establis a mis en place des strategies innovantes pour développer de nouveaux polymers, des architectures de cellules et techniques de caractérisations.

Deux approches différentes ont été utilisées pour améliorer la stabilité à long terme des dispositifs. La première a été l'introduction de nouveaux matériaux, l'amélioration des processus technologiques et des études complètes de vieillissement. La deuxième approche a été adoptée afin de clarifier les corrélations entre les propriétés optoélectroniques, les mécanismes de transfert de charge, la photochimie et la stabilité des matériaux.

Les objectifs scientifiques, nécessaires pour atteindre l'objectif du projet, peuvent être divisés en quatre groupes: (i) production de matériaux avec une stabilité améliorée ; (ii) explication des voies de dégradation photo(chimique) et mécaniques ; (iii) traitement des OSC avec contamination des inter-couches reduite et une adhésion interfaciale accrue ; (iv) modélisation du vieillissement photochimique en relation avec les propriétés optoélectroniques. Les chercheurs ont donc été répartis en quatre groupes de travail (Figure 1.8) avec des tâches spécifiques et une large compétence multi-disciplinaire.

1 Motivation et contexte
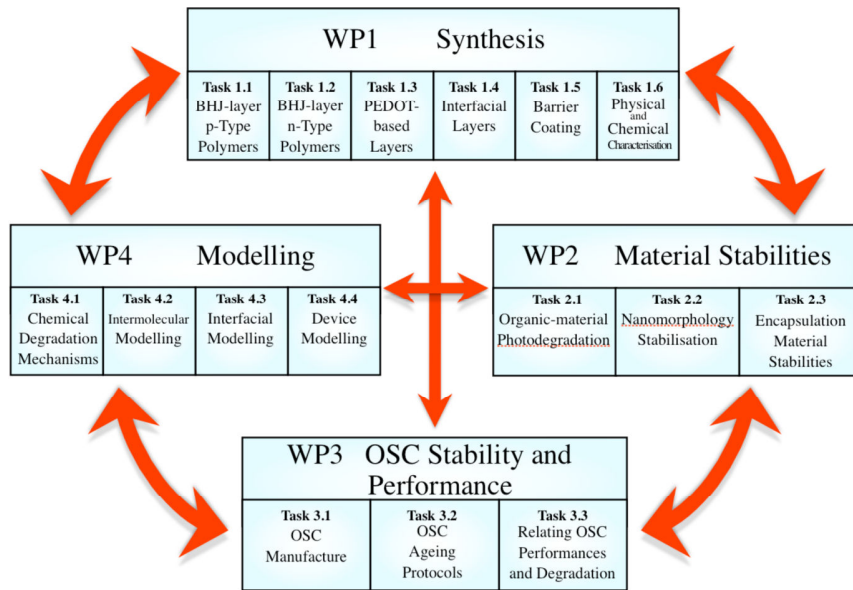
Figure 1.8 Establis modules de travail et les tâches relatives.

Les différents partenaires (P) et partenaires associés (AP) avec les ER et ESR correspondants du projet Establis sont présentés dans le Tableau 1.1.

Table 1.1 Establis partenaires et boursiers concernés.

P1	Université de PAU et des pays de l'Adour	Hugo Santos Silva (ESR1)
		Alberto Gregori (ESR2)
P2	Belectric OPV GmbH (formerly Konarka Technologies GmbH)	Dr. Simon A. Dowland (ER1)
		Dr. Dargie Deribew (ER2)
P3	Vilniaus Universitetas	Meera Stephen (ESR3)
P4	Merck Chemicals Ltd	Dr. Grahgam Morse (ER3)
P5	Instituto Madrileno de Estudios Avanzados	Safakath Karuthedath (ESR4)
P6	Heraeus Precious Metals GmbH & Co KG	Dr. Stefan Schumann (ER4)
P7	Johannes Kepler Universität Linz	Olena Kozlova (ESR5)
P8	Aston University	Joanna Kolomanska (ESR6)
		Anna Isakova (ESR7)
P9	Institut de Chimie de Clermont-Ferrand (Centre National de Recherche Scientifique)	Isabel Fraga Dominguez (ESR8)
		Evgeniia Topolniak (ESR9)
P10	Eberhard-Karls-Universität Tibingen	Aurélien Tournebize (ESR10)
P11	Medzinarodne Laserove Centrum	Mamadou Abass Seck (ESR11)
AP1	Evonik Degussa GmbH	

AP2	Siemens Corporate Technology	
AP3	AMCOR	

1.1.5 Objectifs du travail

Le but de ce projet de thèse était de synthétiser de nouveaux polymères à faible bande interdite (LBG) et de les appliquer dans des dispositifs OPV pour en améliorer la stabilité. La synthèse et la caractérisation de nouveaux polymères LBG à base de dithienosilole et diketopyrrolopyrrole ou dithienyl-thienopyrazine est décrite, ainsi que leurs résultats dans des dispositifs photovoltaïques OPV.

La stabilité mécanique des dispositifs est fondamentale pour l'application à long terme et l'investigation dans ce domaine n'a commencé que récemment. Une nouvelle technique expérimentale a été développée afin de caractériser la force d'adhésion dans les dispositifs OPV et elle est présentée, avec deux voies possibles pour améliorer l'adhésion à l'interface la plus faible, soit par l'utilisation de nouveaux matériaux soit par de nouvelles architectures.

Le travail présenté dans les chapitres suivants a été fait en collaboration avec certains des autres ER et ESR, dans l'esprit de collaboration du projet. La conception et la synthèse des deux séries de polymères à faible bande interdite (LBGs) a été fait par moi-même à l'Université de Pau, avec les conseils du Dr Graham Morse (Merck Chemicals Ltd), qui a également effectué une partie de la caractérisation chimique. Dr Simon A. Dowland, Dr Mirella El Gemayel et Dr. Dargie Deribew m'ont formé dans la fabrication de dispositifs au cours de mon déplacement chez Belectric OPV GmbH et nous avons aussi travaillé ensemble sur la fabrication et la caractérisation de dispositifs intégrant les LBGs synthétisés à l'Université de Pau. Safakath Karutedath (Imdea Nanociencia) a été impliqué dans la caractérisation du comportement des porteurs de charge dans le mélange polymère:$PC_{61}BM$, par spectroscopie d'absorption transitoire (TAS). Isabel Fraga Domínguez (Université Blaise Pascal) a travaillé sur la stabilité d'une série de polymères (**PSBDPP**) seuls et en mélange avec le $PC_{61}BM$, en condition de photo- et thermo-oxydation. Dans le but de relier le taux de dégradation avec leurs propriétés physico-chimiques, elle a caractérisé le contenu en espèces paramagnétiques par Résonance Paramagnétique Electronique (RPE), la cristallinité des films minces par diffraction des

rayons X (XRD) et les propriétés thermiques par Rapid Heat-Cool Calorimétrie (RHC) de cette série de polymère.

Dr. Stefan Schumann a été impliqué dans le développement de set-up pendant son déplacement à Pau, puis nous avons collaboré en testant les propriétés adhésives de dispositifs intégrant différentes formulations de **PEDOT:PSS** developpées par notre partenaire Heraeus Deutschland GmbH & Co. KG, visant à une amélioration de la force adhesion à l'interface entre la couche active/**PEDOT:PSS**. La deuxième stratégie pour améliorer la force d'adhésion a été l'introduction d'une couche de copolymère à blocs à cette interface. Ces copolymères à blocs ont été conçus et synthétisés par Joanna Kolomanska (Université Aston). J'ai également participé à la synthèse de ces copolymères à blocs pendant mon déplacement à l'Université d'Aston. Aurélien Tournebize (Université de Tübingen) a été également impliqué dans la caractérisation par XPS et AFM, des surfaces après les tests d'ahésion, afin d'acquérir une meilleure compréhension de l'effet de ces nouveaux matériaux.

Tous les résultats présentés, résultent de la discussion avec mes superviseurs (Dr Christine Dagron-Lartigau, Prof. Ahmed Allal, Dr Roger C. Hiorns et Dr Andreas Distler) ainsi qu'avec les autres chercheurs impliqués (Dr. Stefan Schumann, Aurélien Tournebize, Dr Simon A. Dowland, Dr Dargie Deribew, Dr Graham Morse, Isabel Fraga Dominguez, Joanna Kolomanska, Safakath Karuthedath et Dr Mirella El Gemayel du projet POCAONTAS). Remerciements spécifiques sont donnés lorsque leurs données sont présentés au cours de la discussion.

Cette thèse est structurée comme suit: après ce premier chapitre qui présente le contexte socio-économique, environnemental et politique qui contextualise le travail scientifique, le manuscrit procède à une introduction des concepts de base et de l'évolution de l'OPV, présentant les principes de conception et synthèse de polymères, de la formation des couches minces et de l'architecture du dispositif, qui ont conduit à l'état de l'art actuel. Dans les chapitres 3 et 4, les résultats en termes de synthèse, caractérisation chimique et performances des dispositifs basés sur les nouveaux polymères push-pull LBGs basé sur le dithienosilole (unité de donneur) et le diketopyrrolopyrrole ou le dithienylthienopyrazine (unité accepteur) sont présentés. Le chapitre 5 décrit le développement d'un dispositif expérimental pour caractériser les forces d'adhésion entre les couches minces dans le cas de dispositifs réels. La technique a ensuite été étendue à de nouveaux matériaux et architecture développés au sein du projet Establis.

1.2 References

[1]   International Energy Agency, "WORLD ENERGY OUTLOOK 2014," 2015.

[2]   C. S. Leung and P. Meisen, "How electricity consumption affects social and economic development by comparing low, medium and high human development countries," no. 153, pp. 1–12, 2005.

[3]   National Research Council, "Advancing the Science of Climate Change," *Natl. Acad. Press*, pp. 1–4, 2010.

[4]   IPCC, "Intergovernmental Panel on Climate Change. Climate Change 2014 Synthesis Report," p. 80, 2014.

[5]   "THE MONTREAL PROTOCOL ON SUBSTANCES THAT DEPLETE THE OZONE LAYER." [Online]. Available: http://ozone.unep.org/en/treaties-and-decisions/montreal-protocol-substances-deplete-ozone-layer.   [Accessed: 24-Nov-2015].

[6]   European Climate Foundation, "Roadmap 2050," vol. Volume 2, 2010.

[7]   F. Umbach, "Global energy security and the implications for the EU," *Energy Policy*, vol. 38, no. 3, pp. 1229–1240, 2010.

[8]   IEA,   "What   is   energy   security?"   [Online].   Available: http://www.iea.org/topics/energysecurity/subtopics/whatisenergysecurity/. [Accessed: 02-Oct-2015].

[9]   IRENA - International Renewable Energy Agency, "Renewable Power Generation Costs," no. November 2012, p. 12, 2012.

[10]   D. G. Nocera and M. P. Nash, "For the '"In This Issue"' summary," vol. 104, no. 42, 2007.

[11]   "Solarmer Energy." [Online]. Available: http://www.solarmer.com/home.html. [Accessed: 11-Mar-2015].

2 Introduction

2.1 Brief history

Organic solar cells found their origin in the 1950s when the dark conductivity of halogen-doped organic compounds was studied [1], even if the photoconductivity of condensed polyaromatic systems was known since the beginning of the 20th century [2]. Although many of these compounds were not stable, many investigations focused on the understanding of the charge transport electronic properties of these conjugated systems. The first generation of OSCs was based on a single organic layer sandwiched between two metal electrodes with appropriate work function [3]. These devices showed very low power conversion efficiency (*PCE*) due to poor charge carrier generation and ineffective charge transport. In the following years, researchers focused on the understanding and improvement of the PCE, through the investigation of the effect of the metal/organic contact [4], the introduction of new organic dyes [5] [6] and semitransparent electrodes [7], leading to OPVs surpassing 1% efficiencies in 1978.

In 1986, Tang introduced a new architecture in the effort to improve the photocurrent of the solar cell device: the bilayer heterojunction (Figure 2.1) [8]. The photoconductivity of laminated organic systems was first studied in 1958 by Kearns and Calvin [9]; it involves two different organic layers: a *p*-type layer (donor material) for hole transport and a *n*-type layer (acceptor material) for electron transport. Through this innovation the devices reported by Tang showed a PCE of almost 1%. He utilized a phtalocyanine derivative for the *p*-type semiconductor and a perylene derivative for the *n*-type semiconductor. Indium tin oxide (ITO) was used as transparent electrode, while the back electrode was metallic [8].

In contrast to inorganic photovoltaics, absorption of a photon by the photoactive layer of organic devices produces a neutral excited state (exciton) instead of free charge carriers. This Frenkel exciton has to diffuse to the donor-acceptor (D-A) interface in order to dissociate and form free charge carriers *via* electron-transfer. Then, the charge carriers are free to migrate to the respective electrodes. This migration is supported by the internal electric field, which in turn generates the photocurrent and the photovoltage. In such devices, only excitons created within the distance of about 10 nm [10] from the interface can reach the latter. This leads to the deactivation of excitons being formed further away from the interface, resulting in lower quantum efficiencies. Consequently, the performance of bilayer heterojunction devices is strongly limited by the small effective interfacial area between the donor and acceptor [11], [12].
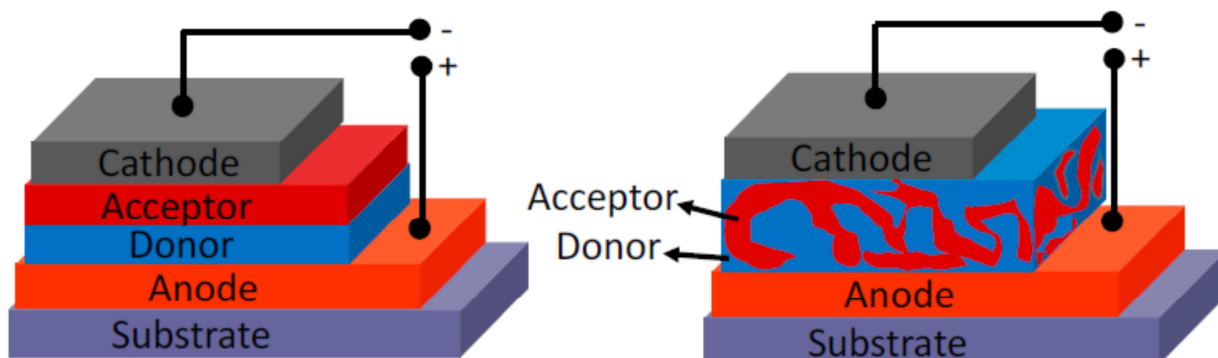
Figure 2.1 Bilayer (left) and bulkheterojunction (right) solar cell architectures. Image reproduced from reference [13]**.**

The following development was introduced taking into account the short exciton diffusion length. The effective charge-generating area is increased by augmenting the interface between *p*- and *n*-type materials. In 1991, scientists from Osaka University made the first bulk heterojunction solar cell (Figure 2.1) by co-sublimation of the two dyes, reaching a *PCE* of 0.7% [14]. In 1992, Heeger's group at UC Santa Barbara reported for the first time the photoinduced electron transfer between poly[2-methoxy-5-(2'-ethyl-hexyloxy)-*p*-phenylenevinylene (**MEH-PPV**) and fullerene (**C$_{60}$**) [15]. This system showed an efficient photoinduced electron transfer and an increased photocurrent. In 1995, the same group applied this new concept and reported the first bulk heterojunction polymer solar cell, again using **C$_{60}$** and **MEH-PPV** [16]. In a BHJ, an interpenetrating network with a large D-A interfacial area can be achieved by controlling the phase separation between the two components. In the ideal situation any absorbing site in the blend is within few nanometers from the *D/A* interface, leading to an enhanced quantum efficiency of charge separation. The formation of a bicontinuous and interpenetrating network ensures the presence of two channels which transport holes in the donor domain, and electrons in the acceptor one, resulting in efficient charge collection.

2.2 Working principle
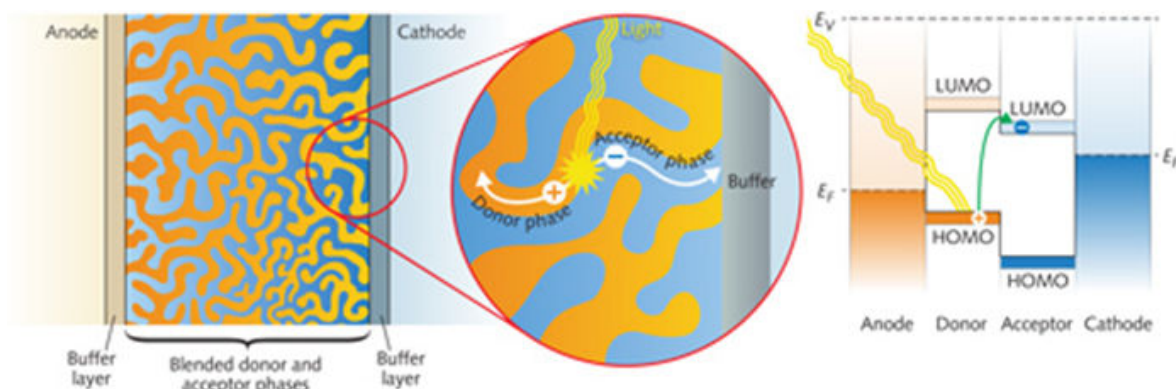
Figure 2.2 Working principle in BHJ solar cell. Image reproduced from reference [17]**.**

The first step is the absorption of photons emitted by the sun (Figure 2.2). The absorption of incident radiation by the material of the active layer causes excitation of the molecules with the passage of an electron from the highest occupied molecular orbital (HOMO) to the lowest unoccupied molecular orbital (LUMO). The band-gap (E_g) of a polymer is defined as the energy difference between the HOMO and the LUMO, and is typically expressed in electronvolt (eV). Once in its excited state, the molecule can decay to its ground state through a radiative (fluorescence or phosphorescence) or non-radiative (thermal relaxation) process. This internally bound electron-hole pair, called an exciton, is at the origin of the photovoltaic effect. Its lifetime is of the order of a few nanoseconds. Excitons formed are considered Frenkel type, bound by strong electrostatic interaction with a binding energy between 0.1 and 0.5 eV. Excitons can diffuse through the material to reach a dissociation site at the interface between the donor (*p*-type) and acceptor (*n*-type) materials. In the case of π-conjugated polymers, the exciton diffusion length varies from 10 to 20 nm [18]. If the dissociative sites are further than the exciton diffusion length, the Frenkel exciton will relax to the ground state. For this reason, the morphology and the domain size of the active layer play a decisive role in avoiding the exciton deactivation. At the *D/A* interface, an electric field is created by the difference in the potential of the two materials. Indeed, these two materials have different energy levels, inducing a local electric field capable of compensating for the attraction between the electron and the hole. If the exciton reaches this interface, it can be separated into an electron in the LUMO of the acceptor and a hole in the HOMO of the donor via charge transfer. To promote this transfer, it is necessary that the energy of the exciton is greater than the difference between the donor ionization energy and electron affinity of the acceptor.

Finally, the separated charges have to reach the electrodes. This step is determined by the mobility of the charge carriers in the active layer ($\mu < 1$ cm$^2 \cdot$V$^{-1} \cdot$s^{-1} for organic materials). This low value may be compensated for either by improving the crystallinity of the active layer [19] or by using intermediate layers. These layers, which are sandwiched between the active layer and the electrodes, increase the internal field and let selectively pass only one type of charge carriers. For example, a layer of poly(3,4-ethylenedioxythiophene) doped with poly(styrene sulfonate) (*PEDOT:PSS*) can promote the collection of holes [20] and a lithium fluoride layer (**LiF**), which promote the collection of electrons [21]. Transporting electrical loads are very dependent on the purity of the materials, as impurities act as traps that greatly reduce the mobility.

2.3   Device structures

The two most common structures of BHJ solar cells are the normal and inverted architectures (Figure 2.3). The definition of the two geometries is related to the direction in which the charges flow.

In a normal geometry solar cell the bottom electrode is the positive electrode and the top electrode is then the negative one. In the inverted geometry, the two electrodes and the charge selective layers are swapped, such that the bottom electrode is the negative one while the top electrode is the positive one. Different buffer layers can be added to improve the diffusion of holes/electrons in a certain direction (hole/electron transporting layers, HTL or ETL) and to tune the work function of an adjacent layer. In the normal geometry, the most common transparent hole-collecting electrode is an inorganic oxide (indium tin oxide, **ITO**). On top of it, a layer of the conductive polymer **PEDOT:PSS** is deposited to reduce the roughness of the **ITO** and to act as an HTL. Then, the photoactive layer (AL) is deposited by solution processing a blend of the donor and the acceptor materials and, finally, an aluminum layer that serves as electron collecting electrode (cathode) is deposited by vacuum evaporation or printing. It has been shown [22] that the **PEDOT:PSS** layer and the low work function electrode limit the lifetime of the devices.

In the inverted geometry, the most popular bottom electrode is again **ITO**. An extra electron transporting layer (**ZnO, TiO**, etc) is presented to improve the device performance. The interface between the hole collecting electrode and the active layer can be improved by a buffer layer such as **PEDOT: PSS**, **V$_2$O$_5$**, the **WO$_3$** and **MoO$_3$** in order to reduce the recombination of electrons and holes and increase the charge collection.
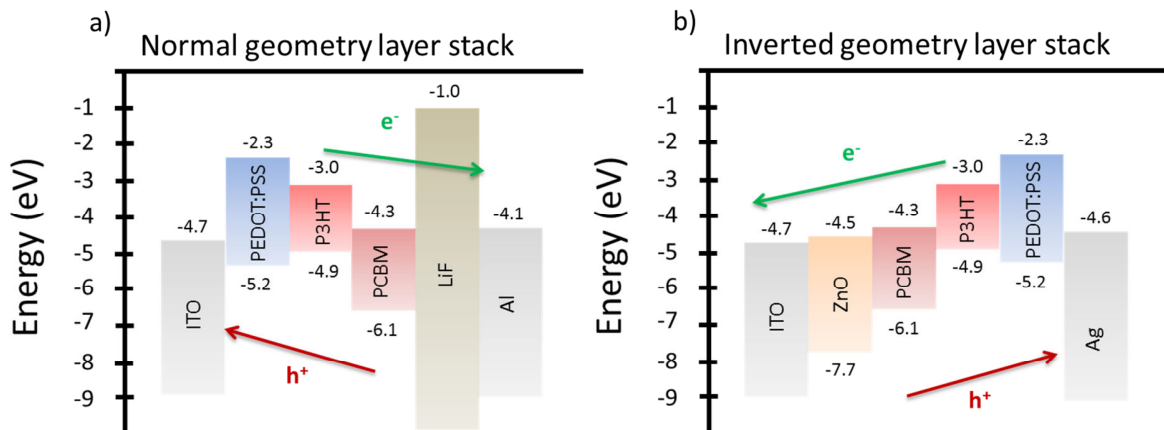
Figure 2.3 Energy levels of materials in P3HT:PC$_{61}$BM BHJ solar cell for normal (a) and inverted (b) geometries.

Another common architecture is the tandem solar cell. In this case the objective is to absorb most of the solar emission spectrum and thus increase the efficiency of the device by increasing the photocurrent. The approach is to fabricate p-n, p-i-n or other diode structures combining semiconductors of different band gaps and connect them to form a single device that may be able to improve the photovoltaic conversion. To make such a cell, there are two possible ways to connect the diodes: in series or in parallel. Currently, the series connection is the most widely used. Adjacent devices are connected by a junction, the open circuit voltage of the tandem cell is equal to the sum of the voltages of the two different cells [23], while the short-circuit current of the tandem cell is determined by the lowest one of the two separated cells.
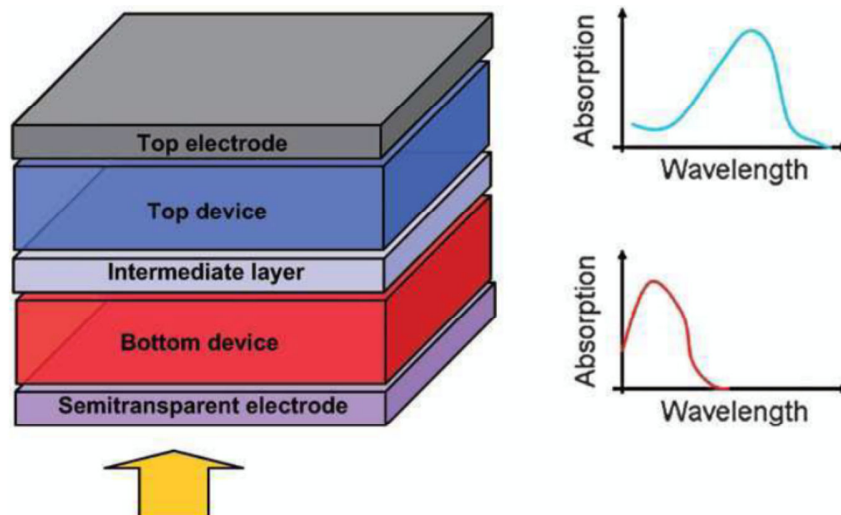
Figure 2.4 Layer stack of tandem OPV with possible absorption spectra of a combination of polymers for the photoactive layers. Image reproduced from reference [24].

A record *PCE* of over 11.5% has been obtained for single junction devices [25], while for tandem solar cells the record efficiency is over 12% [26].

2.4 Parameters governing overall performance of solar cells

The *power conversion efficiency* (*PCE*) of a solar cell is defined as the ratio between the output power (P_{out}) and the incoming power (P_{in}), where P_{out} can be expressed as the product of the *open-circuit* voltage (V_{OC}), the *short-circuit* current density (J_{SC}) and the *Fill Factor* (*FF*) [27][28] (equation (2.1)):

$$PCE = \frac{P_{out}}{P_{in}} = \frac{V_{OC} \times J_{SC} \times FF}{Pin}$$

(2.1)

The V_{OC} is defined as the voltage between the terminals when no current is drawn (infinite load resistance) and J_{SC} is the current when the terminals are connected to each other (zero load resistance).
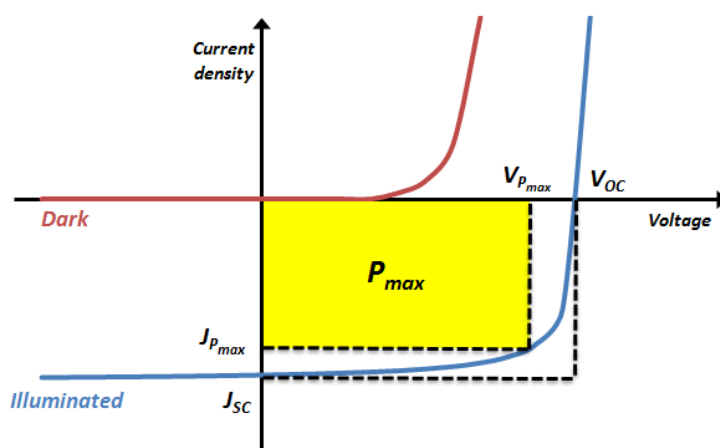
Figure 2.5 Current-voltage (J-V) characteristics of a typical solar cell.

The V_{OC} represents the maximum voltage that can be yielded by the solar cell under open-circuit conditions. For bulk heterojunction solar cells it depends on the organic material and in particular on their frontier orbitals. In fact, according to the models proposed by Scharber [29] and Koster [30], V_{OC} is determined as the difference between the HOMO level of the donor and the LUMO of the acceptor.

When $PC_{61}BM$ is employed as acceptor, whose LUMO level is -4.2 eV, the ideal LUMO level of the polymer should be around -3.9 eV. An offset of around 0.3 eV between the LUMO energy levels of the polymer and acceptor is required for an efficient exciton dissociation. It has also been proposed

that lowering the HOMO of the polymer and increasing the LUMO of the acceptor will cause an increase in the V_{OC} resulting in higher efficiency [29][30]. Furthermore, it has been found that the V_{OC} does not strongly depend on the work functions of the electrodes [31][32].

The J_{SC} is the maximum photocurrent that could be obtained in a given solar cell when no voltage is applied. It mainly depends on the photon absorption of the photoactive layer. Thus, maximizing the matching between the absorption spectra of the donor-acceptor blend and the solar emission spectra will maximize the number of excitons generated and consequently the J_{SC}.

While the measured V_{oc} matches closely the theoretical value, the short-circuit current is always found to be lower than the theoretically predicted values. This is due to a series of loss mechanisms, which are strongly related to the morphology as well as to the lifetime and mobility of the charge carriers [33][34]. For example, if the domain size is too large, excitons can be lost due to exciton decay (the exciton diffusion length is on the order of 10 nm). On the other hand, domains being too small can induce an enhanced recombination of the charge carriers [35]. Moreover, the donor and acceptor domains need to form percolative paths towards the electrodes, in order to enable charge collection.

The *Fill Factor* describes the quality of the solar cell and is determined by the following equation (2.2):

$$FF = \frac{V_{P_{max}} \times I_{P_{max}}}{V_{OC} \times I_{SC}}$$

(2.2)

The *FF* depends on the competition between charge carrier recombination and transport processes. Additionally, a high series resistance and a low shunt resistance can significantly influence the *FF* and thus should be minimized and maximized, respectively.

A solar cell can be described through its equivalent circuit, a generator in parallel to a diode (Figure 2.6):
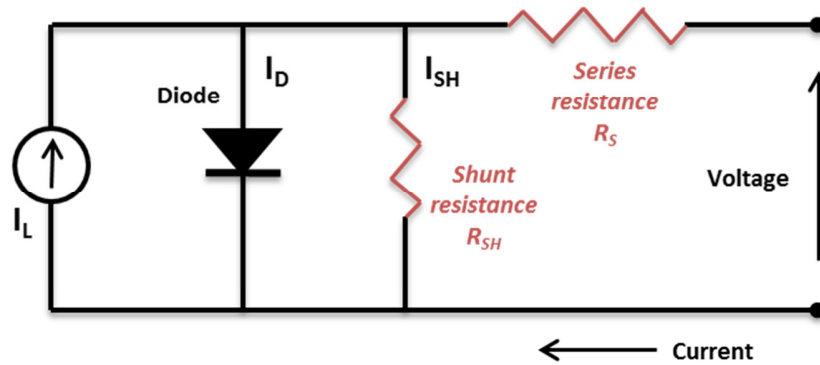
Figure 2.6 Equivalent circuit of an organic solar cell.

Resistive effects in solar cells can reduce its efficiency by dissipating power in the resistances. The two most common parasitic resistances are the *series resistance (R_S)* and the *shunt resistance (R_{SH})*.

The total current through the circuit can be expressed as (equation (2.3)):

$$I = I_L - I_D - I_{SH} \qquad\qquad (2.3)$$

where I_L is the photogenerated current, I_D is the current flowing through the *diode* and I_{SH} is the current through the *shunt resistance*.

R_S depends on the resistivity of the materials in the solar cell and on the contact resistance at their interfaces. Its main impact is to reduce the *FF*, while high values may also reduce the J_{SC} (equation (2.4)):

$$I = I_L - I_0 \times e^{\frac{q(V + IR_S)}{nkT}} \qquad\qquad (2.4)$$

where *I* is the cell output current, I_L is the photocurrent, *V* is the voltage across the cell terminals, *T* is the temperature, *q* is the electron charge, *k* is the Boltzmann constant, *n* is the ideality factor, and R_S is the series resistance. Series resistance does not affect the solar cell at *open-circuit voltage* since the overall current flow through the equivalent circuit is zero. However, near the open-circuit voltage, the I-V curve is strongly affected by R_S. A straight-forward method of estimating the series resistance of a solar cell is to find the slope of the I-V curve at the open-circuit voltage point.

R_{sh} is a parallel resistance, that corresponds to a current dispersion of the diode. The effect of a shunt resistance is particularly severe at low light levels, since there will be less light-generated current and the loss of this current to the shunt therefore has a larger impact. In addition, at lower

voltages where the effective resistance of the solar cell is high, the impact of a low resistance in parallel is large.

The equation for a solar cell in presence of a *shunt resistance* is (equation (2.5)):

$$I = I_L - I_0 \times e^{\frac{qV}{nkT}} - \frac{V}{R_{SH}}$$

(2.5)

where *I* is the cell output current, I_L is the light generated current, *V* is the voltage across the cell terminals, *T* is the temperature, *q* is the electron charge, *k* is the Boltzmann constant, *n* is the ideality factor and R_{SH} is the cell shunt resistance.

In conclusion, in the presence of both *series* and *shunt resistances*, the I-V curve of the solar cell is given by (equation (2.6)):

$$I = I_L - I_0 e^{\frac{q(V+IR_S)}{nkT}} - \frac{V + IR_S}{R_{SH}}$$

(2.6)

2.5 Materials for the PhotoActive Layer

2.5.1 Acceptor Materials

In this sub-section a brief overview of the main acceptor materials [36] will be presented. The acceptor material is the material which accepts the electron from the donor material, ensuring the exciton separation and the electron transport to the electrode. In general it participates poorly in the absorption process. Acceptors can be divided in two categories: fullerene-based and non-fullerene.

2.5.1.1 Materials based on fullerene

Due to its reduced solubility, fullerene (**C_{60}**) has been replaced by its derivatives, among which the most common is **phenyl-C_{61}-butyric** acid methyl ester (**$PC_{61}BM$**) [37], which is soluble in most organic solvents. Moreover, it has a good electron mobility (4.2×10^{-3} $cm^2V^{-1}s^{-1}$) [38], good acceptor properties, and good miscibility with conductive polymers. Many efforts have been performed to further improve the solubility and to optimize the phase segregation of fullerene derivatives in the bulk, without reducing its optoelectronic properties. Few examples are reported in Figure 2.7: phenyl-C_{61}-butyric acid alkyl ester **$PC_{61}BB$** [39] in which the alkyl-chain length is explored, thienyl-C_{61}-butyric

---
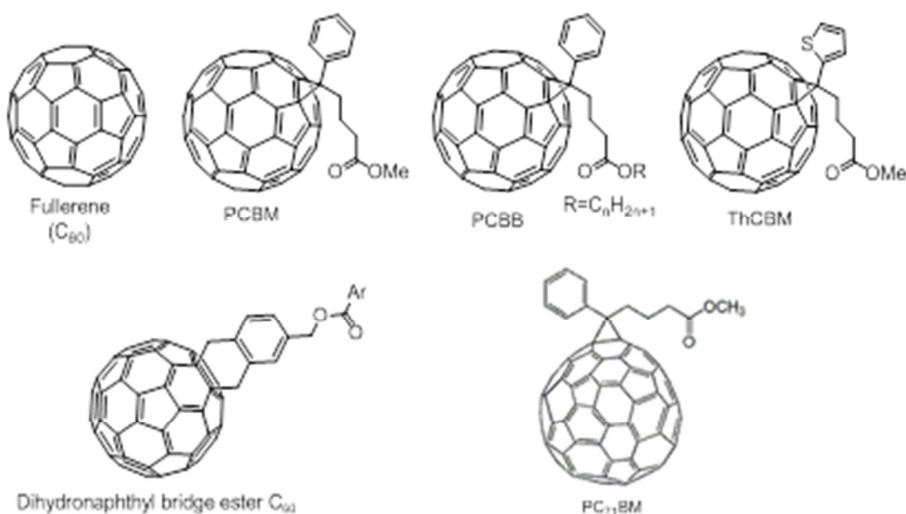
Figure 2.7 Different derivatives of fullerene.

acid methyl ester (**ThC$_{61}$BM)** [40] in which the aryl substituent is thiophene instead of phenyl and the **dihydronaphtyl bridge ester C$_{60}$** [41] in which is the methylene bridge to be substituted.

Another fullerene used in organic photovoltaics is **C$_{70}$** and its derivative phenyl-C$_{71}$-butyric acid methyl ester (**PC$_{71}$BM**) [42]. **C$_{70}$** has an asymmetric structure and a stronger absorption in the visible region than **C$_{60}$**. It has been used in combination with many π-conjugated polymers and in particular with LBG polymers [43][44].

2.5.1.2 Other types of acceptors

Even though fullerene derivatives are the most diffused acceptors in OPVs, some drawbacks such as a limited absorption in the visible region and hardly tunable LUMO levels are pushing the research for new materials. With this aim both small molecules and polymers have been investigated.
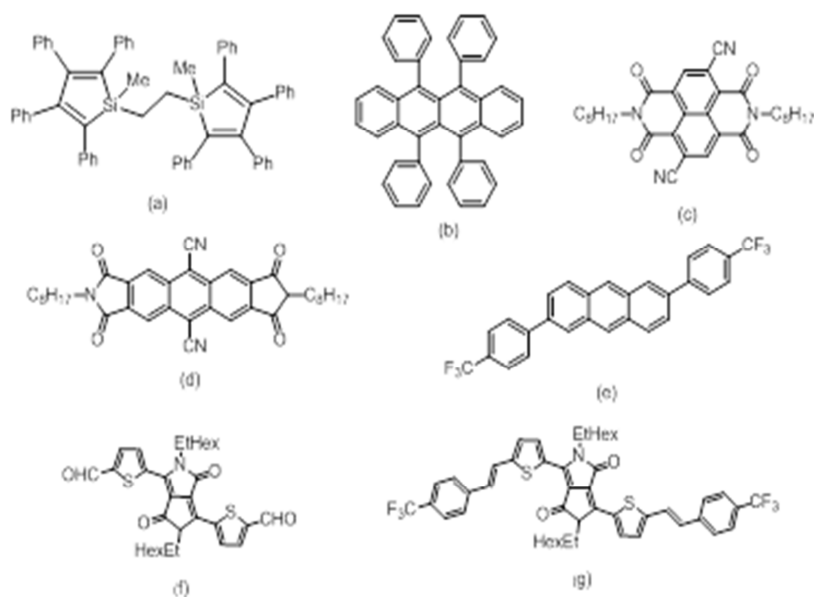
Figure 2.8 Examples of small molecule acceptors for OPV and OFET application.

Amongst the small molecules considered, there are derivatives of siloles (Figure 2.8 (a) [45]), acenes (Figure 2.8 (b) [47], (d) [48], perylenediimides (Figure 2.8 (c) [46]) and (e) [49]), diketopyrrolopyrrole (Figure 2.8 (f) [50], and (g) [51]), etc.

Polymers have also been studied as acceptors. In their case, the main advantage is the easy

tunability of their energy levels, ensuring efficient exciton dissociation and charge transport in the active layer. In some cases electron withdrawing groups have been attached to donor polymer (Figure 2.9 (a) [52]) or polymer which contains the aforementioned small molecules in their backbones (Figure 2.9 (b) [53], (c) and (d) [54]) or as lateral groups (Figure 2.9 (e) [55]).
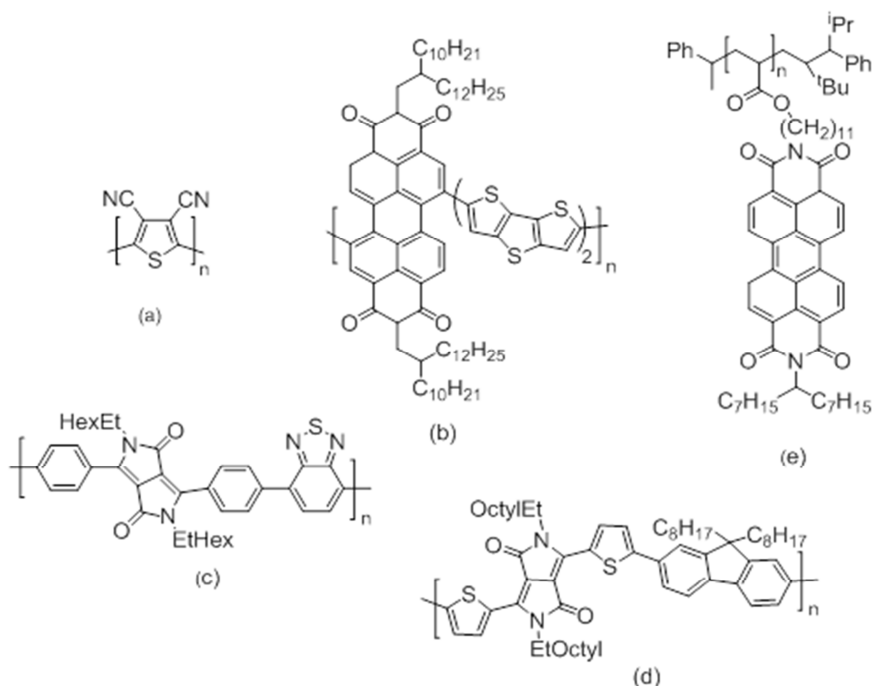
Figure 2.9 Examples of n-type polymers used as acceptors in OPV and OFET applications.

2.5.2 Donor materials

This sub-section opens with a brief overview of the main donor materials both small molecules and conjugated polymers, to then introduce low band-gap polymers, the subject of this thesis.

2.5.2.1 Small molecules

Small molecules present some advantages with respect to other donor materials, maintaining performance comparable to polymer solar cells, with a record *PCE* of 12% [26]. For example, high reproducibility is achievable due to the well-defined molecular structure and to the vapour deposition processes, which leads to highly controlled and well defined layers of high purity. During the last 10 years many other molecules have been synthesized and proposed as donor materials [56].

Since 2005, interest in this area has rapidly increased, leading to the synthesis and to a different application of many classes of π-conjugated molecules (Figure 2.10 [57]) such as oligothiophenes (a) [58], triphenylamines (b) [59], **EDOT**-based systems (c) [60], diketopyrrolopyrroles

(d) [61], dicyanopyrane derivatives (e) [62], merocyanines (f) [63], oligoacenes (g) [64], squaraines (h) [65], indigos (i) [66], *etc.*
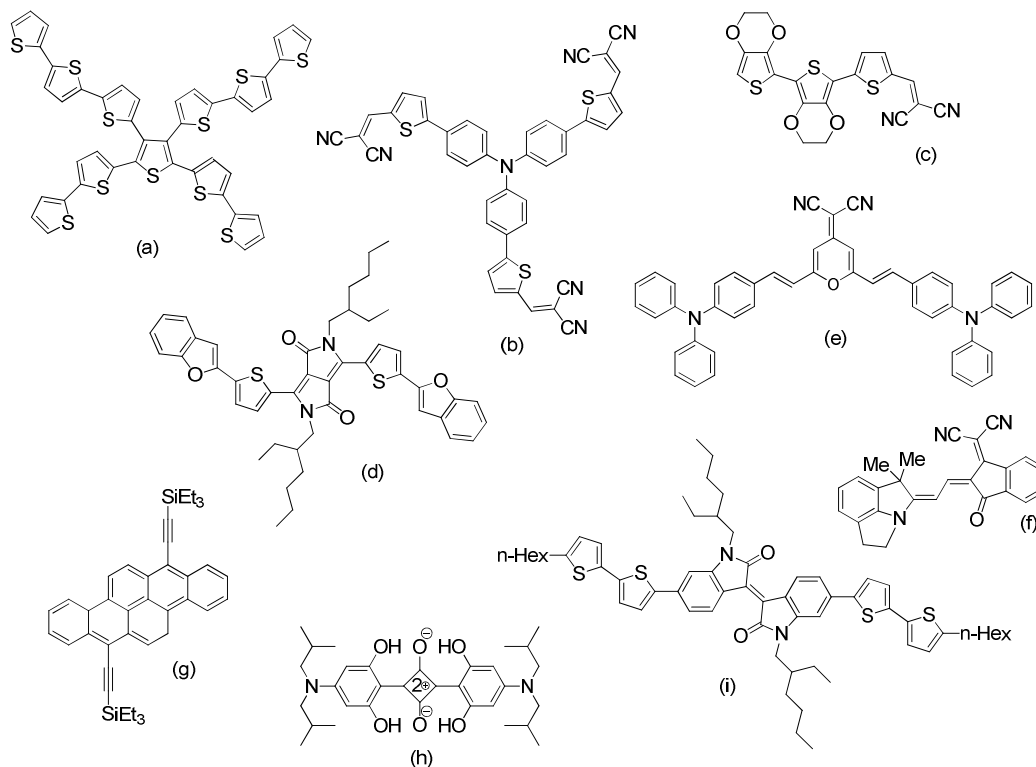
Figure 2.10 Examples of small molecules used as donors in OPVs: oligothiophenes *PCE*=0.80% (a) [58], triphenylamines *PCE*=4.3% (b) [59], EDOT-based systems *PCE*=0.70% (c) [60], diketopyrrolopyrroles *PCE*=4.4% (d) [61], dicyanopyrane derivatives *PCE*=1.5% (e) [62], merocyanines *PCE*=4.3% (f) [63], oligoacenes *PCE*=2.25% (g) [64], squaraines *PCE*=3.1% (h) [65], indigos *PCE*=1.76%. (i) [66].

2.5.2.2 *Π-conjugated polymers*

Since their discovery 2.1.1.1 π-conjugated polymers have found increasing application interest for the realization of different types of electronic devices (OLEDs, solar cells, sensors, transistors, electrochromic devices), thanks to their mechanical characteristics, low cost, and the possibility of tuning the electronic structure to obtain the desired properties. Different monomers present different HOMO and LUMO energy levels from which are derived the different bandgaps and optical properties of the polymer. In addition, the relative positions of the HOMO and LUM*O* energy levels, and thus the optical properties, can be controlled by appropriate structural changes. For example this is possible by introducing electron-rich and electron-poor substituents, but also by taking advantage of steric interactions and varying the degree of delocalization of π electrons along the polymer chain. Since the optical characteristics of π-conjugated polymers are primarily determined by the chemical nature of

the constituting monomers, it is common to classify them into families based on the monomer units [67].

Polyaniline is probably the first conjugated polymer produced and studied, since it has been firstly synthesized in the 19th century. It can be synthesized either by electrochemical or oxidative polymerization techniques and the polymer obtained exhibits multiple electrochromic behavior, depending on its oxidation state. In 1977, Alan J. Heeger, Alan MacDiarmid, and Hideki Shirakawa reported similar high conductive polyacetylene. For this research, they were awarded the Nobel Prize in Chemistry 2000 "for the discovery and development of conductive polymers".

There are two forms of polyacetylene as presented in Figure 2.11, *trans*-and *cis*-polyacetylene [68].

Figure 2.11 *Trans*-polyacetylene (right) and *cis*-polyacetylene (left). In the blue and red box are reported the repeat units.

Trans-polyacetylene has two carbon atoms in the repeat unit, while for *cis*-polyactylene, there are four. *Trans*-(CH)x is a semiconductor with an energy gap of approximately 1.8 eV [68][69]. *Cis*- and trans-polyacetylene are examples of the First Generation semiconducting polymers. Even if *cis*-polyacetylene is easily achieved by the Ziegler–Natta catalyst used in the Shirakawa synthesis, *trans*-(CH)$_x$ is the stable form. *Cis*-polyacetylene can be thermally converted to *trans*-polyacetylene [70]. Polyacetylene itself did not find practical applications, but drew the attention of scientists and encouraged the rapid growth of the field.

poly(*p*-phenylene) (PPP)

poly(*p*-phenylene vinylene (PPV)

polythiophene (PT)

polypyrrole (PPy)

polyethylene dioxythiophene (PEDOT)

poly(2,5-dialkoxy)
p-phenylene vinylene (e. g. MEH-PPV)

poly(3-alkylthiophene)
(P3AT)

polyfluorene (PFO)

poly(2,5-dialkoxy)
p-phenylene cyano-vinylene (CN-PPV)

polyaniline (PANI)
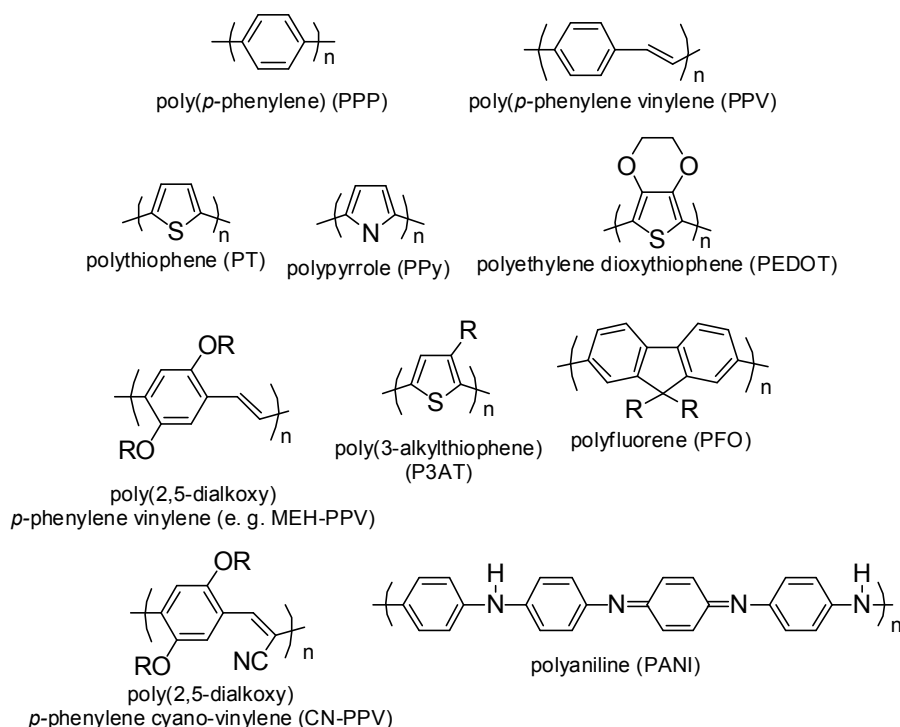
Figure 2.12 Second Generation of semiconducting polymers (reproduced from reference [71]**, with modifications).**

To the Second Generation of semiconducting polymers ([71], Figure 2.12) belong the poly(*p*-phenylene)s (**PPP**s), poly(*p*-phenylenvinylene)s (**PPV**s) and poly(thiophene)s (**PT**s) as well as their more processable alkyl- and alkoxy-derivatives. Poly(aniline) is another important example of this Second Generation.

Poly(*p*-phenylenevinylene) (**PPV**) has been one of the first π-conjugated polymers that have thoroughly been studied, due to its conductivity and its photoluminescent properties. **PPV** has been the first polymer used in polymer-based LEDs [72] and its derivatives remain between the most studied π-conjugated polymers for this application as well as for organic photovoltaics. The HOMO and LUMO levels of the unsubstituted **PPV** were reported at -5.1 and -2.7 eV, respectively, with a bandgap of 2.4 eV. The introduction of two alkoxy groups on the phenylene ring allowed to disrupt the molecular orbitals and to reduce the bandgap to 2.2 eV [73]. Another way to tune the energy levels of **PPV** derivatives is the incorporation of substituents on the vinylene bridge. Based on this idea, **PPV** derivatives containing a cyano group attached to the double bond have been synthesized (**CN-PPV**).

In the first years of polymer solar cells, **MEH-PPV:C$_{60}$** blends have been the dominant materials, later replaced by a combination of **MDMO-PPV** and **C$_{60}$** (**PCBM**) which allowed better

device performances [34], [74], [75]. However, the large band gap and the low mobility of **PPV** derivatives limit the power conversion efficiency to only 3% [21], [76], [77]. Therefore, the interest in this class of polymers for photovoltaic application has disappeared.

Polythiophene is one of the most common π-conjugated polymers and it is used in a wide range of applications such as chemical sensors, light-emitting diodes, field-effect transistors, and organic solar cells due to its improved electronic and electrical properties, thermal and chemical stability, when compared to **PPVs**. The unsubstituted polythiophene can be easily prepared by oxidative chemical polymerization and the resulting polymer is highly conductive, thermally stable but absolutely insoluble. Starting from 1990's, soluble and thus processable [78]–[80] polythiophenes were obtained by several groups, adding a flexible side-chain. In particular, poly(3-hexylthiophene) (**P3HT**) became really popular after McCullough *et al*. [81] have reported a very effective polymerization method of 3-alkylthiophene. This method allows to achieve regioregular head-to-tail poly(3-alkylthiophene-2,5-diyl)s, without any major defects. Later, he himself reported a more economical method led to poly(3-alkylthiophene) with 99% of regioregularity (**rr-P3AT**), called Grignard metathesis (**GRIM**) [82]. Alternative strategies have been developed involving Rieke metals [83], direct arylation polymerization (**DARP**) [84] or Stille cross-coupling [85]. Nowadays, highly regioregular **P3HT** is relatively easy to synthesize and process, relatively stable and affordable [86]. The efficiency of a **P3HT:PC$_{61}$BM** solar cell is typically 4-5%, which is close to the optimal performance for this system [87]–[90]. Several groups have tried to improve that

Figure 2.13 Absorption Spectra of P3HT (purple), a LBG (green) and the Solar Emission Spectra at AM 1.5D (black). Image reproduced from reference [98]**.**

performance by optimizing several factors such as morphology, device architecture, the molar mass, the electron acceptor but this has not resulted in significant improvements in conversion efficiency. The main drawback of **P3HT** is still its relatively large bandgap (1.9 eV), which does not allow a good overlap of its absorption spectra with the sun emission spectrum (Figure 2.13).

With the aim to overcome the limits of the previous generations, a *Third Generation* of semiconducting polymers ([71], Figure 2.14), the so-called *Low band-gap* polymers, has been developed in the past few years [91]. This new class of π-conjugated polymers shows a better overlap between the absorption spectrum of the polymer and the solar spectrum [92][93][94]. Record efficiencies of 11.5% have been reported, for both single junction [25] and tandem [95] devices. The goal now is to reach the 15% efficiency [96].

poly[(2,6-bis-(2-alkyl)-4H-cyclopenta(2,1-*b*;3,4-*b*)-dithiophene)-*alt*-4,7-(2,1,3-benzothiadiazole)]
(PCPDTBT)

poly[(4,4'-bis(2-dialkyl)dithieno(3,2-*b*;2',3'-*d*)silole)-2,6-diyl-*alt*-(2,1,3-benzothiadiazole)-4,7-diyl)]
(PSBTBT)

poly(9,9-dialkylfluorene-*co*-bithiophene) (F8T2)

poly(2,5-bis(3-alkylthiophen-2-yl)thieno(3,2-*b*)thiophene) (PBTTT)

poly[(4,8-bis[(2-ethylhexyl)oxy]benzo[1,2-*b*:4,5-*b'*]dithiophene-2,6-diyl)-*alt*-(3-fluoro-2-[(2-ethylhexyl)carbonyl]thieno[3,4-*b*]thiophenediyl)]
(PTB7)

poly[3,6-bis-(4'-dodecyl-[2,2']bithiophenyl-5-yl)-2,5-bis-(2-ethyl-hexyl)-2,5-dihydropyrrolo[3,4-]pyrrole-1,4-dione]
(pBBTDPP2)

Figure 2.14 Third Generation semiconducting polymers. R=alkyl chain ([71] **and** [97]**, with modifications).**

2.5.2.3 **Why aiming at LBGs** [98]

Many techniques allow to measure the band-gap of organic molecules. The two most important are the optical band-gap estimated from UV-vis spectroscopy and the electronichemical band-gap determined through cyclic voltammetry (CV). A polymer is usually considered a low band-gap polymer when its band-gap is less than 1.8 eV, so that its absorption edge is at wavelengths (λ) longer than 620 nm.

It is clear from Figure 2.13 that the low band gap polymers absorb light where **P3HT** and **MEH-PPV** do not. The *photon flux (f(λ))* as a function of the wavelength gives a good picture of how many photons can be harvested and is calculated by equation (2.7):

$$f(\lambda) = \frac{I_S(\lambda)}{E_\lambda(\lambda)} \qquad (2.7)$$

where and $I_S(\lambda)$ is the sun irradiance in W m^{-2}nm^{-1} and $E_\lambda(\lambda)$ is the photon energy, both expressed as a function of the wavelength λ (equation (2.8)):

$$E_\lambda(\lambda) = h\nu = h\frac{c}{\lambda} \qquad (2.8)$$

where h is *Planck constant (6.626x10^{-34}Js)*, c is the *speed of light (2.998x10^8 ms^{-1})*.

The *integrated photon flux (F(λ))* evaluated by equation (2.9):

$$F(\lambda) = \frac{\int_{\lambda=280}^{\lambda} f(\lambda)d\lambda}{A} = \frac{\Delta\lambda \sum_{\lambda=280}^{\lambda} f(\lambda)}{A} \qquad (2.9)$$

is obtained by dividing the value of the integration of photon flux $f(\lambda)$ for the area under the sun irradiance curve, which, in turn, is determined by equation (2.10)

$$A_S = \int_{\lambda=280}^{\lambda=4000} f(\lambda)d\lambda = \Delta\lambda \sum_{\lambda=280}^{\lambda=4000} f(\lambda) \qquad (2.10)$$

The integration range from 280 to 4000 nm has been chosen, because the sun irradiance is practically zero beyond these limits (Figure 2.15).

Assuming that every photon is converted to one electron, F(λ) can be used to calculate the maximum theoretical current (integrated current I_t, equation (2.11))

$$I_t = F(\lambda) \cdot e \qquad (2.11)$$

where e is the elementary charge (1.602x10^{-19} C).

The photon flux, the integrated photon flux and the integrated current are plotted as a function of the wavelength and we see that absorption at longer wavelengths results in a higher maximal theoretical current (Figure 2.15).
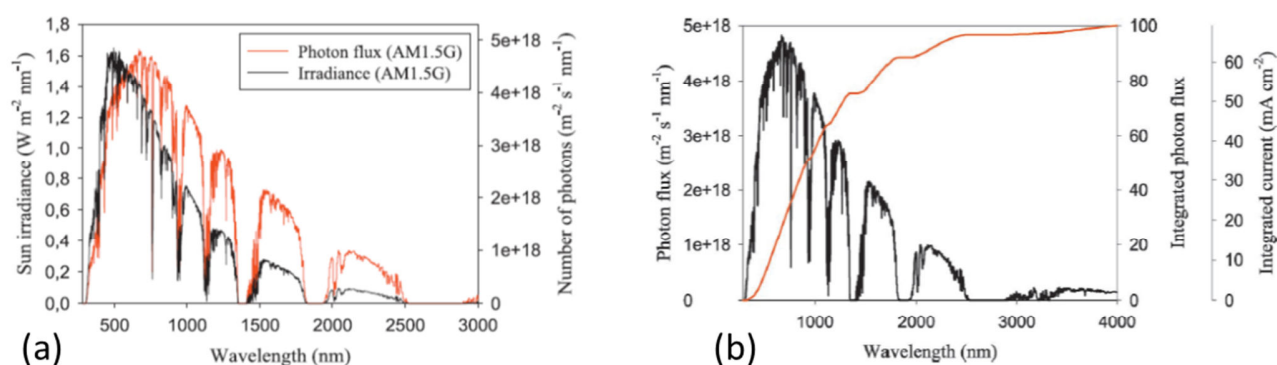
Figure 2.15 (a) Sun irradiance (black) and photon flux (red) as a function of wavelength. (b) Photon flux as a function of wavelength (BLACK). The integral (RED) is shown with two axes showing the integrated photons and the theoretical current. Image reproduced from reference [98]**.**

The absorption spectrum of the polymer does not correspond completely to the photon flux, and hence the maximum theoretical current is not I_t. Moreover, in OPVs, the actual current depends on several factors, such as morphology, layers thickness, carrier mobilities, etc. To obtain a more precise calculation the *incident photon to current efficiency (IPCE)* should be taken into account.
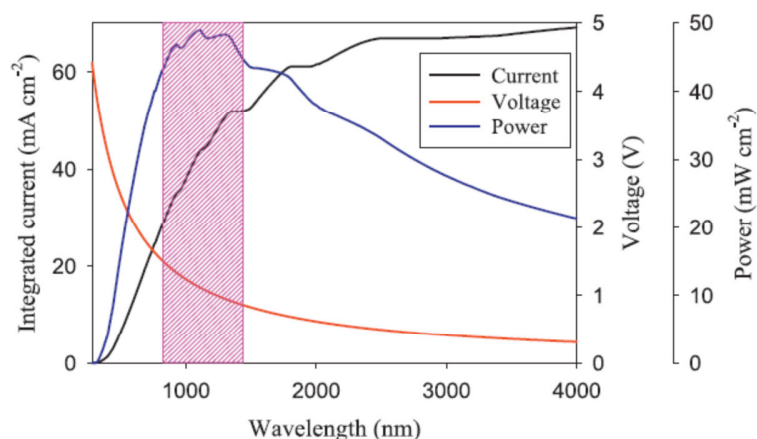
Figure 2.16 Maximum power obtainable in OPVs based on the AM 1.5G emission spectrum. The power is taken as the product of the integrated current assuming an IPCE of 100% and the voltage of the device as the value for the bandgap. Thus, the power is the maximum theoretical value, neglecting thermodynamic effects and losses. The pink box is the range of bandgaps where the most efficient devices can be found. Image reproduced from reference [98]**.**

The improved overlap of low bandgap polymer absorption spectra with the solar spectrum has a strong effect on the short-circuit current, but it has also an influence on the corresponding open-circuit voltage. Indeed, the maximum voltage obtainable decreases as a function of wavelength and the optimum bandgap is in the region of 0.9–1.2 eV. Another important factor that influences the V_{OC} is the energy level alignment between the polymer, the electron acceptor and the electrodes.

Π-conjugated polymers in the ground state have two different resonance structures with non-degenerate energy. The first one is called the aromatic form, where each aromatic unit maintains its aromaticity, confining the π-electrons. While in the quinoid form, the aromaticity of each unity is broken, leading to the delocalization of the π-electrons along all the π-conjugated chain. Compared to the aromatic form, the quinoid form is energetically less stable and hence has a smaller bandgap because adopting a quinoid structure requires destruction of the aromaticity and a loss in the stabilization energy.

Figure 2.17 Aromatic and Quinoid form of poly(phenylene), poly(*p*-phenylenvinylene), poly(thiophene) and poly(isothianaphtene). Image reproduced from reference [138]**.**

The ratio between the population of the aromatic and the quinoid forms can be defined through a geometrical parameter: the bond length alternation (*BLA*). The *BLA* is defined as the average of the difference in length between adjacent *C-C* bonds in polyene chain. If the aromatic form prevails in the ground state, a larger *BLA* value will be obtained. For example, by inserting a double bond between two benzenes in the backbone of poly(*p*-phenylenevinylene) the aromaticity is reduced and the value of the bandgap decreases from 3.2 to 2.4 eV. Thiophene has a lower degree of aromaticity compared to benzene; so polythiophene is more likely to adopt a quinoid form and thus it has a band gap lower than 2.0 eV.

The band-gap of a π-conjugated polymer depends on the combined effect of many different parameters, such as intra-chain charge transfer, bond-length alternation, substituents effects, intermolecular interactions, π-conjugation length, etc. [99] All these parameters should be carefully considered when designing new low bandgap polymers.

Various strategies to reduce the bandgap are based on the molecular modification of the main backbone, playing with steric or electronic effects on π-conjugated main chains. In the following paragraph the most diffused strategy will be presented.

2.5.2.4 Donor-acceptor strategy and Quinoid stabilization

In the last years, a strategy to develop semiconducting polymers with broader and stronger absorption with respect to P3HT, the most common and studied donor material for OPV, has been explored. This strategy consists of the coupling of an electron-rich (donor) unit and with an electron-deficient (acceptor) unit. The bandgap of the resulting alternate polymer is determined by the combination of the energy levels of the acceptor and donors units. The internal charge transfer between donor and acceptor units increases the overall absorption [100], while the π-electron delocalization is facilitated thanks to the planar configuration adopted by the π-conjugated backbone, leading to a smaller band gap. This concept basically suppresses the *Peierls effect* [101][102].

This strategy was first proposed in 1993 by Havinga *et al*. [103] and most of the low band gap polymers reported in literature are based on thiophene derivates or on thiophene as part of a fused ring system [104][105][106]. The alternance of donor and acceptor units promotes the formation of the mesomeric quinoid form $(D - A \leftrightarrow D^+ = A^-)$, through the introduction of a push-pull driving force that significantly reduces the BLA value.

As said, the bandgap of these polymers is determined by the value of HOMO of the donor unit and the LUMO of the acceptor unit (Figure 2.18). A low bandgap polymer is the result of a high energy level of the HOMO coupled with a low energy level of the LUMO of the acceptor [107][108]. In fact, according to the rules of perturbation theory, the HOMO of the donor unit interacts with the HOMO of the acceptor unit allowing the formation of two new HOMO levels for the D-A system. In the same way, two new LUMO levels are produced by the interaction of the LUMO donor level with the acceptor one. A higher lying HOMO and lower lying LUMO level are formed after the electron redistribution from their original non-interacting orbitals to the new hybridized orbitals of the D-A polymer system.

Figure 2.18 Orbital interaction of donor and acceptor units leading to a reduced band gap in a D-A system.

The intermolecular interactions have also a strong effect on the bandgap value. As demonstrated with **P3HT**, the inter-chain organization in the solid-state produces a red shift of the

absorption spectrum, reducing the band-gap [109]. A high stereoregular structure and an extended planar conformation are necessary to obtain closely packed and ordered crystalline domains. If the conjugation length increases [110] the bandgap is lowered, and the torsion angle can be reduced enhancing the backbone planarity, further reducing the bandgap of the polymer [111].

Substituents on the donor and acceptor units play two fundamental roles because they can influence their energy levels and the solid state nanostructure and morphology. The degree of bandgap reduction is strongly dependent on the donor and acceptor strengths. This can be easily done by using electron withdrawing groups (EWG) on the acceptor unit and electron donating groups on the donor. An electron donating group, such as alkoxy- or amine-, raises the HOMO energy because its electron density is pushed into the π-orbitals of the main aromatic unit. In this way it is easier to remove an electron from the HOMO energy level. On the other hand an electron accepting group, such as cyano, quinoxalines, pyrazines, thiadiazole or trifluoromethyl, lowers the LUMO due to the lowered reduction potential, making it easier to push an electron into the LUMO.

Alkyl chains do not have any strong effect on the energy levels but they are introduced in order to improve molecular weight, solubility, and processability of the π-conjugated polymers. On the other hand, they can have a strong effect on intermolecular interactions, introducing supramolecular ordering to enhance the solid-state packing.

2.5.3 Polymerization Techniques

According to the polymerization mechanism, it is possible to distinguish three main classes of reactions: polyaddition, polycondensations and chain polymerization (Figure 2.19-a) [112]. In polyaddition and polycondensation (also called step-growth), polymer chain growth proceeds by reactions between molecules of all degrees of polymerization, either by addition or condensation reaction. While in chain polymerizations, the chain is extended through the reaction of a monomer with the active site of the polymer chain, regenerating the active site at the same

Figure 2.19 Step-growth polymerization mechanism and (b) comparison between step-growth and chain-growth polymerization by Chem538grp5w09 - Own work. Licensed under Public Domain via Wikimedia Commons.

time. In polyaddition and polycondensation, the monomers are rapidly consumed causing a reduction of the polymerization rate. This leads to a slow increase of the polymer molecular weight, if compared with monomer conversion (Figure 2.19-b). The polymerization ends when the concentration of functional groups or the mobility of the reactive chain-end is too low. One of the most important factors that affects the molecular weight of the final polymer is the stoichiometric balance of the two monomers. Purity of the monomers is mandatory if high molecular weight polymers are desired.

Many natural and synthetic polymers (polyesters, polyamides, polyurethanes, polycarbonates, etc) are produced by *addition* polymerizations, including the first synthetic polymer, bakelite, reported by Baekeland in 1907. In the 1930s Carother, developed a new synthetic route for polyesters with a *polycondensation* mechanism. Carothers and Flory developed a theory to describe mathematically many aspects of the *addition* polymerization, such as kinetics, stoichiometry, molecular weight distribution, etc.

The main reactions for the synthesis of conjugated polymers are *polycondensation* reactions. They are generally catalyzed by Pd(0) and involve two different bi-functionalized aromatic co-monomers: Mizoroki-Heck [113], Stille [114], Suzuki-Miyaura [115], and direct arylation [116].

2.5.3.1 Stille coupling reaction

The first report of a cross-coupling reaction between organostannanes and electrophilic compounds was in 1976 and 1977 by Eaborn [117] and Kosugi [118][119], while the first publication by Stille where he synthesized ketones by reacting acyl chloride and organostannanes through a palladium-catalyzed cross coupling reactions appeared in 1978 [120], with a review of the methodology in 1986 [114]. The Stille reaction quickly became one of the most useful tools for forming sp^2 carbon-carbon bonds.

The Stille coupling between stannanes and aryl halides has become a versatile synthetic methodology and has been widely applied to the synthesis of different organic compounds [121][122]. This is due to many advantages, as the fact that the Stille reaction is stereospecific, regioselective and typically gives excellent yields. It can tolerate many functional groups and it requires mild reaction conditions. Moreover, the organometallic compounds involved are far less oxygen- and moisture-sensitive than many of other organometallic analogues.

$$\text{n X-R-X} + \text{n R''}_3\text{Sn-R'-SnR''}_3 \xrightarrow[\text{ligand}]{\text{Pd(0)}} \left[\!\!\left[\text{R-R'}\right]\!\!\right]_n + \text{2n X-SnR''}_3$$
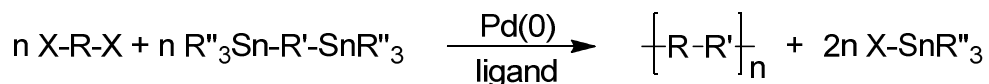
R'' = alkyl;
R and R' = aryl, alkenyl;
X = I, Br, Cl, OTf

Scheme 2.1 Schematic representation of polycondensation by Stille *cross-coupling* reaction.

Thus, the involved organo-halide and organo-tin compounds (Scheme 2.1) can be extensively functionalized without any protecting functionality, giving the chance to design molecules with virtually any functional moieties showing almost any desired property. This feature is particularly important in the synthesis of functional molecules for a wide range of applications, where particular properties are related to the presence of specific functionality (nonlinear optics, biological sensor, OLED, OPV, etc.). One of the most interesting applications of this reaction is the synthesis of conjugated poly-aromatic systems with semiconducting properties.

The first studies about the polymerization of organotin and dihalide monomers appeared at the turn of 1980s and 1990s by Bochmann [123], Schulz [124], and Galarini [125] groups. In 1993, Yu's group optimized a polycondensation methodology for the synthesis of heteroaromatic diblock copolymers with high molecular weight [126][127] and after that the Stille polymerization has been extended on a wide range of different substrates [128].

2.5.3.2 *Suzuki coupling reaction*

The first to observe the possibility to use boronic acids in cross-coupling reactions in presence of Pd(0) had been Heck in 1975 [129]. But it was in 1979 that Suzuki reported the palladium-catalyzed cross-coupling between 1-alkenylboranes and aryl halides (Scheme 2.2) [130]. The Suzuki–Miyaura reaction has been developed into a powerful and general method for the formation of sp^2 C-C bonds [115]. For his pioneering work he has been awarded with the 2010 chemistry's Nobel Prize, jointly to Heck and Negishi.

Its success is due to many advantageous features, among which the most important are the easily handled and usually air and moisture stable organoboron starting materials and the facile removal of less-toxic inorganic byproducts, certainly with respect to the toxic Stille polycondensation. With the other cross-coupling reactions it shares the stereospecific, regioselective, mild and convenient reaction conditions and a wide freedom in the choice of functionality. These aspects make the Suzuki–Miyaura coupling reaction especially useful for industrial applications. On the other hand

the two phase system altogether to the required basic conditions are important drawbacks that limit its application or that require more complex solutions.

$$n\ X\text{-}R\text{-}X + n\ R''_2B\text{-}R'\text{-}BR''_2 \xrightarrow[\substack{\text{base,}\\\text{ligand}}]{Pd(0)} \left[R\text{-}R'\right]_n + 2n\ X\text{-}BR''_2$$
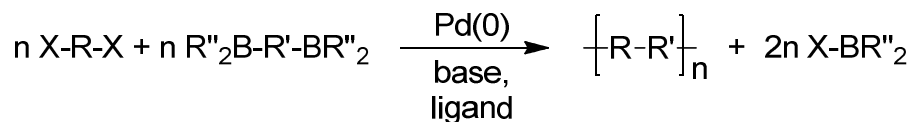
R'' = alkyl, hydroxy, alkoxy;
R and R' = aryl, alkenyl, alkyl;
X = I, Br, Cl, OTf

Scheme 2.2 Schematic representation of polycondensation by Suzuki cross-coupling reaction.

The first studies involving the polymerization of organoborane and dihalide monomers appeared in 1989 by Schluter's group succeeded in the synthesis of poly(*para*-phenylene) (PPP) [131] and then applied to a wide number of aromatic compounds [132].

2.5.3.3 General mechanism

The general mechanism of these Pd(0)-mediated reactions has been thoroughly investigated [133][134][115]. In a highly simplified way (Scheme 2.3), the mechanism can be divided in three different steps: an ***oxidative addition* (1)**, followed by a ***transmetalation* (2)** and a final ***reductive elimination* (3)**, which yields the cross-coupling product and regenerates the catalyst. As already stated, the Pd(0) species is the active catalyst, but Pd(II) catalysts are more common and diffused mainly due to their higher stability. When used the Pd(II) has to be reduced to Pd(0) prior to its entry into the catalytic cycle, constituting an additional initial (0) step.
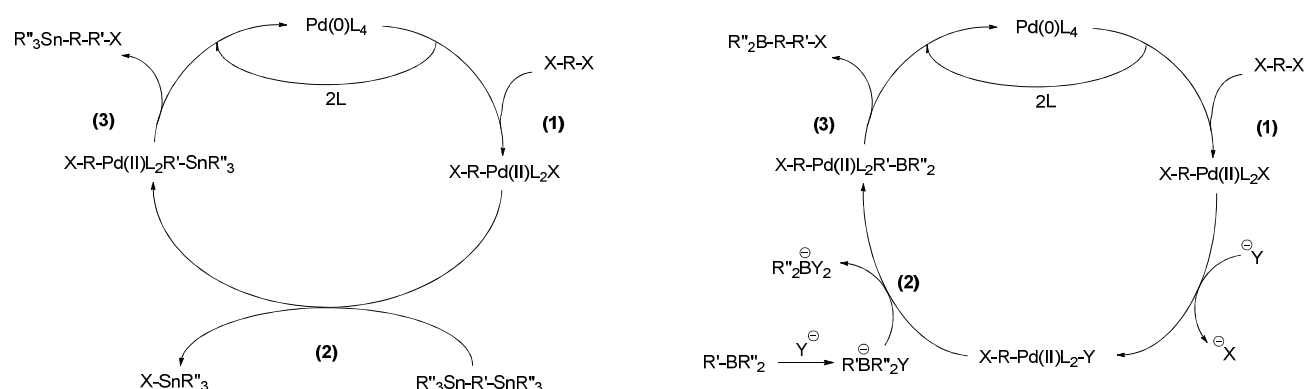
Scheme 2.3 General Stille (left) and Suzuki (right) catalytic cycles.

The first step in the catalytic cycle, the ***oxidative addition* (1)** (Scheme 2.4) occurs when the organohalide or triflate oxidatively adds to the Pd(0) active catalyst, forming a Pd(II) intermediate [X-

R-Pd(II)L$_2$-X]. This step is followed by a rapid *cis-trans* isomerization, the final configuration depends on the R group of the halide.

$$X\text{-}R-\overset{\overset{\displaystyle X}{|}}{\underset{\underset{\displaystyle L}{|}}{Pd(II)}}-L \quad \rightleftharpoons \quad X\text{-}R-\overset{\overset{\displaystyle L}{|}}{\underset{\underset{\displaystyle L}{|}}{Pd(II)}}-X$$
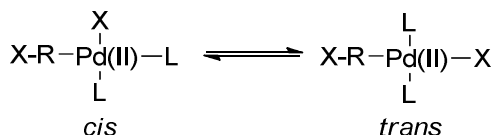
$$\textit{cis} \qquad\qquad\qquad \textit{trans}$$

Scheme 2.4 General mechanism of cis-trans isomerization.

The second major step in the process, the ***transmetalation (2)***, is generally regarded to be the rate-determining step [134]. This step is the most complex and many possible mechanisms have been proposed. The transmetalation process in general is a process of ligand substitution on a Pd(II) complex and, in this case, it is cleavage of the Sn-C or B-C bond by an electrophilic Pd(II) complex. Organostannane directly undergoes *transmetalation* while organoboron does it only in presence of a base, thus it is commonly accepted that the role of the base is to activate the organoboron compound.

Reductive elimination (3) (Scheme 2.5) is the final step in the process, which generates the desired product and allows the palladium catalyst to regenerate and to reenter the catalytic cycle. A *trans-cis* isomerization precedes this step, in order to place the coupling partners *cis* to one another (M is –SnR''$_3$ or –BR''$_2$):

$$X\text{-}R-\overset{\overset{\displaystyle R'M}{|}}{\underset{\underset{\displaystyle L}{|}}{Pd(II)}}-L \quad \rightleftharpoons \quad X\text{-}R-\overset{\overset{\displaystyle L}{|}}{\underset{\underset{\displaystyle L}{|}}{Pd(II)}}-R'M$$

$$\textit{cis} \qquad\qquad\qquad \textit{trans}$$
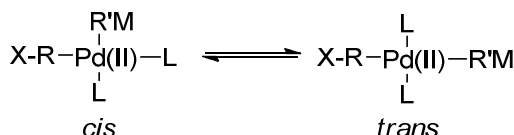
Scheme 2.5 General mechanism of trans-cis isomerization.

This is reported to be a fast step in the process following which the product is quickly eliminated and the Pd(0) catalyst is eliminated.

The choice of ligands, solvents, and additives all play a major role in the success of the cross-coupling reactions, and alternative mechanistic pathways have been shown to exist on the basis of varying reaction conditions. While the simplified steps mechanism reported is generally accepted, the process itself is far more complex and has been the subject of extensive mechanistic studies [134].

2.5.3.4 Critical parameters

In the Stille polycondensation, the solvent has to be chosen considering all the different parameters. It has to dissolve the starting monomers, to stabilize the catalyst, and to support its

activity. Furthermore, it must also keep the growing polymer in solution for as much as possible in order to achieve high molecular weights. The most employed solvents are toluene, xylene, THF, DMF, NMP, DMSO, dioxane, and chloroform. That the solvent must also sustain the high temperatures (120 °C to 150 °C) is an additional problem. In the case of Suzuki reaction, the two solvents system required presents a more complicated problem. The mixed aqueous/organic solvent system (water/toluene, THF, dioxane, dimethylformamide) can affect the nature of the boron reagent itself (boronic acid, boronic ester, etc). Thus, the associated purity issue is often an unknown factor.

In both Suzuki and Stille reactions, to achieve high molecular weight polymers the choice of the reagents is a key parameter, as well as their precise stoichiometry. In polycondensations a slight deviance from equivalence can have a huge negative effect on the degree of polymerization. Homocoupling of the ditin compound can pose a problem in maintaining a stoichiometric match. Furthermore, since extremely pure monomers are required to have precise stoichiometry, the intrinsic instability of many organotin compounds is a limit to purification options. The exact nature of the organo-boron species has profound effect on the efficacy of a given transformation. Another important parameter in the Suzuki–Miyaura reaction is the choice of the base.

In both Stille and Suzuki reactions, the polymerization is carried out using bisfunctionalized monomers. Generally, diiodomonomers are more reactive than dibromo monomers, while aryl chlorides have been barely used due to their low reactivity in oxidative addition to Pd(0). Usually, the coupling of electron-rich organo-tin or organo-boron with electron-deficient organohalide promotes the synthesis of high molecular weight polymers. This is probably related to the fact that oxidative addition is facilitated by electron-withdrawing groups. Similarly the transmetalation step could also be facilitated by electron-rich organotin compounds.

Even if these polycondensations use the same catalysts, ligands and solvents, optimizing the reaction conditions for each set of polymers is often necessary and it passes through a trial-and-error process.

2.5.3.5 *Direct arylation*

A new alternative to standard *cross-coupling* reactions for the formation of sp^2 C-C bonds is the coupling of aryl halides with catalytically activated aryl C-H bonds [135], in presence of a base to assist C-H bond activation and to neutralize the acid byproduct of the condensation (Scheme 2.6). This reaction is called direct arylation and it is the combination of the same standard cross-coupling

reaction with the oxidative-coupling of unsubstituted arenes [116]. Direct (hetero)arylation has been widely applied to the coupling of a number of different arene and heteroarene systems [135].

The mechanism by which C-H activation occurs has been studied experimentally and computationally, and possible mechanisms include electrophilic aromatic substitution, Heck-type coupling and concerted metalation-deprotonation (CMD) [136]. For most heterocycles a base-assisted CMD route is considered the most probable option. To further promote the CMD, carboxylate or carbonate anions are often used to coordinate in situ the Palladium center and to assist in the deprotonation transition state.

$$n \ H\text{-}R\text{-}H + n \ Br\text{-}R'\text{-}Br \xrightarrow[\text{base/acid}]{\text{Pd(0)}} \left[R\text{-}R' \right]_n$$
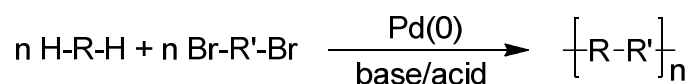
R and R' = aryl;

Scheme 2.6 Schematic representation of polycondensation by direct arylation cross-coupling reaction.

Direct arylation has been applied to π-conjugated polymers only recently [137] and can potentially give access to polymers previously inaccessible or difficult to prepare by traditional methods. Poor C-H bond selectivity during polymerization and insoluble cross-linked material can occur. A proper choice and design of monomers is necessary to achieve linear high molecular weight polymers.

2.6   References

[1]   M. R. Bryce, "Recent progress on conducting organic charge-transfer salts," *Chem. Soc. Rev.*, vol. 20, no. 3, p. 355, 1991.

[2]   W. Moore and M. Silver, "Generation of Free Carriers in Photoconducting Anthracene," *J. Chem. Phys.*, vol. 33, no. 6, p. 1671, 1960.

[3]   G. a. Chamberlain, "Organic solar cells: A review," *Sol. Cells*, vol. 8, no. 1, pp. 47–83, 1983.

[4]   P. H. Fang, "Analysis of conversion efficiency of organic-semiconductor solar cells," *J. Appl. Phys.*, vol. 45, no. 10, pp. 4672–4673, 1974.

[5]   V. Y. Merritt and H. J. Hovel, "Organic solar cells of hydroxy squarylium," *Appl. Phys. Lett.*, vol. 29, no. 7, pp. 414–415, 1976.

[6]   A. K. Ghosh and T. Feng, "Merocynanine organic solar cells," *J. Appl. Phys.*, vol. 49, no. 12, pp. 5982–5989, 1978.

[7]   D. L. Morel, a. K. Ghosh, T. Feng, E. L. Stogryn, P. E. Purwin, R. F. Shaw, and C. Fishman, "High-efficiency organic solar cells," *Appl. Phys. Lett.*, vol. 32, no. 8, pp. 495–497, 1978.

[8]   C. W. Tang, "Two-layer organic photovoltaic cell," *Appl. Phys. Lett.*, vol. 48, no. 2, pp. 183–185, 1986.

[9]   D. Kearns and M. Calvin, "Photovoltaic Effect and Photoconductivity in Laminated Organic Systems," *J. Chem. Phys.*, vol. 29, no. 4, p. 950, 1958.

[10]   C. Deibel and V. Dyakonov, "Polymer–fullerene bulk heterojunction solar cells," *Reports Prog. Phys.*, vol. 73, no. 9, p. 096401, Sep. 2010.

[11]   J. J. M. Halls, K. Pichler, R. H. Friend, S. C. Moratti, and a. B. Holmes, "Exciton diffusion and dissociation in a poly(p-phenylenevinylene)/C60 heterojunction photovoltaic cell," *Appl. Phys. Lett.*, vol. 68, no. 22, pp. 3120–3122, 1996.

[12]   M. Theander, a. Yartsev, D. Zigmantas, V. Sundström, W. Mammo, M. Andersson, and O. Inganäs, "Photoluminescence quenching at a polythiophene/C60 heterojunction," *Phys. Rev. B*, vol. 61, no. 19, pp. 12957–12963, 2000.

[13]   P. Kumaresan, S. Vegiraju, Y. Ezhumalai, S. Yau, C. Kim, W.-H. Lee, and M.-C. Chen, "Fused-Thiophene Based Materials for Organic Photovoltaics and Dye-Sensitized Solar Cells," *Polymers (Basel).*, vol. 6, no. 10, pp. 2645–2669, 2014.

[14]   M. Hiramoto, H. Fujiwara, and M. Yokoyama, "Three-layered organic solar cell with a photoactive interlayer of codeposited pigments," *Appl. Phys. Lett.*, vol. 58, no. 10, pp. 1062–1064, 1991.

[15]   N. S. Sariciftci, L. Smilowitz, a J. Heeger, and F. Wudi, "Photoinduced Electron Transfer from a Conducting Polymer to Buckminsterfullerene," *Science (80-.).*, vol. 258, pp. 1474–1476, 1992.

[16]   G. Yu, J. Gao, J. C. Hummelen, F. Wudl, and a. J. Heeger, "Polymer Photovoltaic Cells: Enhanced Efficiencies via a Network of Internal Donor-Acceptor Heterojunctions," *Science (80-.).*, vol. 270, pp. 1789–1791, 1995.

[17]   "ORGANIC PHOTOVOLTAICS: Transition metal oxides increase organic solar-cell power conversion - Laser Focus World." [Online]. Available: http://www.laserfocusworld.com/articles/print/volume-48/issue-06/features/transition-metal-oxides-increase-organic-solar-cell-power-conversion.html. [Accessed: 09-Aug-2015].

[18]   B. Kannan, K. Castelino, and A. Majumdar, "Design of Nanostructured," *Nano*, 2003.

[19]   J.-L. Brédas, J. E. Norton, J. Cornil, and V. Coropceanu, "Molecular understanding of organic solar cells: the challenges.," *Acc. Chem. Res.*, vol. 42, no. 11, pp. 1691–1699, 2009.

[20]   B. Friedel, P. E. Keivanidis, T. J. K. Brenner, A. Abrusci, C. R. McNeill, R. H. Friend, and N. C. Greenham, "Effects of layer thickness and annealing of PEDOT:PSS layers in organic photodetectors," *Macromolecules*, vol. 42, no. 17, pp. 6741–6747, 2009.

[21]   C. J. Brabec, S. E. Shaheen, C. Winder, N. S. Sariciftci, and P. Denk, "Effect of LiF/metal electrodes on the performance of plastic solar cells," *Appl. Phys. Lett.*, vol. 80, no. 7, pp. 1288–1290, 2002.

[22]   N. Grossiord, J. M. Kroon, R. Andriessen, and P. W. M. Blom, "Degradation mechanisms in organic photovoltaic devices," *Org. Electron.*, vol. 13, no. 3, pp. 432–456, 2012.

[23]   K. Kawano, N. Ito, T. Nishimori, and J. Sakai, "Open circuit voltage of stacked bulk heterojunction organic solar cells," *Appl. Phys. Lett.*, vol. 88, no. 7, pp. 073514–073514–3, Feb. 2006.

[24]   T. Ameri, G. Dennler, C. Lungenschmied, and C. J. Brabec, "Organic tandem solar cells: A review," *Energy Environ. Sci.*, vol. 2, no. 4, p. 347, 2009.

[25]   "Prof. Yan's Research Group » Best Research Organic Solar Cell Efficiency." [Online]. Available: http://blog.ust.hk/yanlab/2015/06/09/best-research-cell/. [Accessed: 05-Sep-2015].

[26] "Heliatek consolidates its technology leadership by establishing a new world record for organic solar technology with a cell efficiency of 12% - Heliatek – The future is light." [Online]. Available: http://www.heliatek.com/en/press/press-releases/details/heliatek-consolidates-its-technology-leadership-by-establishing-a-new-world-record-for-organic-solar-technology-with-a-cell-effi. [Accessed: 05-Sep-2015].

[27] V. Shrotriya, G. Li, Y. Yao, T. Moriarty, K. Emery, and Y. Yang, "Accurate measurement and characterization of organic solar cells," *Adv. Funct. Mater.*, vol. 16, pp. 2016–2023, 2006.

[28] J. M. Kroon, M. M. Wienk, W. J. H. Verhees, and J. C. Hummelen, "Accurate efficiency determination and stability studies of conjugated polymer/fullerene solar cells," *Thin Solid Films*, vol. 403–404, pp. 223–228, 2002.

[29] M. C. Scharber, D. Mühlbacher, M. Koppe, P. Denk, C. Waldauf, A. J. Heeger, and C. J. Brabec, "Design rules for donors in bulk-heterojunction solar cells - Towards 10 % energy-conversion efficiency," *Adv. Mater.*, vol. 18, no. 502783, pp. 789–794, 2006.

[30] L. J. a Koster, V. D. Mihailetchi, and P. W. M. Blom, "Ultimate efficiency of polymer/fullerene bulk heterojunction solar cells," *Appl. Phys. Lett.*, vol. 88, no. 2006, pp. 30–33, 2006.

[31] C. J. Brabec, A. Cravino, D. Meissner, N. Serdar Sariciftci, T. Fromherz, M. T. Rispens, L. Sanchez, and J. C. Hummelen, "Origin of the open circuit voltage of plastic solar cells," *Adv. Funtional Mater.*, vol. 11, no. 5, pp. 374–380, 2001.

[32] H. Frohne, S. E. Shaheen, C. J. Brabec, D. C. Müller, N. S. Sariciftci, and K. Meerholz, "Influence of the anodic work function on the performance of organic solar cells.," *Chemphyschem*, vol. 3, no. 9, pp. 795–799, 2002.

[33] C. J. Brabec, "Organic photovoltaics: Technology and market," *Sol. Energy Mater. Sol. Cells*, vol. 83, pp. 273–292, 2004.

[34] S. E. Shaheen, C. J. Brabec, N. S. Sariciftci, F. Padinger, T. Fromherz, and J. C. Hummelen, "2.5% Efficient Organic Plastic Solar Cells," *Appl. Phys. Lett.*, vol. 78, no. 6, pp. 841–843, 2001.

[35] R. Kroon, M. Lenes, J. C. Hummelen, P. W. M. Blom, and B. de Boer, *Small Bandgap Polymers for Organic Solar Cells* (Polymer Material Development in the Last 5 Years), vol. 48, no. April. 2008.

[36] J. E. Anthony, A. Facchetti, M. Heeney, S. R. Marder, and X. Zhan, "N-Type organic semiconductors in organic electronics," *Adv. Mater.*, vol. 22, pp. 3876–3892, 2010.

[37] Y. He and Y. Li, "Fullerene derivative acceptors for high performance polymer solar cells.," *Phys. Chem. Chem. Phys.*, vol. 13, pp. 1970–1983, 2011.

[38] R. Pacios, J. Nelson, D. D. C. Bradley, and C. J. Brabec, "Composition dependence of electron and hole transport in polyfluorene:[6,6]-phenyl C[sub 61]-butyric acid methyl ester blend films," *Appl. Phys. Lett.*, vol. 83, no. 2003, p. 4764, 2003.

[39] L. Zheng, Q. Zhou, X. Deng, M. Yuan, Y. Gang, and Y. Cao, "Mehtanofullerenes used as acceptors in polymer photovoltaic devices," *J. Phys. Chem. B*, vol. 108, no. Scheme 1, pp. 11921–11926, 2004.

[40] L. M. Popescu, P. Van 'T Hof, A. B. Sieval, H. T. Jonkman, and J. C. Hummelen, "Thienyl analog of 1-(3-methoxycarbonyl)propyl-1-phenyl-[6,6]- methanofullerene for bulk heterojunction photovoltaic devices in combination with polythiophenes," *Appl. Phys. Lett.*, vol. 89, no. 2006, pp. 87–90, 2006.

[41] S. a Backer, K. Sivula, D. F. Kavulak, and J. M. J. Fréchet, "High Efficiency Organic Photovoltaics Incorporating a New Family of Soluble Fullerene Derivatives," *Chem. Mater.*, vol. 19, no. 17, pp. 2927–2929, 2007.

[42] M. M. Wienk, J. M. Kroon, W. J. H. Verhees, J. Knol, J. Hummelen, Pa. Hal, and R. a J. Janssen, "Efficient methano [70] fullerene/MDMO‐PPV bulk heterojunction photovoltaic cells," *Angew. Chemie*, vol. 115, pp. 3493–3497, 2003.

[43] B. a. Collins, Z. Li, J. R. Tumbleston, E. Gann, C. R. Mcneill, and H. Ade, "Absolute measurement of domain composition and nanoscale size distribution explains performance in PTB7:PC71bm solar cells," *Adv. Energy Mater.*, vol. 3, pp. 65–74, 2013.

[44] Y. Yao, C. Shi, G. Li, V. Shrotriya, Q. Pei, and Y. Yang, "Effects of C70 derivative in low band gap polymer photovoltaic devices: Spectral complementation and morphology optimization," *Appl. Phys. Lett.*, vol. 89, pp. 15–17, 2006.

[45] H. Murata, Z. H. Kafafi, and M. Uchida, "Efficient organic light-emitting diodes with undoped active layers based on silole derivatives," *Appl. Phys. Lett.*, vol. 80, pp. 189–191, 2002.

[46] B. a. Jones, A. Facchetti, T. J. Marks, and M. R. Wasielewski, "Cyanonaphthalene diimide semiconductors for air-stable, flexible, and optically transparent n-channel field-effect transistors," *Chem. Mater.*, vol. 19, no. 11, pp. 2703–2705, 2007.

[47] J. E. Anthony, "The larger acenes: Versatile organic semiconductors," *Angew. Chemie - Int. Ed.*, vol. 47, pp. 452–483, 2008.

[48] Z. Wang, C. Kim, A. Facchetti, and T. J. Marks, "Anthracenedicarboximides as air-stable N-channel semiconductors for thin-film transistors with remarkable current on-off ratios," *J. Am. Chem. Soc.*, vol. 129, pp. 13362–13363, 2007.

[49] S. Ando, J. I. Nishida, E. Fujiwara, H. Tada, Y. Inoue, S. Tokito, and Y. Yamashita, "Novel p- and n-type organic semiconductors with an anthracene unit," *Chem. Mater.*, vol. 17, no. 6, pp. 1261–1264, 2005.

[50] A. J. Janssen, B. P. Karsten, and J. C. Bijleveld, "Diketopyrrolopyrroles as Acceptor Materials in Organic Photovoltaics," *Macromol. Rapid Commun.*, vol. 31, pp. 1554–1559, 2010.

[51] P. Sonar, S. P. Singh, Y. Li, M. S. Soh, and A. Dodabalapur, "A Low-Bandgap Diketopyrrolopyrrole-Benzothiadiazole-Based Copolymer for High-Mobility Ambipolar Organic Thin-Film Transistors," *Adv. Mater.*, vol. 22, no. 47, pp. 5409–5413, 2010.

[52] Y. Greenwald, X. Xu, M. Fourmigue, G. Srdanov, C. Koss, F. Wudl, and a J. Heeger, "Polymer-polymer rectifying heterojunction based on poly(3,4-dicyanothiophene) and MEH-PPV," *J. Polym. Sci. Part a-Polymer Chem.*, vol. 36, pp. 3115–3120, 1998.

[53] Z. Tan, E. Zhou, X. Zhan, X. Wang, Y. Li, S. Barlow, and S. R. Marder, "Efficient all-polymer solar cells based on blend of tris(thienylenevinylene)-substituted polythiophene and poly[perylene diimide-alt-bis(dithienothiophene)]," *Appl. Phys. Lett.*, vol. 93, no. 2008, pp. 10–13, 2008.

[54] M.-F. Falzon, A. P. Zoombelt, M. M. Wienk, and R. a J. Janssen, "Diketopyrrolopyrrole-based acceptor polymers for photovoltaic application.," *Phys. Chem. Chem. Phys.*, vol. 13, pp. 8931–8939, 2011.

[55] S. Hüttner, M. Sommer, and M. Thelakkat, "N-type organic field effect transistors from perylene bisimide block copolymers and homopolymers," *Appl. Phys. Lett.*, vol. 92, no. 2008, pp. 2006–2009, 2008.

[56] J. Roncali, P. Leriche, and P. Blanchard, "Molecular materials for organic photovoltaics: Small is beautiful," *Adv. Mater.*, vol. 26, pp. 3821–3838, 2014.

[57] M. T. Lloyd, J. E. Anthony, and G. G. Malliaras, "Photovoltaics from soluble small molecules," *Mater. Today*, vol. 10, no. 11, pp. 34–41, 2007.

[58] X. Sun, Y. Zhou, W. Wu, Y. Liu, W. Tian, G. Yu, W. Qiu, S. Chen, and D. Zhu, "X-shaped oligothiophenes as a new class of electron donors for bulk-heterojunction solar cells," *J. Phys. Chem. B*, vol. 110, pp. 7702–7707, 2006.

[59] H. Shang, H. Fan, Y. Liu, W. Hu, Y. Li, and X. Zhan, "A solution-processable star-shaped molecule for high-performance organic solar cells," *Adv. Mater.*, vol. 23, pp. 1554–1557, 2011.

[60] D. Demeter, T. Rousseau, and J. Roncali, "3,4-Ethylenedioxythiophene (EDOT) as building block for the design of small molecular donors for organic solar cells," *RSC Adv.*, vol. 3, p. 704, 2013.

[61] A. B. Tamayo, M. Tantiwiwat, B. Walker, and T. Nguyen, "Design , Synthesis , and Self-assembly of Oligothiophene Derivatives with a Diketopyrrolopyrrole Core," *J. Phys. Chem. C*, vol. 112, pp. 15543–15552, 2008.

[62] L. Xue, J. He, X. Gu, Z. Yang, B. Xu, and W. Tian, "Efficient bulk-heterojunction solar cells based on a symmetrical D-??-A-??-D organic dye molecule," *J. Phys. Chem. C*, vol. 113, pp. 12911–12917, 2009.

[63] V. Steinmann, N. M. Kronenberg, M. R. Lenze, S. M. Graf, D. Hertel, H. Bürckstümmer, F. Würthner, and K. Meerholz, "A simple merocyanine tandem solar cell with extraordinarily high open-circuit voltage," *Appl. Phys. Lett.*, vol. 99, pp. 19–22, 2011.

[64] K. N. Winzenberg, P. Kemppinen, G. Fanchini, M. Bown, G. E. Collis, C. M. Forsyth, K. Hegedus, T. B. Singh, and S. E. Watkins, "Dibenzo [b,def] chrysene derivatives: Solution-processable small molecules that deliver high power-conversion efficiencies in bulk heterojunction solar cells," *Chem. Mater.*, vol. 21, no. 18, pp. 5701–5703, 2009.

[65] S. Wang, E. I. Mayo, M. D. Perez, L. Griffe, G. Wei, P. I. Djurovich, S. R. Forrest, and M. E. Thompson, "High efficiency organic photovoltaic cells based on a vapor deposited squaraine donor," *Appl. Phys. Lett.*, vol. 94, pp. 10–13, 2009.

[66] J. Mei, K. R. Graham, R. Stalder, and J. R. Reynolds, "Synthesis of isoindigo-based oligothiophenes for molecular bulk heterojunction solar cells," *Org. Lett.*, vol. 12, no. 5, pp. 660–663, 2010.

[67] G. A. Pagani, "Conductive Polymers (Chap 7)," *Mater. Sci. Dep. - UNIMIB*.

[68] a. J. Heeger, S. Kivelson, J. R. Schrieffer, and W. P. Su, "Solitons in conducting polymers," *Rev. Mod. Phys.*, vol. 60, no. 3, pp. 781–850, 1988.

[69] A. J. Heeger, "Nobel Lecture:,ÄSemiconducting and metallic polymers:,ÄÉThe fourth generation of polymeric materials," *Rev. Mod. Phys.*, vol. 73, no. 3, pp. 681–700, 2001.

[70] C. K. Chiang, C. R. Fincher, Y. W. Park, a. J. Heeger, H. Shirakawa, E. J. Louis, S. C. Gau, and A. G. MacDiarmid, "Electrical conductivity in doped polyacetylene," *Phys. Rev. Lett.*, vol. 39, no. 17, pp. 1098–1101, 1977.

[71] A. J. Heeger, "Semiconducting polymers: the Third Generation.," *Chem. Soc. Rev.*, vol. 39, no. 7, pp. 2354–2371, 2010.

[72]   J. H. Burroughes, D. D. C. Bradley, A. R. Brown, R. N. Marks, K. Mackay, R. H. Friend, P. L. Burns, and A. B. Holmes, "Light-emitting diodes based on conjugated polymers," *Nature*, vol. 347, pp. 539–541, 1990.

[73]   M. M. Alam and S. a. Jenekhe, "Polybenzobisazoles are efficient electron transport materials for improving the performance and stability of polymer light-emitting diodes," *Chem. Mater.*, vol. 14, no. 11, pp. 4775–4780, 2002.

[74]   G. Yu, J. Gao, J. C. Hummelen, F. Wudl, and a. J. Heeger, "Polymer Photovoltaic Cells: Enhanced Efficiencies via a Network of Internal Donor-Acceptor Heterojunctions," *Science (80-.).*, vol. 270, no. 5243, pp. 1789–1791, 1995.

[75]   N. S. Sariciftci, D. Braun, C. Zhang, V. I. Srdanov, a. J. Heeger, G. Stucky, and F. Wudl, "Semiconducting polymer-buckminsterfullerene heterojunctions: Diodes, photodiodes, and photovoltaic cells," *Appl. Phys. Lett.*, vol. 62, no. 6, pp. 585–587, 1993.

[76]   P. W. M. Blom, M. J. M. de Jong, and S. Breedijk, "Temperature dependent electron-hole recombination in polymer light-emitting diodes," *Appl. Phys. Lett.*, vol. 71, no. 7, p. 930, 1997.

[77]   C. Melzer, E. J. Koop, V. D. Mihailetchi, and P. W. M. Blom, "Hole transport in poly(phenylene vinylene)/methanofullerene bulk-heterojunction solar cells," *Adv. Funct. Mater.*, vol. 14, no. 9, pp. 865–870, 2004.

[78]   Y. Wei, C. C. Chan, J. Tian, G. W. Jang, and K. F. Hsueh, "Electrochemical polymerization of thiophenes in the presence of bithiophene or terthiophene: kinetics and mechanism of the polymerization," *Chem. Mater.*, vol. 3, no. 5, pp. 888–897, 1991.

[79]   R. M. S. Maior, K. Hinkelmann, H. Eckert, and F. Wudl, "Synthesis and characterization of two regiochemically defined poly(dialkylbithiophenes): a comparative study," *Macromolecules*, vol. 23, no. 5, pp. 1268–1279, 1990.

[80]   J. Roncali, "Conjugated Poly(thiophenes) - Synthesis, Functionalization, and Applications," *Chem. Rev.*, vol. 92, no. 4, pp. 711–738, 1992.

[81]   R. D. McCullogh, S. P. Williams, S. Tristam-Nagle, M. Jayaraman, P. C. Ewbank, and L. Miller, "The first synthesis and new properties of regioregular, head-to-tail coupled polythiophenes," *Synth. Met.*, vol. 69, no. 1–3, pp. 279–282, 1995.

[82]   B. R. S. Loewe, S. M. Khersonsky, and R. D. Mccullough, "A Simple Method to Prepare Head-to-Tail Coupled, Regioregular Poly(3-alkylthiohenes) Using Grignard Metathesis," *Adv. Mater.*, vol. 11, no. 3, pp. 250–253, 1999.

[83]   T. Chen, X. Wu, and R. D. Rieke, "Regiocontrolled Synthesis of Poly(3-alkylthiophenes) Mediated by Rieke Zinc: Their Characterization and Solid-state Properties," *J. Am. Chem. Soc.*, vol. 117, pp. 233–244, 1995.

[84]   A. E. Rudenko, C. a. Wiley, S. M. Stone, J. F. Tannaci, and B. C. Thompson, "Semi-random P3HT analogs via direct arylation polymerization," *J. Polym. Sci. Part A Polym. Chem.*, vol. 50, no. 18, pp. 3691–3697, 2012.

[85]   A. Iraqi and G. W. Barker, "Synthesis and characterisation of telechelic regioregular head-to-tail poly(3-alkylthiophenes)," *J. Mater. Chem.*, vol. 8, no. 1, pp. 25–29, 1998.

[86]   M. T. Dang, L. Hirsch, and G. Wantz, "P3HT:PCBM, best seller in polymer photovoltaic research," *Adv. Mater.*, vol. 23, no. 31, pp. 3597–3602, 2011.

[87]   P. Schilinsky, C. Waldauf, and C. J. Brabec, "Recombination and loss analysis in polythiophene based bulk heterojunction photodetectors," *Appl. Phys. Lett.*, vol. 81, no. 20, pp. 3885–3887, 2002.

[88]   F. Padinger, F. Padinger, R. S. Rittberger, R. S. Rittberger, N. S. Sariciftci, and N. S. Sariciftci, "Effects of postproduction treatment om plastic solar cells," *Adv. Funct. Mater.*, vol. 13, no. 1, p. 85, 2003.

[89]   M. Reyes-Reyes, K. Kim, J. Dewald, R. López-Sandoval, A. Avadhanula, S. Curran, and D. L. Carroll, "Meso-structure formation for enhanced organic photovoltaic cells," *Org. Lett.*, vol. 7, no. 26, pp. 5749–5752, 2005.

[90]   W. Ma, C. Yang, X. Gong, K. Lee, and A. J. Heeger, "Thermally Stable, Efficient Polymer Solar Cells with Nanoscale Control of the Interpenetrating Network Morphology," *Adv. Funct. Mater.*, vol. 15, no. 10, pp. 1617–1622, 2005.

[91]   E. Bundgaard and F. C. Krebs, "Low band gap polymers for organic photovoltaics," *Sol. Energy Mater. Sol. Cells*, vol. 91, no. 11, pp. 954–985, Jul. 2007.

[92]   J. Nelson, "Organic photovoltaic films," *Curr. Opin. Solid State Mater. Sci.*, vol. 6, no. 1, pp. 87–95, 2002.

[93]   H. Neugebauer, C. Kvarnström, C. Brabec, N. S. Sariciftci, R. Kiebooms, F. Wudl, and S. Luzzati, "Infrared spectroelectrochemical investigations on the doping of soluble poly(isothianaphthene methine) (PIM)," *J. Chem. Phys.*, vol. 110, no. 24, p. 12108, 1999.

[94]   B. C. J. Brabec, C. Winder, N. S. Sariciftci, J. C. Hummelen, A. Dhanabalan, P. a Van Hal, and R. a J. Janssen, "A Low-Bandgap Semiconducting Polymer for Photovoltaic Devices and Infrared Emitting Diodes," *Adv. Funct. Mater.*, vol. 12, no. 10, pp. 709–712, 2002.

[95]   "Organic polymer tandem cell reaches record 11.5% efficiency." [Online]. Available: http://www.pv-magazine.com/news/details/beitrag/organic-polymer-tandem-cell-reaches-record-115-efficiency_100015832/#axzz39hwxf8Ng. [Accessed: 11-Mar-2015].

[96]   "UCLA engineers create tandem polymer solar cells that set record for energy-conversion." [Online]. Available: http://www.engineer.ucla.edu/newsroom/featured-news/archive/2012/ucla-engineers-create-tandem-polymer-solar-cells-that-set-record-for-energy-conversion. [Accessed: 11-Mar-2015].

[97]   B. Tieke, A. R. Rabindranath, K. Zhang, and Y. Zhu, "Conjugated polymers containing diketopyrrolopyrrole units in the main chain," *Beilstein J. Org. Chem.*, vol. 6, pp. 830–845, 2010.

[98]   F. C. Krebs, *Polymer Photovoltaics: A Practical Approach*. SPIE PRESS, 2003.

[99]   C. Winder and N. S. Sariciftci, "Low bandgap polymers for photon harvesting in bulk heterojunction solar cells," *J. Mater. Chem.*, vol. 14, p. 1077, 2004.

[100] H. Zhou, L. Yang, and W. You, "Rational Design of High Performance Conjugated Polymers for Organic Solar Cells," *Macromolecules*, 2011.

[101] C. Kitamura, S. Tanaka, and Y. Yamashitau, "Synthesis of New Narrow Bandgap Polymers Based on 5,7-Di(2-thienyl)thieno[3,4-b]pyrazine and its Derivatives," *J. Chem. Soc.*, pp. 1585–1586, 1994.

[102] A. Ajayaghosh, "Donor-acceptor type low band gap polymers: polysquaraines and related systems.," *Chem. Soc. Rev.*, vol. 32, pp. 181–191, 2003.

[103] E. E. Havinga, W. ten Hoeve, and H. Wynberg, "Alternate donor-acceptor small-band-gap semiconducting polymers; Polysquaraines and polycroconaines," *Synth. Met.*, vol. 55, pp. 299–306, 1993.

[104] C. L. Chochos and S. a. Choulis, "How the structural deviations on the backbone of conjugated polymers influence their optoelectronic properties and photovoltaic performance," *Prog. Polym. Sci.*, vol. 36, no. 10, pp. 1326–1414, 2011.

[105] P. M. Beaujuge, J. M. J. Fréchet, and J. M. J. Fr, "Molecular design and ordering effects in π-functional materials for transistor and solar cell applications.," *J. Am. Chem. Soc.*, vol. 133, pp. 20009–29, 2011.

[106] J. Hou, T. L. Chen, S. Zhang, L. Huo, S. Sista, and Y. Yang, "An easy and effective method to modulate molecular energy level of poly(3-alkylthiophene) for High-VocPolymer Solar Cells," *Macromolecules*, vol. 42, pp. 9217–9219, 2009.

[107] C. Kitamura, S. Tanaka, and Y. Yamashita, "Design of Narrow-Bandgap Polymers. Syntheses and Properties of Monomers and Polymers Containing Aromatic-Donor and o-Quinoid-Acceptor Units," *Chem. Mater.*, vol. 8, no. 26, pp. 570–578, 1996.

[108] M. Jayakannan, P. a. Van Hal, and R. a J. Janssen, "Synthesis and structure-property relationship of new donor-acceptor-type conjugated monomers and polymers on the basis of thiophene and benzothiadiazole," *J. Polym. Sci. Part A Polym. Chem.*, vol. 40, pp. 251–261, 2002.

[109] U. Salzner, J. B. Lagowski, P. G. Pickup, and R. a. Poirier, "Comparison of geometries and electronic structures of polyacetylene, polyborole, polycyclopentadiene, polypyrrole, polyfuran, polysilole, polyphosphole, polythiophene, polyselenophene and polytellurophene," *Synth. Met.*, vol. 96, no. 1998, pp. 177–189, 1998.

[110] K. Sivula, C. K. Luscombe, B. C. Thompson, and J. M. J. Fréchet, "Enhancing the thermal stability of polythiophene:fullerene solar cells by decreasing effective polymer regioregularity," *J. Am. Chem. Soc.*, vol. 128, pp. 13988–13989, 2006.

[111] J. Roncali, "Synthetic Principles for Bandgap Control in Linear π-Conjugated Systems," *Chem. Rev.*, vol. 97, no. i, pp. 173–206, 1997.

[112] R. G. Jones, E. S. Wilks, W. V. Metanomski, J. Kahovec, M. Hess, and R. Stepto, *Compendium of Polymer Terminology and Nomenclature*, vol. 24, no. 2. 2010.

[113] Y. Lee, Y. Liang, and L. Yu, "The Heck Polycondensation for Functional Polymers," *Synlett*, vol. 2006, no. 18, pp. 2879–2893, Nov. 2006.

[114] J. K. Stille, "The Palladium-Catalyzed Cross-Coupling Reactions of Organotin Reagents with Organic Electrophiles," *Angew. Chemie*, vol. 25, pp. 508–524, 1986.

[115] A. Suzuki, "Recent advances in the cross-coupling reactions of organoboron derivatives with organic electrophiles , 1995 – 1998," *J. Organomet. Chem.*, vol. 576, pp. 147–168, 1999.

[116] L. G. Mercier and M. Leclerc, "Direct (Hetero) Arylation : A New Tool for Polymer Chemists," *Acc. Chem. Res.*, vol. XXX, no. Xx, 2012.

[117] D. Azarian, S. S. Dua, C. Eaborn, and D. R. M. Walton, "Reactions of Organic Halides with R3mmr3 Compounds (M=Si,Ge,Sn) in Presence of Tetrakis(Triarylphosphine) Palladium," *J. Organomet. Chem.*, vol. 117, p. C55, 1976.

[118] M. Kosugi, H. Arai, A. Yoshino, and T. Migita, "REACTION OF α-CHLORO CONTROL OF REACTION KETONES WITH ALLYLTRI-n-BUTYLTIN.CONTROL OF REACTION SITE BY THE VARIATION OF REACTION CONDITIONS," *Chem. Lett.*, pp. 795–796, 1978.

[119] M. Kosugi and K. Fugami, "A historical note of the Stille reaction," *J. Organomet. Chem.*, vol. 653, pp. 263–283, 2002.

[120] D. Milstein and J. K. Stille, "A general, selective, and facile method for ketone synthesis from acid chlorides and organotin compounds catalyzed by palladium," *J. Am. Chem. Soc.*, vol. 100, no. I, pp. 3636–3638, 1978.

[121] W. J. S. V. Farina, V. Krishnamurthy, "The Stille Reaction," *Organic Reactions*, vol. 50. pp. 3–664, 1997.

[122] T. N. MITCHELL, "Palladium-catalysed reactions of organotin compounds," *Synthesis (Stuttg).*, no. 9, pp. 803–815.

[123] M. Bochmann and K. Kelly, "Palladium catalysed Cross-Coupling Reactions with Difunctional Tin Reagents: A General Route to Aromatic Polymers," *J. Chem. Soc. Chem. Commun.*, pp. 532–534, 1989.

[124] R. Giesa and R. C. Schulz, "Soluble poly(l,4-phenyleneethynylene)s," *Makromol. Chem.*, vol. 191, pp. 857–867, 1990.

[125] R. Galarini, A. Musco, R. Pontellini, A. Bolognesi, S. Destri, M. Catellani, M. Mascherpa, and G. Zhuo, "A New Synthetic Route to Polyheteroarenediylvinylenes," *J. Chem. Soc. Chem. Commun.*, pp. 364–365, 1991.

[126] Z. Bao, W. Chan, and L. Yu, "Synthesis of Conjugated Polymer by the Stille Coupling Reaction," *Chem. Mater.*, vol. 5, no. m, pp. 2–3, 1993.

[127] Z. Bao, W. K. Chan, and L. Yu, "Exploration of the Stille coupling reaction for the syntheses of functional polymers," *J. Am. Chem. Soc.*, vol. 117, no. 16, pp. 12426–12435, 1995.

[128] B. Carsten, F. He, H. J. Son, T. Xu, and L. Yu, "Stille Polycondensation for Synthesis of Functional Materials," *Chem. Rev.*, vol. 111, no. 3, pp. 1493–1528, Mar. 2011.

[129] H. a Dieck and R. F. Heck, "Palladium-catalyzed conjugated diene synthesis from vinylic halides and olefinic compounds," *J. Org. Chem.*, vol. 40, pp. 1083–1090, 1975.

[130] N. Miyaura and A. Suzuki, "Stereoselective Synthesis of Arylated (E) -Alkenes by the Reaction of Alk-1 -enylboranes with Aryl Halides in the Presence of Palladium Catalyst," *J. Chem. Soc., Chem. Commun.*, pp. 866–867, 1979.

[131] M. Rehahn, A.-D. Schlüter, G. Wegner, and W. J. Feast, "Soluble poly(para-phenylene)s. 2. Improved synthesis of poly(para-2,5-di-n-hexylphenylene) via Pd-catalysed coupling of 4-bromo-2,5-di-n-hexylbenzeneboronic acid," *Polymer (Guildf).*, vol. 30, no. 6, pp. 1060–1062, 1989.

[132] J. Sakamoto, M. Rehahn, G. Wegner, and A. D. Schlüter, "Suzuki Polycondensation: Polyarylenes à la Carte," *Macromol. Rapid Commun.*, vol. 30, no. 9–10, pp. 653–687, 2009.

[133] J. K. Stille, "The chemistry of the metal-carbon bond (Volume 2) The nature and cleavage of metal-carbon bonds," *Work*, vol. 2, pp. 625–788, 1985.

[134] P. Espinet and A. M. Echavarren, "The mechanisms of the Stille reaction," *Angew. Chemie - Int. Ed.*, vol. 43, pp. 4704–4734, 2004.

[135] D. Alberico, M. E. Scott, and M. Lautens, "Aryl – Aryl Bond Formation by Transition-Metal-Catalyzed Direct Arylation," *Chem. Rev.*, vol. 107, pp. 174–238, 2007.

[136] S. I. Gorelsky, D. Lapointe, and K. Fagnou, "Analysis of the palladium-catalyzed (aromatic)C-H bond metalation-deprotonation mechanism spanning the entire spectrum of arenes," *J. Org. Chem.*, vol. 77, pp. 658–668, 2012.

[137] A. Facchetti, L. Vaccaro, and A. Marrocchi, "Semiconducting polymers prepared by direct arylation polycondensation," *Angew. Chemie - Int. Ed.*, vol. 51, pp. 3520–3523, 2012.

[138] M. Chen, E. Perzon, M. R. Andersson, S. Marcinkevicius, S. K. M. Jönsson, M. Fahlman, and M. Berggren, "1 Micron wavelength photo- and electroluminescence from a conjugated polymer," *Appl. Phys. Lett.*, vol. 84, no. 2004, pp. 3570–3572, 2004.

3 Synthesis and Characterization of LBGs

3.1 Π-Conjugated Silole-Based Polymers

Silacyclopentadienes [1] are pentatomic heterocycles that possess σ*–π* conjugation arising from the interaction between the σ* orbital of the two exocyclic σ-bonds on the silicon atom and the π* orbital of the butadiene moiety [2][3]. The calculated LUMO level of a silole ring is lower than that of the corresponding cyclopentadiene (Figure 3.1-a) and of other heterocyclopentadienes (Figure 3.1-b), such as pyrrole, furan, and thiophene [2]. The unique aromaticity and the low-lying LUMO level offer the siloles interesting optoelectronic properties. Siloles displayed in Figure 3.2 a-d, are the typical building blocks to synthesize various silicon π-conjugated polymers.
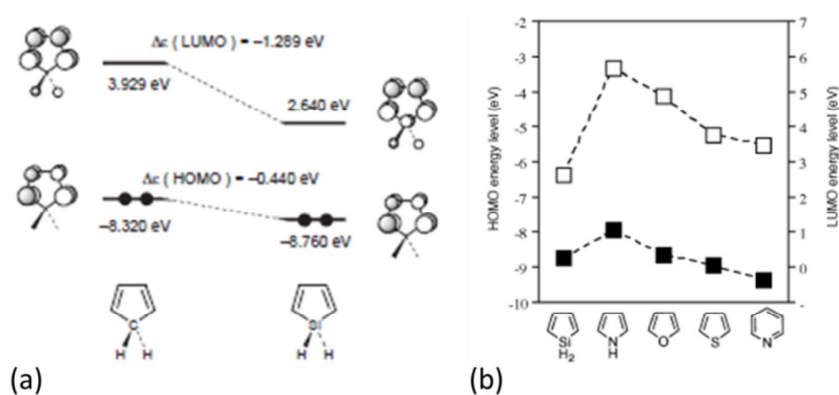
Figure 3.1 (a) Relative energy levels of the HOMO and LUMO for silole and cyclopentadiene, based on the HF/6-31G* calculations; (b) Relative HOMO and LUMO levels for silole and other hetero- cycles, based on HF/6-31G* calculations [2]**.**

The optoelectronic properties of the simple silacyclopentadiene ring (Figure 3.2-a) can be tuned thanks to the possibility of substituting up to 6 groups on the ring. 2,3,4,5-tetraarylsiloles are usually characterized by a non co-planar geometry and they possess interesting optoelectronic properties in the solid-state [4]. Dibenzosilole or 9-silafluorene (Figure 3.2-b) [5], dithienosilole or silicon-bridged bithiophene (Figure 3.2-c) [6] and bis-silicon-bridged stilbene (Figure 3.2-d) [7], are examples of silole containing heterocycles. The enlarged skeletons of the siloles are coplanar, showing normal photoluminescence (PL) properties of typical organic emitters.
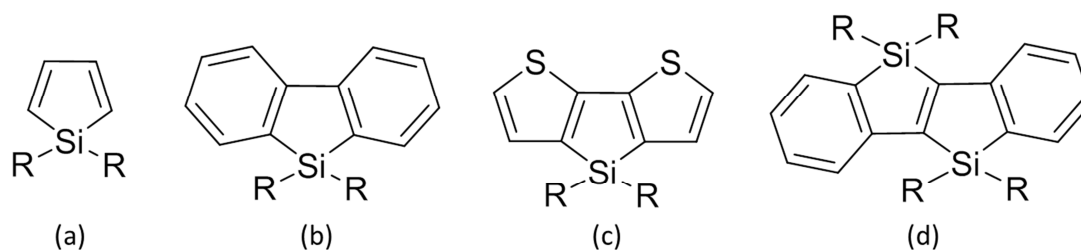
Figure 3.2 Different molecules incorporating the silacyclopentadiene unit: (a) silacyclopentadiene; (b) dibenzosilole; (c) dithienosilole; (d) bis-silicon-bridged-stilbene.

The incorporation of siloles in polymers is of interest and importance in chemistry and materials science [8]. The first synthesis of *Silicon-Containing Polymers (SCPs)* was reported by Tamao *et al.* in 1992 [9]. Since then, many research groups had investigated this class of polymers and many types of SCPs, such as main chain-type π-conjugated, main chain-type σ-conjugated, with silole pendants, and hyperbranched or dendritic, have been synthesized [8]. These polymers find applications in many fields of organic electronics such as Organic Field-Effect Transistor (OFETs), fluorescent chemosensor, red-green-blue (RGB) lights, bulk-heterojunction (BHJ) solar cells, RGB and white ElectroLuminescent (EL) devices.

In this paragraph the principal silicon main chain π-conjugated polymers will be introduced and a particular attention will be dedicated to dithienosiloles copolymers.

3.1.1 Silacyclopentadiene-Based Polymers

Poly(2,5-silole)s are the simplest π-conjugated poly(silole)s. However, these polymers were not so easily synthesized. The first successful synthesis was reported in 1999 and required the careful choice of a well-designed 2,5-difunctionalized silole unit (Figure 3.3-a) [10]. Afterwards, research interests moved to the synthesis of copolymers including this moiety. Silole–thiophene copolymers were the first to be synthesized [9]. Alternating silole–bithiophene, silole–terthiophene, and silole–quaterthiophene copolymers were prepared by Stille coupling reactions (Figure 3.3-b) [11] [12]. Reynolds and coworkers synthesized a silole-BEDOT (Figure 3.3-c) by electrochemical oxidative polymerization [13], which showed a very narrow bandgap of 1.3–1.4 eV.
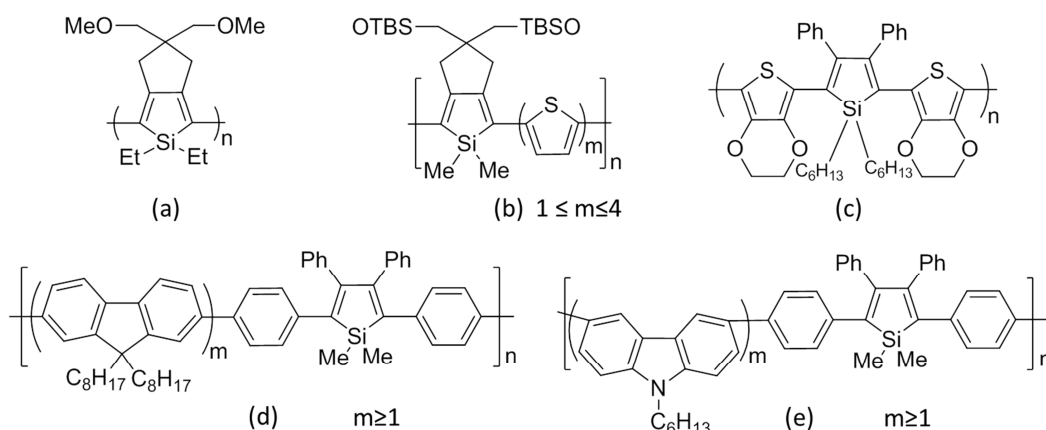
Figure 3.3 Homopolymers (a) and copolymers (b-e) incorporating the silacyclopentadiene ring as unit.

Random and alternating copolymers derived from fluorene and 2,5-diphenylsilole were prepared by Suzuki coupling reactions (Figure 3.3-d) [14], as possible materials for emitting applications. Similarly, 3,6-carbazole-2,7-fluorene-silole random copolymers (Figure 3.3-e) were synthesized by Suzuki coupling reactions [15].

3.1.2 Dibenzosilole-Based Polymers

In 2005, the phenyl end-capped poly(2,7-dibenzosilole) (Figure 3.4-a) was synthesized by Suzuki polycondensation, with a high yield of 93% [16] and a M_n of 31 000 g/mol. Its HOMO and LUMO levels were -5.77 and -2.18 eV, respectively. It showed good photo- and electro-luminescence properties with high yields and emission maxima at 425 nm and 431 nm, respectively.
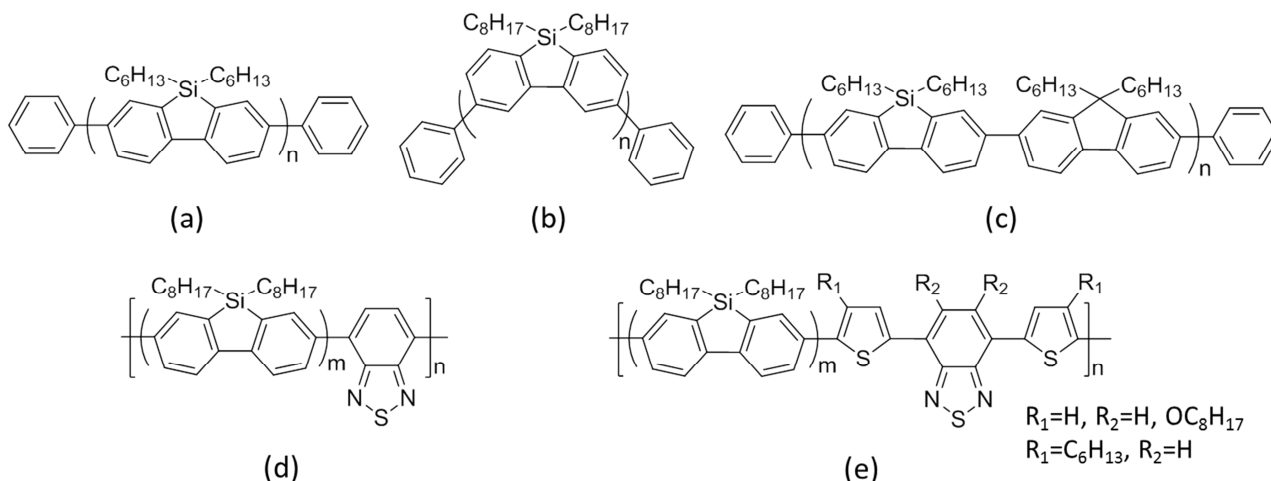
Figure 3.4 Homopolymers (a, b) and copolymers (c-e) containing the dibenzosilole unit.

Holmes and coworkers prepared a poly(3,6-dibenzosilole) (Figure 3.4-b) via a Suzuki coupling reaction in a yield of 93% [17] and a M_n of 11 000 g/mol. The energy levels are a little lower than that

of the analogous poly(2,7-dibenzosilole) at -5.65 eV and -2,15 eV against -5.77 eV and -2.18 eV, respectively for the HOMO and LUMO of the two polymers. A fluorene-2,7-dibenzosilole alternating copolymer (Figure 3.4-c) was prepared by the Suzuki coupling reaction with a yield of 94% [16] and M_n of 109000 g/mol. Its absorption and fluorescent properties were quite similar to those of poly(2,7-dibenzosilole) (Figure 3.4-a).

Random copolymers of 2,7-dibenzosilole and 2,1,3-benzothiadiazole (Figure 3.4-d and -e) [18] were synthesized with m=9. The copolymer (d) showed a green emission with λ_{em}(PL) of 530nm while for (e) λ_{em}(PL) was 629 nm. This was due to the different efficiency of the intramolecular energy transfer from dibenzosilole unit to benzothiadiazole (d) and dithienylbenzothiadiazole (e). Leclerc and coworkers prepared the corresponding alternating copolymer of (e) (m=1) [19]. Its electrochemical HOMO and LUMO levels were −5.7 and −3.81 eV respectively, giving an electrochemical bandgap of 1.89 eV that matched the optical bandgap. Application in a photovoltaic device gave a PCE of 1.6%. Song *et al.* prepared the dioctyloxybenzothiadiazole derivatives of (d) [20]. Its HOMO and LUMO levels moved to -5.44 and -3.51 eV, giving a band gap of 1.93 eV. Performances in a photovoltaic device were dramatically improved, with a PCE up to 4.81%.

3.1.3 Dithienosilole-Based Polymers

The silicon atom bridging the two thiophene rings in dithienosiloles has a similar effect on the electronic states of the bithiophene system, even if it is reduced when compared to the silacyclopentadiene [21]. The LUMO level of the polymer is lowered thanks to the interaction between the silicon σ*-orbital and bithiophene π*-orbital. Furthermore the silicon bridge forces the bithiophene ring to retain a *syn* configuration with respect to the alkyl units [22], increasing the system planarity and facilitating the overlap of π-orbitals.

The first full-synthetic route to dithienosiloles has been reported by Ohshita *et al.* [21] and then further optimized by Usta *et al*. (Scheme 3.1) [23]. The lithiation of 3,3'-dibromo-2,2'-bithiophene and its cyclization with dialkylsilylchloride directly affords the dithienosilole. Reaction with N-bromosuccinimide (NBS) gave the dibromodithienosilole, furtherly transformed in the corresponding bis(trimethylstannyl) compound, an important silole monomer for Stille polycondensations.
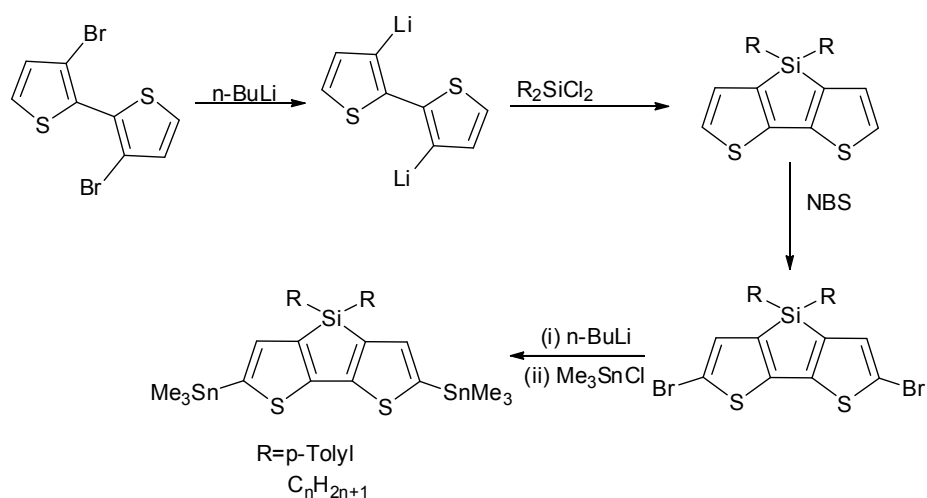
Scheme 3.1 Synthetic route to the dithienosilole monomer [23]

Dithienosilole homopolymers have been obtained by anodic oxidation polymerization [6] and by Stille polycondensation [24]. For the anodic oxidation polymerization the starting monomer is a ditrimethylsilyldithienosilole (Scheme 3.2-a), while for the Stille polymerization both dibrominated- and distannilated-dithienosilole monomers are necessary (Scheme 3.2-b).
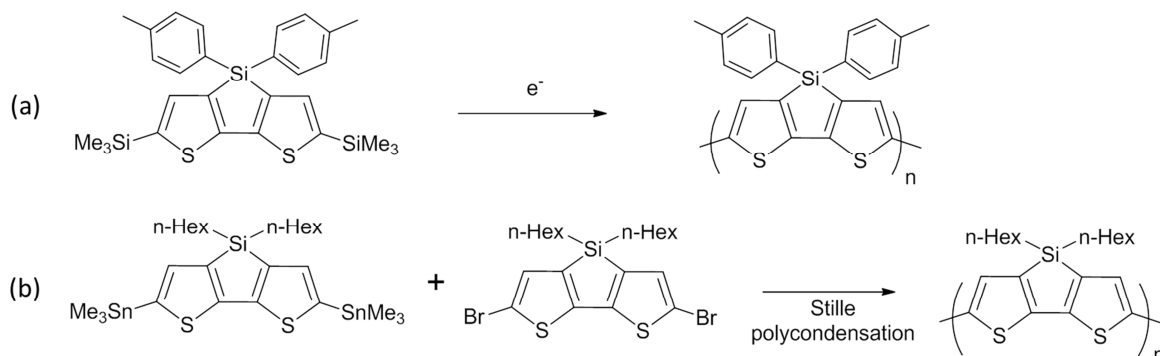
Scheme 3.2 Polymerization of leading to the dithienosilole homopolymer [6], [24].

The absorption spectra of the *p*-tolyl homopolymer showed different features according to polymerization conditions, indicating different polymer structures, due to the low stability of the trimethylsilyl group. The polymer displayed red-light photoemission with λ_{em} at ≈660 nm. A single-layer EL device also emitted a red light, with a low brightness even at a high voltage. The *n*-hexyl homopolymer showed higher Mw due to the better solubility of the alkyl chains compared to the *p*-tolyl groups. The copolymer showed poor photovoltaic performance, with a *PCE* up to only 0.05%.
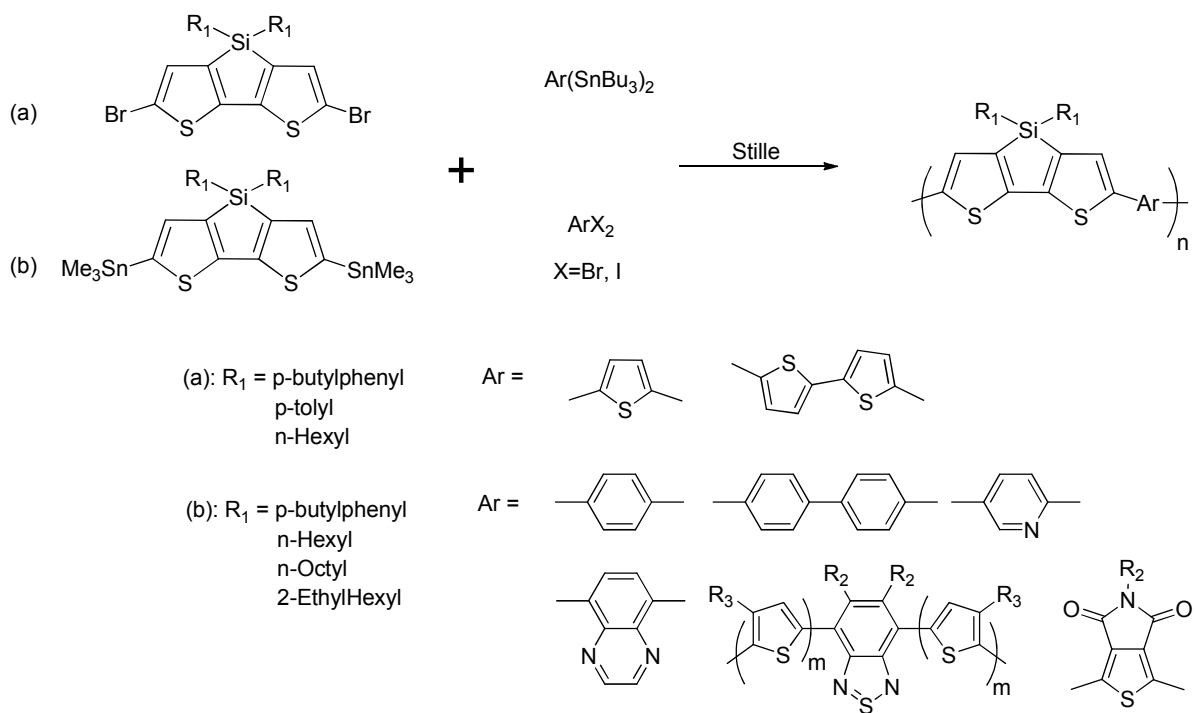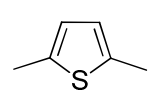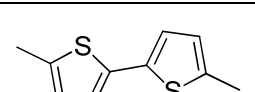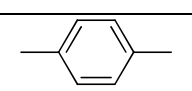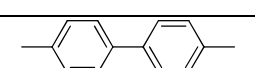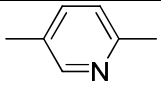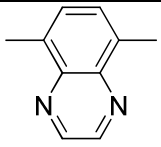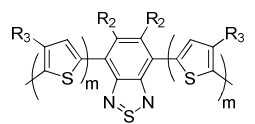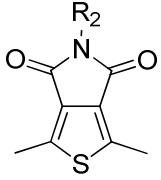
Scheme 3.3 Different synthetic routes to dithienosilole copolymers.

Dithienosilole had then been used as co-monomer for light-emitting, OFET and BHJ devices. Ohshita *et al.* reported synthesis and properties of dithienosilole–thiophene alternating copolymer (Table 3.1, **P1-3**) [25]. Usta *et al.* [26] prepared two dithienosilole–thiophene copolymers and investigated their OFET characteristics; both showed high field-effect hole mobilities in air.

Table 3.1 Different copolymers including dithienosilole as repeating unit.

Polymer	R$_1$	Comonomer	R$_2$	M_n (g/mol)	Đ	λ_{max} (nm)	Ref.
1	p-Butylphenyl		/	6900	1.4	546	[25]
2	P-Tolyl		/	5100	1.6	555	[25]
3	C$_6$H$_{13}$		/	10000	1.9	521	[23]
4	p-Butylphenyl		/	7500	1.7	532	[25]
5	P-Tolyl		/	6100	1.6	529	[25]
6	C$_6$H$_{13}$		/	14000	2.9	544	[23]
7	p-Butylphenyl		/	4000	1.3	482	[27]
8	p-Butylphenyl		/	4300	1.3	450	[27]

			R2	R3	m				
9	p-Butylphenyl		/			3100	1.3	460	[27]
10	p-Butylphenyl		/			4500	1.4	583	[27]
11	C_6H_{13}		$OC_{14}H_{29}$	H	1	26400	2.8	597	[28]
12	C_6H_{13}		H	$C_{12}H_{25}$	1	22400	2.4	590	[28]
13	$CH_2CH(C_2H_5)(C_4H_9)$		H	H	0	18000	1.2	680	[29]
14	C_6H_{13}		H	H	1	29200	5.2	563	[24]
15			C_8H_{17}			31000	1.6	610	[30]
16	$CH_2CH(C_2H_5)(C_4H_9)$		C_6H_{13}			26000	1.6	/	[30]
17			C_4H_9			25000	1.6	/	[30]

Ohshita *et al.* [6] synthesized a series of polydithienosilole copolymers, using phenyl (**P7**), diphenyl (**P8**), o-pyridine (**P9**) and quinoxaline (**P10**) units as co-monomers. Chu *et al.* [30] synthesized a series of copolymers with thienopyrroldiones, investigating the effect of the Mw and of the side chain on device performances. For **P15** they were able to obtain a *PCE* ranging from 3.1% for the shortest polymer (10000 g/mol) to 7.7% for the longest (31000 g/mol). **P16** and **P17** showed a reduced *PCE* of 5.3% and 6.4% respectively.

Hou *et al.* [29] prepared a copolymer of dithienosilole with 2,1,3-benzodithiazole (**P13**) and Liao et al. [24] with 4,7-dithienyl-2,1,3-benzothiadiazole (**P14**). The thiophene bridging unit moves the absorption maxima from 680 nm to 563 nm and 593 nm in solution and film, respectively. The copolymer showed λ_{max}(abs) at 563 nm for solution and 593 nm for thin film. The electrochemical HOMO and LUMO levels change from −5.05 and −3.27 eV to −5.13 and −3.23 eV respectively. **P13** in combination with **PC$_{71}$BM** (1:1 w/w) gave photovoltaic devices with a PCE of 5.1% (optimized cell), while **P14** had a *PCE* only up to 0.18% (not-optimized cell). Helgesen *et al.* [28] synthesized and reported the photovoltaic performance and stability of the derivatives of (**P14**), attaching side-chains

on both the *BT* and thiophenes units. They synthesized **P11** and **P12**, and characterized their performances in devices in combination with **PC$_{61}$BM**, achieving a *PCE* of 1.99% and 1.26%.

Scharber *et al.* [31] thoroughly investigated the effect of the silicon substitution in the cyclopentadiene ring, comparing **P13** with the analogous carbon-cyclopentadithiophene (**PCPDTBT**). They found that **P13** forms a highly efficient nanomorphology when blended with **PC$_{71}$BM**, giving a certified *PCE* of 5.2%. This was possible because **P13** showed a higher crystallinity, improved charge transport properties, reduced bimolecular recombination, and a reduced formation of charge transfer complexes in the blend than the **PCPDTBT**. All these improvements can be correlated to the presence of the Si atom, which introduces a small distortion of the cyclopentadithiophene unit. The longer Si–C bond [32] modifies the geometry of the fused dithiophene unit which is enough to achieve a better ordering of the polymer chains. In a successive investigation, Morana *et al.* [33] correlate this higher crystallinity and subsequent morphology, characterized by the presence of small fullerene crystallites, to the absence of charge transfer complex (CTC). These CTC are involved in a multi-step charge-recombination process in **PCPDTBT**:fullerene blend, where polymer and fullerene are finely mixed. On the other hand, in **P13:C$_{60}$** blend this recombination process is significantly quenched or rendered inactive.

Also Chen *et al.* [22] studied the effect of the silicon atom substitution, obtaining even higher *PCE* of 5.6% for *P13* and 3.1% for **PCPDTBT**. They confirmed that this difference is not related to different electronic structures, which are very similar. DFT calculation confirmed also that the C-Si bond is significantly longer than the *C-C* bond, which has two effects. The first is that the *syn* conformation of both thiadiazole units is preferred. The second is that the reduced steric hindrance allows a high crystalline structure, as experimentally measured by Grazing Incidence X-ray Diffraction (GIXRD). They studied also the effect of thermal annealing on the two polymers, seeing an improvement in the devices performances for *P13* and no effect on **PCPDTBT**. Similarly, they found that the charge carrier mobility in *TFTs* based on *P13* increased by a factor of five upon annealing. This behavior confirms different self-assembly characteristics for the two polymers.

Helgesen *et al.* [34], compared the device performances of **P11/P12** and the corresponding **PCPDT-DBT**, with the same side-chains on the *DBT* units but different on the **CPDT** (2-ethylhexyl) and **DTS** (*n*-hexyl) units. The best performance was obtained by the **PCPDT-DBT** polymer with a tetradecyloxy substituent on the **BT** unit. Also the bridging atom in the dithiophene unit has a slight

influence on the band gap, which is reduced for **P11/P12**, indicating a higher degree of π-delocalization in the silicon-bridged polymers. Moreover, they investigated the photostability of these polymers, measuring the amount of absorbed photons *versus* the ageing time. The results clearly showed that the two **CPDT** polymers are by far the less stable, because the quaternary carbon site on the cyclopentadithiophene ring can be easily oxidized. The substitution of the carbon with the silicon resulted in a significant stability improvement by a factor 5.

Manceau *et al.* [28] reported an extended study in which they investigated the stability of many common monomers used in *LBG* polymers. The samples were photooxidized under 1 sun illumination in ambient air whilst monitoring the relative humidity but without having any control upon it. To quantitatively compare all the different materials, they used the total amount of absorbed photons versus the ageing time, over all the polymer absorption spectra. The dithienosilole resulted as one of the more stable units between the donors (Figure 3.5), with respect to photooxidation, in combination with many different acceptor units, such as: dithienylthienopyrazine derivatives, dithienylbenzothiadiazole derivatives, thienothiophene derivatives and benzothiadiazole.
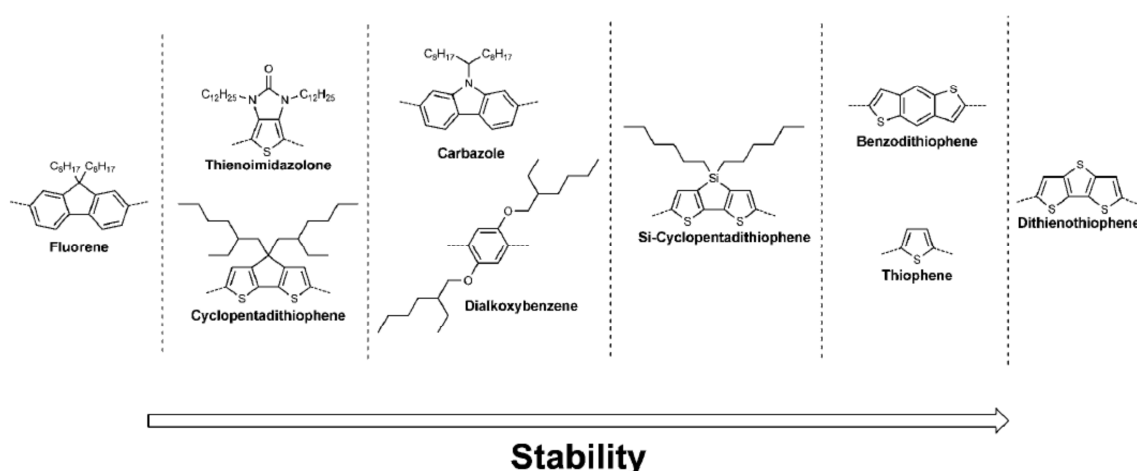
Figure 3.5 Stability of common donor units employed in LBG polymers [28].

Recently Fraga Domínguez *et al.* [35] explored the degradation mechanisms of **P13** under photooxidative conditions. In order to monitor the evolution of the thin film, they combined a wide range of analytical techniques such as UV–vis and IR spectroscopies, atomic force microscopy (AFM), and profilometry. Gas phases were monitored too [headspace solid-phase microextraction (HS- SPME) coupled with gas chromatography/mass spectrometry (GC-MS)] to check the presence of any low molecular weight byproducts released during degradation. Also molecular modeling was used to gain

a better understanding of the degradation mechanism. The results showed a complicated picture, in which the polymer side-chains started to degrade at the beginning of the irradiation, through the formation of chain oxidation products, cross-linking reactions, and releasing low molecular weight oxidation products. The loss of these low *Mw* products resulted in a significant modification of the surface topography. The photodegradation of the polymer backbone mainly involved the oxidation of the sulfur units of the bithiophene, even if oxidation of the N and Si atoms was also identified. Nonetheless, the degradation rate of *P13* was confirmed to be slower than for other common p-type polymers, such as *P3HT* and *PCDTBT*. In order to explain this, the stability of the macroradicals created upon hydrogen abstraction in the alkyl chain of both *P13* and *PCPDTBT* was explored by DFT. Calculation revealed a higher delocalization, thus improved stability, in the case of *PCPDTBT* than *P13*, resulting in a reduced stability of the former.

For its improved stability and superior electronic properties dithienosilole has been chosen as donor monomer for the two series of polymers presented in the next sube-section.

3.2   Side-chain effect

As briefly stated in the general introduction, the side-substituents on π-conjugated polymers have a dual effect of tuning the electronic levels and increasing their solubility which leads to easy processability. The importance of side-chains has been underestimated for a long time, while research was focused on the π-conjugated backbone. Recently research has moved to the investigation of the influence of the side-chains on electronic properties [36], polymer and blend nanomorphology [37] [38], stability [34] and processability [39].

Similar studies have been conducted on polymers made with 2,1,3-benzothiadiazole, thiophene, and thieno-[3,2-*b*]thiophene [40], thieno[3,4-*b*]thiophene benzo[1,2-*b*:4,5-*b'*]dithiophene [41], thieno[3,4-*c*]pyrrole-4,6-dione and dithiophene [42], diketopyrrolopyrrole and dialkoxylphenylenevinylene [43], dithienosilole and thieno[3,4-*c*]pyrrole-4,6-dione [30], di-2-thienyl-2,1,3-benzothiadiazole and fluorene [44], dithienosilole and thiazolothiazole [45], benzo[1,2-b:4,5-*b'*]dithiophene and bithiazole [46], 2,7-carbazole and quinoxaline [47], di-2-thienyl-2,1,3-benzothiadiazole and benzo[1,2-*b*:4,5-*b'*]dithiophene [48]. Yang *et al.* [49] conducted an investigation by systematically varying the side-chain on a naphtho[2,1-*b*:3,4-*b'*]dithiophene (NDT) and 4,7-di(thiophen-2-yl)benzothiadiazole (DTBT) donor-acceptor polymer. The different side-chains significantly impacted the photovoltaic characteristics of the corresponding devices. Yang *et al.* were

able to establish a quantitative relationship between side-chains and photovoltaic properties; long and branched side-chains weaken the *π-π intermolecular interaction*, reducing the J_{sc} whilst improving the V_{oc}. On the other hand, short and straight side-chains would promote the *π-π interaction*, which increased the J_{sc} but reduced the V_{oc}. However, J_{sc} is also affected by the film morphology of the blend and by the density of the conjugated backbone, which is strongly dependent on the length of the alkyl side-chain. Rumer *et al.* [42] and Zhang *et al.* [43] investigated the effect and the position of branching versus linear chains. They found that both the length and the branching of a side-chain are factors to be considered. It is the overall steric induced effect to be responsible for changes in the properties of a polymer series. The use of a *C1-branched* side-chain promoted crystallinity and solid-state packing.

In their review, Mei and Bao [50] collected and analyzed the effects of side-chains on many parameters. Electron-donating side-chains, such as alkoxy-, alkylthio-, alkylamino-, etc. can donate some electron density to the conjugated polymer backbones which raises the HOMO energy levels of the polymer. In a similar way electron-withdrawing side-chains, such as acetyl-, ester-, amide-, etc. are capable of pulling electron density from the π-conjugated backbones, therefore lowering the energy levels. Moreover, these side-chains can improve the planarity of the backbone through intramolecular interactions. On the other hand, the side-chains can have a negative impact promoting a twisting of the backbone, that reduces the π-π interactions along the conjugated chain. Aromatic side-chains are also very attractive because they usually affect both *HOMO* and *LUMO* levels, extending the conjugation of the polymer and broadening the absorption spectra in the visible region. They can also improve the hole mobility through the strengthening of intermolecular polymer-polymer interactions. As drawbacks, aromatic units may cause backbone twisting and steric hindrance and cause repulsion between polymer and **PC$_{61}$BM**.

The Krebs group [37] [51] investigated thermocleavable ester side-chains, which have the advantage to enable preparing polymer solar cells via solution processing and then to remove the solubilizing side-chains after the active layer has been deposited. Moreover, removing the side-chains increases chromophore density and the more rigid system prevents polymer/fullerene phase segregation and provides stabilization of the nanomorphology.

Another way to stabilize the blend morphology is to use end-functionalized side-chains, in which the end group can modify the interaction between the polymer and **PC$_{61}$BM**. An example of

this strategy was given by Park *et al.* [52], that investigated the effect of a *o*-dichlorobenzyl *(DCBZ)* group on a benzodithiophene-thienothiophene polymer. The *DCBZ* increased the polymer/PC$_{71}$BM compatibility and this stronger interaction between induced a change in the **PC$_{71}$BM** molecular geometry and electronic structure. This led to the increase of the **PC$_{71}$BM** LUMO level and thereby an enhanced V_{oc}. The introduction of monomers with fullerene-compatible functional groups can be an effective way for tuning the photovoltaic characteristic of BHJ devices by controlling the nanomorphology and the electronic structure of acceptors in the donor/acceptor blend.

The effect of the molecular arrangement at the donor:fullerene interfaces on the performance of *OPV* materials, has been recently reviewed by Graham *et al.* [38]. Higher-performing donor-acceptor polymers generally have acceptor units that are sterically accessible for interactions with the fullerene derivative, whereas the corresponding donor units tend to have branched alkyl substituents that sterically limit interactions with the fullerene. The observation of this trend can help to further rationalize the past work and guide future design of materials. Nonetheless further theoretical and experimental studies are required, including determination of which intermolecular interaction leads to a favorable energy environment, the effects on charge separation, etc.

Manceau *et al.* [34] investigated the influence of the nature of side-chains on the stability of the polymers under photoxidative conditions. They studied different alternating polymers based on cyclopentadithiophene-dithienobenzothiadiazole units, varying the substituent (unsubstituted, ester or ether side-chain). The resulting stability trend was: -CO$_2$R < -OR < -H. The unsubstituted *BTD* demonstrated the highest stability among the three samples, but surprisingly the difference with the others was remarkably small. In another study, Manceau *et al.* [53] investigated the photochemical stability of thermo-cleavable polymers. They found that the side-chain cleavage led to an improvement of the material stability. These findings confirmed that side-chains play a key role in the degradation of π-conjugated polymers.

Morse *et al.* [54] recently investigated a series of low band-gap polymers based on units, bearing different side-chains. The physical properties of the polymers were similar in absorption, mobility, energy levels, and molecular weights. Photodegradation of encapsulated inverted devices exposed to AM1.5 solar irradiation at 50 °C was monitored by UV-vis and FTIR spectroscopies for over 110 hours. Degradation occurred at different rates, confirming the key role of the polymer chemical structure itself. Moreover, they have been able to link the PCE loss with the evolution of the active

layer morphology and the **PC$_{61}$BM** dimerization, monitored through AFM, XRD, and UV-Vis analysis of the blend films. Also, they had been able to correlate the stability to the polymer:**PC$_{61}$BM** ratio, reducing **PC$_{61}$BM** amount in the blend improved the device stability, suggesting that the device degradation and **PC$_{61}$BM** migration is diffusion limited in these films. Amongst the polymer series they had shown that an even distribution of side-chains, preferably linear alkyl, promoted device stability by reducing **PC$_{61}$BM** diffusion rates, while alkoxy and thienyl-ethylhexyl side-chains increase the **PC$_{61}$BM** diffusion rates, reducing the overall stability.

The effect of side-groups was studied and is discussed in the following sub-sections. To study the effect of different alkyl chains, DPP was chosen as co-monomer for its facile functionalization, its well-known stability as dye and its electronic properties. Dithienopyrazine was chosen as co-monomer to study the effect of two different aromatic substituents (thiophene and ethylenedioxybenzene) on the properties of the polymers.

3.3 Synthesis and characterization of LBGs based on DTS and DPP units

In this sub-section the synthesis and chemical characterization of low band gap copolymers based on dithienosilole (DTS) and diketopyrrolopyrrole (DPP) are described. A literature review have been used as introduction to explain and justify the choice of these monomers units.

3.3.1 Introduction

Diketopyrrolo[3,4-*c*]pyrrole (DPP) and its derivatives represent a key structural unit in an important class of yellow to red pigments with deep color, which are commercialized since the 1980s [55]. Many DPP derivatives have since been synthesized, with colours ranging from orange to red to purple. Many DPP derivatives exhibit a high photostability in the solid-state, weather fastness, deep colour, luminescence with large Stokes-shift enabling technical applications in coloring of fibers, plastics and surface coatings [56][57]. In the last 20 years, a growing number of researchers in organic electronics focused their attention on DPPs since its monomers and DPP-containing polymers exhibit interesting light-emitting and photovoltaic properties [58][59].
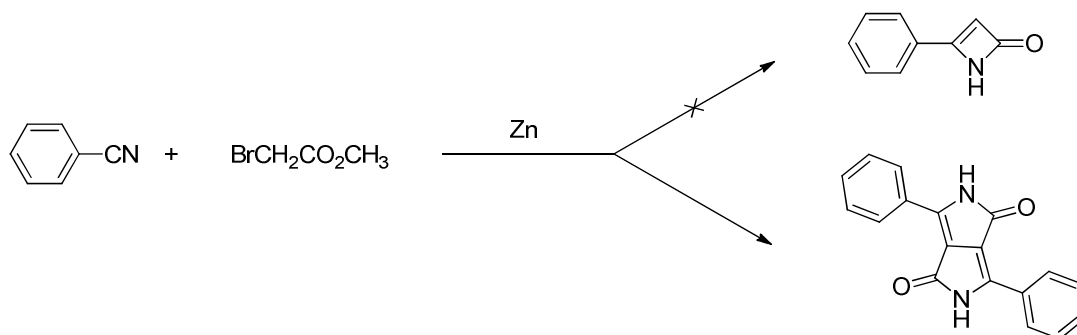
Scheme 3.4 First DPP synthetic route [60]

3,6-Diphenyl-substituted DPP was first reported by Farnum *et al.* in 1974 (Scheme 3.4) [60] with a really low yield, ranging from between 5-20%. In 1983, Iqbal, Cassar and Rochat reported an elegant and effective synthetic pathway for DPP derivatives (Scheme 3.5) [61]. In this route DPP derivatives can be obtained in high yields, by a one-step reaction of aromatic nitriles with succinic acid diester derivatives.
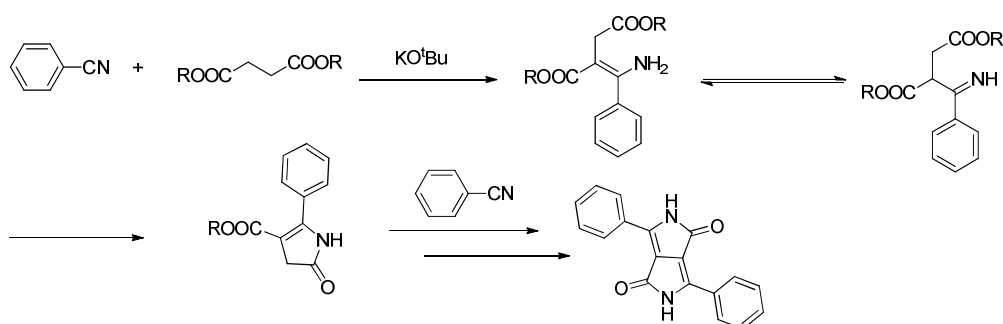
Scheme 3.5 Second DPP synthetic route through succinic acid diester [61]

Importantly, the presence of two electron-withdrawing amide functional groups causes the DPP to have a high electron affinity, making it a good acceptor for donor–acceptor (D–A) organic π-conjugated materials [62] [63]. In the solid-state, the formation of hydrogen bonds between lactam units of different DPP molecules causes the formation of a physically cross-linked chain structures, which is at the origin of its poor solubility [64]. Short distances between the chromophore planes and phenyl ring planes enable π-π-interactions via molecular orbital overlapping and exciton coupling effects [64][65], whilst electronic interactions and strong intermolecular forces lead to a high thermal stability of up to 500 °C. The DPP core is commonly substituted in the 3 and 6 positions with phenyl [66] or thienyl [67] substituents, but also furan [68] and selenophene [69] substituted DPP have been reported. The smaller, 5-membered heterocyclic rings reduce the dihedral angles between the DPP

core and the pendant substituent, improving the planarity of the molecular backbone, thus increasing π-delocalization and intermolecular π-π interactions. Moreover, thiophene is a stronger electron donor than phenyl, enhancing intramolecular charge transfer transitions. These effects result in dithienyl based materials typically exhibiting smaller bandgaps and greater charge transport properties than the corresponding diphenyl derivatives [70][71].

For the preparation of π-conjugated DPP-based polymers, palladium-catalyzed polycondensation reactions such as Suzuki [72], Stille [73] and Heck [74] coupling are especially useful, but electrochemical polymerization [75] has been also reported. To make DPPs suitable for polymerization, it is necessary to prevent the hydrogen-bond formation and to enhance the solubility of DPP compounds. A possible strategy is the functionalization of the amide-nitrogen atom by N-alkylation [76], N-arylation [77] or N-acylation [78]. While the N-alkylation proceeds directly in good yield, the introduction of aryl units in most cases involves a specific synthetic route, requiring the synthesis of the corresponding diketofurofuran compound that is subsequently converted into the N-aryl-lactam by reaction with an arylamine [77]. Common polymerizable groups, such as halogen atoms (**Br** and **I**), hydroxyl or aldehyde, have to be attached either to the DPP's lateral aryl units in position 3 and 6 [79], or to the lactam substituent groups [80]. For the preparation of brominated diphenyl-DPPs, it is necessary to start from bromobenzonitrile and a succinic acid ester and to prepare first the dibromophenyl-DPP pigment, which is subsequently N-alkylated to yield the soluble dibromo-dialkyl derivative. When the aryl unit is thiophene, direct bromination with N-bromosuccinimide is possible [81].
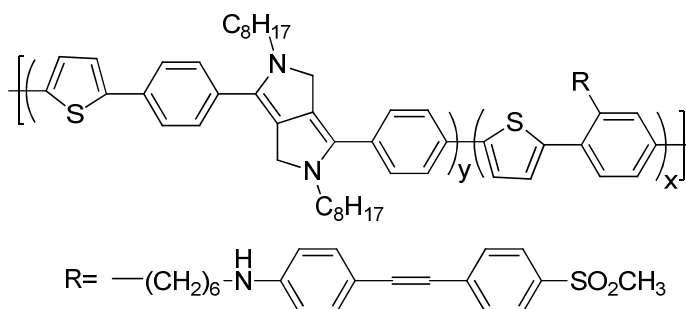
Figure 3.6 First synthesized DPP-based polymers in 1993 [79]**.**

The first DPP-based polymer was reported by Yu *et al.* in 1993 (Figure 3.6) [79], block copolymers containing phenylene, thienylene and N-alkyl substituted diphenyl DPP units in the main chain were synthesized by Stille coupling. In 1997, Eldin and coworkers described DPP-containing

polymers obtained by radical polymerization of bis-acryloyl DPP derivatives [80]. The first synthesis of conjugated DPP-polymers and copolymers via Suzuki coupling was reported by Tieke and Beyerlein in 2000 [82]. While in 2002, the same group studied for the first time the electroluminescent (EL) properties of a DPP-containing π-conjugated polymer [83]. In Figure 3.7-a collection from the literature of low bandgap polymers that include diphenyl-DPP as building-block is reported.
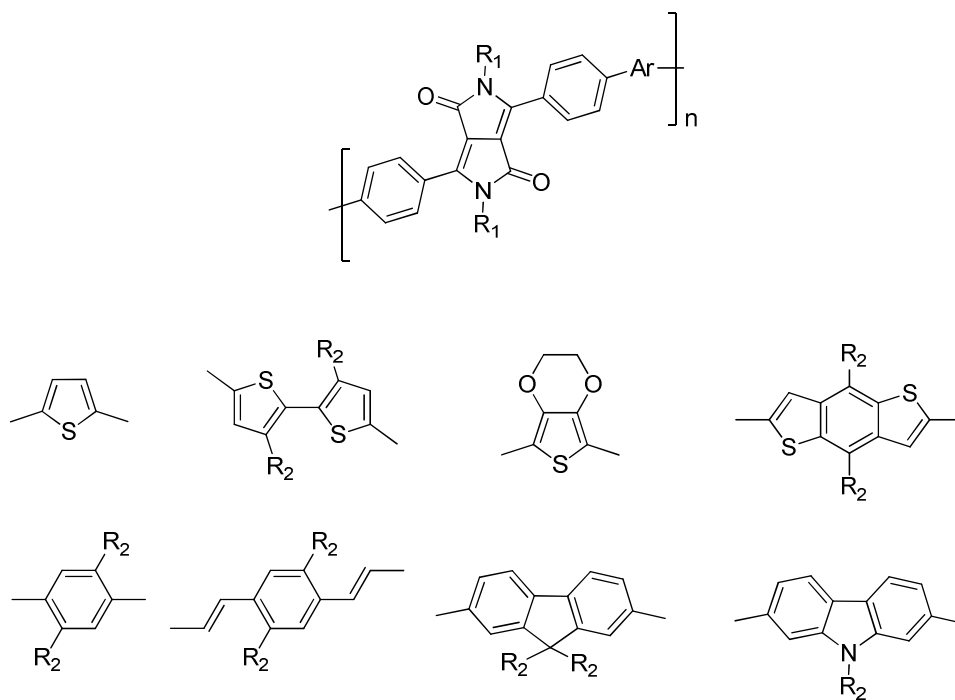
Figure 3.7 Typical comonomers employed in the synthesis of diphenyl-DPPs LBG polymers. R$_1$ and R$_2$ represent alkyl chains.

The replacement of the phenyl groups in the 3,6-diphenyl-DPP derivatives by a thiophene group resulted in 3,6-(2-thiophenyl)-substituted DPP derivatives. The absorption maxima of these thieno-DPPs is at about 550 nm, red-shifted by around 50 nm as compared to the corresponding phenyl-DPPs. Π-conjugated polymers containing dithieno-DPP in the main-chain exhibit absorption maxima between 600 and 900 nm. Due to their small band gaps and high charge carrier mobilities, these polymers are interesting for applications in field-effect transistors (OFETs) and organic photovoltaic cells [84]–[86], and in particular they have found application in tandem solar cells [87].

Encouraged by the good performance of dithieno-DPP-based solar cells, further polymers were recently synthesized (Figure 3.8) and their chemical (Table 3.2) and electronic and photovoltaic properties investigated (Table 3.3). Among these were alternating copolymers containing dithieno-DPP and carbazole [86], [88], [89], fluorene [88]–[91], dibenzosilole [87], dithienosilole [88],

benzo[1,2-*b*;3,4-*b*]dithiophene [91], dithieno[3,2-*b*;2′,3′-*d*]pyrrole [89], [92] and cyclopenta[2,1-*b*;3,4-*b*′]-dithiophene [91] as comonomer units.
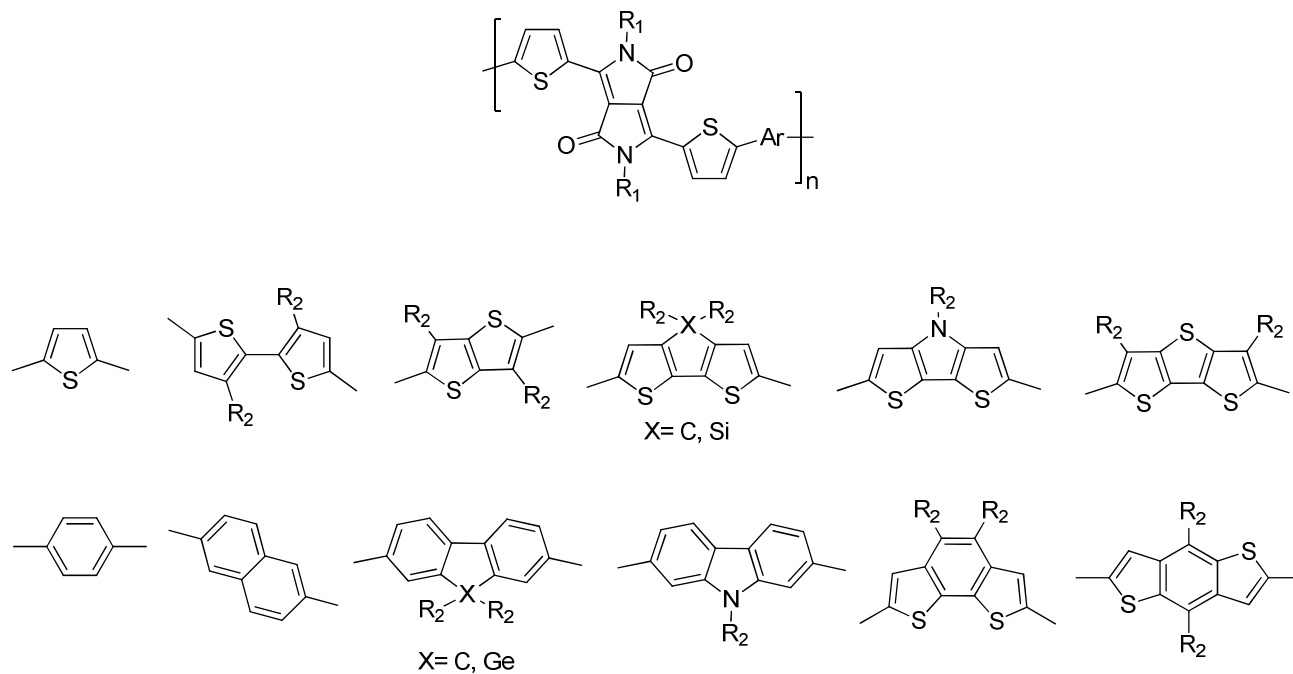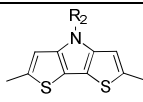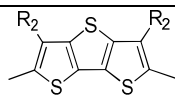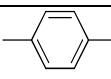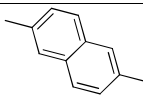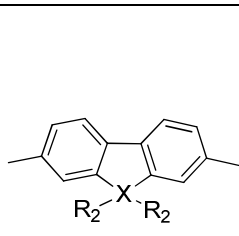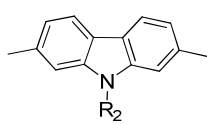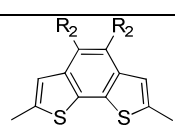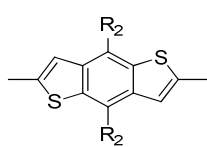
Figure 3.8 Typical comonomers employed in the synthesis of dithieno-DPPs LBG polymers. R_1 and R_2 represent alkyl chains.

Table 3.2 Chemical structure and properties of dithieno-DPPs conjugated D-A polymers.

Polymer	R_1	Ar	R_2		Mw (g/mol)	Ref
1	-$C_6H_{12}C_{10}H_{21}$		/		54	[67]
2	-$C_6H_{12}C_2H_5$		H, -$C_{12}H_{25}$		/	[93]
3			-$C_{12}H_{25}$		67	[93]
4			-2-Th-5-$C_6H_{12}C_2H_5$		/	[94]
5	-$C_6H_{12}C_{10}H_{21}$		H		/	[95]
6	-$C_6H_{12}C_2H_5$		-4-$C_2H_5C_8H_{16}$		/	[95]
7			-C_6H_{12}		/	[96]
8	-$C_8H_{16}C_4H_9$		X = C	-C_8H_{17}	68	[91]
9	-$C_6H_{12}C_2H_5$			-C_8H_{17}	12	[91]

No.	R_1	Structure	X	R_2	Yield	Ref.
10	$-C_6H_{12}C_2H_5$		X = Si	$-C_6H_{12}C_2H_5$	31	[90]
11	$-C_6H_{12}C_2H_5$	R_2 / N-bridged dithiophene		$-CH(C_6H_{12}C_2H_5)_2$	15	[89]
12	$-C_4H_9$			$-CH(C_6H_{12}C_2H_5)_2$	19	[92]
13	$-C_6H_{12}C_2H_5$	R_2, S, R_2 fused thiophene		$-C_{10}H_{21}$	/	[97]
14	$-C_6H_{12}C_{10}H_{21}$	benzene		/	/	[98]
15	$-C_8H_{16}C_{12}H_{25}$	naphthalene		/	/	[99]
16	$-C_6H_{12}C_2H_5$		X = C	$-C_6H_{12}C_2H_5$	15	[89]
17				$-C_8H_{17}$	19	[90]
18	$-C_6H_{12}C_{10}H_{21}$	$R_2 X R_2$ bridged biphenyl		$-C_8H_{17}$	62	[91]
19	$-C_4H_9C_8H_{17}$			$-C_8H_{17}$	31	[91]
20	$-C_8H_{17}$		X = Ge	$-C_4H_9$	/	[100]
21				$-C_8H_{17}$	/	[100]
22	$-C_8H_{17}$			$-CH(C_8H_{17})_2$	30	[88] [101]
23	$-C_{10}H_{21}$	carbazole, R_2 on N		$-CH(C_{10}H_{21})_2$	/	[102]
24	$-C_6H_{12}C_2H_5$			$-CH(C_{10}H_{21})_2$	91	[89]
25	$-C_6H_{12}C_2H_5$	R_2 R_2 dithiophene		$-C_6H_{12}C_2H_5$	48	[90]
26	$-C_8H_{16}C_{10}H_{21}$			$-C_6H_{12}C_2H_5$	/	[103]
27	$-C_6H_{12}C_2H_5$			$-OC_8H_{17}$	20	[90]
28	$-C_6H_{13}$	R_2, S fused thiophene		$-OC_6H_{13}$	19	[84]
29	$-C_8H_{17}$			$-C_6H_{12}C_{10}H_{21}$	/	[104]
30	$-C_4H_8C_8H_{17}$			$-C_4H_8C_8H_{17}$	/	[104]
31	$-(C_2H_4)_2CHC_5H_{11}C_8H_{17}$			$-C_8H_{17}$	/	[104]

Table 3.3 Electronic and photovoltaic properties of dithieno-DPPs conjugated D-A polymers.

Polymer	λ_{max} (nm)	E_g^{opt} (eV)	HOMO (eV)	LUMO (eV)	E_g^{el} (eV)	PCE (%)	Ref
1	/	/	-5.17	-3.61	1.50	4.90	[67]
2	/	/	/	/	/	4.00	[93]
3	810	/	/	/	1.40	3.20	[93]
4	/	1.55	-5.17	-3.62	1.55	1.67	[94]
5	/	1.31	-5.33	-3.84	1.49	1.20	[95]
6	/	1.33	-5.31	-3.92	1.39	2.30	[95]
7	/	1.33	-5.24	-3.50	1.74	1.90	[96]
8	778	1.35	-4.75	-3.30	1.45	0.90	[91]
9	773	1.31	-4.95	-3.31	1.49	1.70	[91]
10	798	1.29	-5.04	-3.47	1.57	2.10	[90]
11	852	1.13	-5.02	-3.64	1.17	1.12	[89]
12	770	1.13	-4.90	-3.63	1.27	2.71	[92]
13	/	1.51	-5.24	-3.74	1.50	0.29	[97]
14	/	1.53	-5.35	-3.53	1.82	5.50	[98]
15	/	1.50	-5.29	-3.30	1.99	4.70	[99]
16	653	1.75	-5.42	-3.64	1.78	0.88	[89]
17	649	1.31	-5.23	-3.60	1.63	0.78	[90]
18	663	1.74	-5.04	-3.25	1.79	0.60	[91]
19	657	/	/	/	1.79	0.60	[91]
20	/	1.63	-5.38	-3.70	1.68	1.5	[100]
21	/	1.64	-5.38	-3.64	1.74	1.2	[100]
22	642	1.57	-5.44	-3.92	1.52	1.60	[88] [101]
23	/	/	-5.40	-3.90	1.50	3.80	[102]
24	658	1.63	-5.35	-3.62	1.59	2.26	[89]
25	727	1.34	-5.21	-3.63	1.58	4.45	[90]
26	/	1.29	-5.21	-3.60	1.61	0.43	[103]
27	750	1.31	-5.16	-3.51	1.65	2.53	[90]

28	638	1.43	-5.15	-3.69	1.46	2.93	[84]
29	/	1.45	-5.15	-3.28	1.87	2.30	[104]
30	/	1.51	-5.14	-3.34	1.80	4.10	[104]
31	/	1.36	-5.10	-3.31	1.79	1.40	[104]

3.3.2 Synthesis of monomers

The dithieno-DPP monomers **M2** and **M3** have been synthesized according to the synthetic route represented in Scheme 3.6 and based on the procedure developed by Iqbal, Cassar and Rochat in 1983 [61]. The dithieno-DPP (Scheme 3.6-**1**) can be prepared in high yield in a single step by reacting 2-thiophene-carbonitryle with di-isopropylsuccinate [105].
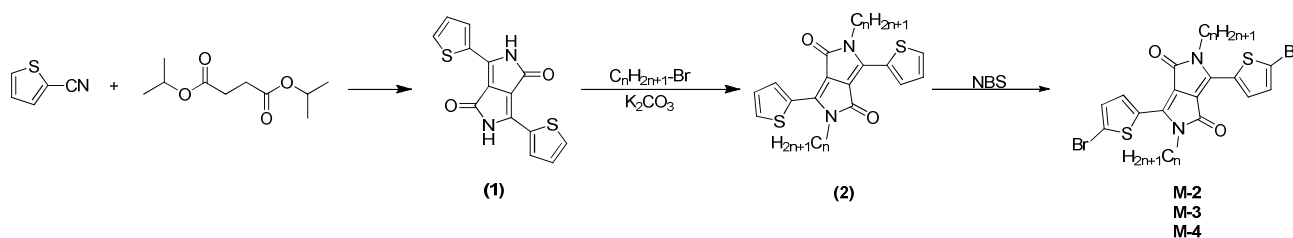
<p align="center">Scheme 3.6 Synthetic route to DPP monomers.</p>

To improve the solubility of the dithieno-DPP, the lactam units need to be N-functionalized to prevent the formation of hydrogen bonding between different DPP units. In this work, the dithieno-DPPs have been N-alkylated (Scheme 3.6-2) using the corresponding bromo-alkanes in presence of K_2CO_3 and 18-crown-6 [105]. To employ these molecules as building blocks for π-conjugated polymers, it is necessary to introduce suitable polymerizable groups on the thiophene units. The dithieno-DPPs have been functionalized with bromine atoms by free-radical substitution, using N-bromosuccinimide (NBS) as brominating agent. NBS has been preferred to the direct utilization of a **Br$_2$/HBr** mixture. In fact it is very important to keep Br$_2$ and HBr concentrations low, in order to prevent multiple bromination or other side reactions. Moreover, using NBS allows having a low but constant concentration of these reagents, which are generated in situ. CCl$_4$ was the solvent of choice because NBS is poorly soluble and the resulting succinimide is insoluble and thus form a suspension.

The detailed experimental procedures and chemical characterization are reported in Annex 1.

3.3.3 Polymer synthesis

The polymers have been synthesized by Stille polycondensation, reacting the dibrominated dithieno-DPPs monomers (Scheme 3.7, **M-2**, **M-3** and **M-4**) with 4,4'-Bis(2-ethylhexyl)-5,5'-bis(trimethyltin)-dithieno[3,2-*b*:2,3-*d*]silole (Scheme 3.7, **M-1**). The monomers **M-1** to **4** were polymerized according to the synthetic pathway in Scheme 3.7 to obtain the corresponding polymers **PSBDPP_C12, PSBDPP_C16 and PSBDPP_C10C6**.
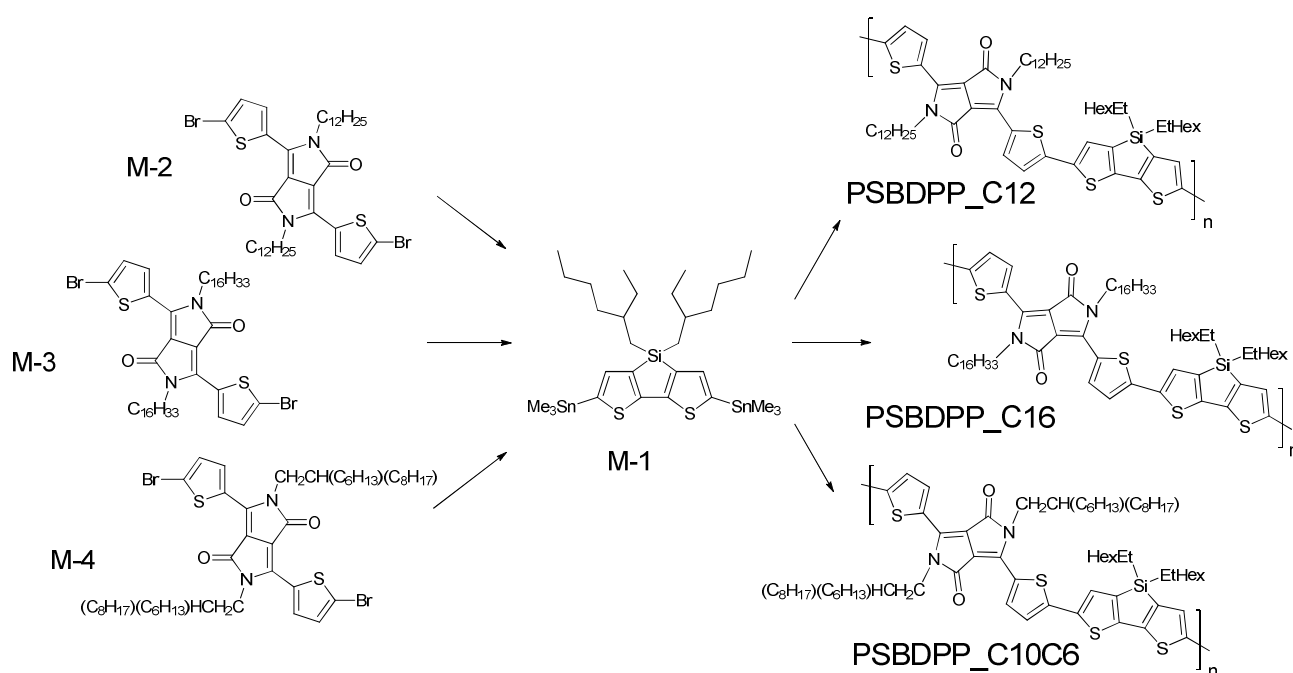
The polymerization was conducted in anhydrous chlorobenzene with **Pd(0)** as catalyst at 150°C for few hours. The Pd(0) was generated in situ from bis(dibenzylideneacetone)-palladium(0) [Pd$_2$(dba)$_3$] and tris(2-methylphenyl)phosphine [(*o*-Tolyl)$_3$P] as ligand [106]. This catalyst-ligand couple has been chosen according to the higher air stability of the Pd$_2$(dba)$_3$ and to the increased steric bulk of the (*o*-tolyl)$_3$P which leads to faster coupling. Moreover the ligand in excess does not affect the Stille coupling as it happens in the case of tri-phenylphosphine (PPh$_3$).

The detailed experimental procedures and chemical characterization are reported in Annex 1.

3.3.4 Molecular weight and dispersity

Gel permeation chromatrography (GPC) was performed with an Agilent Technologies 1260 infinity eluted at 1mL/min with HPLC grade chlorobenzene (Aldrich) at 50°C through a PLgel 10 µm Mixed-B (300×7.5 mm) GPC column. The polymers were analyzed with a refractive index detector

calibrated with narrow polystyrene standards. Samples were dissolved in HPLC grade chlorobenzene at a concentration of 1-4 mg/mL and filtered before injection. The measurement and the calculation of molecular weights (M_n, M_w and M_p) and dispersities (M_w/M_n) have been performed by Dr. Graham Morse at Merck Chemicals Ltd in the framework of ESTABLIS project.

Most of the π-conjugated polymers can be considered as rigid rods. Such macromolecules have a larger hydrodynamic volume than flexible ones. This means that the GPC molar mass of a rod polymer is always overestimated [107], since its hydrodynamic volume is higher than the flexible polystyrene (PS) or polymethylmethacrylate (PMMA) used to calibrate the machine.

Further complications may arise from the tendency to form aggregates, typical of rodlike polymers. Thus, it requires additional attention in considering if the elution curves really refer to molecularly dissolved polymer.

Some studies assessed the relation between GPC and other techniques, such as Matrix-Assisted Laser Desorption/Ionization-Time of Flight Mass Spectroscopy (MALDI-TOF MS), Static Light-Scattering (SLS) and Membrane Osmometry (MO). In particular Khöler *et al.* [108] studied the relation between the absolute molecular weight (measured by STS, MO and GPC using Universal Calibration) to the relative GPC value for a poly(*p*-phenylene) (PPP) derivative. A quantification of this difference reveals that PS-GPC overestimates the real molecular weight of PPP by a factor of ≈2. With the same aim, McCulloch *et al.* [109] investigated the correlation between GPC and MALDI-TOF MS for different poly(3-alkylthiophenes) (P3ATs) with narrow dispersity. They found that GPC overestimates the absolute molecular weight measured by MALDI-TOF MS by a factor of 1.2-2.3, depending on the absolute molecular weight.

Although substituents certainly have an effect on the stiffness and thereby on the hydrodynamic volume of a polymer chain, it is reasonable to assume that this effect will normally be small. It is therefore possible to make a comparison in between the series of polymers with the same π-conjugated backbone with a similar side substituent.

The GPC data showed that the side-chain on the dithieno-DPP unit has a strong influence on the molecular weight of the polymer. From Figure 3.9 and Table 3.4 it is possible to see that the corresponding fractions obtained from Soxhlet extraction using the same solvent have a different M_n. In particular, the fractions of polymers soluble in cyclohexane show that **PSBDPP_C16** has a M_n of 2.5 times the **PSBDPP_C12** and **PSBDPP_C10C6** even 6 times higher. The high solubility of these polymers

makes it harder to separate the different **Mw**. From the GPC traces in Figure 3.9 is possible to see that every sample, excluding **PSBDPP_C12** in chlorobenzene, shows a second peak corresponding to lower masses. This leads to the high dispersity ($Đ = {^{M_W}}/_{M_n}$) of the samples.

Longer linear side-chains have shown to significantly improve the polymer solubility. Moreover, branched alkyl side-chains with the same number of carbon atoms have demonstrated to dramatically enhance the polymer solubility.
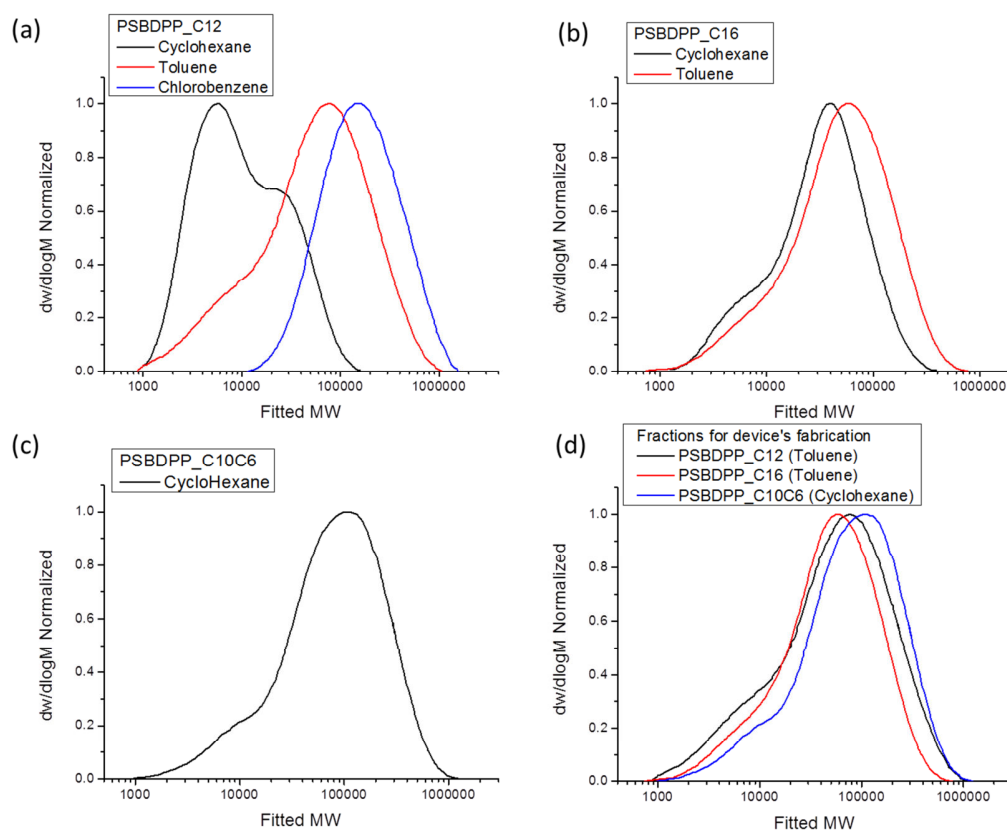
Figure 3.9 GPC curves of DPP series for different fractions after Soxhlet.

Table 3.4 M_n, M_w and dispersity of DPP series.

Polymer	Fraction	M_n (kg/mol)	M_w (kg/mol)	Đ
PSBDPP_C12	Cyclohexane	6.3	16.6	2.7
	Toluene	19.1	100	5.2
	Chlorobenzene	69.6	243	3.5
PSBDPP_C16	Cyclohexane	16.5	45.5	2.8
	Toluene	21.9	76.9	3.5
PSBDPP_C10C6	Cyclohexane	31.5	125.3	4.0

3.3.5 Optical properties
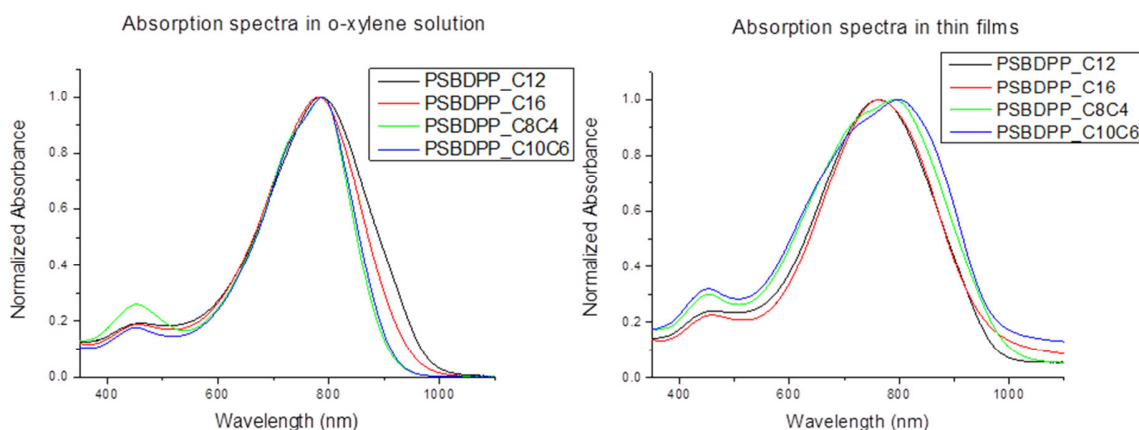
Figure 3.10 Absorption spectra in o-xylene solution and thin films of DPP series.

Figure 3.10 shows the UV-visible absorption spectra of **PSBDPP_C12, PSBDPP_C10C6** and **PSBDPP_C16** in o-xylene solution and in thin film. In this section will be presented the characterization of an additional polymer, **PSBDPP_C8C4**, independently synthesized by Dr. Graham Morse at Merck Chemicals Ltd in the framework of the ESTABLIS project. Electronic absorption data including the absorption peak wavelength (λ_{max}), the absorption edge wavelength (λ_{edge}), and the optical band gap (E_g^{opt}) are collected in Table 3.5.

All the samples show a broad absorption band in solution covering a range from 350 to 1000 nm. The peak between 400 and 500 nm corresponds to a π-π* transition, while the main peak, which corresponds to intramolecular charge transfer (ICT) from the donor to the acceptor moieties [84][110], shows a different feature according to the linear or branched side-chain. In the case of

linear side-chain the peak is Gaussian while, for branched chain, a shoulder at higher energy is visible. This feature has been associated to a torsion of the backbone due to the side-chain [81] [111].

Table 3.5 Optical properties of PSBDPP_C12, PSBDPP_C16, PSBDPP_C8C4 and PSBDPP_C10C6.

Polymer	Solution[a]	Film[b]		
	λ_{max} (nm)	λ_{max} (nm)	λ_{edge} (nm)	E_g^{opt} (eV)[c]
PSBDPP_C12	786	763	1005	1.2
PSBDPP_C16	782	763	991	1.2
PSBDPP_C8C4	789	792	1016	1.2
PSBDPP_C10C6	790	797	1005	1.2

a) Measured in o-xylene solution; b) Doctor bladed on glass from o-xylene solution; c) Bandgap calculated from the absorption edge wavelength of the optical absorption spectra

Thin films show a broader absorption spectra with the same feature visible in the solution's spectra. For **PSBDPP_C8C4** and **PSBDPP_C10C6**, with branched side-chain, a bathochromic shift of the absorption peak is visible, while for **PSBDPP_C12** and **PSBDPP_C16**, that bear linear side-chains, a stronger hypsochromic shift is present. This suggest a different aggregation of the polymers related to the different hindrance of the side-chains [112], [113].

To have a better understanding of the electronic structure of the polymers, photoluminescence (PL) emission spectra have been recorded (Figure 3.11). The samples were prepared by doctor-blade technique in air of polymer solutions in o-xylene on glass slides. The absorption spectra were recorded and the slides transferred in the glove box, to reduce at the minimum the oxidation of the samples. The samples were then encapsulated inside the glove box with a ring encapsulation, in which the adhesive is only at the border of the plates and does not get in touch with the measured area. The PL measurements were conducted at the Materials for Electronics and Energy Technology laboratory (I-MEET) at the Friedrich-Alexander-Universität Erlangen-Nürnberg, directed by Prof C. J. Brabec with the support of Dr H-J Egelhaaf, Dr M. Salvador, Dr A. Osvet in collaboration with Dr S. A. Dowland (ER2 at Belectric OPV GmbH).
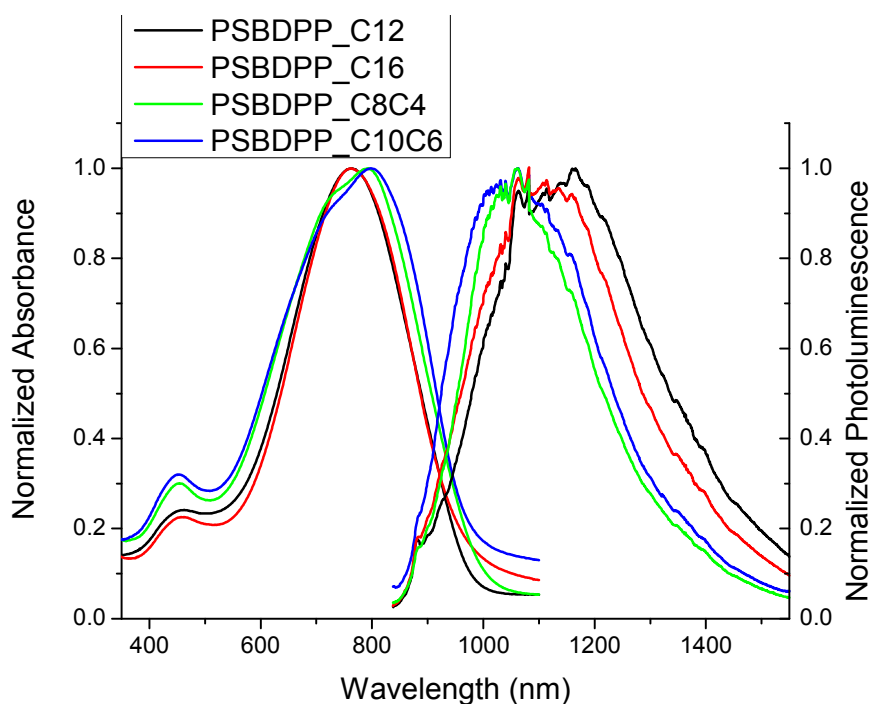
Figure 3.11 Absorption and emission spectra of thin films of DPP's series polymers. The samples were encapsulated in glass and excitation wavelength was 796 nm.

The PL curves shows again a different behavior related to the side-chains, for **PSBDPP_C12** and **PSBDPP_C16** the emission is at lower energy than that of **PSBDPP_C8C4** and **PSBDPP_C10C6**, while their shape does not show any particular feature. The features at 850 and 1100 nm are due to the interference of the glass slides.

3.3.6 Electrochemical properties

Cyclic voltammetry was performed using a Princeton Applied Research VersaSTAT 4 potentiostat. Films of the polymers were cast from a concentrated chloroform solution onto a platinum wire working electrode. These solid films were measured in an anhydrous acetonitrile solution containing 0.1 M tetrabutyl ammonium tetrafluoroborate electrolyte with a platinum wire counter electrode and 0.1 M Ag/AgNO$_3$ in acetonitrile reference electrode. The solutions were purged with N$_2$ gas prior to use. The samples were referenced to an external ferrocene solution which was also used to calculate the LUMO position [114]:

$$E_{LUMO} = -\left(E_{onset,\ reduction} + 5.1\right) eV \qquad \text{(3.1)}$$

The cyclic voltammetry measurements and HOMO/LUMO calculations were performed by Dr Graham Morse at Merck Chemicals Ltd in the framework of the ESTABLIS project.

Figure 3.12 Cyclovoltammograms of PSBDPP_C12 (a), PSBDPP_C16 (b) and PSBDPP_C10C6 (c).

The cyclovoltammograms are presented in Figure 3.12. According to equation (3.1), the HOMO level of the copolymer was −5.28 eV for **PSBDPP_C12**, -5.31 eV for **PSBDPP_C16** and -5.41 eV for **PSBDPP_C10C6**, while the corresponding LUMO is -3.9 eV for all of them (Table 3.6). The small difference in the HOMO levels can be due to different effects: different side-chain or different MW. In fact both the **PSBDPP_C12** and **PSBDPP_C16** analyzed have a linear side-chain and similar MW (19.1 and 21.9 kg/mol, respectively), while the **PSBDPP_C10C6** has branched side-chain and higher MW (31.5 Kg/mol). The approximate E_g^{opt} is ≈1.2 eV (E_g^{opt}=1240/λ_{edge}), lower than the electronic bandgap calculated from the CV. This is often observed and it is due to the exciton binding energy, which require additional energy (coulomb energy) to unbind hole and electron.

The **PSBDPPs** polymers have LUMO and HOMO levels and band gap similar to those of other DPP based low bandgap copolymers [88], [95], [102], [115].

Table 3.6 Electronic characteristics of the PSBDPP series. For comparison, also PSBDPP_C8C4, synthesized by Dr Graham Morse.

Polymer	E_{HOMO} (eV)	E_{LUMO} (eV)	E_g^{el} (eV)	E_g^{opt} (eV)
PSBDPP_C12	-5.3	-3.9	1.4	1.2
PSBDPP_C16	-5.3	-3.9	1.4	1.2
PSBDPP_C8C4	-5.2	-3.8	1.4	1.2
PSBDPP_C10C6	-5.4	-3.9	1.5	1.2

3.3.7 Thermal properties

Thermogravimetric Analysis (TGA) has been conducted to investigate the thermal stability of the polymers and in particular to compare the stability of the different side-chains. The analyzes have been done under inert atmosphere (N_2), with a ramp of 10°C/min from 40 to 590°C.

From Figure 3.13 we can see that for all the PSBDPPs, the thermal degradation occurs in one step between 380 and 500°C for the two polymers with linear side-chains, while for the branched one the degradation ends at 520°C. The weight loss experimentally obtained corresponds to the theoretical value (equation (3.2)) calculated in the hypothesis that all the alkyl chains are removed:

$$WL_{Theo}(\%) = \frac{Mw_{Monomer} - Mw_{Backbone}}{Mw_{Monomer}} \cdot 100 \qquad \textbf{(3.2)}$$

where $Mw_{Monomer}$ is the Mw of the repeating unit, while $Mw_{Backbone}$ is the Mw of the repeating unit without any alkyl chain. The results are reported in Table 3.7.

The difference between experimental and calculated values could be due to the presence of low Mw polymers (Figure 3.9). These short chains can degrade completely or still bear the polymerizable groups, which readily decompose via a chain-end unzipping reaction.
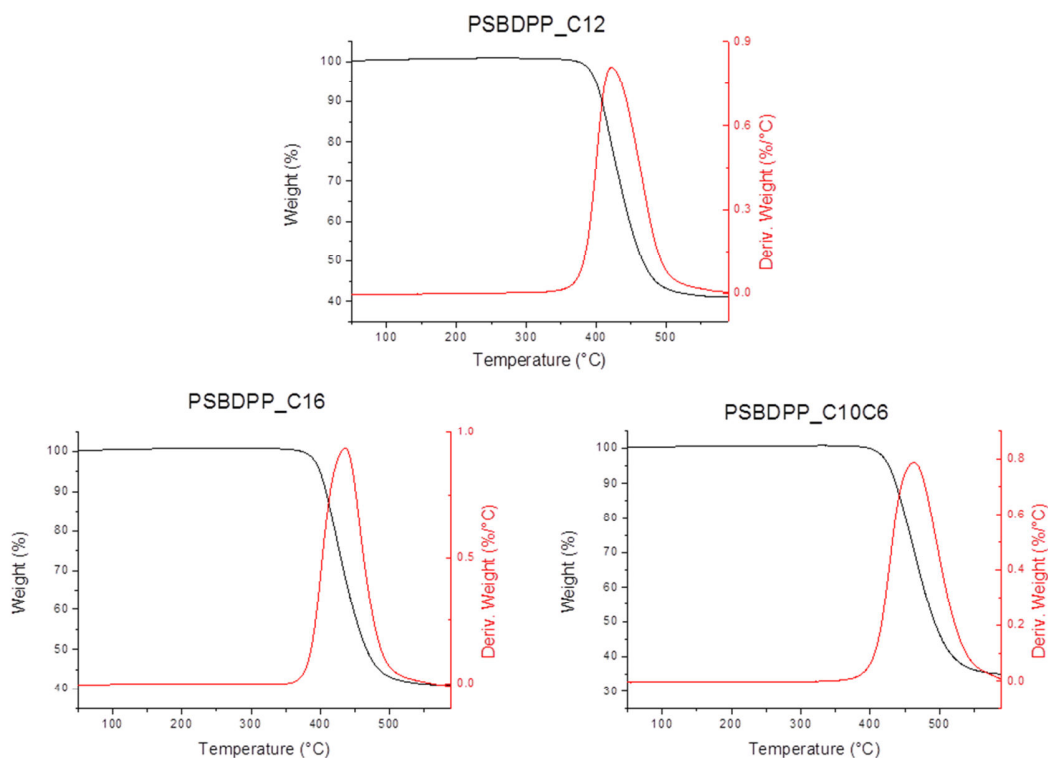
Figure 3.13 Thermogravimetric curves (black) and first derivatives (red) of PSBDPP series.

Table 3.7 Thermal stability of PSBDPP series.

Sample	5% Weight loss (°C)	WL$_{exp}$ (%)	WL$_{Theo}$(%)
PSBDPP_C12	415	59.0	53.6
PSBDPP_C16	425	62.3	58.1
PSBDPP_C10C6	425	65.5	58.1

The Differential Scanning Calorimetry (DSC) analysis have been performed with a TA-Q100, using different temperature ramp of 2, 10 and 25°C/min, in order to have a better understanding of the phase transitions of the polymers. The output signal of this analysis is the relative heat flow, the absolute value is not relevant, only its variation. The heat flow is calculated according to equation (3.3):

$$\frac{dH}{dt} = C_p \cdot \frac{dT}{dt} + f(T, t)$$

(3.3)

91

where $\frac{dH}{dt}$ is the DSC signal, C_p is the sample heat capacity, $\frac{dT}{dt}$ is the heating rate and $f(T, t)$ is the heating flow, that is a function of time at a given temperature. The important factors to keep into account are the sample size, the purge gas, heating rate and the sample thermal history. Increasing the sample mass will increase the sensitivity decreasing its resolution. Similarly, a faster heating rate increases sensitivity which decreases the resolution. The purge gas provides a dry and inert atmosphere and ensures an even heating and helps to eliminate any gas might have been released.

Here all the three polymers are discussed, but only the curves with a heating rate of 2°C/min are reported (Figure 3.14), complete graphics and data are presented in Annex 1.
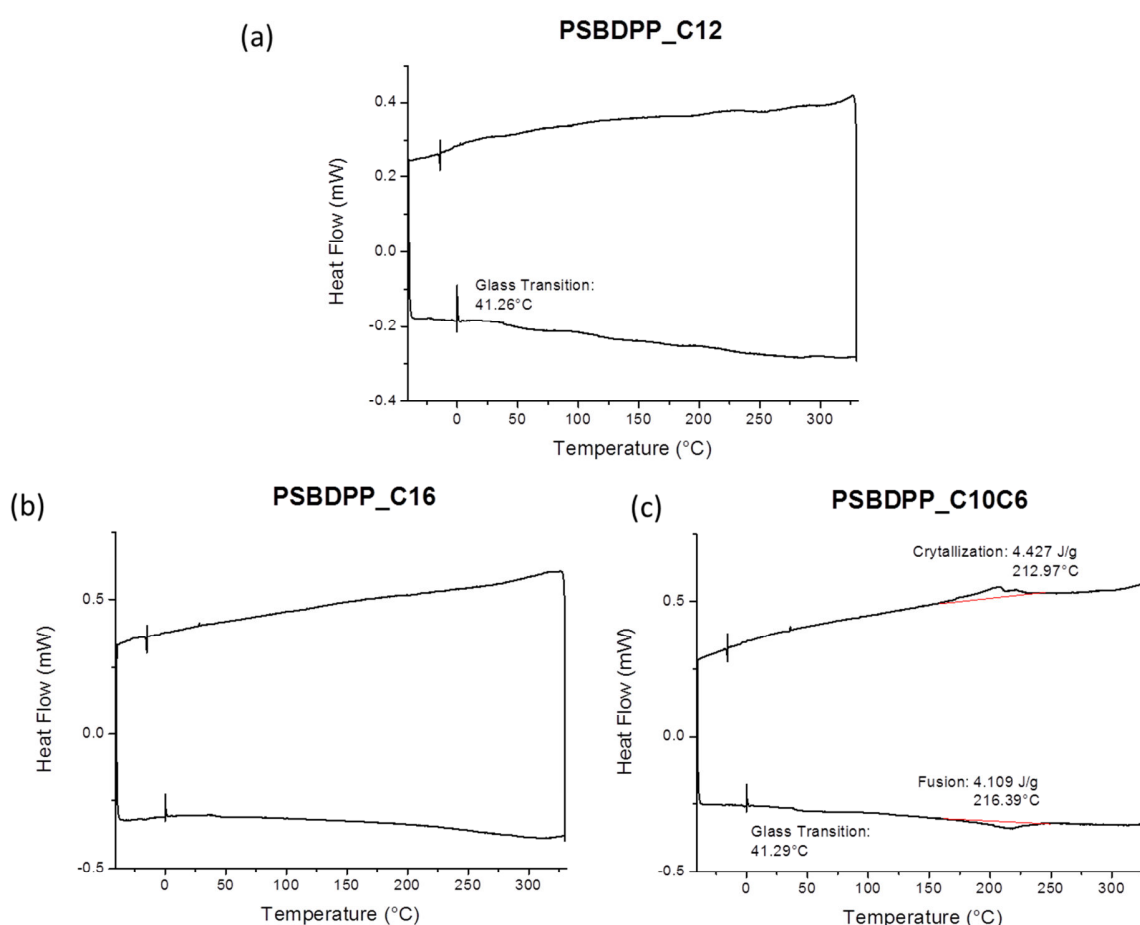
Figure 3.14 DSC thermograms at 2°C of DPP series.

From the DSC thermograms it is possible to see different behavior according to the different DPP side-chain. For the **PSBDPP_C10C6**, it is possible to see a glass transition around 40°C and a fusion/crystallization at 215°C, while in the case of **PSBDPP_C12** only a glass transition at 40°C is visible. This glass transition at such low temperature is due to the side-chains [116], while the melting

at 215°C can be ascribed to a phase transition of the whole polymer. In the case of **PSBDPP_C16**, no phase transition is visible. The spike around 0 °C is present in all the graphs and is an artifact of the machine, due to the non anhydrosity of the purge gas.

These results suggest that DSC is not the most suitable technique to characterize the thermal properties of these π-conjugated polymers. In order to have a better understanding further analysis, both in bulk (Flash-DSC [117] and Dynamic Mechanical Thermal Analysis (DMTA) [118]) and in thin film (Confocal Raman Spectroscopy [119]) are on course, in collaboration with Aurélien Tournebize (ESR10) and Isabel Fraga Domínguez (ESR8) in the framework of ESTABLIS project.

3.4 Synthesis and characterization of LBGs Based on DTS and DTP Units

In this sub-section, the synthesis and the chemical characterization of two low band gap polymers based on dithienosilole (DTS) and dithienopyrazine (DTP) is presented. A state of the art of the current research on DTP is also presented as introduction to explain and support the choice of these donor and acceptor units.

3.4.1 Introduction

One of the possible chemical approaches to lower and to tune the bandgap of π-conjugated polymers, is the use of ring-fused thiophene units, due to their extended π-conjugation and more rigid structures [120]. Both features would contribute to reduce the polymer bandgap and to promote the intermolecular interactions in solid films.
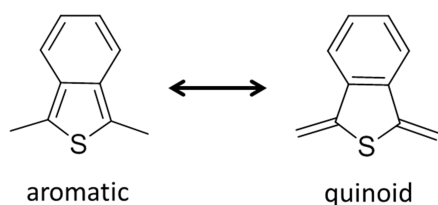
Figure 3.15 Aromatic and quinoid form of benzo[c]thiophene.

One of the first materials on this idea was poly(isothianaphthene) (**PITN**). Wudl *et al.* reported in 1984 [121], the electrochemical polymerization of isothianaphthene, better known as benzo*[c]*thiophene. Both theoretical and experimental investigations [122] demonstrated that the fused benzene ring in benzo*[c]*thiophene increases the quinoid character of the electronic ground-state in **PITN** (Figure 3.15), causing a bandgap of ~1.0 eV, which is about half that of polythiophene (2.0 eV) [123].

Alkyl- or alkoxy-substituted soluble **PITNs** (Figure 3.16-a) were also synthesized. This chemical modification did not lead to any significant changes in the bandgap of the polymers, which showed

bandgaps of ≈1.0 eV [124], [125]. Dithienylbenzo*[c]*thiophene (Figure 3.16-b) was synthesized independently by different research groups [126] [127]. Its bandgap was 1.6 eV, i.e., between those of **PITN** and polythiophene [126].

$R_{1,2,3}$= -H, -C_nH_{2n+1}, -OC_nH_{2n+1}
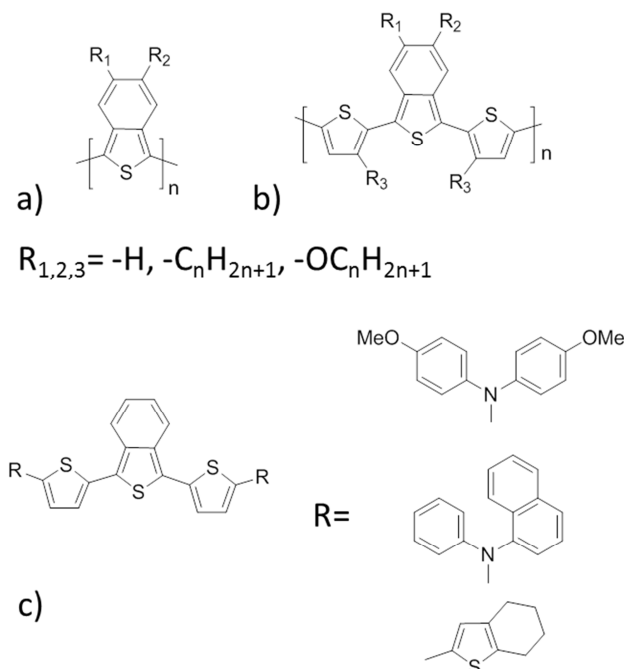
Figure 3.16 Substituted PITNs (a and b) and oligomers (c).

Bauerle's group developed a series of end-capped benzo*[c]*thiophene-based oligomers (Figure 3.16-c3) [128]. In comparison with the corresponding α-oligothiophenes, these oligomers exhibited a significant bathocromic shift in the absorption spectra. Diarylamino-capped 1,3-dithienylbenzo[c]thiophene oligomers (Figure 3.16-c1) and copolymers (Figure 3.16-c2) were synthesized by Kisselev and Thelakkat [129]. These compounds exhibited extensive absorptions in the range 300–620 nm. The electron-donating diarylamino groups increased
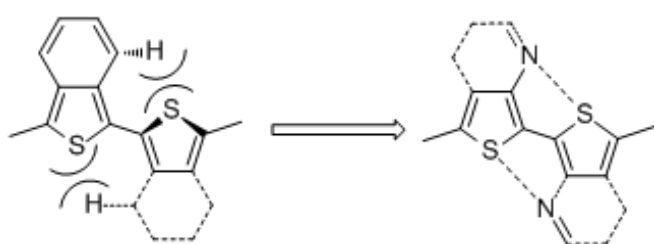
Figure 3.17 Intramolecular interactions in poly(benzo[c]thiophene) and N-substituted poly(benzo[c]thiophene) [120].

the HOMO energy, making them promising candidates for light-harvesting and hole-transport materials in organic solar cells.

In poly(benzo*[c]*thiophene) systems such as **PITN**, the steric hindrance between phenyl-H and thiophene-S atoms of adjacent thiophene rings causes a torsion, which results in a reduction of the π-conjugation of the polymeric backbone. Replacement of the 4-CH group in the benzo*[c]*thiophene unit

by nitrogen (Figure 3.17) would diminish steric hindrance, which has been proven by X-ray structure analysis. The torsion angle between the central thienopyridine moiety and the thiophene unit on the nitrogen side is only 3.5°, whereas it is 39° and much larger on the CH side [130]. Based on these findings, heteroaromatic ring-fused thiophene molecules, such as thieno[3,4-*b*]pyrazine (Figure 3.18-a), thienothiadiazole (Figure 3.18-c) and thiadiazolothienopyrazine (Figure 3.18-d), were proposed as fused thiophene building block for low-bandgap polymers.

a)   b)   c)   d)
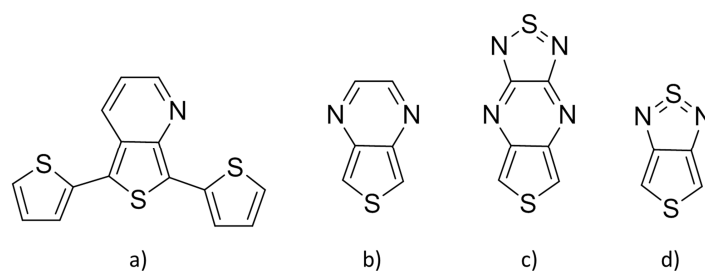
Figure 3.18 Examples of N-substituted benzo[c]thiophene.

Substituted thieno[3,4-*b*]pyrazines are generally synthesized by condensation of 3,4-diaminothiophene with substituted 1,2-diones [124] [131], to give the corresponding di-imine groups. Through this synthetic approach, various alkyl-substituted thieno[3,4-*b*]pyrazines were synthesized and polymerized to give the corresponding homo- and co-polymers (Figure 3.19, **P1-P11**, Table 3.8). **P1-P4** were synthesized by oxidative polymerization with $FeCl_3$ and electrochemical polymerization. The resulting polymers were highly soluble in organic solvents due to the alkyl side-chains and had low bandgaps ranging between 0.8–1.1 eV. **P5** and **P6** were synthesized by Stille polycondensation [132] and showed an optical bandgap of 0.88 and 0.90 eV and an electrochemical bandgap of 1.00 and 1.06 eV. The saturation field-effect hole mobility of **P5** was 1.7 $10^{-2} \cdot cm^2 \cdot V^{-1} \cdot s^{-1}$, which was significantly higher than that of the **P6** with 8.1 $10^{-4} \cdot cm^2 \cdot V^{-1} \cdot s^{-1}$. Thus, the vinylene bridge provided better charge-transporting characteristics than the ethynylene. The small band gaps and high charge carrier mobility of these two copolymers make them suitable for application in near-infrared electronic and optoelectronic devices. **P7** and **P8** were synthesized by Sonogashira polycondensation [133] and showed a bandgap of ≈1.6 eV. Their application in BHJ devices on flexible substrate, showed a PCE up to 2.37% for a **P7:PC$_{61}$BM** active layer. **P9** and **P10** were synthesized by Suzuki polycondensation [134] and the positions of the hexyl side-chains on the 3HT units were varied to adjust the co-planarity of the copolymers. **P9** and **P10** showed an optical bandgap of 1.27 and 1.44 eV, respectively, while the electrochemical bandgap was 1.63 and 1.76 eV, respectively. The HOMO and

LUMO were tuned by the number of hexylthiophene (HT) units and by the break of co-planarity along the main chain, depending on the position of the hexyl side-chain. Copolymer **P11** was synthesized by electrochemical polymerization. It showed excellent stability under reductive redox cycling conditions and a very small bandgap of only 0.36 eV [135]. As drawback, its solubility was poor, which the authors attributed to the tight molecular packing of the polymeric chains originating from the intra- and intermolecular N-S and O-S interactions.

In 1994, Kitamura *et al.* [136] reported a series of 5,7-di(thienyl)thieno[3,4-b]pyrazines (**P12-P15**, Figure 3.20, Table 3.9). They were synthesized either by electrochemical polymerization or oxidative polymerization with $FeCl_3$. Their bandgaps varied from 1.0 to 1.5 eV depending on the substitution pattern [137] [138]. The polymers covered a very broad absorption range (300 to 980 nm), but their application in BHJ **P15:PC$_{61}$BM** (1:1) exhibited a maximum *PCE* of only 0.8%.
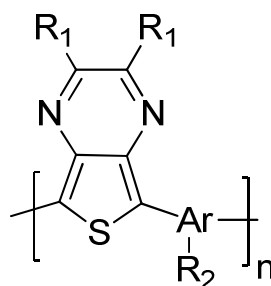
Figure 3.19 General structure of thienopyrazine co-polymers.

Table 3.8 Polymers which bears thienopyrazine as monomer units.

Polymer	R$_1$	Ar	R$_2$	Ref
1	-C$_6$H$_{13}$			
2	-C$_8$H$_{17}$	/	/	[124]
3	-C$_{10}$H$_{21}$			
4	-C$_{12}$H$_{25}$			
5	-p(C$_6$H$_4$)-OCH$_2$CH(C$_2$H$_5$)(C$_4$H$_9$)		/	[132]
6			/	
7	-(C$_6$H$_5$)		/	[133]

96

8			-OC$_{12}$H$_{25}$	
9	-C$_2$H$_5$			
10	-C$_6$H$_{13}$		-C$_6$H$_{13}$	[134]
11			/	[135]

Polymers based on 2,3-di(3-thienyl)thieno[3,4-*b*]pyrazine (**P16-P18**) have been synthesized by electrochemical or oxidative polymerization [139] [140]. They have attracted much attention due to their green color and application prospects in electrochromic devices. More recently, **P19** and **P20** were synthesized by an Ni(COD)$_2$-catalyzed condensation polymerization [141]. Both polymers were soluble in organic solvents and had an intense absorption ranging from 600 to 950 nm. Polymer **P20** had a bandgap of 1.20 eV, which is slightly smaller than that of **P19** (1.28 eV). Application in BHJ devices resulted in poor photovoltaic properties, which can be attributed to the low oxidation potential and the therefore high-lying HOMOs of the polymers.
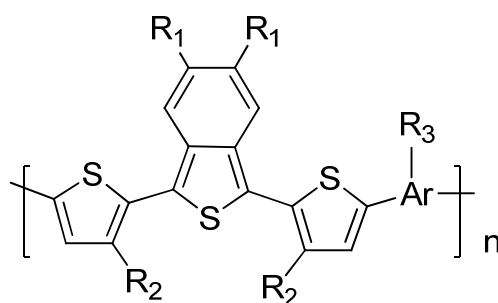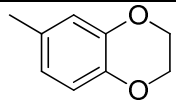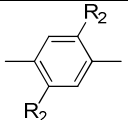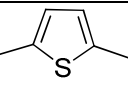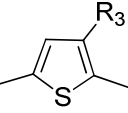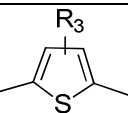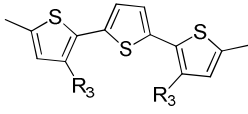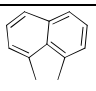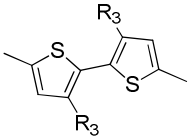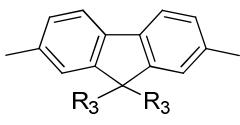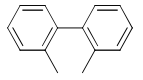
Figure 3.20 General structure of dithenyl-Thienopyrazine co-polymers.
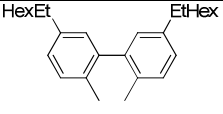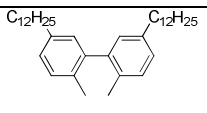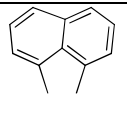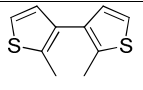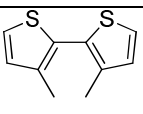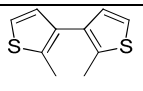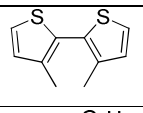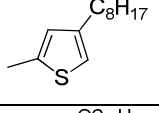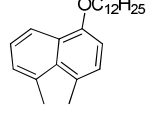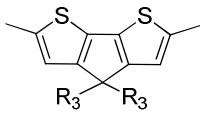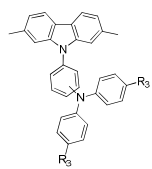
Table 3.9 Coplymers that bears Dithenyl-thienopyrazine as constitutive units.

Polymer	R$_1$	R$_2$	Ar	R$_3$	Ref
12	/	-C$_{12}$H$_{25}$	/	/	[136] [137]
13	-C$_8$H$_{17}$	-C$_8$H$_{17}$			[136]

14	-CH$_2$CH(C$_2$H$_5$)(C$_4$H$_9$)				[138]
15		-CH$_2$OC$_4$H$_9$			
16	-2-Thiophene	-H			[139]
17		-C$_8$H$_{17}$			
18		-C$_6$H$_{13}$			[140]
19	-(C$_6$H$_5$)	-OCH$_2$CH(C$_2$H$_5$)(C$_4$H$_9$)			[141]
20	-3,5-(C$_6$H$_3$)-OCH$_2$CH(C$_2$H$_5$)(C$_4$H$_9$)	/			
21	(benzodioxane)	-C$_6$H$_{13}$			[140]
22	/	-C$_12$H$_{25}$	(benzene, R$_2$)	-OC$_{10}$H$_{21}$	[137]
23		-C$_12$H$_{25}$	(thiophene)	/	[137]
24	-3,5-(C$_6$H$_3$)-OCH$_2$CH(C$_2$H$_5$)(C$_4$H$_9$)	-C$_8$H$_{17}$	(thiophene, R$_3$)	/	[142]
25		/	(thiophene, R$_3$)	-C$_12$H$_{25}$	
26	-C$_2$H$_5$	-C$_6$H$_{13}$	(thiophene, R$_3$)	-C$_6$H$_{13}$	[134]
27	-3,5-(C$_6$H$_3$)-OCH$_2$CH(C$_2$H$_5$)(C$_4$H$_9$)	/	(terthiophene, R$_3$)	-C$_8$H$_{17}$	[142]
28	-C$_2$H$_5$	-C$_6$H$_{13}$	(bithiophene, R$_3$)	-C$_6$H$_{13}$	[134]
29	(naphthalene)	-CH$_2$CH(C$_2$H$_5$)(C$_4$H$_9$)			[143]
30		-C$_12$H$_{25}$		-C$_12$H$_{25}$	
31	(biphenyl)	-CH$_2$CH(C$_2$H$_5$)(C$_4$H$_9$)			
32	/	-C$_12$H$_{25}$	(fluorene, R$_3$)	-C$_8$H$_{17}$	[137]
33	-(C$_6$H$_5$)	/			[144]
34	-p(C$_6$H$_4$)CH$_2$CH(C$_2$H$_5$)(C$_4$H$_9$)	/			[145]
35	(biphenyl)	-CH$_2$CH(C$_2$H$_5$)(C$_4$H$_9$)		-CH$_2$CH(C$_2$H$_5$)(C$_4$H$_9$)	[146], [143]

36		/		$-CH_2CH(C_2H_5)(C_4H_9)$	[146]
37		/		$-C_{12}H_{25}$	
38		$-CH_2CH(C_2H_5)(C_4H_9)$		$-CH_2CH(C_2H_5)(C_4H_9)$	[143]
39		$-C_{12}H_{25}$		$-C_{12}H_{25}$	
40		$-CH_2CH(C_2H_5)(C_4H_9)$		$-CH_2CH(C_2H_5)(C_4H_9)$	[147]
41					
42					
43					
44		/		$-OC_{12}H_{25}$	[148]
45					
46	$-(C_6H_5)$	/		Para linked arylamine	[149]
47	$-p(C_6H_4)CH_2CH(C_2H_5)(C_4H_9)$				
48	$-(C_6H_5)$			Meta linked arylamine	
49	$-p(C_6H_4)CH_2CH(C_2H_5)(C_4H_9)$				

P22 and **P23** were synthesized by Suzuki and Stille polycondensation [137], they presented broad absorption bands at extended towards the near-infrared region. They exhibited ambipolar redox properties with low ionization potentials and the field-effect mobility of holes of 1.1×10^{-3} $4.2 \times 10^{-4} \cdot cm^2 \cdot V^{-1} \cdot s^{-1}$, respectively. **P24-P27** were synthesized by Yamamoto or Suzuki polymerization [134] [142], showing a broad absorption, extended to the NIR. According to the number of thiophene units the bandgap varied from 1.3 to 1.5 eV, mainly due to the backbone distortion related to the side-chains. The best BHJ cells gave a power conversion efficiency of 1.4% for **P24:PC$_{61}$BM** blend. **P28-P31** were synthesized by Suzuki and Stille polycondensation [143]. They showed an electrochemical bandgap ranging from 1.2 to 1.6 eV and field-effect mobility from 2.1 to $6.5 \times 10^{-3} \cdot cm^2 \cdot V^{-1} \cdot s^{-1}$. Power

conversion efficiencies (PCE) up to 0.3% was achieved in BHJ solar cells. For **P32-P41** the co-monomer chosen was fluorene and they were synthesized by Suzuki polycondensation [137] [143] [144] [145] [146] [147]. All the polymers presented broad absorption spectra which extends to the NIR and good field-effect mobilities. In particular the use of fused aromatic thienopyrazine (**P35-P41**) furthermore increased the mobility values (up to $0.012 \cdot cm^2 \cdot V^{-1} \cdot s^{-1}$) due to enhanced crystallinity of the films, which formed lamellar structures as seen by GISAXS. The substitution of fluorine with cyclopentadithiophene (**P42** and **P43**) furtherly improved the field-effect mobility, due to decreased lamellar d-spacings. On the other hand BHJ solar cells have low efficiencies that never exceeds 1.5%. **P44** and **P45** were obtained by Stille polymerization [148]. Both polymers exhibit good solubility in common organic solvents and a broad absorption band in the visible to NIR regions. The film optical band gaps of the polymers are 1.2 and 1.3 eV, respectively, while the electrochemical bandgap is 1.7 eV for both of them. BHJ solar cells, with **PC$_{61}$BM** as acceptor material, showed a PCE up to 0.80% in combination with **P44**. **P46-P49**, obtained by Suzuki polycondensation [149], exhibited different optoelectronic properties according to the position of the triarylamine substituent on the carbazole units. When the triarylamine group is in meta- position there is a slight bathochromic shift of the absorbance maxima, compared to the para- position. These results indicated stereoelectronic effects of the substituents on the backbones. This stereo-electronic effects was not visible in BHJ solar cells, which in combination with **PC$_{71}$BM** showed a PCE of 0.60% for all polymers.
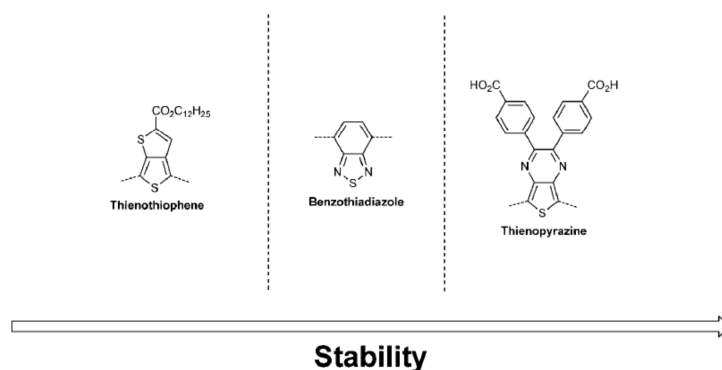
Figure 3.21 Stability scale of acceptors units [34].

Moreover, Manceau *et al.* [34] investigated the stability of co-polymers based on dithienylthienopyrazine bearing thermo-cleavable tertiary esters on the pyrazine ring, alternating with different donor groups: fluorene, cyclopentadithiophene (CPDT), dithienosilole (DTS) and thiophene. Their stability under photooxidative conditions is: fluorene<CPDT<DTS<thiophene. The

same ranking is observed with the cleaved materials, but on a very different timescale. Comparing these cleaved dithienylthienopyrazine based co-polymers with other co-polymers constituted by benzothiadiazole, thienothiophene and the same donor units, they were able to establish the stability ranking shown in Figure 3.21.

In the following sub-section, syntheses of DTPs monomers (used in this thesis) and their polymerization is presented and their chemical and physical characterizations is discussed. Two different side groups, namely thiophene and 1,4-benzodioxane, have been chosen. These two monomers, bearing different side-chains on the thenyl units, are already known in the literature [139] [140], but to the best of our knowledge, never before utilized in donor-acceptor LBG co-polymers. No alkyl side-chains have been used to promote the planarity of the backbone and improve the overall chemical stability of the polymers.

3.4.2 Monomer synthesis

DTP monomers **M-5** and **M-6** have been synthesized according to the synthetic route reported in Scheme 3.8 [144]. The first step consists in the Stille condensation of 2-tributyltinthiophene with 2,5-dibromo-3,4-dinitrothiophene to give the dinitro-terthiophene (1). The second step is the bromination of (1) to give the corresponding dibromo-dinitro-terthiophene (2). The reduction of the nitro-group to the amine (3) was performed using metallic iron (Fe) in acetic acid (AcOH). The amine was not isolated due to its low stability; iron powder was eliminated by filtration and the crude product was utilized in the following synthetic step without further purification. The α-dione (4) had been synthesized by direct acylation of the oxalyl chloride through a Grignard reaction in the presence of CuBr/LiBr [150].
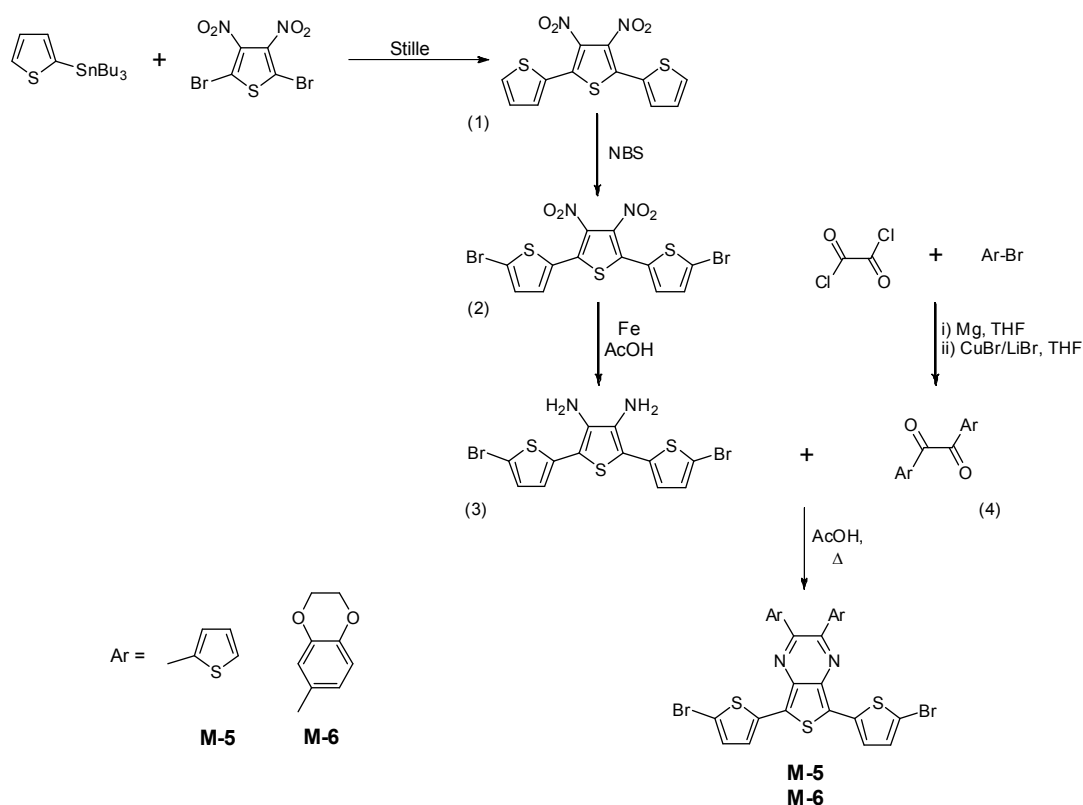
Scheme 3.8 Synthetic route to the dithienyl-thienopyrazine.

The condensation of the dibromo-diamine-terthiophene (3) with the α-dione (4), to give the corresponding ketimine, was performed in AcOH to obtain the dibromo-dithieno-thieno pyrazine (DTP). From the ^{1}H-NMR spectrum, it is possible to see signals corresponding to impurities in aromatic region that can correspond to α-diones used in large excess for the reaction and not completely eliminated during the product purification.

The detailed experimental procedures and chemical characterization are reported in Annex 1.

3.4.3 Polymer synthesis

The polymers have been synthesized by Stille polycondensation, reacting the dibrominated-DTPs monomers (Scheme 3.8, **M-5** and **M-6**) with 4,4'-bis(2-ethylhexyl)-5,5'-bis(trimethyltin)-dithieno[3,2-b:2,3-d]silole (Scheme 3.8, **M-1**). The monomers **M-1**, **M-5** and **M-6** were polymerized according to the synthetic pathway in Scheme 3.9 to obtain the corresponding polymers **PSBDTP_Th**, and **PSBDTP_EDOPh**.
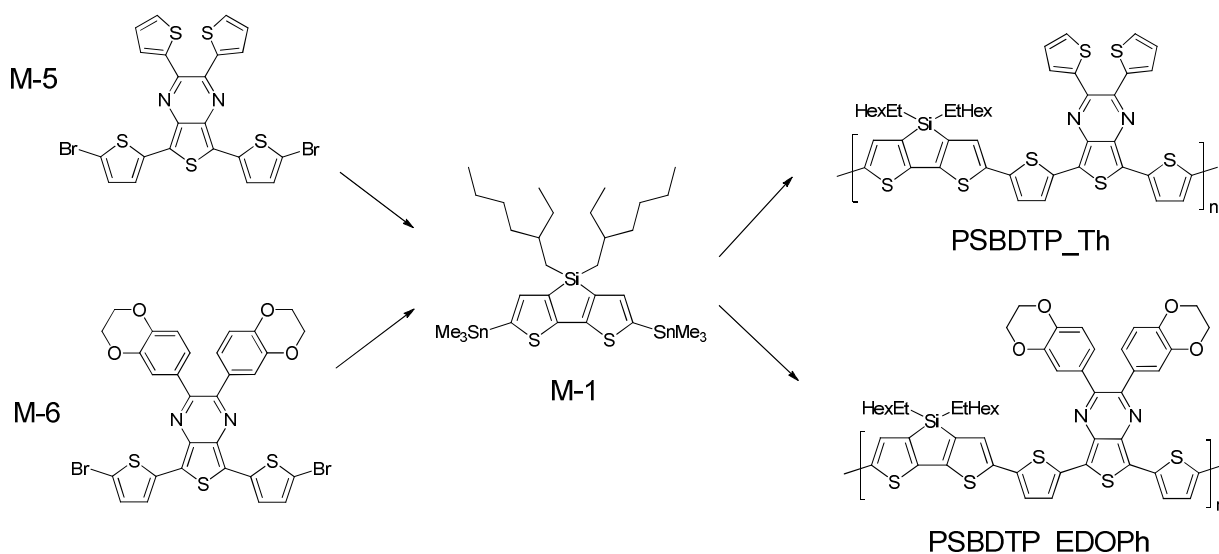
Scheme 3.9 Synthesized polymers containing by DTS and DTP units.

The polymerization was conducted in anhydrous chlorobenzene with Pd(0) as catalyst at 150°C a for few hours. The Pd(0) was generated in situ from bis(dibenzylideneacetone)-palladium(0) [Pd$_2$(dba)$_3$] and tri(2-methylphenyl)phosphine [(o-tolyl)$_3$P] as ligand [106]. This catalyst-ligand couple was chosen according to the higher air stability of the Pd$_2$(dba)$_3$ and to the increased steric bulk of the (o-tolyl)$_3$P which leads to faster coupling. Moreover the excess of ligand does not affect the Stille coupling as it happens in the case of tri-phenylphosphine (PPh$_3$).

The detailed experimental procedures and chemical characterizations are reported in Annex 1.

3.4.4 Molecular mass

Gel permeation chromatrography (GPC) was performed with an Agilent Technologies 1260 infinity eluted at 1mL/min with HPLC grade chlorobenzene (Aldrich) at 50°C through a PLgel 10 μm Mixed-B (300×7.5 mm) GPC column. The polymers were analyzed with a refractive index detector calibrated against narrow polystyrene standards. Samples were dissolved in HPLC grade chlorobenzene at a concentration of 1-4 mg/mL and filtered before injection. The measurement and the calculation of molecular weights (M$_n$, M$_w$ and M$_p$) and dispersities (M$_w$/M$_n$) have been performed by Dr Graham Morse at Merck Chemicals Ltd in the framework of ESTABLIS project.
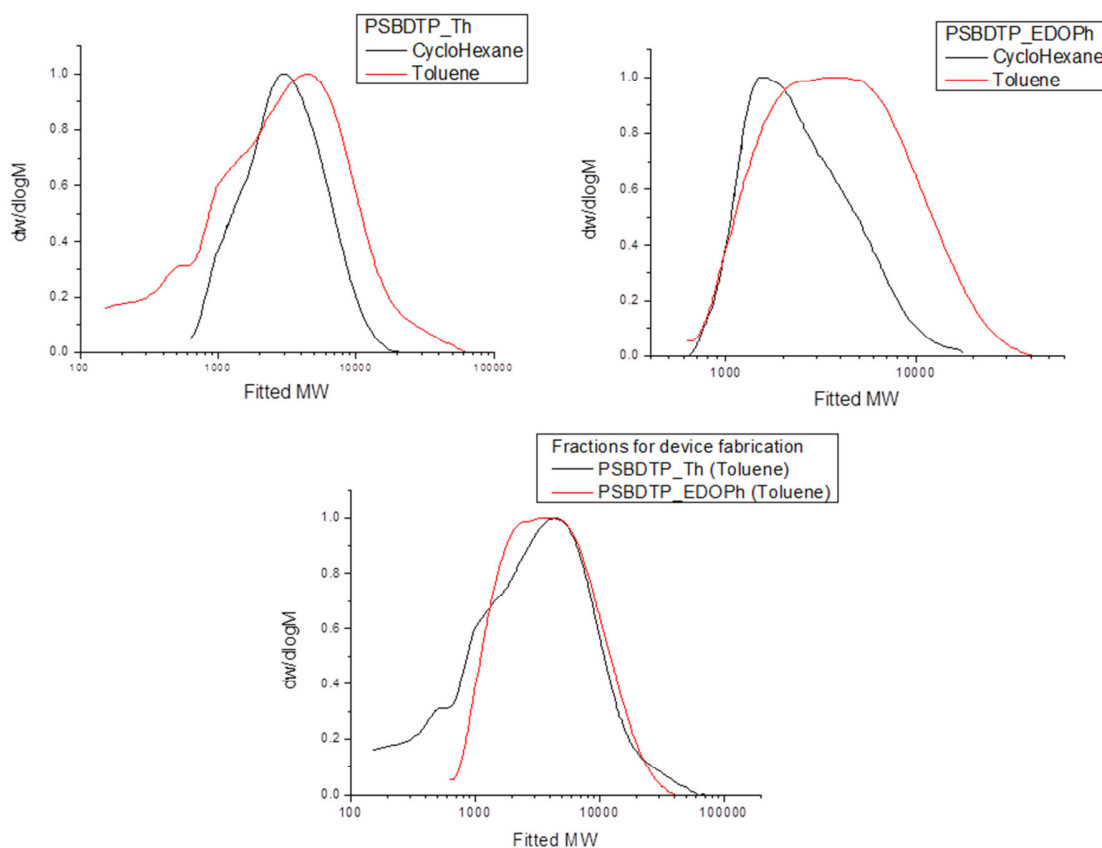
Figure 3.22 GPC curves of the PSBDTP copolymers.

The GPC data (Figure 3.22) show that the polymerization were not completely successful. In fact, for both **PSBDTP_Th** and **PSBDTP_EDOPh**, the M_n measured correspond to few repetitive units (Table 3.10). As discussed in the introductive chapter, this might be caused by two different issues related the Stille polymerization: low monomer purity or low oligomers solubility. In this case, the low purity of the acceptor monomers was more probable rather than the low solubility. In fact, the oligomers were completely soluble in most common organic solvents (chloroform, toluene, o-xylene,...) at room temperature.

On the other hand, the fact that the toluene fraction present a lower M_n than with cyclohexane and chlorobenzene for the **PSBDTP_Th** is a clear indication that additional side-chains are required, in order to have a processable polymer. This additional substituent could be either on the pendent aromatic substituent of the ketimine or on the bridge thiophene between the dithienosilole and the thienopyrazine units. Mondal *et al.* [146] investigated the effect of alkyl substituent in the aforementioned positions. They found that moving the side-chain awayfrom the backbone improved

its planarity and that linear chains are more suitable, in order to promote film crystallinity with a high carrier mobility.

Table 3.10 Molecular weight and dispersity of PSBDTPs polymers.

Polymer	Fraction	Mn (kg/mol)	Mw (kg/mol)	Đ
PSBDTP_Th	Cyclohexane	2.4	3.7	1.5
	Toluene	1.3	5.0	3.7
	Chlorobenzene[a]	-	-	-
PSBDTP_EDOPh	Cyclohexane	2.1	3.0	1.5
	Toluene	2.9	5.4	1.9

[a]Not soluble enough to be measured

3.4.5 Optical Properties

Figure 3.23 shows the UV-visible absorption spectra of **PSBDTP_Th** and **PSBDTP_EDOPh** in o-xylene solution and in thin film. Electronic absorption data including the absorption peak wavelength (λ_{max}), the absorption-edge wavelength (λ_{edge}), and the optical band gap (E_g^{opt}) are collected in Table 3.11.

All the samples exhibited a broad absorption band covering a range from 300 to 1000 nm. The main band between 400 and 500 nm corresponds to π-π* transition, while at longer wavelengths (600-1000 nm) there is a second band, which corresponds to intramolecular charge transfer (ICT) from the donor to the acceptor moieties. In Figure 3.23-a, the DTP monomers are compared to the corresponding polymers in o-xylene solution. It is possible to see the strong influence of the D-A coupling on the optical properties, the π-π* undergoes a bathochromic shift of ≈100 nm, that is even more pronounced for the ICT transition, whose relative intensity is augmented by a factor 3.
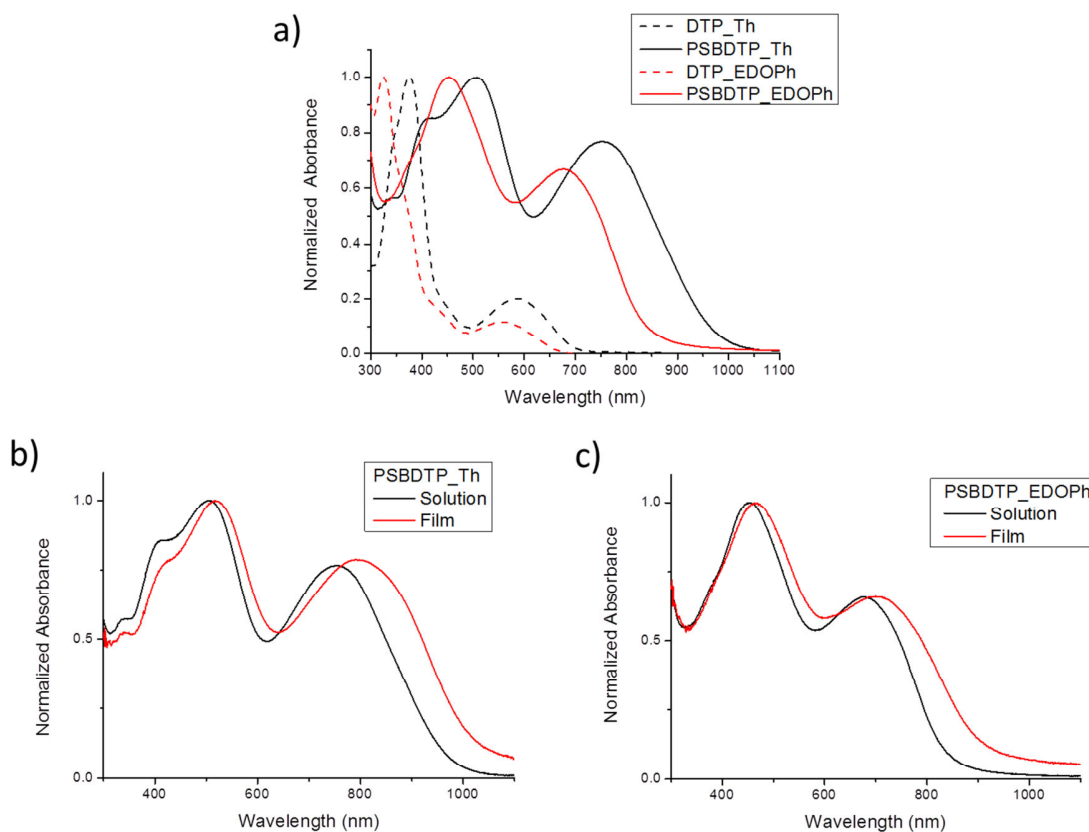
Figure 3.23 Absorption spectra of a) PSBDTPs and corresponding monomers in o-xylene solution; o-xylene solution and thin film of b) PSBDTP_Th and c) PSBDTP_EDOPh.

Table 3.11 Optical properties of PSBDTPs.

Polymer	Solution[a]	Film[b]		
	λ_{max} (nm)	λ_{max} (nm)	λ_{edge} (nm)	E_g^{opt} (eV)[c]
PSBDTP_Th	508	515	960	1.3
PSBDTP_EDOPh	453	466	1057	1.1

a) Measured in o-xylene solution; b) doctor bladed on glass from o-xylene solution; c) Bandgap calculated from the absorption edge wavelength of the optical absorption spectra of the film

Thin films show a broader absorption spectra with the same main feature visible in the solution spectra (Figure 3.23-b and –c). The bathochromic shift for the ICT band (25-40 nm) is more pronounced than the one for the π-π* transition (15 nm). From the band shape no particular aggregation is visible.

3.4.6 Electrochemical Properties

Cyclic voltammetry was performed using a Princeton Applied Research VersaSTAT 4 potentiostat. Films of the polymers were cast from a concentrated chloroform solution onto a platinum wire working electrode. These solid films were measured in an anhydrous acetonitrile solution containing 0.1 M tetrabutyl ammonium tetrafluoroborate electrolyte with a platinum wire counter electrode and 0.1 M Ag/AgNO$_3$ in acetonitrile reference electrode. The solutions were purged with N$_2$ gas prior to use. The samples were referenced to an external ferrocene solution which was also used to calculate the LUMO position [114]:

$$E_{LUMO} = -\left(E_{onset,\ reduction} + 5.1\right) eV \qquad\qquad (\ 3.1\ )$$

The cyclic voltammetry measurements and HOMO/LUMO calculations were performed by Dr Graham Morse at Merck Chemicals Ltd in the framework of the ESTABLIS project.

Figure 3.24 Cyclovoltammograms of PSBDTP_Th and PSBDTP_EDOPh.

According to equation (3.1), the HOMO level of the copolymer was −5.1 eV for **PSBDTP_Th** and -5.2 eV for **PSBDTP_EDOPh**, while the corresponding LUMO is -3.9 and-3.8 eV (Figure 3.24, Table 3.12) respectively. The small difference in the HOMO and LUMO levels is due to the different electronic effect of the thienyl and 1,4-benzodioxane. The higher donor capacity of ethylenedioxy groups on pendant phenyl rings leads to decrease in the electron-withdrawing capability of thienopyrazine unit, that results in a reduction of the HOMO. The approximate E_g^{opt} is ≈1.3 and 1.1 eV (E_g^{opt}=1240/λ_{edge}), for **PSBDTP_Th** and **PSBDTP_EDOPh** respectively, are close the electronic bandgap calculated from the CV.

The **PSBDTPs** polymers have LUMO and HOMO levels and band gap similar to those of other DTP's low bandgap copolymers [137] [144] [147].

Polymer	E_{HOMO} (eV)	E_{LUMO} (eV)	E_g^{el} (eV)	E_g^{opt} (eV)
PSBDTP_Th	-5.1	-3.9	1.2	1.3
PSBDTP_EDOPh	-5.2	-3.8	1.4	1.1

3.4.7 Thermal Properties

Thermogravimetric Analysis (TGA) was conducted to investigate the thermal stability of the polymers and in particular to compare the stability of the different side-chains. The analysis have been done under inert atmosphere (N$_2$), with a ramp of 10°C/min from 40 to 590°C.

Figure 3.25 shows that for both the **PSBDTP**, the thermal degradation happens in one step between 300 and 550°C. The weight loss obtained is higher than the theoretical value (equation (3.2)) calculated in the hypothesis that the alkyl chains on the dithienosilole unit are completely removed:

$$WL_{Theo}(\%) = \frac{Mw_{Monomer} - Mw_{Backbone}}{Mw_{Monomer}} \cdot 100 \qquad (\ 3.2\ )$$

where $Mw_{Monomer}$ is the Mw of the repeating unit, while $Mw_{Backbone}$ is the Mw of the repeating unit without any alkyl chain.
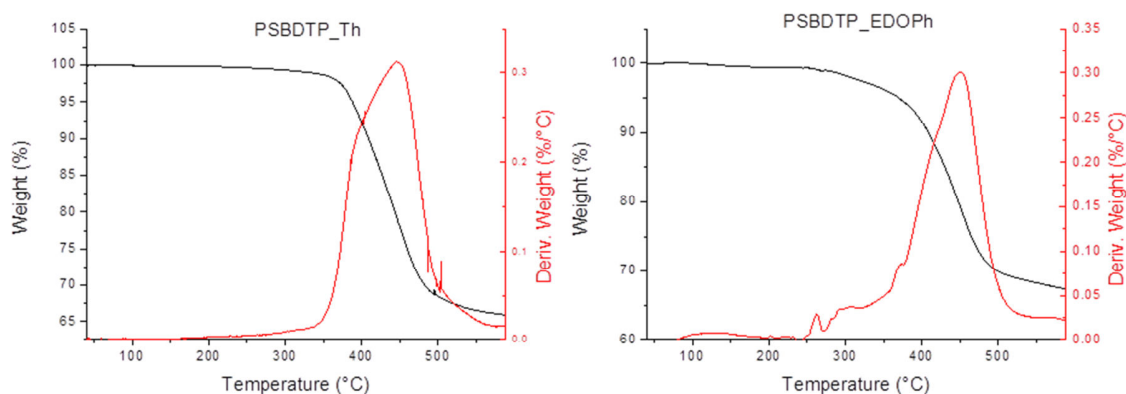
Figure 3.25 Thermo gravimetric analysis of PSBDTPs.

The difference in the weight loss compared to the theoretical values (Table 3.13) can be due to the degradation of the -Sn(Me)$_3$ groups, that in the case of such short oligomers constitute a relevant part of the total Mw.

Table 3.13 Thermal characteristics of PSBDTPs.

Sample	5% Weight loss (°C)	WL_{exp} (%)	WL_{Theo}(%)
PSBDTP_Th	388	34.1	25.5
PSBDTP_EDOPh	370	31.8	22.8

The *DSC* analysis was performed with a temperature ramp of 10°C/min with a first cycle to erase the polymers thermal history and a second one shown in Figure 3.26. The results do not show any phase transition, indicating that there is no particular aggregation of the oligomer chains.
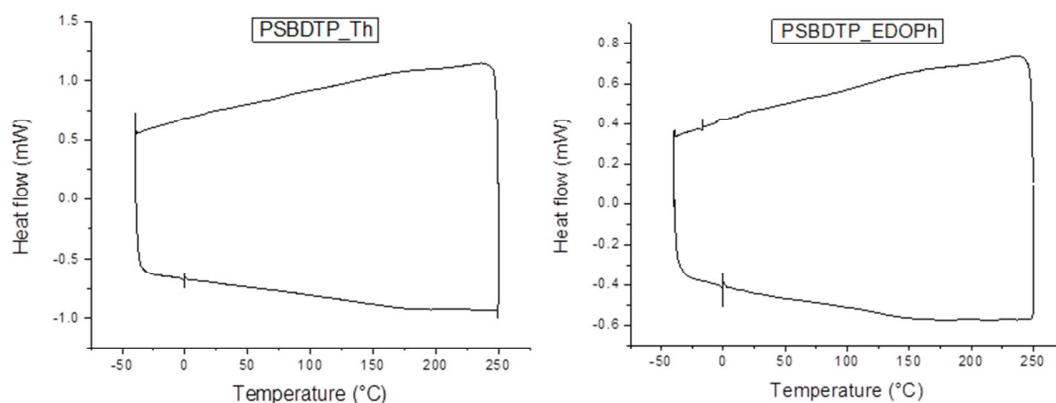
Figure 3.26 DSC thermograms of PSBDTP_Th and PSBDTP_EDOPh.

3.5 Conclusions

In this chapter the synthesis and chemical characterization of two series of Low BandGap polymers have been presented. The good solubility, the NIR-absorption and optoelectronic properties of **PSBDPPs** make them promising materials for application in OPV and organic electronics. A initial study of the OPV application of these materials is presented in the next chapter. Further studies, in collaboration with Isabel Fraga Domíngues (ESR8), Aurélien Tournebize (ESR10) and Simon A. Dowland (ER1), are still ongoing and the results will be presented in their manuscript and future publications. In particular, their stability to photo- and thermal-oxidation has been investigated and first results show superior stability compared to **P3HT** and other LBG polymers of the ESTABLIS library. Moreover, GIWAXS/GISAXS analyzes have been performed to evaluate the effect of the side-chain on the crystallinity of polymer films. The effect of side-chains on polymer thermal properties is also

under investigation by FLASH-DSC, DMTA and Raman spectroscopy. Side-chain dependence of optoelectronic properties and photo-oxidative stability of polymer:PCBM blend are under investigation within the ESTABLIS project.

The synthesis of **PSBDTP** polymers has not been successful due to a not optimized synthesis procedure. Nonetheless, the wide absorption and the electronic properties of these polymers make them promising materials for organic electronics.

3.6 References

[1] M. Leclerc and J.-F. Morin, *Design and Synthesis of Conjugated Polymers*. 2010.

[2] S. Yamaguchi and K. Tamao, "Silole-containing σ- and π-conjugated compounds," *J. Chem. Soc., Dalt. Trans.*, pp. 3693–3702, 1998.

[3] J. Dubac, A. Laporterie, and G. Manuel, "Group 14 Metalloles. 1. Synthesis, Organic Chemistry, and physicochemical Data," *Chem. Rev.*, vol. 90, pp. 215–263, 1990.

[4] J. Chen, C. C. W. Law, J. W. Y. Lam, Y. Dong, S. M. F. Lo, I. D. Williams, D. Zhu, and B. Z. Tang, "Synthesis, light emission, nanoaggregation, and restricted intramolecular rotation of 1,1-substituted 2,3,4,5-tetraphenylsiloles," *Chem. Mater.*, vol. 15, no. 7, pp. 1535–1546, 2003.

[5] D. Wittenberg and H. Gilman, "Organosilylmetallic compounds: their formation and reactions, and comparison with related types," *Q. Rev. Chem. Soc.*, vol. 13, no. 2, p. 116, 1959.

[6] J. Ohshita, "Conjugated Oligomers and Polymers Containing Dithienosilole Units," *Macromol. Chem. Phys.*, vol. 210, no. 17, pp. 1360–1370, 2009.

[7] S. Yamaguchi, C. Xu, and K. Tamao, "Bis-Silicon-Bridged Stilbene Homologues Synthesized by New Intramolecular Reductive Double Cyclization," *J. Am. Chem. Soc.*, vol. 125, no. 45, pp. 13662–13663, 2003.

[8] J. Chen and Y. Cao, "Silole-containing polymers: Chemistry and optoelectronic properties," *Macromol. Rapid Commun.*, vol. 28, no. 17, pp. 1714–1742, 2007.

[9] Y. Tamao, K.; Yamaguchi, S.; Shiozaki, M.; Nakawaga, Y.; Ito, "Thiophene-Silole Cooligomers and Copolymers," *J. Am. Chem. Soc.*, vol. 114, no. 4, pp. 5867–5869, 1992.

[10] S. Yamaguchi, R. Jin, Y. Itami, T. Goto, K. Tamao, and R. V August, "The First Synthesis of Well-Defined Poly (2 , 5-silole) linked homopolymers , have been target molecules for enthusiastic theoretical studies , because of their analogous structures to all- trans- s -cis polyacetylene as well as their potential applicab," no. 13, pp. 10420–10421, 1999.

[11] D. S. Hong, S. Y.; Marynick, "Conformations and Electronic Structures of New Conjugated Polymers Based on Poly(cyclopentadienylene) and Polysilole," *Macromolecules*, vol. 28, pp. 4991–4995, 1995.

[12] K. Tamao, S. Yamaguchi, Y. Ito, Y. Matsuzaki, T. Yamabe, M. Fukushima, and S. Mori, "Silole-Containing .pi.-Conjugated Systems. 3.1 A Series of Silole-Thiophene Cooligomers and Copolymers: Synthesis, Properties, and Electronic Structures," *Macromolecules*, vol. 28, no. 25, pp. 8668–8675, 1995.

[13] Y. Lee, S. Sadki, B. Tsuie, and J. R. Reynolds, "A New Narrow Band Gap Electroactive ethylenedioxy) thienyl } silole]," *Communications*, no. 6, pp. 2234–2236, 2001.

[14] F. Wang, J. Luo, K. Yang, J. Chen, F. Huang, and Y. Cao, "Conjugated fluorene and silole copolymers: Synthesis, characterization, electronic transition, light emission, photovoltaic cell, and field effect hole mobility," *Macromolecules*, vol. 38, no. 6, pp. 2253–2260, 2005.

[15] Z. Liu, J. Zou, J. Chen, L. Huang, J. Peng, and Y. Cao, "Largely enhanced LED efficiency of carbazole-fluorene-silole copolymers by using TPBI hole blocking layer," *Polymer (Guildf).*, vol. 49, no. 6, pp. 1604–1610, 2008.

[16] K. L. Chan, M. J. McKiernan, C. R. Towns, and A. B. Holmes, "Poly(2,7-dibenzosilole): A Blue Light Emitting Polymer," *J. Am. Chem. Soc.*, vol. 127, no. 21, pp. 7662–7663, Jun. 2005.

[17] K. L. Chan, S. E. Watkins, C. S. K. Mak, M. J. McKiernan, C. R. Towns, S. I. Pascu, and A. B. Holmes, "Poly(9,9-dialkyl-3,6-dibenzosilole)--a high energy gap host for phosphorescent light emitting devices.," *Chem. Commun. (Camb).*, no. 46, pp. 5766–5768, 2005.

[18] E. Wang, C. Li, W. Zhuang, J. Peng, and Y. Cao, "High-efficiency red and green light-emitting polymers based on a novel wide bandgap poly(2,7-silafluorene)," *J. Mater. Chem.*, vol. 18, no. 7, p. 797, 2008.

[19] P. L. T. Boudreault, A. Michaud, and M. Leclerc, "A new poly(2,7-dibenzosilole) derivative in polymer solar cells," *Macromol. Rapid Commun.*, vol. 28, no. 22, pp. 2176–2179, 2007.

[20] J. Song, C. Du, C. Li, and Z. Bo, "Silole-containing polymers for high-efficiency polymer solar cells," *J. Polym. Sci. Part A Polym. Chem.*, vol. 49, no. 19, pp. 4267–4274, 2011.

[21] J. Ohshita, M. Nodono, H. Kai, T. Watanabe, A. Kunai, K. Komaguchi, M. Shiotani, A. Adachi, K. Okita, Y. Harima, K. Yamashita, and M. Ishikawa, "Synthesis and Optical , Electrochemical , and Electron-Transporting Properties of Silicon-Bridged Bithiophenes," *Organometallics*, vol. 2, no. 7, pp. 1453–1459, 2000.

[22] H.-Y. Chen, J. Hou, A. E. Hayden, H. Yang, K. N. Houk, and Y. Yang, "Silicon Atom Substitution Enhances Interchain Packing in a Thiophene-Based Polymer System," *Adv. Mater.*, vol. 22, no. 3, pp. 371–375, 2010.

[23] H. Usta, G. Lu, A. Facchetti, and T. J. Marks, "Dithienosilole– and Dibenzosilole–Thiophene Copolymers as Semiconductors for Organic Thin-Film Transistors," *J. Am. Chem. Soc.*, vol. 128, no. 28, pp. 9034–9035, Jul. 2006.

[24] L. Liao, L. Dai, A. Smith, M. Durstock, J. Lu, J. Ding, and Y. Tao, "Photovoltaic-Active Dithienosilole-Containing Polymers," *Macromolecules*, vol. 40, no. 26, pp. 9406–9412, Dec. 2007.

[25] J. Ohshita, K. Kimura, K.-H. Lee, A. Kunai, Y.-W. Kwak, E.-C. Son, and Y. Kunugi, "Synthesis of silicon-bridged polythiophene derivatives and their applications to EL device materials," *J. Polym. Sci. Part A Polym. Chem.*, vol. 45, no. 20, pp. 4588–4596, 2007.

[26] H. Usta, G. Lu, A. Facchetti, and T. J. Marks, "Dithienosilole- and dibenzosilole-thiophene copolymers as semiconductors for organic thin-film transistors," *J. Am. Chem. Soc.*, vol. 128, no. 28, pp. 9034–9035, 2006.

[27] J. Ohshita, H. Kai, K. Kimura, K.-H. Lee, and A. Kunai, "Synthesis of Alternate Copolymers Composed of Dithienosilole and π-Conjugated Units," *Polym. J.*, vol. 41, no. 6, pp. 482–485, 2009.

[28] M. Helgesen, T. J. Sørensen, M. Manceau, and F. C. Krebs, "Photochemical stability and photovoltaic performance of low-band gap polymers based on dithiophene with different bridging atoms," *Polym. Chem.*, vol. 2, no. 6, pp. 1355–1361, May 2011.

[29] J. Hou, H.-Y. Chen, S. Zhang, G. Li, and Y. Yang, "Synthesis, Characterization, and Photovoltaic Properties of a Low Band Gap Polymer Based on Silole-Containing Polythiophenes and 2,1,3-Benzothiadiazole," *J. Am. Chem. Soc.*, vol. 130, no. 48, pp. 16144–16145, Dec. 2008.

[30] T.-Y. Chu, J. Lu, S. Beaupré, Y. Zhang, J.-R. Pouliot, J. Zhou, A. Najari, M. Leclerc, and Y. Tao, "Effects of the Molecular Weight and the Side-Chain Length on the Photovoltaic Performance of Dithienosilole/Thienopyrrolodione Copolymers," *Adv. Funct. Mater.*, vol. 22, no. 11, pp. 2345–2351, 2012.

[31] M. C. Scharber, M. Koppe, J. Gao, F. Cordella, M. A. Loi, P. Denk, M. Morana, H.-J. Egelhaaf, K. Forberich, G. Dennler, R. Gaudiana, D. Waller, Z. Zhu, X. Shi, and C. J. Brabec, "Influence of the Bridging Atom on the Performance of a Low-Bandgap Bulk Heterojunction Solar Cell," *Adv. Mater.*, vol. 22, no. 3, pp. 367–370, 2010.

[32] R. G. Jones, W. Ando, and J. Chojnowski, *Silicon-Containing Polymers*. 2000.

[33] M. Morana, H. Azimi, G. Dennler, H.-J. Egelhaaf, M. Scharber, K. Forberich, J. Hauch, R. Gaudiana, D. Waller, Z. Zhu, K. Hingerl, S. S. van Bavel, J. Loos, and C. J. Brabec, "Nanomorphology and Charge Generation in Bulk Heterojunctions Based on Low-Bandgap Dithiophene Polymers with Different Bridging Atoms," *Adv. Funct. Mater.*, vol. 20, no. 7, pp. 1180–1188, 2010.

[34] M. Manceau, E. Bundgaard, J. E. Carlé, O. Hagemann, M. Helgesen, R. Søndergaard, M. Jørgensen, and F. C. Krebs, "Photochemical stability of π-conjugated polymers for polymer solar cells: a rule of thumb," *J. Mater. Chem.*, vol. 21, no. 12, pp. 4132–4141, Mar. 2011.

[35] I. Fraga Domínguez, P. D. Topham, P.-O. Bussière, D. Bégué, and A. Rivaton, "Unravelling the Photodegradation Mechanisms of a Low Bandgap Polymer by Combining Experimental and Modeling Approaches," *J. Phys. Chem. C*, vol. 119, no. 4, pp. 2166–2176, 2015.

[36] R. L. Uy, S. C. Price, and W. You, "Structure-property optimizations in donor polymers via electronics, substituents, and side chains toward high efficiency solar cells," *Macromol. Rapid Commun.*, vol. 33, no. 14, pp. 1162–1177, 2012.

[37] E. Bundgaard, M. Helgesen, J. E. Carlé, F. C. Krebs, and M. Jørgensen, "Advanced functional polymers for increasing the stability of organic photovoltaics," *Macromol. Chem. Phys.*, vol. 214, no. 14, pp. 1546–1558, 2013.

[38] K. R. Graham, C. Cabanetos, J. P. Jahnke, M. N. Idso, A. El Labban, G. O. N. Ndjawa, T. Heumueller, K. Vandewal, A. Salleo, B. F. Chmelka, A. Amassian, P. M. Beaujuge, and M. D. Mcgehee, "Importance of the donor : fullerene intermolecular arrangement for high-efficiency organic photovoltaics Importance of the donor : fullerene intermolecular arrangement for high-efficiency organic photovoltaics," *J. Am. Chem. Soc.*, 2014.

[39] E. Bundgaard, O. Hagemann, M. Manceau, M. Jørgensen, and F. C. Krebs, "Low Band Gap Polymers for Roll-to-Roll Coated Polymer Solar Cells," *Macromolecules*, vol. 43, no. 19, pp. 8115–8120, Oct. 2010.

[40] L. Biniek, S. Fall, C. L. Chochos, D. V. Anokhin, D. a. Ivanov, N. Leclerc, P. Ĺev̂Eque, and T. Heiser, "Impact of the alkyl side chains on the optoelectronic properties of a series of photovoltaic low-band-gap copolymers," *Macromolecules*, vol. 43, no. 23, pp. 9779–9786, 2010.

[41] T. Yamamoto, T. Ikai, M. Kuzuba, T. Kuwabara, K. Maeda, K. Takahashi, and S. Kanoh, "Synthesis and characterization of thieno[3,4-b]thiophene-based copolymers bearing 4-substituted phenyl ester pendants: Facile fine-tuning of homo energy levels," *Macromolecules*, vol. 44, no. 17, pp. 6659–6662, 2011.

[42] J. W. Rumer, C. K. L. Hor, I. Meager, C. P. Yau, Z. Huang, C. B. Nielsen, S. E. Watkins, H. Bronstein, and I. McCulloch, "Alkyl side-chain branching point effects in thieno[3,4- c]pyrrole-4,6-dione copolymers," *J. Org. Semicond.*, vol. 1, no. 1, p. 30, 2013.

[43]   G. Zhang, H. Xu, K. Liu, Y. Li, L. Yang, and M. Yang, "Synthesis, characterization and comparative photovoltaic behavior of diketopyrrolopyrrole (DPP)-containing poly(phenylene vinylene)s varying at N-alkyl or 3,6-aryl substituents in DPP units," *Synth. Met.*, vol. 160, no. 17–18, pp. 1945–1952, 2010.

[44]   K. W. Song, H. J. Song, T. H. Lee, S. W. Heo, and D. K. Moon, "An effect on the side chain position of D-pi-A-type conjugated polymers with sp(2)-hybridized orbitals for organic photovoltaics," *Polym. Chem.*, vol. 4, pp. 3225–3235, 2013.

[45]   S. Subramaniyan, H. Xin, F. S. Kim, S. Shoaee, J. R. Durrant, and S. A. Jenekhe, "Effects of Side Chains on Thiazolothiazole-Based Copolymer Semiconductors for High Performance Solar Cells," *Adv. Energy Mater.*, vol. 1, no. 5, pp. 854–860, Oct. 2011.

[46]   Q. Shi, H. Fan, Y. Liu, J. Chen, L. Ma, W. Hu, Z. Shuai, Y. Li, and X. Zhan, "Side Chain Engineering of Copolymers Based on Bithiazole and Benzodithiophene for Enhanced Photovoltaic Performance," *Macromolecules*, vol. 44, no. 11, pp. 4230–4240, Jun. 2011.

[47]   E. Wang, L. Hou, Z. Wang, Z. Ma, S. Hellström, W. Zhuang, F. Zhang, O. Inganäs, and M. R. Andersson, "Side-chain architectures of 2,7-carbazole and quinoxaline-based polymers for efficient polymer solar cells," *Macromolecules*, vol. 44, pp. 2067–2073, 2011.

[48]   Y. Li, Y. Chen, X. Liu, Z. Wang, X. Yang, Y. Tu, and X. Zhu, "Controlling blend film morphology by varying alkyl side chain in highly coplanar donor-acceptor copolymers for photovoltaic application," *Macromolecules*, vol. 44, no. 16, pp. 6370–6381, 2011.

[49]   L. Yang, H. Zhou, and W. You, "Quantitatively analyzing the influence of side chains on photovoltaic properties of polymer-fullerene solar cells," *J. Phys. Chem. C*, vol. 114, no. 39, pp. 16793–16800, 2010.

[50]   J. Mei and Z. Bao, "Side chain engineering in solution-processable conjugated polymers," *Chem. Mater.*, vol. 26, no. 1, pp. 604–615, 2014.

[51]   M. Helgesen, "Thermocleavable π-Conjugated Polymers - Synthesis and photovoltaic applications," vol. 54, no. October, 2009.

[52]   S. Park, D. Seo, T. I. Ryu, G. Ahn, K. Kwak, H. Kim, C. H. Cheon, N.-G. Park, B. Kim, M. J. Ko, D.-K. Lee, J. Y. Kim, H. Kim, and H. J. Son, "Enhancement of Organic Photovoltaic Efficiency via Nanomorphology Control using Conjugated Polymers Incorporating Fullerene Compatible Side-Chains," *Macromolecules*, 2015.

[53]   M. Manceau, M. Helgesen, and F. C. Krebs, "Thermo-cleavable polymers: Materials with enhanced photochemical stability," *Polym. Degrad. Stab.*, vol. 95, no. 12, pp. 2666–2669, 2010.

[54]   G. E. Morse, A. Tournebize, A. Rivaton, N. Blouin, and S. Tierney, "The Effect of Side-Chains on Polymer Solar Cell Stability," pp. 1–3, 2015.

[55]   A. Iqbal, M. Jost, R. Kirchmayr, and A. Rochat, "THE SYNTHESIS AND PROPERTIES OF 1,4-DIKETO-PYRROLO[3,4-C]PYRROLES," *Bull. la Soc. Chim. Belge*, vol. 97, no. 8–9, pp. 615–643, 1988.

[56]   Z. Hao and A. Iqbal, "Some aspects of organic pigments," *Chem. Soc. Rev.*, vol. 26, pp. 203–213, 1997.

[57]   O. Wallquist and R. Lenz, "20 years of DPP pigments - Future perspectives," *Macromol. Symp.*, vol. 187, pp. 617–629, 2002.

[58]   B. Tieke, A. R. Rabindranath, K. Zhang, and Y. Zhu, "Conjugated polymers containing diketopyrrolopyrrole units in the main chain," *Beilstein J. Org. Chem.*, vol. 6, pp. 830–845, 2010.

[59]   S. Qu and H. Tian, "Diketopyrrolopyrrole (DPP)-based materials for organic photovoltaics," *Chem. Commun.*, vol. 48, pp. 3039–3051, 2012.

[60]   D. G. Farnum, G. Mehta, G. G. I. Moore, and F. P. Siegal, "Attempted Reformatskii Reaction of Benzonitrile, 1,4-diketo-3,6-diphenylpyrrolo-[3,4-c]pyrrole. A Lactam Analogue of Pentalene.," *Tetrahedron Lett.*, vol. 29, pp. 2549–2552, 1974.

[61]   A. Iqbal and L. Cassar, "PROCESS FOR DYEING HIGH-MOLECULAR ORGANIC MATERIAL, AND NOVEL POLYCYCLIC PIGMENTS," 1983.

[62]   Y.-J. Cheng, S.-H. Yang, and C.-S. Hsu, "Synthesis of conjugated polymers for organic solar cell applications," *Chem. Rev.*, vol. 109, no. 11, pp. 5868–5923, Nov. 2009.

[63]   D. Gendron and M. Leclerc, "New conjugated polymers for plastic solar cells," *Energy Environ. Sci.*, vol. 4, p. 1225, 2011.

[64]   J. MIZUGUCHI and A. GRUBENMANN, "Structures of 3,6-bis(3-chlorophenyl)pyrrolo[3,4-c]pyrrole-1,4-dione and 3,6-bis(4-chlorophenyl)pyrrolo[3,4-c]pyrrole-1,4-dione," *Acta Crystallogr.*, vol. B49, pp. 1056–1060, 1993.

[65]   J. Mizuguchi, "Correlation between Crystal and Electronic Structures in Diketopyrrolopyrrole Pigments as Viewed from Exciton Coupling Effects," *J. Phys. Chem. A*, vol. 104, pp. 1817–1821, 2000.

[66] C. Kim, J. Liu, J. Lin, A. B. Tamayo, B. Walker, G. Wu, and T. Q. Nguyen, "Influence of structural variation on the solid-state properties of diketopyrrolopyrrole-based oligophenylenethiophenes: Single-crystal structures, thermal properties, optical bandgaps, energy levels, film morphology, and hole mobility," *Chem. Mater.*, vol. 24, pp. 1699–1709, 2012.

[67] J. Bijleveld, A. P. Zoombelt, S. G. J. Mathijssen, M. M. Wienk, M. Turbiez, D. M. de Leeuw, and R. A. J. Janssen, "Poly(diketopyrrolopyrrole-terthiophene) for Ambipolar Logic and Photovoltaics," *J. …*, vol. 131, pp. 16616–16617, 2009.

[68] C. H. Woo, P. M. Beaujuge, T. W. Holcombe, O. P. Lee, and J. M. J. Fréchet, "Incorporation of furan into low band-gap polymers for efficient solar cells," *J. Am. Chem. Soc.*, vol. 132, pp. 15547–15549, 2010.

[69] A. J. Kronemeijer, E. Gili, M. Shahid, J. Rivnay, A. Salleo, M. Heeney, and H. Sirringhaus, "A selenophene-based low-bandgap donor-acceptor polymer leading to fast ambipolar logic," *Adv. Mater.*, vol. 24, pp. 1558–1565, 2012.

[70] S. Stas, J. Y. Balandier, V. Lemaur, O. Fenwick, G. Tregnago, F. Quist, F. Cacialli, J. Cornil, and Y. H. Geerts, "Straightforward access to diketopyrrolopyrrole (DPP) dimers," *Dye. Pigment.*, vol. 97, pp. 198–208, 2013.

[71] H. Bürckstümmer, A. Weißenstein, D. Bialas, and F. Würthner, "Synthesis and Characterization of Optical and Redox Properties of Bithiophene-Functionalized Diketopyrrolopyrrole Chromophores," *J. Org. Chem.*, vol. 76, pp. 2426–2432, 2011.

[72] J. Sakamoto, M. Rehahn, G. Wegner, and A. D. Schlüter, "Suzuki Polycondensation: Polyarylenes à la Carte," *Macromol. Rapid Commun.*, vol. 30, no. 9–10, pp. 653–687, 2009.

[73] B. Carsten, F. He, H. J. Son, T. Xu, and L. Yu, "Stille Polycondensation for Synthesis of Functional Materials," *Chem. Rev.*, vol. 111, no. 3, pp. 1493–1528, Mar. 2011.

[74] W. Cabri and I. Candiani, "Recent Developments and New Perspectives in the Heck Reaction," *Acc. Chem. Res.*, vol. 28, no. c, pp. 2–7, 1995.

[75] Y. Zhu, K. Zhang, and B. Tieke, "Electrochemical Polymerization of Bis(3,4-ethylenedioxythiophene)-Substituted 1,4-Diketo-3,6-diphenyl-pyrrolo[3,4-c]pyrrole (DPP) Derivative," *Macromol. Chem. Phys.*, vol. 210, no. 6, pp. 431–439, 2009.

[76] T. Potrawa, "Fluoreszenzfarbstoffe mit groBen Stokes-Shifts," *Chem. Ber.*, vol. 120, pp. 1075–1078, 1987.

[77] H. Langhals, T. Grundei, T. Potrawa, and K. Polborn, "Highly Photostable Organic Fluorescent Pigments - A Simple Synthesis of N-Arylpyrrolopyrrolediones (DPP)," *Liebigs Ann.*, pp. 679–682, 1996.

[78] S. J. Zambounis, Z. Hao, and A. Iqbal, "Latent pigments activated by heat," *Nature*, vol. 388, p. 131, 1997.

[79] W.-K. Chan, Y. Chen, Z. Peng, and L. Yu, "Rational Designs of Multifunctional Polymers," *J. Am. Chem. Soc.*, no. 115, pp. 11735–11743, 1993.

[80] S. H. Eldin, A. Iqbal, and Z. Hao, "Polymerisable diketopyrrolopyrroles and polymers prepared with same," EP 07877301997.

[81] A. B. Tamayo, M. Tantiwiwat, B. Walker, and T. Nguyen, "Design , Synthesis , and Self-assembly of Oligothiophene Derivatives with a Diketopyrrolopyrrole Core," *J. Phys. Chem. C*, vol. 112, pp. 15543–15552, 2008.

[82] T. Beyerlein and B. Tieke, "New photoluminescent conjugated polymers with 1,4-dioxo-3,6-diphenylpyrrolo[3,4-c]pyrrole (DPP) and 1,4-phenylene units in the main chain," *Macromol. Rapid Commun.*, vol. 21, pp. 182–189, 2000.

[83] T. Beyerlein, B. Tieke, S. Forero-lenger, and W. Bru, "Red electroluminescence from a 1,4-diketopyrrolo[3,4-c]pyrrole (DPP)-based conjugated polymer," *Synth. Met.*, vol. 130, pp. 115–119, 2002.

[84] C. Kanimozhi, P. Balraju, G. D. Sharma, and S. Patil, "Synthesis of Diketopyrrolopyrrole Containing Copolymers : A Study of Their Optical and Photovoltaic Properties," *J. Phys. Chem. B*, vol. 114, pp. 3095–3103, 2010.

[85] Y. Zou, D. Gendron, A. Najari, Y. Tao, and M. Leclerc, "A High-Mobility Low-Bandgap Poly(2,7-carbazole) Derivative for Photovoltaic Applications," *Macromolecules*, vol. 42, pp. 2891–2894, 2009.

[86] L. Huo, J. Hou, H.-Y. Chen, S. Zhang, Y. Jiang, T. L. Chen, and Y. Yang, "Bandgap and Molecular Level Control of the Low-Bandgap Polymers Based on 3,6-Dithiophen-2-yl-2,5-dihydropyrrolo[3,4-c]pyrrole-1,4-dione toward Highly Efficient Polymer Solar Cells," *Macromolecules*, vol. 42, no. 17, pp. 6564–6571, Sep. 2009.

[87] Y. Zou, D. Gendron, R. Neagu-Plesu, and M. Leclerc, "Synthesis and Characterization of New Low-Bandgap Diketopyrrolopyrrole-Based Copolymers," *Macromolecules*, vol. 42, no. 17, pp. 6361–6365, Sep. 2009.

[88] Y. Zou, D. Gendron, R. Badrou-Aïch, A. Najari, Y. Tao, and M. Leclerc, "A High-Mobility Low-Bandgap Poly(2,7-carbazole) Derivative for Photovoltaic Applications," *Macromolecules*, vol. 42, no. 8, pp. 2891–2894, Apr. 2009.

[89] E. Zhou, Q. Wei, S. Yamakawa, Y. Zhang, K. Tajima, C. Yang, and K. Hashimoto, "Diketopyrrolopyrrole-based semiconducting polymer for photovoltaic device with photocurrent response wavelengths up to 1.1 ??m," *Macromolecules*, vol. 43, no. 2, pp. 821–826, 2010.

[90]   E. Zhou, S. Yamakawa, K. Tajima, C. Yang, and K. Hashimoto, "Synthesis and photovoltaic properties of diketopyrrolopyrrole-based donor-acceptor copolymers," *Chem. Mater.*, vol. 21, no. 17, pp. 4055–4061, 2009.

[91]   C. Kanimozhi, P. Balraju, G. D. Sharma, and S. Patil, "Diketopyrrolopyrrole-based donor-acceptor copolymers as organic sensitizers for dye sensitized solar cells," *J. Phys. Chem. C*, vol. 114, no. 7, pp. 3287–3291, 2010.

[92]   A. P. Zoombelt, S. G. J. Mathijssen, M. G. R. Turbiez, M. M. Wienk, and R. a. J. Janssen, "Small band gap polymers based on diketopyrrolopyrrole," *J. Mater. Chem.*, vol. 20, no. 11, p. 2240, 2010.

[93]   M. M. Wienk, M. Turbiez, J. Gilot, and R. a. J. Janssen, "Narrow Bandgap DiketoPyrroloPyrrole Polymer Solar Cells: The Effect of Processing on the Performance," *Adv. Mater.*, vol. 20, no. 13, pp. 2556–2560, 2008.

[94]   J. H. Tsai, W. Y. Lee, W. C. Chen, C. Y. Yu, G. W. Hwang, and C. Ting, "New two-dimensional thiophene-acceptor conjugated copolymers for field effect transistor and photovoltaic cell applications," *Chem. Mater.*, vol. 22, no. 10, pp. 3290–3299, 2010.

[95]   J. C. Bijleveld, R. a. M. Verstrijden, M. M. Wienk, and R. a. J. Janssen, "Copolymers of diketopyrrolopyrrole and thienothiophene for photovoltaic cells," *J. Mater. Chem.*, vol. 21, no. 25, p. 9224, 2011.

[96]   J. Min, B. Peng, Y. Wen, Z. G. Zhang, M. Zhang, J. Zhang, Q. Xie, Y. Liu, and Y. Li, "Low bandgap copolymer of 1,4-diketopyrrolo[3,4-c]pyrrole and thieno[3,2-b]thiophene: Synthesis and applications in polymer solar cells and field-effect transistors," *Synth. Met.*, vol. 161, no. 17–18, pp. 1832–1837, 2011.

[97]   A. V. Patil, W.-H. Lee, K. Kim, H. Park, I. N. Kang, and S.-H. Lee, "Synthesis and photovoltaic properties of narrow band gap copolymers of dithieno[3,2-b:2′,3′-d]thiophene and diketopyrrolopyrrole," *Polym. Chem.*, vol. 2, no. 12, p. 2907, 2011.

[98]   J. C. Bijleveld, V. S. Gevaerts, D. Di Nuzzo, M. Turbiez, S. C. J. Mathijssen, D. M. De Leeuw, M. M. Wienk, and R. a J. Janssen, "Efficient solar cells based on an easily accessible diketopyrrolopyrrole polymer," *Adv. Mater.*, vol. 22, no. 35, pp. 242–246, 2010.

[99]   P. Sonar, S. P. Singh, Y. Li, Z.-E. Ooi, T. Ha, I. Wong, M. S. Soh, and A. Dodabalapur, "High mobility organic thin film transistor and efficient photovoltaic devices using versatile donor–acceptor polymer semiconductor by molecular design," *Energy Environ. Sci.*, vol. 4, no. 6, p. 2288, 2011.

[100] N. Allard, R. B. Aïch, D. Gendron, P. L. T. Boudreault, C. Tessier, S. Alem, S. C. Tse, Y. Tao, and M. Leclerc, "Germafluorenes: New heterocycles for plastic electronics," *Macromolecules*, vol. 43, no. 5, pp. 2328–2333, 2010.

[101] L. Huo, J. Hou, H.-Y. Chen, S. Zhang, Y. Jiang, T. L. Chen, and Y. Yang, "Bandgap and Molecular Level Control of the Low-Bandgap Polymers Based on 3,6-Dithiophen-2-yl-2,5-dihydropyrrolo[3,4-c]pyrrole-1,4-dione toward Highly Efficient Polymer Solar Cells," *Macromolecules*, vol. 42, no. 17, pp. 6564–6571, Sep. 2009.

[102] J. Jo, D. Gendron, A. Najari, J. S. Moon, S. Cho, M. Leclerc, and A. J. Heeger, "Bulk heterojunction solar cells based on a low-bandgap carbazole- diketopyrrolopyrrole copolymer," *Appl. Phys. Lett.*, vol. 97, no. 20, pp. 1–4, 2010.

[103] J. Pretula, K. Kaluzynski, B. Wisniewski, R. Szymanski, T. Loontjens, and S. Penczek, "Formation of poly(ethylene phosphates) in polycondensation of H3PO4 with ethylene glycol. Kinetic and mechanistic study," *J. Polym. Sci. Part a-Polymer Chem.*, vol. 46, no. 3, pp. 830–843, 2008.

[104] Z. Li, Y. Zhang, S. W. Tsang, X. Du, J. Zhou, Y. Tao, and J. Ding, "Alkyl side chain impact on the charge transport and photovoltaic properties of benzodithiophene and diketopyrrolopyrrole-based copolymers," *J. Phys. Chem. C*, vol. 115, no. 36, pp. 18002–18009, 2011.

[105] Y. Li, "Diketopyrrolopyrrole-based derivatives for thin film transistors (EP2034537 (A2))," 2009.

[106] W. J. S. V. Farina, V. Krishnamurthy, "The Stille Reaction," *Organic Reactions*, vol. 50. pp. 3–664, 1997.

[107] S. Holdcroft, "Determination of Molecular Weights and Mark-Houwink Constants for Soluble Electronically Conducting Polymers," *J. Polym. Sci. Part B Polym. Phys.*, vol. 29, pp. 1585–1588, 1991.

[108] S. Vanhee, R. Rulkens, and U. Lehmann, "Synthesis and characterization of rigid rod poly (p-phenylenes)," *Macromolecules*, vol. 6, no. 29, pp. 5136–5142, 1996.

[109] J. Liu, R. S. Loewe, and R. D. Mccullough, "Employing MALDI-MS on Poly (alkylthiophenes): Analysis of Molecular Weights, Molecular Weight Distributions, End-Group Structures, and End-Group Modifications End-Group Modifications," *Macromolecules*, vol. 32, pp. 5777–5785, 1999.

[110] M. Tantiwiwat, A. Tamayo, N. Luu, X. Dang, and T. Nguyen, "Oligothiophene Derivatives Functionalized with a Diketopyrrolopyrrolo Core for Solution-Processed Field Effect Transistors : Effect of Alkyl Substituents and Thermal Annealing," *J. Phys. Chem. C*, vol. 112, no. 44, pp. 17402–17407, 2008.

[111] A. B. Tamayo, X. Dang, B. Walker, J. Seo, and T. Kent, "A low band gap , solution processable oligothiophene with a dialkylated diketopyrrolopyrrole chromophore for use in bulk heterojunction solar cells A low band gap , solution processable oligothiophene with a dialkylated diketopyrrolopyrrole chromophore fo," *Appl. Phys. Lett.*, vol. 94, 2014.

[112] F. C. Spano and C. Silva, "H- and J-aggregate behavior in polymeric semiconductors.," *Annu. Rev. Phys. Chem.*, vol. 65, pp. 477–500, 2014.

[113] M. Kirkus, L. Wang, D. Beljonne, and S. C. J. Meskers, "Optical Properties of Oligothiophene Substituted Diketopyrrolopyrrole Derivatives in the Solid Phase: Joint J- and H - Type Aggregation," *J. Phys. Chem. A*, vol. 116, pp. 7927–7936, 2012.

[114] C. M. Cardona, W. Li, A. E. Kaifer, D. Stockdale, and G. C. Bazan, "Electrochemical considerations for determining absolute frontier orbital energy levels of conjugated polymers for solar cell applications," *Adv. Mater.*, vol. 23, no. 20, pp. 2367–2371, 2011.

[115] L. Huo, H.-Y. Chen, J. Hou, T. L. Chen, and Y. Yang, "Low band gap dithieno[3,2-b:2′,3′-d]silole-containing polymers, synthesis, characterization and photovoltaic application," *Chem. Commun.*, no. 37, p. 5570, 2009.

[116] J. R. Matthews, W. Niu, A. Tandia, A. L. Wallace, J. Hu, W.-Y. Lee, G. Giri, S. C. B. Mannsfeld, Y. Xie, S. Cai, H. H. Fong, Z. Bao, and M. He, "Scalable Synthesis of Fused Thiophene-Diketopyrrolopyrrole Semiconducting Polymers Processed from Nonchlorinated Solvents into High Performance Thin Film Transistors," *Chem. Mater.*, vol. 25, no. 5, pp. 782–789, Mar. 2013.

[117] C. Schick, "Flash-DSC, a new technique for thermal analysis," pp. 6–8.

[118] R. F. Cossiello, G. C. Faria, E. R. de Azavedo, T. J. Bonagamba, and T. D. Z. Atvars, "The polymeric thermal relaxation of conjugated- groups in polyfluorenes-derivatives."

[119] H. Liem, J. Cabanillas-Gonzalez, P. Etchegoin, and D. D. C. Bradley, "Glass transition temperatures of polymer thin films monitored by Raman scattering," *J. Phys. Condens. Matter*, vol. 16, no. 6, pp. 721–728, 2004.

[120] I. F. Perepichka and D. F. Perepichka, *Handbook of Thiophene-based Materials : Photonics*. John Wiley & Sons Ltd, 2009.

[121] F. Wudl, M. Kobayashi, and a. J. Heeger, "Poly(isothianaphthene)," *Am. Chem. Soc.*, vol. 49, no. 18, pp. 3382–3384, 1984.

[122] M. Kertesz, C. H. Choi, and S. Yang, "Conjugated polymers and aromaticity," *Chem. Rev.*, vol. 105, no. 10, pp. 3448–3481, 2005.

[123] M. Kobayashi, N. Colaneri, M. Boysel, F. Wudl, and A. J. Heeger, "The electronic and electrochemical properties of the TiFe1-xNix alloys," *J. Chem. Phys.*, vol. 82, no. 12, p. 5717, 1985.

[124] M. Pomerantz, B. Chaloner-Gill, L. O. Harding, J. J. Tseng, and W. J. Pomerantz, "New processable low band-gap, conjugated polyheterocycles," *Synth. Met.*, vol. 55, no. 2–3, pp. 960–965, 1993.

[125] D. L. Vangeneugden, R. H. L. Kiebooms, D. J. M. Vanderzande, and J. M. J. V. Gelan, "A general synthetic route towards soluble poly(1,3-dithienylisothianaphthene) derivatives," *Synth. Met.*, vol. 101, no. 1–3, pp. 120–121, 1999.

[126] D. Lorcy and M. P. Cava, "Poly(isothianaphthene-bithiophefe): A new regularly structured polythiophene analogue," *Adv. Mater.*, vol. 4, no. 9, pp. 562–564, 1992.

[127] P. Bauerle, G. Gotz, P. Emerle, and H. Port, "Synthesis and Characterization of New Annelated Terheterocycles," *Adv. Mater.*, no. 9, pp. 0–4, 1992.

[128] U. Mitschke and P. Bäuerle, "Synthesis, characterization, and electrogenerated chemiluminescence of phenyl-substituted, phenyl-annulated, and spirofluorenyl-bridged oligothiophenes," *J. Chem. Soc. Perkin Trans. 1*, no. 7, pp. 740–753, 2001.

[129] R. Kisselev and M. Thelakkat, "Synthesis and characterization of poly(triarylamine)s containing isothianaphthene moieties," *Macromolecules*, vol. 37, no. 24, pp. 8951–8958, 2004.

[130] J. P. Ferraris, A. Bravo, W. Kim, and D. C. Hrncir, "Reduction of steric interactions in thiophene?pyridino[c]thiophene copolymers," *J. Chem. Soc. Chem. Commun.*, no. 8, p. 991, 1994.

[131] J. Kastner, H. Kuzmany, D. Vegh, M. Landl, L. Cuff, and M. Kertesz, "Raman spectra and ground state of the new low bandgap polymer poly(thienopyrazine)," *Synth. Met.*, vol. 69, no. 1–3, pp. 593–594, 1995.

[132] C. C. Chueh, M. H. Lai, J. H. Tsai, C. F. Wang, and W. C. Chen, "Syntheses, properties, and field-effect transistors of small band gap quinoxaline- and thienopyrazine-vinylene/ethynylene conjugated polymers," *J. Polym. Sci. Part A Polym. Chem.*, vol. 48, no. 1, pp. 74–81, 2010.

[133] R. S. Ashraf, M. Shahid, E. Klemm, M. Al-Ibrahim, and S. Sensfuss, "Thienopyrazine-based low-bandgap poly(heteroaryleneethynylene)s for photovoltaic devices," *Macromol. Rapid Commun.*, vol. 27, no. 17, pp. 1454–1459, 2006.

[134] C.-Y. Chao, C.-H. Chao, L.-P. Chen, Y.-C. Hung, S.-T. Lin, W.-F. Su, and C.-F. Lin, "Band structure engineering for low band gap polymers containing thienopyrazine," *J. Mater. Chem.*, vol. 22, no. 15, p. 7331, 2012.

[135] S. Akoudad and J. Roncali, "Electrogenerated poly(thiophenes) with extremely narrow bandgap and high stability under n-doping cycling," *Chem. Commun.*, no. 19, pp. 2081–2082, 1998.

[136] C. Kitamura, S. Tanaka, and Y. Yamashita, "Synthesis of new narrow bandgap polymers based on 5,7-di(2-thienyl)thieno[3,4-b]pyrazine and its derivatives," *J. Chem. Soc. Chem. Commun.*, no. 13, p. 1585, 1994.

[137] Y. Zhu, R. D. Champion, and S. a. Jenekhe, "Conjugated donor-acceptor copolymer semiconductors with large intramolecular charge transfer: Synthesis, optical properties, electrochemistry, and field effect carrier mobility of thienopyrazine-based copolymers," *Macromolecules*, vol. 39, no. 25, pp. 8712–8719, 2006.

[138] A. P. Zoombelt, M. a M. Leenen, M. Fonrodona, Y. Nicolas, M. M. Wienk, and R. a J. Janssen, "The influence of side chains on solubility and photovoltaic performance of dithiophene-thienopyrazine small band gap copolymers," *Polymer (Guildf).*, vol. 50, no. 19, pp. 4564–4570, 2009.

[139] G. Sonmez, "Polymeric electrochromics," *Chem. Commun.*, no. 42, pp. 5251–5259, Oct. 2005.

[140] S. Tarkuc, E. K. Unver, Y. A. Udum, C. Tanyeli, and L. Toppare, "The effect of changes in π-conjugated terthienyl systems using thienyl and ethylenedioxybenzene functionalized thieno[3,4-b]pyrazine precursors: Multicolored low band gap polymers," *Electrochim. Acta*, vol. 55, no. 24, pp. 7254–7258, Oct. 2010.

[141] M. M. Wienk, M. G. R. Turbiez, M. P. Struijk, M. Fonrodona, and R. a J. Janssen, "Low-band gap poly(di-2-thienylthienopyrazine):fullerene solar cells," *Appl. Phys. Lett.*, vol. 88, no. 15, pp. 3–5, 2006.

[142] A. P. Zoombelt, J. Gilot, M. M. Wienk, and R. A. J. Janssen, "Effect of Extended Thiophene Segments in Small Band Gap Polymers with Thienopyrazine," *Chem. Mater.*, vol. 21, no. 8, pp. 1663–1669, Apr. 2009.

[143] R. Mondal, N. Miyaki, H. a. Becerril, J. E. Norton, J. Parmer, A. C. Mayer, M. L. Tang, J. L. Brédas, M. D. McGehee, and Z. Bao, "Synthesis of acenaphthyl and phenanthrene based fused-aromatic thienopyrazine co-polymers for photovoltaic and thin film transistor applications," *Chem. Mater.*, vol. 21, no. 15, pp. 3618–3628, 2009.

[144] F. Zhang, W. Mammo, L. M. Andersson, S. Admassie, M. R. Andersson, and O. Inganäs, "Low-Bandgap Alternating Fluorene Copolymer/Methanofullerene Heterojunctions in Efficient Near-Infrared Polymer Solar Cells," *Adv. Mater.*, vol. 18, no. 16, pp. 2169–2173, Aug. 2006.

[145] F. Zhang, E. Perzon, X. Wang, W. Mammo, M. R. Andersson, and O. Inganäs, "Polymer solar cells based on a low-bandgap fluorene copolymer and a fullerene derivative with photocurrent extended to 850 nm," *Adv. Funct. Mater.*, vol. 15, no. 5, pp. 745–750, 2005.

[146] R. Mondal, S. Ko, E. Verploegen, H. a. Becerril, M. F. Toney, and Z. Bao, "Side chain engineering of fused aromatic thienopyrazine based low band-gap polymers for enhanced charge carrier mobility," *J. Mater. Chem.*, vol. 21, no. 5, p. 1537, 2011.

[147] R. Mondal, H. A. Becerril, E. Verploegen, D. Kim, J. E. Norton, S. Ko, N. Miyaki, S. Lee, M. F. Toney, J.-L. Brédas, M. D. McGehee, and Z. Bao, "Thiophene-rich fused-aromatic thienopyrazine acceptor for donor–acceptor low band-gap polymers for OTFT and polymer solar cell applications," *J. Mater. Chem.*, vol. 20, no. 28, p. 5823, 2010.

[148] M. L. Keshtov, D. V. Marochkin, Y. Fu, Z. Xie, Y. Geng, V. S. Kochurov, and A. R. Khokhlov, "Thienopyrazine or dithiadiazatrindene containing low band gap conjugated polymers for polymer solar cells," *Chinese J. Polym. Sci.*, vol. 32, no. 7, pp. 844–853, 2014.

[149] D. Mohamad, R. G. Johnson, D. Janeliunas, M. Kirkus, H. Yi, D. G. Lidzey, and A. Iraqi, "Aryl amine substituted low energy gap carbazole polymers: preparation and photovoltaic properties," *J. Mater. Chem.*, vol. 20, no. 33, p. 6990, 2010.

[150] F. Babudri, V. Fiandanese, G. Marchese, and A. Punzi, "A Direct Access to tx-Diones from Oxalyl Chloride Francesco," vol. 36, no. 40, pp. 7305–7308, 1995.

4 Application in Inverted Devices

In order to verify the efficiency of the PSBDPP polymers in real applications, devices with inverted architecture have been fabricated at Belectric OPV GmbH. The photovoltaic characteristics of devices processed under different conditions were investigated in order to optimize them.

4.1 Introduction

Solution processing, low cost, short energy payback time, flexibility, lightness are keywords generally associated with organic solar cells, and for the past 30 years the huge potential of producing effective and cheap solar cells has been the driving force for research in this field. The research at laboratory scale started with small area cells, fabricated by simple and relatively inexpensive techniques such as spin coating and thermal evaporation. Currently, most OPVs still need to be fabricated under nitrogen atmosphere, inside gloveboxes, to exclude the detrimental effect of oxygen and moisture on device performance and long-term stability [1], [2]. However, this processing is not suitable for the eventual scale up of production to mass manufacturing applications. Moreover, many researchers claim the scalability of performances obtained on these small scale, laboratory produced devices, which are tested under extremely restrictive conditions. However, the transferring of the delicate and highly empirical equilibrium between multiple fabrication parameters (solvent, deposition, drying and post deposition conditions, materials, etc.) to a scale-up processing is not trivial. The extra requirements of speeding-up the processing and to transfer it in ambient conditions make the task even harder.

In order for the organic solar cells to succeed as a technology, more effort must be directed towards large area fabrication combined with high throughput processing such as roll-to-roll methods (R2R). The main printing and coating techniques which are fully compatible with R2R processing have been subject to review [3], [4]. Examples of printing technique are: (i) wet films through contact: gravure printing, flexographic printing, screen printing, rotary screen printing; and (ii) wet film formation without contact: spray coating, inkjet.

The coating techniques differ from the printing techniques in that the wet film is spun through a meniscus. The two most common coating techniques applied in OPV processing are slot-die coating and knife coating [3]. Knife coating is very similar to doctor blading and, thus, laboratory results can be transferred with more ease to roll-to-roll processing. As the web passes by, the meniscus is fed with new ink by a reservoir located before the knife. Slot-die coating allows to coat stripes of a well-defined width along the web direction, also with a one-dimensional patterning. This is achieved

through the ink supply; the meniscus is fed via a slot and a pump, enabling to adjust the wet thickness by controlling both the speed of the web or the ink supply.

The current attempts to scale up production of OPVs from lab to industrial scale have led to drops in *PCE* [5] and stability [6], compared to heroes devices on laboratory scale with a PCE of 11.5% [7] and a predicted lifetime up to 20 years [8]. Recently, Lucera *et al* [9] analyzed the factors which negatively affect the performance of up-scaled devices, giving guidelines in order to overcome them, while Angmo and Krebs [10] demonstrated the outdoor operational and storage stability of large flexible modules up to two years.

Also, from an industrial point of view, replacing halogenated solvents in the processing of organic solar cells by benign solvents is a required step for the commercialization of this technology, due to industrial and environmental requirements [11]. Of course, a good solubility of the materials is essential to be properly processed. This is even more critical in bulk heterojunction systems, where two (or more) materials are processed from the same solution. Therefore, solvent systems anticipated to be more transferable to sustainable module production, while maintaining high efficiency, are extremely compelling. Water is one of the most favorable processing fluids from cost and sustainability standpoints. However, efficient photoactive materials compatible with aqueous solvents are currently scarce [12], [13] and new environment frendlier solvents systems which can mimic the halogenated solvents properties have been only recently explored [14].

Nowadays, halogen-free organic solvents (e g., toluene and isomers of xylene) are the most attractive processing solvents, since their environmental accumulation can be faced with comparative ease [15], making them more compatible with environmental impact concerns associated with large-scale manufacturing. The use of non-halogenated solvents has been investigated [16], [17] and results comparable to traditional halogenated solvents have been obtained. Large scale production by slot-die coating with *o*-xylene-based inks have been recently explored [18]. It showed reduced device performances compared to doctor-bladed solar cells, improved by the use tetrahydronaphtalene as co-solvent.

Another aspect to take into account is the device architecture. As described in the introduction, the most diffused device architecture is the so-called normal geometry (substrate/cathode/active layer/anode). A valid alternative is represented by the inverted geometry (substrate/anode/active layer/cathode), which offers advantages in terms of stability [19]. These

advantages arise from the fact that the high working function metal electrode is exposed to the air. Moreover, inverted structure avoids the use of **PEDOT:PSS** to tune the **ITO** work function. It has been shown that the acidic nature of **PEDOT:PSS** promotes the etching of **ITO**, with the diffusion of indium to the active layer. Another important feature is that inverted structure gives the possibility of developing a completely vacuum-free solution processing or exotic alternatives such as lamination.

4.2   Polymer:PC$_{61}$BM blend ratio and Solvent System

The donor and acceptor blend ratio significantly influences the device performance of the BHJ solar cell. Indeed, it has been shown that it strongly affects the crystalline order, phase separation, and morphology of the thin film [20]. In order to obtain the best bicontinuous percolation pathways with maximal interfacial area, the optimal D:A ratio (by weight) depends on the choice of materials used [21]. In the **MDMO-PPV:PC$_{61}$BM** (1:4) system, fullerenes tend to be mixable with the amorphous polymers [22]. For the **P3HT:PC$_{61}$BM** solar cell, a D:A ratio of 1:1 or 1:0.8 is needed to achieve a PCE over 4% [23], [24]. For most of LBG polymers the best performances are achieved with a ratio ranging from 1:2 to 1:4 [21], [25].

Due to the limited amount of materials synthetized, the D:A ratio was not optimized with a systematic procedure, but directly fixed at 1:2 (w/w) polymer:**PC$_{61}$BM** ratio, as reported in the most relevant literature about DPP-based π-conjugated polymers [25], [26]. In particular, the only **DPP-DTS** reported polymer [27], where the **DPP** units bear a 2-ethylhexyl alkyl chain, has been integrated in normal geometry devices in blend with **PC$_{71}$BM** in 1:2 (w/w) ratio (J_{SC} 7.5 mA/cm^2; V_{OC} 0.55 V; *FF* 50.8 %; *PCE* 2.10%).

The active layer was coated from a solution of o-xylene, with a polymer concentration of 10 mg/ml. This solvent was chosen according to the general industrial protocol adopted at Belectric OPV GmbH, with the aim to optimize the device under conditions that would have been already compatible and transferable to industrial production. For this same reason, all layers in the device (Figure 4.1) were processed by doctor blading, except for the silver electrode deposed by evaporation.
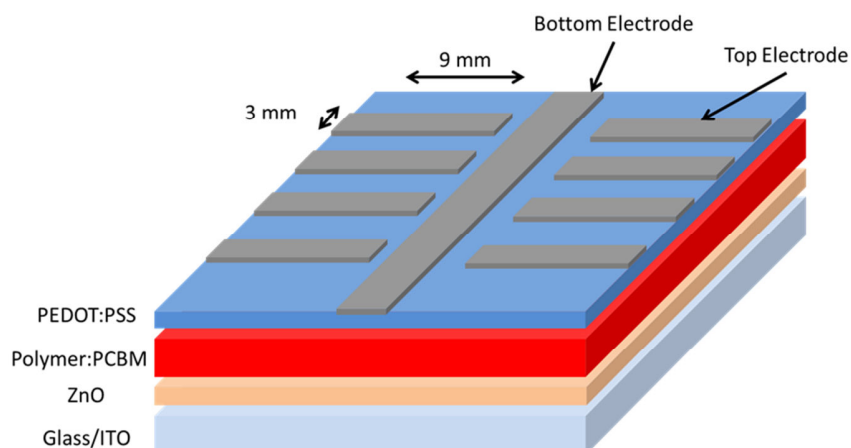
Figure 4.1 Schematic structure of inverted devices fabricated at Belectric OPV GmbH.

4.3 Optimization of Active Layer Coating Temperature

The drying kinetics on the resultant **P3HT:PC$_{61}$BM** blend has a profound influence on the final device characteristics [24], where it was found that slowly dried films had better performance characteristics (higher external quantum efficiency, higher power conversion efficiency, higher fill factor, and lower series resistance) than rapidly dried films. The charge carrier mobility of holes and electrons in **P3HT:PC$_{61}$BM** thick films was shown to have more balanced transport properties and non-dispersive dynamics for the slowly dried films, whereas the rapidly dried films displayed dispersive dynamics and unbalanced transport.

All these differences in performance were explained by the rate of solvent evaporation. As fast solvent loss quenches the phase separation process, and conversely the longer the blend is mobile and contains solvent the more the mixture will proceed to a more phase separated state. Campoy-Quiles *et al.* [28] have studied the morphology changes induced by slow drying and vapour annealing and showed that the PC$_{61}$BM concentration profile changes as the spin-coating speed (and hence the rate of drying) is reduced. Slow drying has a qualitatively similar effect to thermal annealing, whereby the composition gradient becomes more pronounced and the surface-segregated **PC$_{61}$BM** concentration increases.

Schmidt-Hansberg *et al* [29]–[32] used a laboratory scale roll-to-roll compatible knife coating setup and *in-situ grazing incident x-ray diffraction (GIXRD)* to monitor polymer and fullerene crystallization during drying of doctor bladed films. They concluded that the morphology of

P3HT:PC$_{61}$BM blends is improved by low isothermal drying temperature, and slow drying rates, supported by high boiling point solvents. Even if a slow drying rate and low temperature can be beneficial to film morphology, they also provide time for de-wetting processes or the amplification of film instabilities. Thus, films that were coated under meta-stable conditions may become instable during drying since surface tension and surface energy change with time and film composition.

4.3.1 PSBDPP_C10C6:PC$_{61}$BM Based Devices

In order to study the influence of solvent evaporation rate on device performance, active layers were deposited at different temperatures by varying the temperature of the blade coater base and blade. The evaporation rate of a wet film is directly proportional to the vapour pressure of the solvent(s), which in turn is related to the temperature. So, the higher the temperature of the substrate, the faster the drying of the film.

Figure 4.2 and Table 4.1 summarize the results obtained for solar cells from *o-xylene* solution (10 mg/mL of **PSBDPP_*C10C6***) which had different coating temperatures for their active layers. J_{SC}, V_{OC}, *FF* and *PCE* were increased significantly when the coating temperature for active layer was elevated to around 80 °C, with a further improvement when coated at 100 °C.
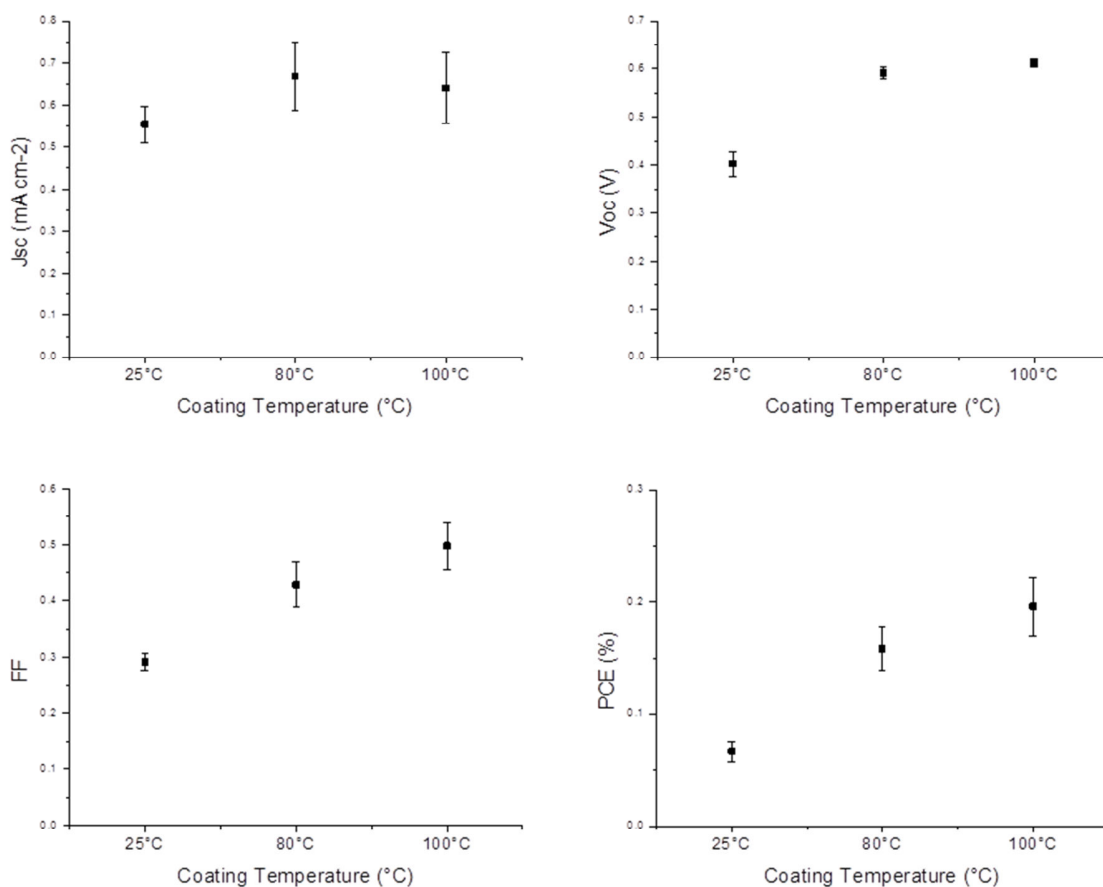
Figure 4.2 Dependence of photovoltaic characteristics of inverted devices with PSBDPP_C10C6:PC$_{61}$BM 1:2 (w/w) on active layer coating temperature.

Table 4.1 Photovoltaic characteristics of devices fabricated from o-Xylene solution at different coating temperature.

Coating Temperature (°C)	Jsc (mA/cm")	Voc (V)	FF	PCE (%)
25	0.55±0.04	0.40±0.03	0.29±0.01	0.07±0.01
80	0.67±0.08	0.59±0.01	0.43±0.04	0.16±0.02
100	0.64±0.08	0.61±0.01	0.50±0.04	0.20±0.03

Figure 4.3 shows representative *J-V* curves of devices that had different coating temperatures for *AL* deposition. The shape of *J-V* curve changed from a rather straight line to a typical diode curve when the coating temperature for the *AL* was elevated from room temperature to 80 and 100 °C. The low R_{SH} visible for the black curve could account for the reduced *FF* observed.
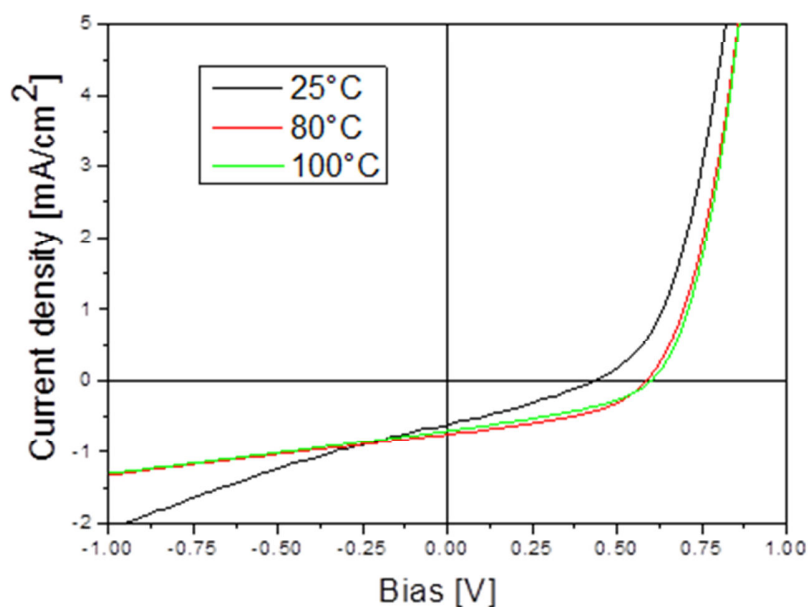
Figure 4.3 Representative J-V curves of devices prepared at different *AL* coating temperatures.

4.3.2 PSBDPP_C12:PC$_{61}$BM Based Devices

Figure 4.4 and Table 4.2 summarize the results obtained from solar cells which had their *AL* coated from *o*-xylene solution (10 mg/mL of ***PSBDPP_C12***) at different temperatures. Conversely to what observed for devices integrating ***PSBDPP*_C10C6**, *J$_{SC}$*, *FF* and *PCE* dramatically drop when the coating temperature is raised to 65 °C and it was furtherly reduced at 90 °C, while *V$_{OC}$* is not affected by the coating temperature as was observed in the previous case. This different behavior could be associated with a different evolution of the morphology related to the variation of drying kinetics.
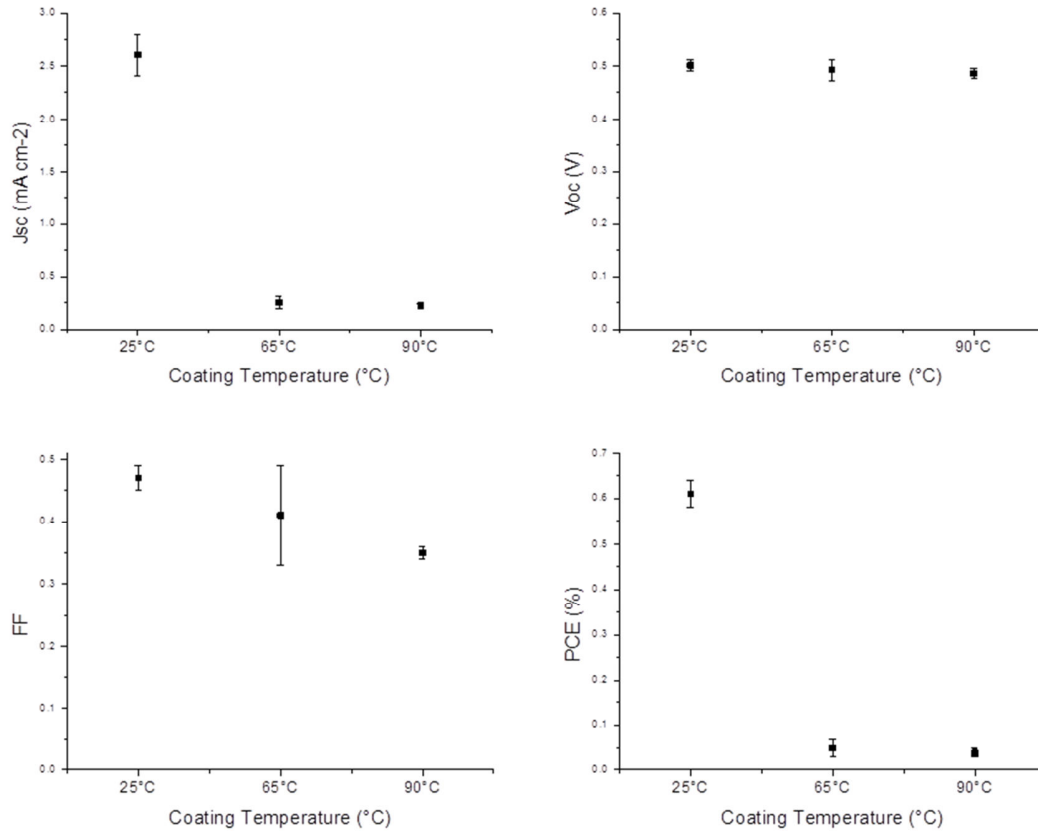
Figure 4.4 Dependence of photovoltaic characteristics of inverted devices with PSBDPP_C12:PC$_{61}$BM 1:2 (w/w) on active layer coating temperature.

Table 4.2 Photovoltaic characteristics of devices fabricated from o-Xylene solution at different coating temperature.

Coating temperature (°C)	Jsc (mA/cm2)	Voc (V)	FF	PCE (%)
25	2.6±0.2	0.50±0.01	0.47±0.02	0.61±0.03
65	0.25±0.06	0.49±0.02	0.41±0.08	0.05±0.02
90	0.22±0.02	0.49±0.01	0.35±0.01	0.04±0.01

Figure 4.5 shows representative J-V characteristics of devices that had different coating temperatures for their AL. The shape of J-V curve in all cases is a typical diode curve, even if for higher coating temperature R$_S$ is higher and affects the *FF*.
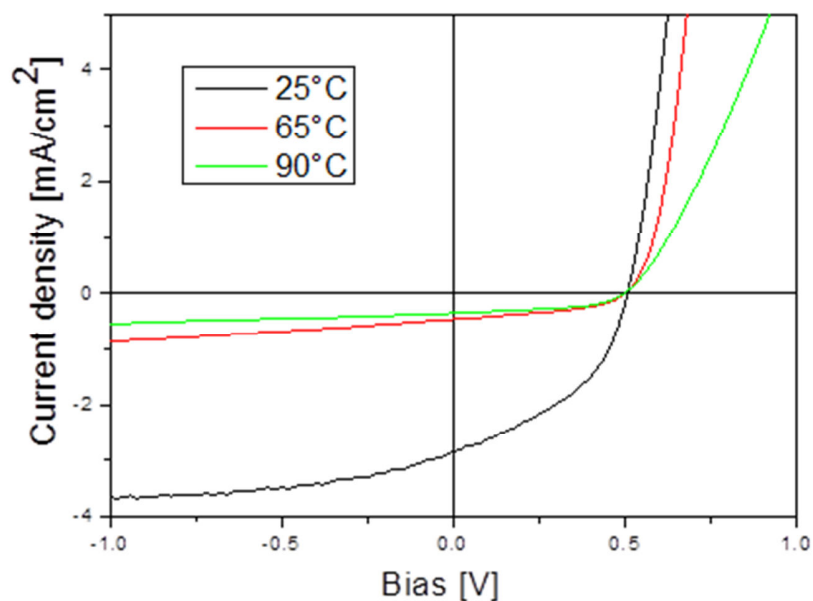
Figure 4.5 Representative J-V curves of devices prepared at different coating temperature.

4.4   Effect of Additives on PSBDPP_C10C6:PC$_{61}$BM Based Devices

In many cases, a large scaled phase separation was observed when polymer:**PC$_{61}$BM** blends are deposited from a single solvent. Solvent mixtures are used in order to change the crystallization behavior of π-conjugated polymer and homogenize the distribution of PC$_{61}$BM in the thin films. Two conditions must be fulfilled to use a solvent as an additive: (i) higher boiling point than the primary solvent; (ii) being a poor solvent for polymer and a good solvent for **PC$_{61}$BM**. Recently, the effect of additives on *AL* morphology has been reviewed [33]–[35]. Even if general guidelines have been proposed, no general rule has been found yet and the morphology optimization by additive is still a challenging trial and error process. The most common additives are 1,8-diiodoctane, 1,8-octanedithiol, triethylene-glycol, 1,8-dibromooctane, 1-chloronaphthalene, 1-methylnaphthalene, nitrobenzene, 4-bromoanisole and polydimethylsiloxane.

An effective solvent system for DPP based polymers has proven to be chloroform/o-dichlorobenzene [36]. In fact, some **DPP** based polymers have been found to be well soluble in chloroform but not in o-dichlorobenzene. The commonly used 1,8-diiodooctane (**DIO**) additive was also found to be effective [27].

Aiming to improve the nanoscale morphology of devices based on **PSBDPP_C10C6** devices, two industrially friendly additives have been tested in combination with *o*-xylene: 1,8-diiodoctane (**DIO**) and 1-methylnaphthalene (**MeNapht**). The photovoltaic characteristics of devices fabricated from an *o*-xylene/5% additive (V/V) are reported in Figure 4.6 and Table 4.3.

In this case, none of the two additives improved the overall device performance. In particular, the photocurrent is strongly reduced compared to pure o-xylene and for **MeNapht** the V_{OC} is also significantly reduced.
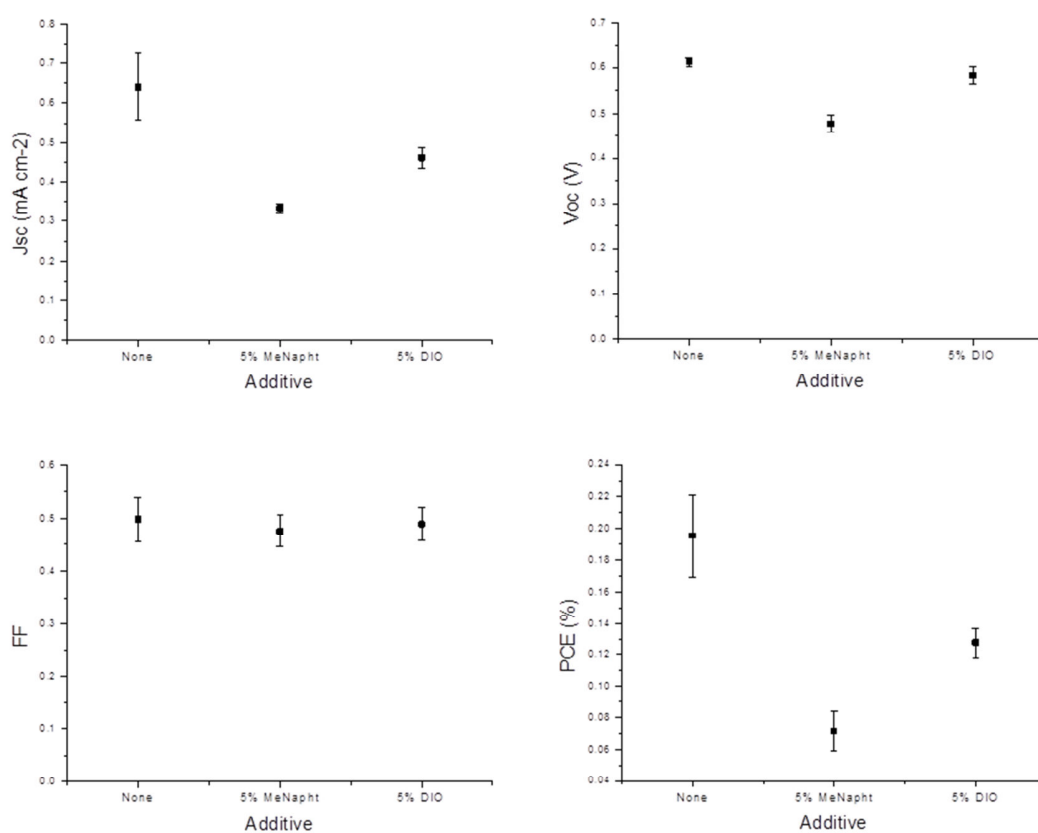
Figure 4.6 Dependence of Photovoltaic characteristics on additives used for the Active Layer coating.

Table 4.3 Photovoltaic characteristics of devices fabricated from *o*-xylene solution with different additives (% V/V).

Solvent	Additive	Jsc (mA/cm")	Voc (V)	FF	PCE (%)
o-xylene	None	0.64±0.08	0.61±0.01	0.50±0.04	0.19±0.03
	5% Me-Napht	0.33±0.01	0.48±0.02	0.48±0.03	0.07±0.01
	5% DIO	0.46±0.03	0.58±0.02	0.49±0.03	0.13±0.01

Figure 4.7 shows the *J-V* curves of representative devices for *AL* deposited from *o*-xylene solution with and without additives. The only positive effect of the additive is to induce a higher R_{SH} compared to pure *o*-xylene.
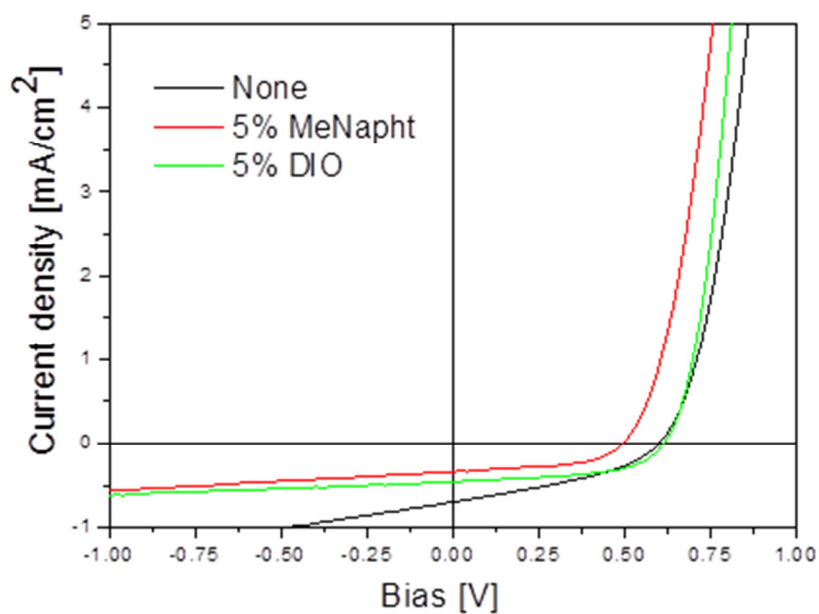
Figure 4.7 Representative J-V curves of devices with active layer deposed from o-xylene solution and from 5% (v/v) of methylnaphthalene/diiodooctane in o-xylene solution.

4.5   Spin-Coated Devices Under Inert Atmosphere

Due to the sensitivity of organic active layer materials to air and water, device fabrication process was completely performed in a glovebox filled with nitrogen. Moreover, in order to minimise the effects of drying rate and temperature on the active layer morphology and device performance, a spin coater rather than a doctor blade was used as it has fewer parameters to control. Thickness was controlled using variable spin speeds. Due to the aim to minimize oxygen exposure absorption spectra were not taken and therefore a relative thickness calculated from spin speed is used to express the thickness variation.

This experiment was conducted at the *Institute of Materials for Electronics and Energy Technology (i-MEET)* of the *Friederich-Alexander University of Erlangen-Nuremeberg*, directed by Prof. Christoph J. Brabec, in collaboration with Dr. Michael Salvador, Dr. Hans-Joachim Egelhaaf and Dr.

Simon A. Dowland. The inverted devices were fabricated with the architecture presented in Figure 4.8.
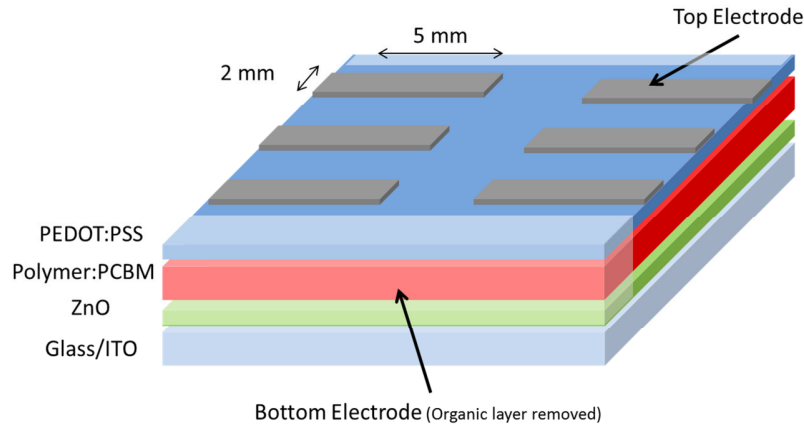
Figure 4.8 Schematic representation of the devices fabricated at i-MEET Laboratory.

The fundamental physical and chemical processes governing the spin-coating process and the methodologies for the preparation of spin-coated polymer thin films have been the object of review [37]. It has been shown that the approximate thickness of a spin coated layer can be expressed by equation (4.1):

$$h = k_1 \omega^\alpha \qquad\qquad (4.1)$$

where k_1 and α are empirically determined constants and ω is the angular velocity. The constants, k_1 and α, are dependent on various parameters, including physical properties of the polymer, the solvent, and the substrate, polymer/solvent interactions and solution/substrate interactions, and thus also rheological properties. Some models further develop k_1 taking into account some of these parameters, focusing on different aspects. By arbitrarily setting ω_0, it is possible to obtain the corresponding h_0 and use it to express the relative thickness of films prepared at different ω_i as multiples of h_0. α is close to -0.5 for most polymer/solvent systems and for the raw analysis done, this value was utilized. The obtained values are shown in Table 4.4.

Table 4.4 Spin-speed coating and relative thickness of devices prepared at i-MEET laboratory.

ω_0 (rpm)	ω_0 (rad/s)	Relative thickness	
500	52.4	*0.14 k_1*	*h_0*
1000	104.7	*0.10 k_1*	*0.7 h_0*
2000	209.4	*0.07 k_1*	*0.5 h_0*
4000	418.9	*0.05 k_1*	*0.4 h_0*
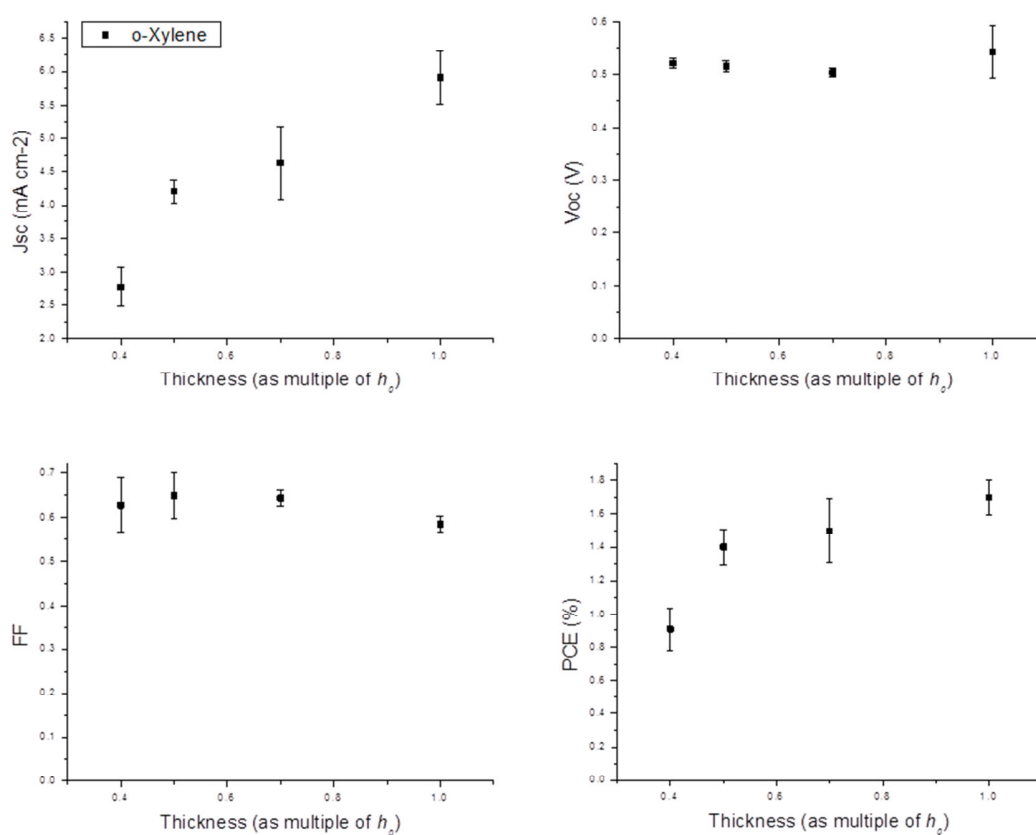
Figure 4.9 Dependence of photovoltaic characteristics of inverted devices with PSBDPP_C12:PC$_{61}$BM 1:2 (w/w) on active layer thickness. The thickness is expressed as relative value, according to the different spin speed used during fabrication.

Table 4.5 Photovoltaic characteristics of devices fabricated from o-Xylene solution.

Thickness	Jsc (mA/cm")	Voc (V)	FF	PCE (%)
h_0	5.9±0.4	0.54±0.05	0.58±0.02	1.7±0.1
0.7 h_0	4.6±0.6	0.50±0.01	0.64±0.02	1.5±0.2
0.5 h_0	4.2±0.2	0.51±0.01	0.65±0.05	1.4±0.1
0.4 h_0	2.8±0.3	0.52±0.01	0.63±0.06	0.9±0.1

Figure 4.10 shows the J-V curves of representative devices for each different AL thickness. As expected, the generated photocurrent rises with the thickness, while the V_{OC} and the *FF* are not affected.
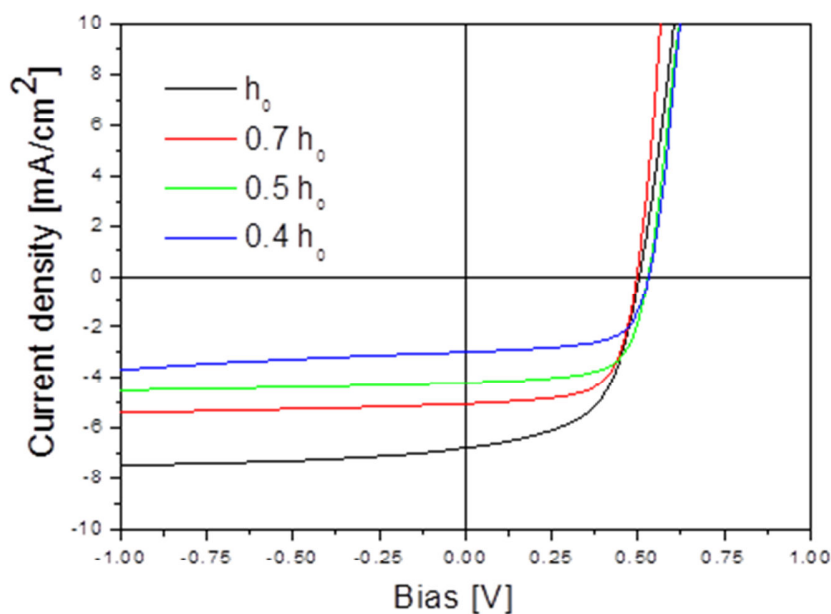
Figure 4.10 J-V curves of best devices depending on active layer thickness.

As compared to the fabrication procedure in air, many reasons account for the higher performance of the devices prepared in an N_2 atmosphere. However it is hard to draw a conclusion since two different deposition techniques were used that can affect the morphology as well as the phase separation. Also materials from different producers have been used for the HTL and ETL layers and the device area was about one third of the previous one fabricated at Belectric OPV GmbH.

4.5.1.1 Comparison with Chlorobenzene as Solvent System

On the basis of the encouraging results obtained for the devices prepared from xylene in the glovebox, another commonly used solvent for device fabrication has been tested. Devices whose AL was processed from chlorobenzene solution (10 mg/ml of **PSBDPP_C12**) show slightly worse performance compared to the corresponding o-xylene devices (Figure 4.11). The same trend in thickness dependence of the device properties is observed.
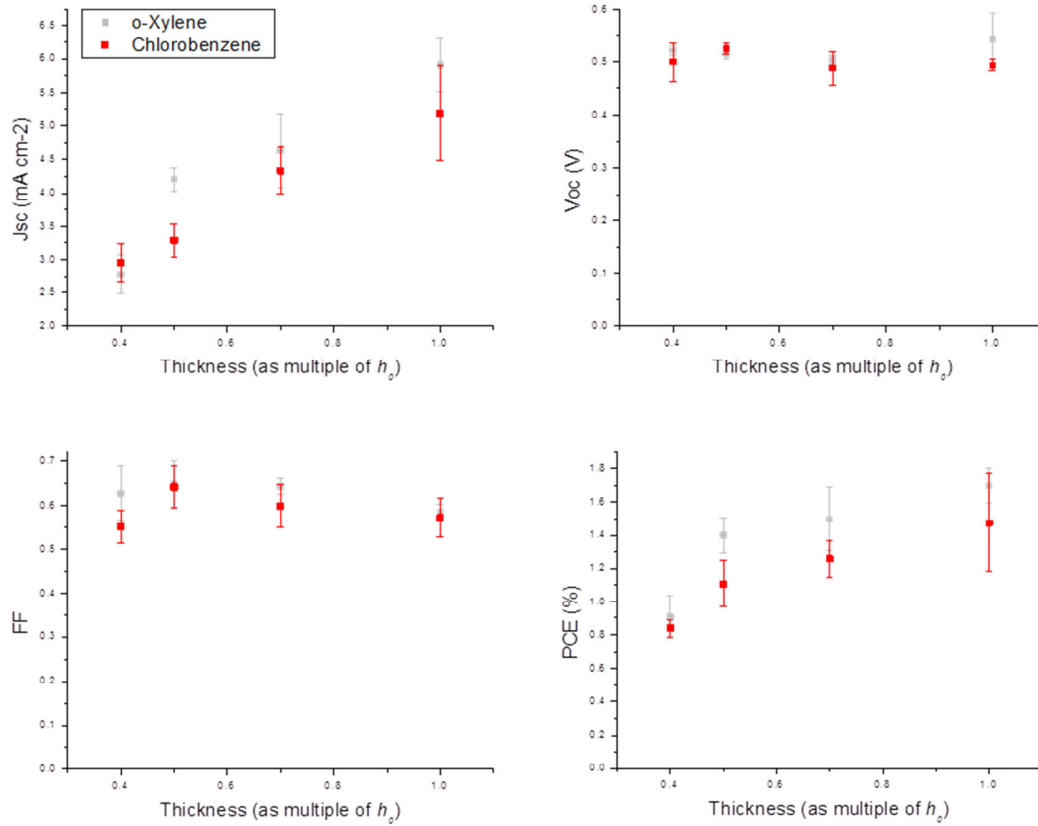
Figure 4.11 Dependence of photovoltaic characteristics of inverted devices with PSBDPP_C12:PC$_{61}$BM 1:2 (w/w) on active layer thickness. The thickness is expressed as relative value, according to the different spin speed used during fabrication.

Table 4.6 Photovoltaic characteristics of devices fabricated from chlorobenzene solution.

Thickness	Jsc (mA/cm")	Voc (V)	FF	PCE (%)
h_0	5.2±0.7	0.49±0.01	0.57±0.05	1.5±0.3
$0.7\,h_0$	4.3±0.3	0.49±0.03	0.60±0.05	1.3±0.1
$0.5\,h_0$	3.3±0.2	0.52±0.01	0.64±0.05	1.1±0.1
$0.4\,h_0$	2.9±0.3	0.50±0.04	0.55±0.04	0.7±0.2

Figure 4.12 shows the *J-V* curves of representative devices with *AL* of different thickness. All the curves show a diode-like behavior, with the thinnest which shows a lower R_{SH} compared to the others, visible from the reduced *FF* and the slope of the curves for negative bias.
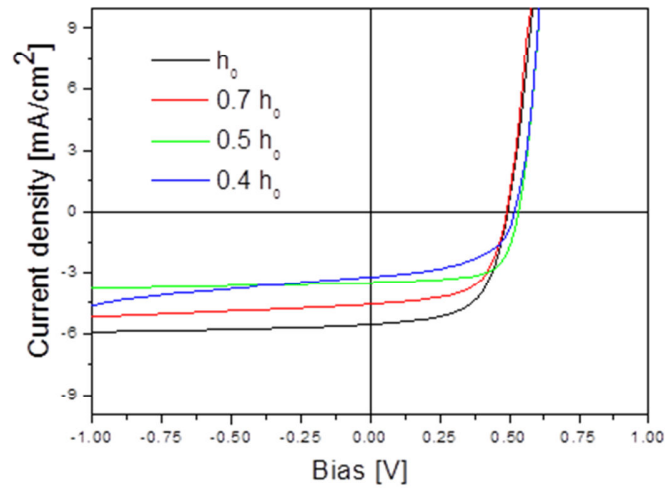
Figure 4.12 J-V curves of best devices depending on active layer thickness from chlorobenzene solution.

4.6 Which is the limiting factor?

As described in the introductive chapter, the efficiency of an OPV device can be expressed as a function of V_{OC}, J_{SC} and *FF*. The FF does not appear to be the limiting factor, since it ranges between 50 and 60% for most of the devices. When the values are lower, either high R_{SH} or low R_S are generally associated with the J-V curves.

From the energy levels of the polymers (Figure 4.13), it is possible to predict an approximated value for V_{OC} (equation (4.2)) [38]:

$$V_{OC} = \frac{1}{e}\left(|E_{HOMO}^{Donor}| - |E_{LUMO}^{PC_{61}BM}|\right) - 0.3\,V \qquad (4.2)$$

where e is the elementary electron charge (1.6 10^{-19} C), E_{HOMO}^{Donor} is the HOMO of the donor polymer (eV), $E_{LUMO}^{PC_{61}BM}$ is the LUMO of the PC$_{61}$BM (acceptor) and 0.3 V is an empirically determined factor. The observed V_{OC} (0.5-0.6 V) is lower compared to the theoretical value (0.8 V) calculated from equation (4.2), but the difference is too small to justify the reduced performance.

Inverted geometry layer stack
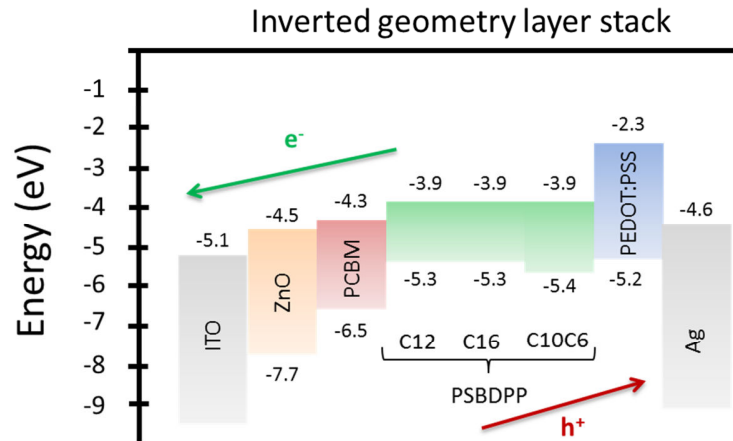
Figure 4.13 Energy levels of materials in the layer stack. For the PSBDPP series the levels have been determined by CV, while for the other materials the values are taken from literature.

On the other hand, the photocurrent observed in the *J-V* curves is much lower than the maximal theoretical value calculated from the superposition of the solar photon flux and the AL blend absorption as described in the introduction (Figure 4.14). Using the absorption spectra is a raw approximation, since not all the absorbed photons are converted into electrons and in order to obtain a more precise calculation the *External Quantum Efficiency (EQE)* should be considered instead. The *EQE* is a device measurement, which describes how much of the incident photons are converted to current accounting for factors such as morphology, layer thickness, carrier mobility, carrier lifetime, and reflection losses ignored when using *A (%)*.
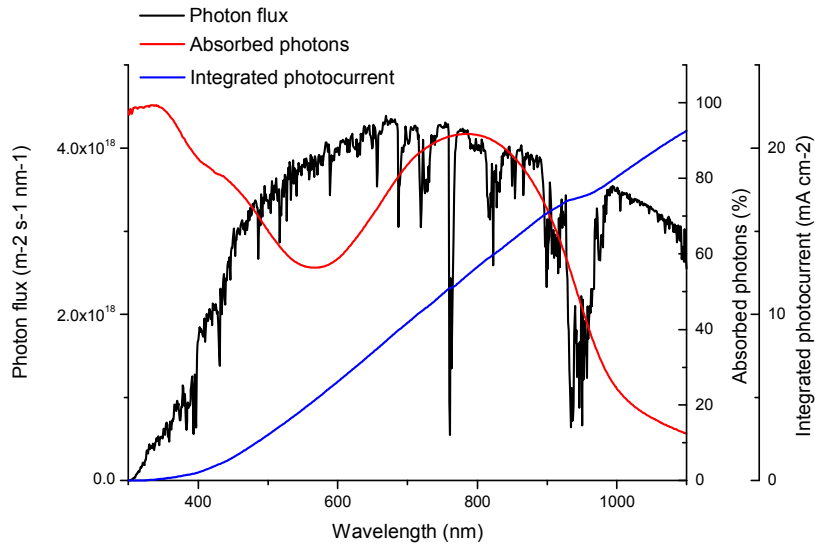
Figure 4.14 Photon flux (black line, left axis), PSBDPP_C12:PC$_{61}$BM 1:2 absorption (%) (red line, right axis) and maximum photocurrent (blue line, right axis) that can be achieved. The photocurrent was corrected with respect to the blend absorption, which is a fraction of the photon flux.

EQE was then measured for all different devices and one of the best devices fabricated at *i-MEET* is reported in Figure 4.15 (red line, right axis) together with the absorption (%) of a corresponding **PSBDPP_*C12*:PC$_{61}$BM** 1:2 (m/m) film (black line, left axis). Similar figures for all devices presented are reported in Annexe 2.
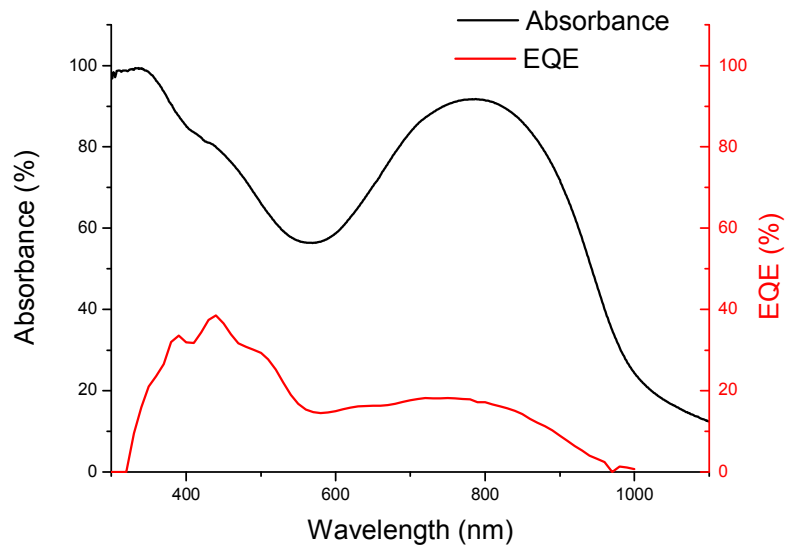
Figure 4.15 Absorbance (%) of PSBDPP_C12:PC$_{61}$BM 1:2 (black, left axis) and corresponding External Quantum Efficiency (EQE) (red line, right axis).

Figure 4.15 shows that the photocurrent is well below the absorption for all wavelengths. In particular, where the donor has its maximum absorption the produced photocurrent is even lower.

In order to understand the reason behind this low photocurrent, three factors were investigated: (i) hole mobility of **PSBDPP_C12** was measured in Organic Field-Effect Transitor (OFET) in bottom-gate bottom-contact (BG-BC) configuration; (ii) blend morphology was mapped by AFM; (iii) charge carrier recombination was studied by *Transient Absorption Spectroscopy (*TAS*)*. The results obtained are discussed in the following sub-sections.

4.6.1 Hole mobility

In order to establish the contribution of hole mobility to the low photocurrent observed, the field effect mobility of neat **PSBDPP_C12** was measured.
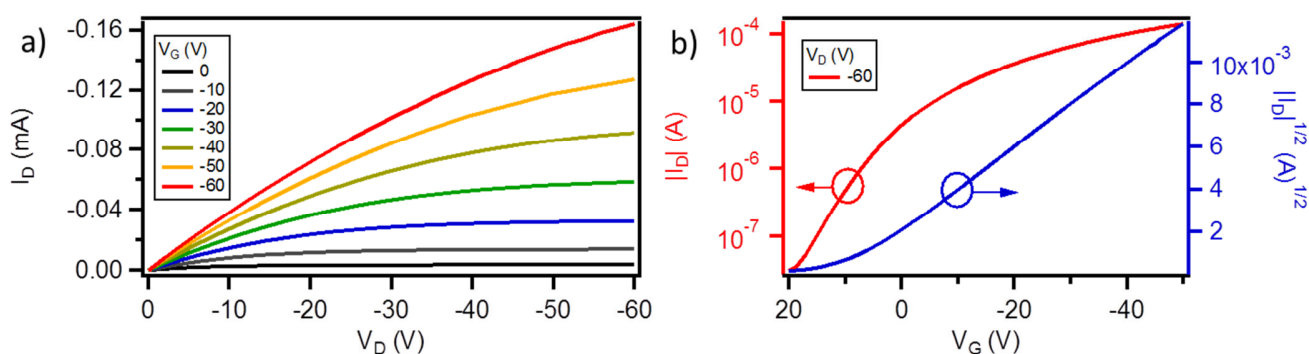
Figure 4.16 Output (a) and transfer (b) characteristics of a 20 µm channel length bottom-gate bottom contact organic field-effect transistor based on PSBDPP-C12. In (b), left axis is in the logarithmic scale.

Output characteristics of a 20 µm channel length device are depicted in Figure 4.16-a which shows typical *p*-type behavior, while *n*-type behavior was not observed. Transfer characteristics also show a typical *p*-type behavior (Figure 4.16-b). The extracted mobility (from the saturation regime at V_D=-60 V), threshold voltage (V_{th}) and I_{on}/I_{off} were 10^{-2} $cm^2 \cdot V^{-1} \cdot s^{-1}$, 10.39 *V* and 4.5 x 10^3 respectively. For the average mobility, V_{th} and I_{on}/I_{off} the values were (9.5±0.9) 10^{-3} $cm^2 \cdot V^{-1} \cdot s^{-1}$, 8.09±2.4 *V* and (3.75±2.18) 10^3 respectively.

These values are similar to the ones reported for other LBGs such as **PSBTBT** (μ_h = 10^{-2} $cm^2 \cdot V^{-1} \cdot s^{-1}$) [39], **PCPDTBT** ($\mu_h$ = 10^{-3} cm^2 V^{-1} s^{-1}) [40], **PCPDTDPP2T** (μ_h = 0.5-2.1 10^{-3} $cm^2 \cdot V^{-1} \cdot s^{-1}$, for different alkyl chains) [41] and many others reported in reference [42]. For **PSBTBT** and **PCPDTBT** a hole mobility in polymer:**PC$_{71}$BM** of, respectively, 10^{-3} and 3 10^{-4} $cm^2 \cdot V^{-1} \cdot s^{-1}$ was reported [39], and it has

been demonstrated to be similar in the case of polymer:**PC$_{61}$BM** [40]. So, the hole mobility does not appear here to be the limiting factor of the device performances.

4.6.2 Morphology of the blends

To investigate the morphology and phase separation of **PSBDPP:PC$_{61}$BM** blends, clean glass slides were coated by doctor blading at 25 °C under the same condition as for the devices. The surface topography was investigated by AFM. The corresponding AFM micrographs are shown in Figure 4.17.
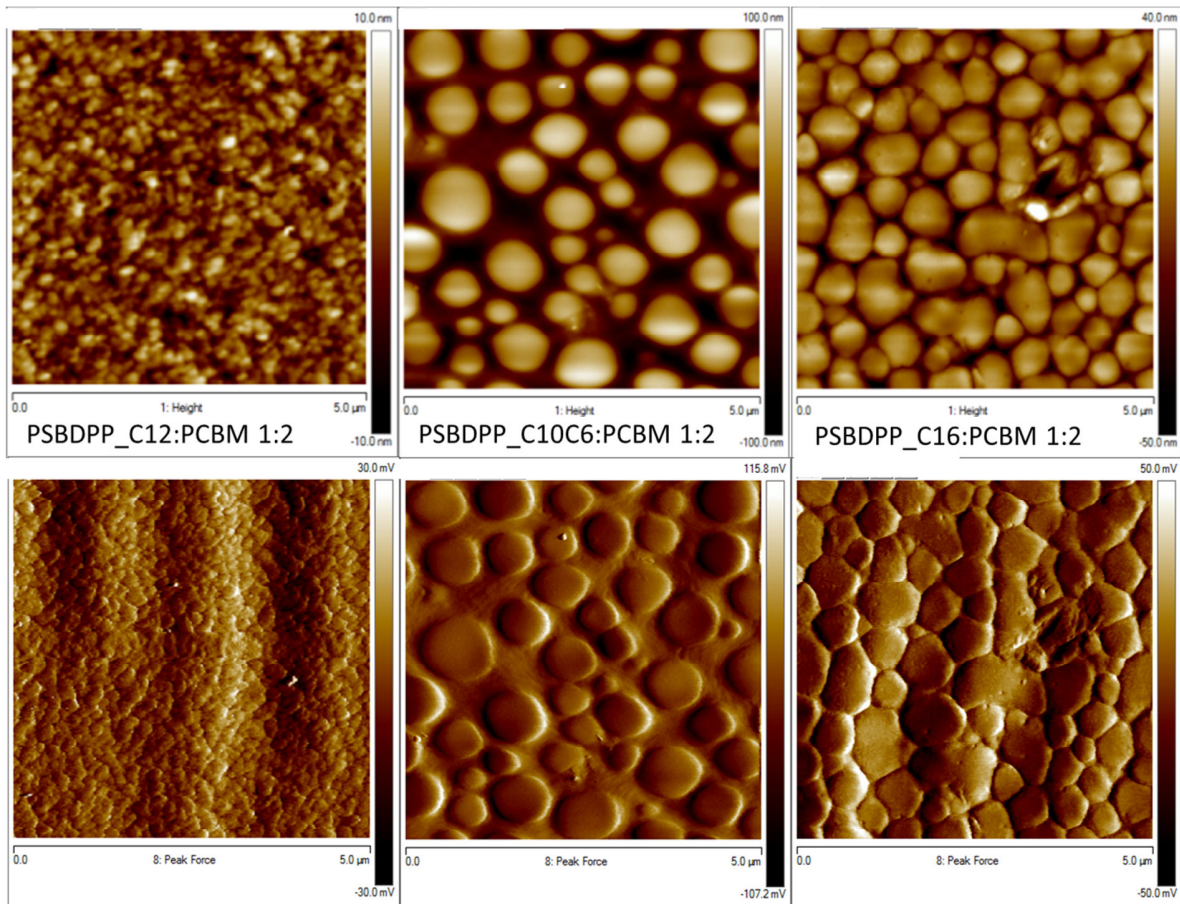
Figure 4.17 Peak-force height (top) and Peak Force (bottom) micrographs (5.0x5.0 ᐧm, z scale reported for each image) of PSBDPP:PC$_{61}$BM (1:2) blends: PSBDPP_C12:PC$_{61}$BM (left), PSBDPP_C10C6:PC$_{61}$BM (center) and PSBDPP_C16:PC$_{61}$BM (right).

The phase separation varies significantly for the different **PSBDPP:PC$_{61}$BM** blends. **PSBDPP_C12:PC$_{61}$BM** blend showed a more flat and homogeneous surface with respect to **PSBDPP_C10C6** and **PSBDPP_C16:PC$_{61}$BM**, where the phase segregation is stronger and results in large features up to 0.3-0.5 μm in diameter.

This difference in morphology can be related to the different performance in devices of **PSBDPP_C12** and **PSBDPP_C10C6**. The higher smoothness and homogeneity of the first one, suggest a

more intimate mixing that can be correlated with the increased J_{SC}. On the other hand, the latter exhibits large features of a few hundreds of nanometers in diameter and a height difference close to 200 nm, which renders the film (not supposed to be much thicker) very rough and inhomogeneous. Similar cases were reported in the literature [21]. One of the most relevant cases was reported by Zoombelt *et al*. [41]. They synthetized DPP-cyclopentadithiophene and DPP-fluorene LBGs with different alkyl side chains, finding a good field-effect mobility for all of them, but very variable device performance. A study of the morphology and phase separation revealed how the poor device performances were related to inhomogeneity of the films. Another important observation, by systematically varying coating parameters and solvent system, they were able to modify the morphology.

The active layer phase segregation appears to be an important limiting factor.

4.6.3 Charge Carrier Recombination

In order to investigate the charge carrier behavior, *femtosecond transient absorption spectroscopy (TAS)* was employed. This technique was chosen since it gives access to important device parameters such as yield of immediate charge carrier formation (from interfacial charge transfer states), yield of delayed charge carrier formation (due to exciton diffusion to interface), picosecond recombination losses, etc. It is also a useful tool to understand their mechanism (CT states, triplet states, etc.). These experiments were performed by Shafakath Karutedath (ESR4) at IMDEA Nanociencia.

Figure 4.18 shows the picosecond *TA* spectra obtained after 400 ps of a pump and probe interaction [excitation wavelength 387 nm (red) and 775 nm (black)]. This timescale was chosen since it ensures that all the singlet excitons are quenched and the remaining states are long lived [43]. The band at 0.9 eV has been assigned to singlet states, since it comes first and it is also present in the polymer films only; the band at 1.05 eV has been assigned to pure polarons while the one at 1.24 eV contain triplets, polarons and singlets together.
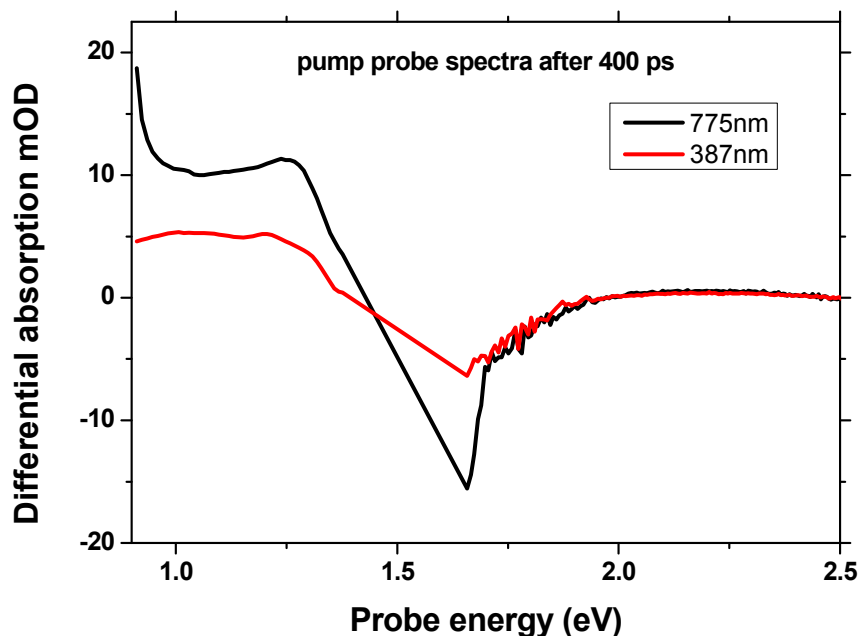
Figure 4.18 Picosecond pump probe spectra after 400 ps at different excitation wavelengths. Black curve represents the spectra for an excitation at 775 nm and the red curve for one at 387 nm. (Data produced by S. Karutedath).

Figure 4.19 shows the TA spectra of a **PSBDPP_C12:PC$_{61}$BM** film, excited at 387 nm (left) and 775 nm (right). Excitation at a wavelength of 775 nm, results in ultrafast triplet production from geminate recombination, while pumping at 387 nm leads to the formation of stable charges, with triplet states which are formed on a much slower time scale.
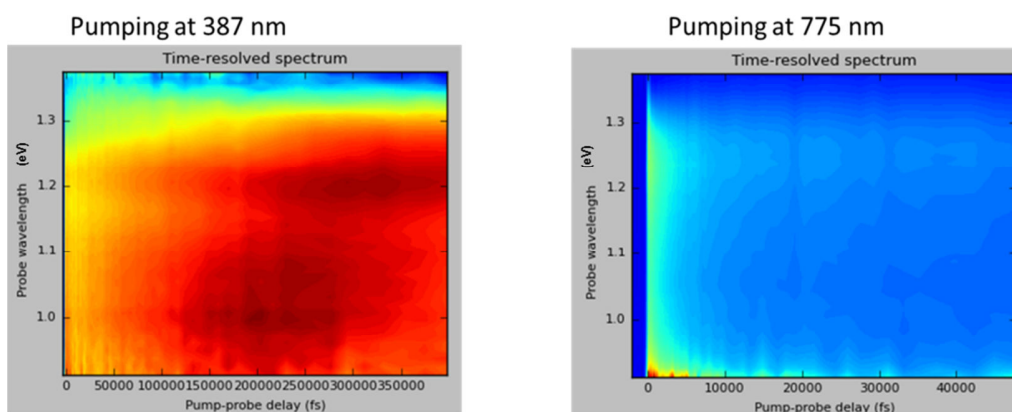
Figure 4.19 Picosecond TA spectra of PSBDPP_C12:PC$_{61}$BM films at 387nm (left) and 775nm excitation (right). (Data produced by S. Karutedath).

Figure 4.20 shows the picosecond *TA* spectra of neat polymer (top) and blend (bottom), excited at 387 nm (left) and at 775 nm (right). In this case, the timescale of the spectra was limited at 3000 ps, to put in evidence the generation phenomena. Upon **PSBDPP_C12:PC$_{61}$BM** blend excitation at 775 nm, there is no sign of geminate recombination, while, upon excitation at 387 nm, singlet, polaron and triplet states are created all at the same time. A tentative possible mechanism from these first results could be that excitons on **PC$_{61}$BM** are converted into polarons on a 100 ps timescale, to furtherly evolve into triplets after 200 ps. Further experiments are planned to gain a better understanding of charge carrier dynamics for all the PSBDPP series.
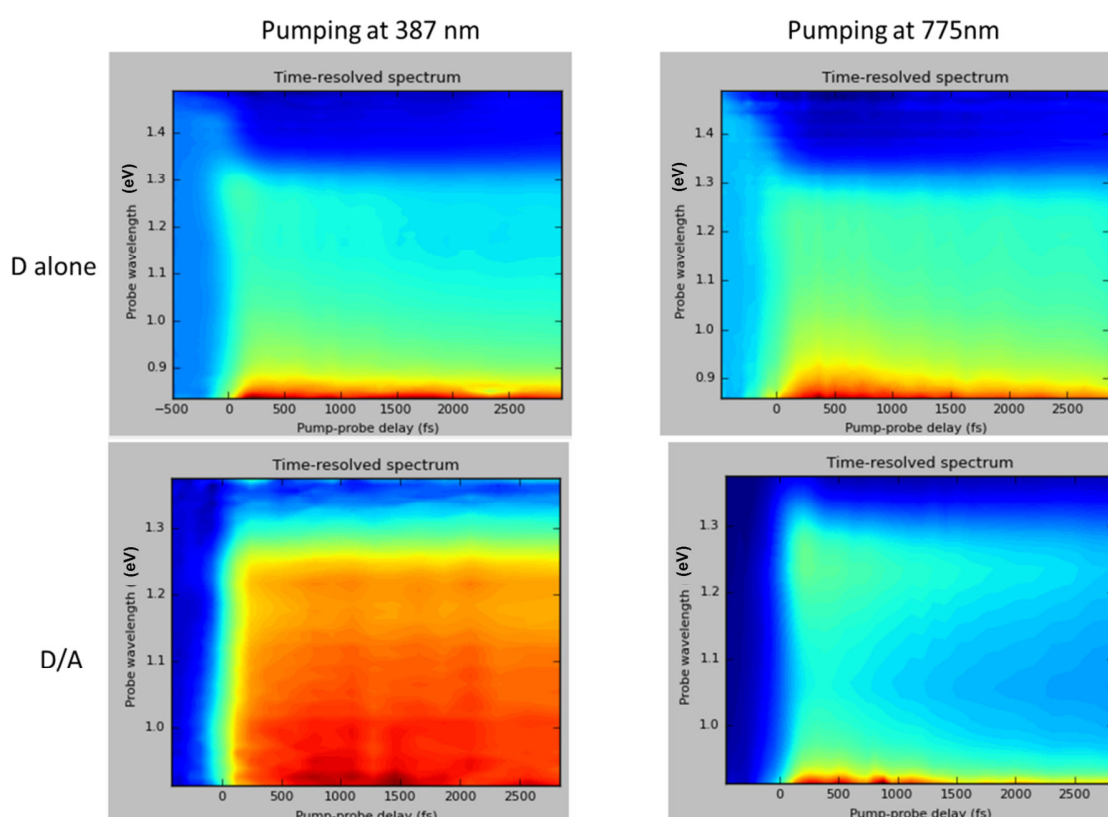
Figure 4.20 Picosecond TAS for neat PSBDPP_C12 (top) and PSBDPP_C12:PC$_{61}$BM blend (bottom), excited at different wavelengths (387 nm, left; 775 nm, right). Spectra are reported up to 3000 fs to put in evidence the generation phenomenon. (Data produced by S. Karutedath).

To confirm the late generation of polarons (in particular from **PC$_{61}$BM**, since the excitation wavelength is 387 nm, where **PC$_{61}$BM** has significant absorption), in Figure 4.21 the time traces at 1000 nm for both 387 nm (black) and 775 nm (red) excitations are reported. Figure 4.21 clearly shows the additional delayed long-lived state generation upon excitation at 387 nm, whereas for 775 nm more than 60% of the initial population disappears within the first few picoseconds, suggesting the

presence of ultrafast recombination channels. These findings could explain the discrepancy within the EQE spectra, which show high photocurrent generation at 400 nm and not at 775 nm, where the polymer absorbs maximum light.
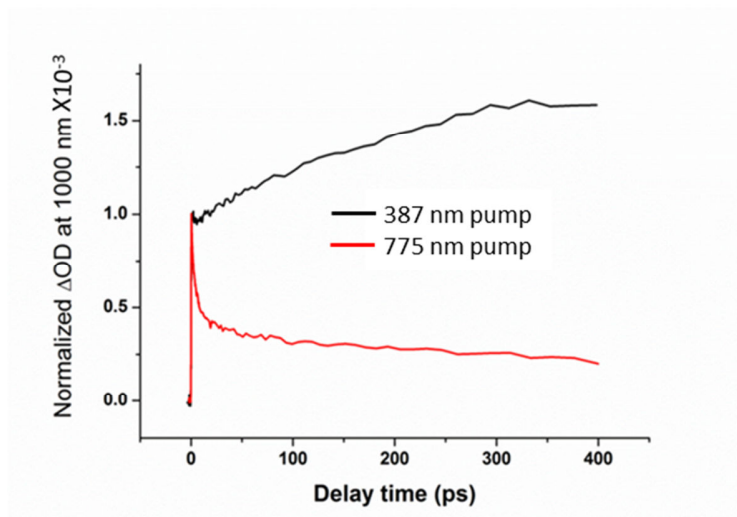
Figure 4.21 Normalized time resolved TA transients at 1000 nm for 387 nm and 775 nm excitation. (Data produced by S. Karutedath).

4.7 Conclusion

Two of the polymers synthetized, **PSBDPP_C12** and **PSBDPP_C10C6**, were used in inverted architecture devices. The devices showed limited performance under different processing conditions. The morphology of the active layer was found to be the major limiting factor. Opposite behavior was observed for both polymers with respect to the coating temperature, which determines the drying kinetics. **PSBDPP_C12** is best performing when coated at room temperature, while with **PSBDPP_C10C6** best performances were achieved for high temperature deposition. Since **PSBDPP_C12** showed largely better characteristics, devices were prepared under inert atmosphere with the active layer deposited by spin-coating. These new conditions led to a further improvement of the photovoltaic characteristics, nonetheless, low photocurrent was still observed. To understand the reason behind it, charge carrier mobility, morphology, phase segregation and charge carrier behavior were investigated. The results showed how, despite favorable energy levels and good charge carrier mobility, unfavorable morphology and charge recombination limit the photocurrent and thus device efficiency.

4.8 References

[1] A. Seemann, H. J. Egelhaaf, C. J. Brabec, and J. a. Hauch, "Influence of oxygen on semi-transparent organic solar cells with gas permeable electrodes," *Org. Electron. physics, Mater. Appl.*, vol. 10, no. 8, pp. 1424–1428, 2009.

[2] C. Y. Nam, D. Su, and C. T. Black, "High-performance air-processed polymer-fullerene bulk heterojunction solar cells," *Adv. Funct. Mater.*, vol. 19, no. 22, pp. 3552–3559, 2009.

[3] F. C. Krebs, "Fabrication and processing of polymer solar cells: A review of printing and coating techniques," *Sol. Energy Mater. Sol. Cells*, vol. 93, no. 4, pp. 394–412, Apr. 2009.

[4] R. Søndergaard, M. Hösel, D. Angmo, T. T. Larsen-Olsen, and F. C. Krebs, "Roll-to-roll fabrication of polymer solar cells," *Mater. Today*, vol. 15, no. 1–2, pp. 36–49, 2012.

[5] F. C. Krebs, S. A. Gevorgyan, and J. Alstrup, "A roll-to-roll process to flexible polymer solar cells: model studies, manufacture and operational stability studies," *J. Mater. Chem.*, vol. 19, no. 30, p. 5442, 2009.

[6] F. C. Krebs, S. A. Gevorgyan, and J. Alstrup, "A roll-to-roll process to flexible polymer solar cells: model studies, manufacture and operational stability studies," *J. Mater. Chem.*, vol. 19, no. 30, pp. 5442–5451, Jul. 2009.

[7] "Prof. Yan's Research Group » Best Research Organic Solar Cell Efficiency." [Online]. Available: http://blog.ust.hk/yanlab/2015/06/09/best-research-cell/. [Accessed: 05-Sep-2015].

[8] W. R. Mateker, I. T. Sachs-Quintana, G. F. Burkhard, R. Cheacharoen, and M. D. McGehee, "Minimal Long-Term Intrinsic Degradation Observed in a Polymer Solar Cell Illuminated in an Oxygen-Free Environment," *Chem. Mater.*, p. 150115155239004, 2015.

[9] L. Lucera, P. Kubis, F. W. Fecher, C. Bronnbauer, M. Turbiez, K. Forberich, T. Ameri, H.-J. Egelhaaf, and C. J. Brabec, "Guidelines for Closing the Efficiency Gap between Hero Solar Cells and Roll-To-Roll Printed Modules," *Energy Technol.*, p. n/a–n/a, 2015.

[10] D. Angmo and F. C. Krebs, "Over 2 Years of Outdoor Operational and Storage Stability of ITO-Free, Fully Roll-to-Roll Fabricated Polymer Solar Cell Modules," *Energy Technol.*, vol. 3, no. 7, p. n/a–n/a, Jun. 2015.

[11] N. Espinosa, R. García-Valverde, A. Urbina, and F. C. Krebs, "A life cycle analysis of polymer solar cell modules prepared using roll-to-roll methods under ambient conditions," *Sol. Energy Mater. Sol. Cells*, vol. 95, pp. 1293–1302, 2011.

[12] M. Bag, T. S. Gehan, L. a Renna, D. D. Algaier, P. M. Lahti, and D. Venkataraman, "Fabrication conditions for e ffi cient organic photovoltaic cells from aqueous dispersions of Nanoparticles," *RSC Adv.*, vol. 4, no. SEPTEMBER, pp. 45325–45331, 2014.

[13] T. R. Andersen, T. T. Larsen-Olsen, B. Andreasen, A. P. L. Böttiger, J. E. Carlé, M. Helgesen, E. Bundgaard, K. Norrman, J. W. Andreasen, M. Jørgensen, and F. C. Krebs, "Aqueous processing of low-band-gap polymer solar cells using roll-to-roll methods," *ACS Nano*, vol. 5, no. 5, pp. 4188–4196, 2011.

[14] I. Burgués-Ceballos, F. Machui, J. Min, T. Ameri, M. M. Voigt, Y. N. Luponosov, S. a. Ponomarenko, P. D. Lacharmoise, M. Campoy-Quiles, and C. J. Brabec, "Solubility based identification of green solvents for small molecule organic solar cells," *Adv. Funct. Mater.*, vol. 24, no. 10, pp. 1449–1457, 2014.

[15] G. Fuchs, M. Boll, and J. Heider, "Microbial degradation of aromatic compounds — from one strategy to four," *Nat. Rev. Microbiol.*, vol. 9, no. 11, pp. 803–816, 2011.

[16] P. Vanlaeke, G. Vanhoyland, T. Aernouts, D. Cheyns, C. Deibel, J. Manca, P. Heremans, and J. Poortmans, "Polythiophene based bulk heterojunction solar cells: Morphology and its implications," *Thin Solid Films*, vol. 511–512, pp. 358–361, 2006.

[17] M. T. Dang, L. Hirsch, and G. Wantz, "P3HT:PCBM, best seller in polymer photovoltaic research," *Adv. Mater.*, vol. 23, no. 31, pp. 3597–3602, 2011.

[18] F. Machui, L. Lucera, G. D. Spyropoulos, J. Cordero, A. S. Ali, P. Kubis, T. Ameri, M. M. Voigt, and C. J. Brabec, "Large area slot-die coated organic solar cells on flexible substrates with non-halogenated solution formulations," *Sol. Energy Mater. Sol. Cells*, vol. 128, pp. 441–446, 2014.

[19] N. Grossiord, J. M. Kroon, R. Andriessen, and P. W. M. Blom, "Degradation mechanisms in organic photovoltaic devices," *Org. Electron.*, vol. 13, no. 3, pp. 432–456, 2012.

[20] D. Chirvase, J. Parisi, J. C. Hummelen, and V. Dyakonov, "Influence of nanomorphology on the photovoltaic action of polymer–fullerene composites," *Nanotechnology*, vol. 15, no. 9, pp. 1317–1323, 2004.

[21] Y. Huang, E. J. Kramer, A. J. Heeger, and G. C. Bazan, "Bulk Heterojunction Solar Cells : Morphology and Performance Relationships," *Chem. Rev.*, vol. 114, pp. 7006–7043, 2014.

[22] S. E. Shaheen, C. J. Brabec, N. S. Sariciftci, F. Padinger, T. Fromherz, and J. C. Hummelen, "2.5% Efficient Organic Plastic Solar Cells," *Appl. Phys. Lett.*, vol. 78, no. 6, pp. 841–843, 2001.

[23] G. Li, V. Shrotriya, Y. Yao, J. Huang, and Y. Yang, "Manipulating regioregular poly(3-hexylthiophene) : [6,6]-phenyl-C61-butyric acid methyl ester blends—route towards high efficiency polymer solar cells," *J. Mater. Chem.*, vol. 17, no. 30, p. 3126, 2007.

[24] G. Li, V. Shrotriya, J. Huang, Y. Yao, T. Moriarty, K. Emery, and Y. Yang, "High-efficiency solution processable polymer photovoltaic cells by self-organization of polymer blends," *Nat. Mater.*, vol. 4, no. 11, pp. 864–868, 2005.

[25] B. Tieke, A. R. Rabindranath, K. Zhang, and Y. Zhu, "Conjugated polymers containing diketopyrrolopyrrole units in the main chain," *Beilstein J. Org. Chem.*, vol. 6, pp. 830–845, 2010.

[26] S. Qu and H. Tian, "Diketopyrrolopyrrole (DPP)-based materials for organic photovoltaics," *Chem. Commun.*, vol. 48, pp. 3039–3051, 2012.

[27] L. Huo, J. Hou, H.-Y. Chen, S. Zhang, Y. Jiang, T. L. Chen, and Y. Yang, "Bandgap and Molecular Level Control of the Low-Bandgap Polymers Based on 3,6-Dithiophen-2-yl-2,5-dihydropyrrolo[3,4- c]pyrrole-1,4-dione toward Highly Efficient Polymer Solar Cells," *Macromolecules*, vol. 42, no. 17, pp. 6564–6571, Sep. 2009.

[28] M. Campoy-Quiles, T. Ferenczi, T. Agostinelli, P. G. Etchegoin, Y. Kim, T. D. Anthopoulos, P. N. Stavrinou, D. D. C. Bradley, and J. Nelson, "Morphology evolution via self-organization and lateral and vertical diffusion in polymer:fullerene solar cell blends.," *Nat. Mater.*, vol. 7, no. 2, pp. 158–164, 2008.

[29] B. Schmidt-Hansberg, M. Sanyal, M. F. G. Klein, M. Pfaff, N. Schnabel, S. Jaiser, A. Vorobiev, E. Müller, A. Colsmann, P. Scharfer, D. Gerthsen, U. Lemmer, E. Barrena, and W. Schabel, "Moving through the phase diagram: Morphology formation in solution cast polymer-fullerene blend films for organic solar cells," *ACS Nano*, vol. 5, no. 11, pp. 8579–8590, 2011.

[30] B. Schmidt-Hansberg, M. F. G. Klein, K. Peters, F. Buss, J. Pfeifer, S. Walheim, a. Colsmann, U. Lemmer, P. Scharfer, and W. Schabel, "In situ monitoring the drying kinetics of knife coated polymer-fullerene films for organic solar cells," *J. Appl. Phys.*, vol. 106, no. 12, pp. 1–8, 2009.

[31] M. Sanyal, B. Schmidt-Hansberg, M. F. G. Klein, C. Munuera, A. Vorobiev, A. Colsmann, P. Scharfer, U. Lemmer, W. Schabel, H. Dosch, and E. Barrena, "Effect of Photovoltaic Polymer/Fullerene Blend Composition Ratio on Microstructure Evolution during Film Solidification Investigated in Real Time by X-ray Diffraction," *Macromolecules*, vol. 44, no. 10, pp. 3795–3800, May 2011.

[32] B. Schmidt-Hansberg, H. Do, a. Colsmann, U. Lemmer, and W. Schabel, "Drying of thin film polymer solar cells," *Eur. Phys. J. Spec. Top.*, vol. 166, no. 1, pp. 49–53, 2009.

[33] F. Liu, Y. Gu, X. Shen, S. Ferdous, H. W. Wang, and T. P. Russell, "Characterization of the morphology of solution-processed bulk heterojunction organic photovoltaics," *Prog. Polym. Sci.*, vol. 38, no. 12, pp. 1990–2052, 2013.

[34] H. C. Liao, C. C. Ho, C. Y. Chang, M. H. Jao, S. B. Darling, and W. F. Su, "Additives for morphology control in high-efficiency organic solar cells," *Mater. Today*, vol. 16, no. 9, pp. 326–336, 2013.

[35] E. Buchaca-Domingo, a. J. Ferguson, F. C. Jamieson, T. McCarthy-Ward, S. Shoaee, J. R. Tumbleston, O. G. Reid, L. Yu, M.-B. Madec, M. Pfannmöller, F. Hermerschmidt, R. R. Schröder, S. E. Watkins, N. Kopidakis, G. Portale, a. Amassian, M. Heeney, H. Ade, G. Rumbles, J. R. Durrant, and N. Stingelin, "Additive-assisted supramolecular manipulation of polymer:fullerene blend phase morphologies and its influence on photophysical processes," *Mater. Horizons*, vol. 1, no. 2, p. 270, 2014.

[36] M. M. Wienk, M. Turbiez, J. Gilot, and R. a. J. Janssen, "Narrow Bandgap DiketoPyrroloPyrrole Polymer Solar Cells: The Effect of Processing on the Performance," *Adv. Mater.*, vol. 20, no. 13, pp. 2556–2560, 2008.

[37] K. Norrman, a. Ghanbari-Siahkali, and N. B. Larsen, "6 Studies of spin-coated polymer films," *Annu. Reports Sect. "C" (Physical Chem.)*, vol. 101, p. 174, 2005.

[38] M. C. Scharber, D. Mühlbacher, M. Koppe, P. Denk, C. Waldauf, A. J. Heeger, and C. J. Brabec, "Design rules for donors in bulk-heterojunction solar cells - Towards 10 % energy-conversion efficiency," *Adv. Mater.*, vol. 18, no. 502783, pp. 789–794, 2006.

[39] M. C. Scharber, M. Koppe, J. Gao, F. Cordella, M. A. Loi, P. Denk, M. Morana, H.-J. Egelhaaf, K. Forberich, G. Dennler, R. Gaudiana, D. Waller, Z. Zhu, X. Shi, and C. J. Brabec, "Influence of the Bridging Atom on the Performance of a Low-Bandgap Bulk Heterojunction Solar Cell," *Adv. Mater.*, vol. 22, no. 3, pp. 367–370, 2010.

[40] M. Morana, M. Wegscheider, A. Bonanni, N. Kopidakis, S. Shaheen, M. Scharber, Z. Zhu, D. Waller, R. Gaudiana, and C. Brabec, "Bipolar charge transport in PCPDTBT-PCBM bulk-heterojunctions for photovoltaic applications," *Adv. Funct. Mater.*, vol. 18, no. 12, pp. 1757–1766, 2008.

[41] A. P. Zoombelt, S. G. J. Mathijssen, M. G. R. Turbiez, M. M. Wienk, and R. a. J. Janssen, "Small band gap polymers based on diketopyrrolopyrrole," *J. Mater. Chem.*, vol. 20, no. 11, p. 2240, 2010.

[42] A. Facchetti, "Semiconductors for organic transistors," *Mater. Today*, vol. 10, no. 3, pp. 28–37, 2007.

[43]   I. a. Howard, R. Mauer, M. Meister, and F. Laquai, "Effect of morphology on ultrafast free carrier generation in polythiophene:fullerene organic solar cells," *J. Am. Chem. Soc.*, vol. 132, no. 42, pp. 14866–14876, 2010.

[44]   J. Zaumseil and H. Sirringhaus, "Electron and ambipolar transport in organic field-effect transistors," *Chem. Rev.*, vol. 107, no. 4, pp. 1296–1323, 2007.

5 Mechanical Integrity of OPV Devices

5.1   Introduction

It has been long known, that inorganic PV thin films exposed to tensile and compressive stress experience increased series resistance, notably due to cracks, as well as to layer delamination [1]. Mechanical integrity of thin-film multilayered structures is generally difficult to maintain as these systems are made of stacks of layers possessing different thicknesses, different chemical, physical and mechanical properties [2]. As a consequence of these different intrinsic material properties and of the manufacturing procedures, residual strains and stresses are present in the layer stack. Under operative conditions, further thermal and mechanical stresses (such as compressive strain or bending), can be developed. The synergistic effect of these different stresses, which vary for each layer, and of defects present in the inorganic layer can lead to a loss of mechanical integrity. The fracture can be due either to cohesive failure modes (cracks) or to adhesive failure modes (buckling and even cracks and delamination), in the case of low interlayer adhesion [3].

Considering the similarity in terms of sample structure and material properties mismatch, OPV modules are extremely likely to undergo the same kind of mechanical integrity loss as PV thin film modules of other technologies. This possibility have been foreseen almost 10 years ago [4], based on observation of OLED device degradation [5]–[11]. Depending on the materials and device architecture (interfaces and diffusive path) considered, several degradation mechanisms can concur to the delamination process. When degradation occurs at the AL/electrode interface, the desired interface properties are diminished resulting in less active area and in a reduction of the charge transfer and extraction. This reduction of AL/electrode interface can be due to both physical loss of contact between the two layers (by delamination [5] or creation of voids [6]) or to chemical reactions at the metal electrode surface, which form electrically insulating patches [7]–[9]. More often is the combination of both chemical and physical factors. Diffused water can react at the AL/electrode weakening the interface, that, for long exposure times or when mechanical stresses are present, which can lead to delamination [10] [11].
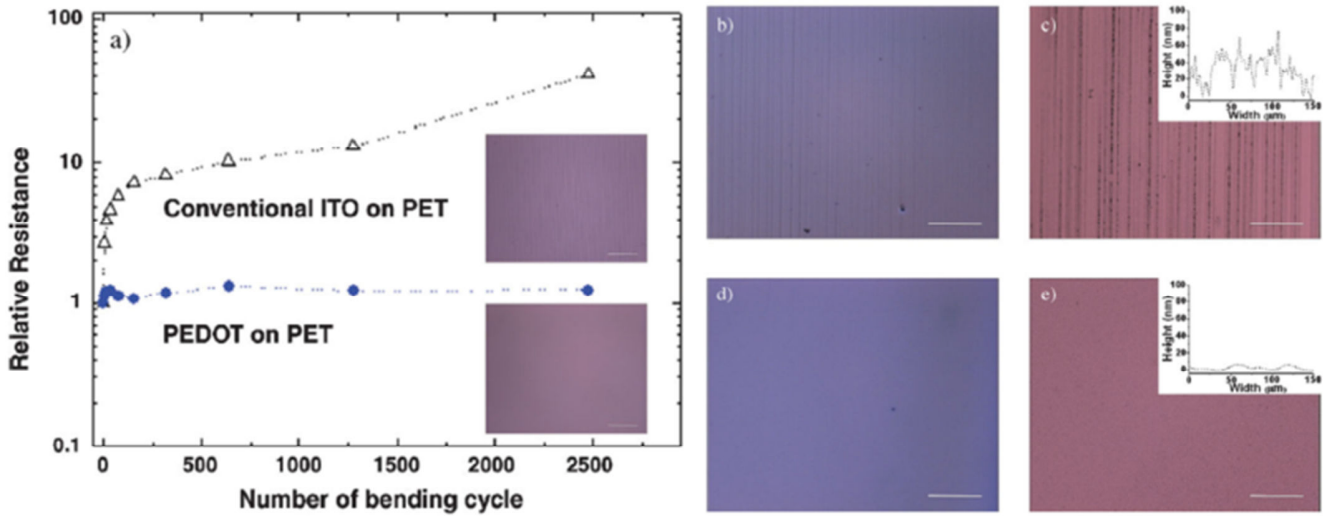
Early examples from the literature focused mainly on organic/inorganic interfaces and their property mismatches [6], [12]. Na *et al.* [12] reported on the different mechanical stabilities of **ITO** and **ITO-free** flexible devices (Figure 5.1), showing how the different nature of the conductive PEDOT:PSS (polymer blend) and of the **ITO** (brittle crystalline material) can enhance the mechanical stability of the device. In a similar way, Lloyd *et al*. [6] studied the effect of a **PEDOT:PSS** as HTL in inverted device architecture under photo-oxidative conditions (Figure 5.2). Upon ageing, there is a loss of active area that has been attributed to delamination. The presence of the HTL strongly reduces the loss of active area and change its occurrence, which is not evenly distributed as in the case of bare Ag contact, but it develops from the edges and through pin-hole defects already present in the pristine samples.
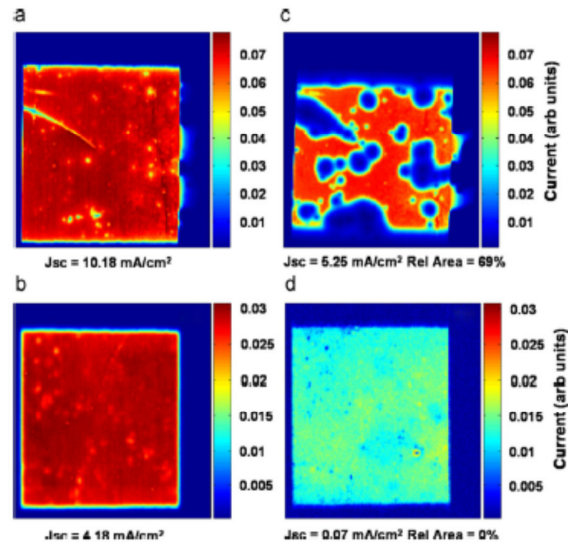
Figure 5.2 Light beam-induced current (LBIC) maps for (a) an inverted device with a PEDOT:PSS HTL and (b) inverted device with bare Ag contacts, both before aging. LBIC measurements were collected for the same diodes after prolonged exposure to illumination for (c) the PEDOT:PSS containing device and (d) the device without an HTL. The magnitude of the current in device (d) was scaled by a factor of 30 in the image in order to be visible on the same scale bar as in (b) [6]**.**

These few publications only reported on the observation of loss of mechanical integrity, without any particular measure of adhesive properties of the materials or of the layer stack. This research field was explored mostly in the last three years and a literature survey is presented.

The structure of this chapter is organized with a first introduction to general concepts and theories about adhesion and techniques commonly used to measure adhesion energy and adhesion strength. Then the state of the art regarding OPV will be presented through a review of the recent literature. Following the development of a new experimental set-up, alternative to the ones present in the literature, is described. The last two paragraphs describe the results concerning two different approaches adopted to enhance the adhesive properties, chosen within the ESTABLIS project framework: the development of a new **PEDOT:PSS** formulation [Dr. Stefan Schumann (ER4) at Heraeus Deutschland GmbH & Co. KG] and the introduction of a block copolymer interlayer [Joanna Kolomanska ESR7, Aston University]. Aurélien Tournebize (ESR10, Eberhard Karls Universität Tübingen) was fully involved in the characterization of the produced samples and in the following scientific discussions. The complete description of their results is discussed in each individual thesis, here only the most relevant data are reported.

5.1.1 Classic Adhesion Models

In the last century, many theories have been presented to explain the adhesion phenomenon in different situations. These classic models originated at a time when there were few, if any, experimental techniques available to study surfaces and interfaces at the nanometer level. Nowadays, we have a clearer understanding of the interfacial region, and a better knowledge of how it affects adhesion. One consequence is that plausible speculation can be made about adhesion mechanisms. For example, it is known that to a changing of surface roughness corresponds a variation of the chemical environment of its surface atoms and molecules. Thus, changing the roughness changes the local chemistry, which will affect the adsorption properties of the surface.

In order to split a solid, the attractive forces which ensure its cohesion must be broken, creating, in the meantime, new surfaces. The work to create a new surface, maintaining the thermodynamic equilibrium, is proportional to the surface energy (equation 5.1):

$$dW = \gamma \cdot dA.$$ (5.1)

where γ is the surface energy of the solid and dA is the corresponding increase in area.

The adhesion forces which act between the surfaces of two different solid bodies in contact is given by the Duprè equation (5.2):

$$W_{1,2} = \gamma_1 + \gamma_2 - \gamma_{1,2}$$ (5.2)

where $W_{1,2}$ is the work of adhesion, γ_1 and γ_2 are the surface energy of the two solids and $\gamma_{1,2}$ is the interfacial energy.

For a molecular solid, only *van der Waals* forces are present and the relative surface energy is weak. However, if the solids are ionic, covalent or metallic, most of the work is done against strong chemical bonds, and the corresponding surface energy is high. So the surface energy of a solid reflects the nature of the bonds between the constituting atoms. In case of different materials joined at the interface, their adhesion energy can be somehow foreseen considering the surface energies of the two individual solids. If two solids have comparable surface energies they will be "compatible" or more keen to establish interactions that improve the interfacial adhesion. The Duprè equation (5.2) has barely any practical use, since surface energy $\gamma_{1,2}$ is not known for most of the interfacial systems. Often, the approximated expression (5.3) is employed:

$$W_{1,2} = C_m(\gamma_1 + \gamma_2)$$ (5.3)

where C_m is the compatibility parameter, which characterizes the affinity between the two materials.

Each of the classical theories emphasizes a different aspect of a more comprehensive model, which, in principle, relates molecular dispositions in the region of the interface to macroscopic properties at the interface. A brief overview of these theories is illustrated in the following [13] [14] [15] [16].

The *mechanical coupling or interlocking* adhesion mechanism (Figure 5.3-a) is based on the mechanical interlocking of polymer into the pores and other superficial asperities of a substrate. Nowadays, the contribution of interlocking to explain adhesion is under debate. It is still believed that mechanical interlocking provides higher adhesion strength, but often the roughening of the surface is considered as only a mean to increase the surface area, to enhance molecular bonding interactions.
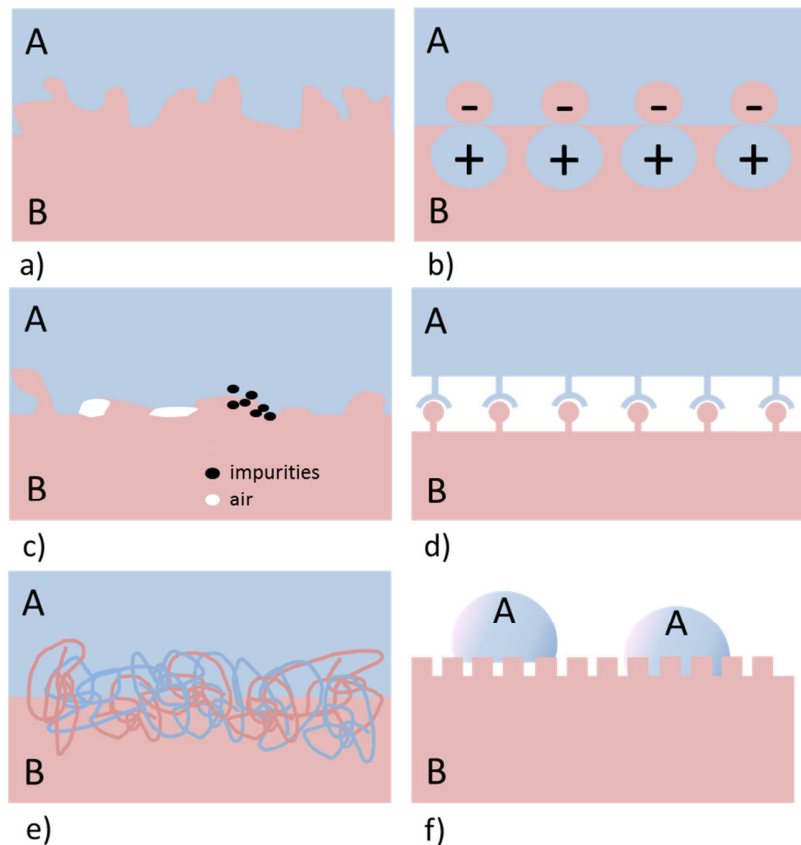
Figure 5.3 Schematic representation of classic models: a) mechanical interlocking; b) electric model; c) weak boundary layer; d) chemical adhesion; e) diffusion model; f) adsorption (or wetting) model.

The *electrical adhesion mechanism* (Figure 5.3-b) is valid for two materials joining at the interface having two different band structures such that at contact there is a mutual sharing of electrons. The system is treated as a plate capacitor, whose plates consist of the electrical double

layer which occur at the interface. The adhesion energy is considered equal to the energy of separation of the two plates.

The original theory of *weak boundary layers* (Figure 5.3-c) has been completely abandoned. It was important as it was thought that the interface between adhesive and substrate would not fail, but that failure was due to the formation of a weak boundary layer. Still, the presence of interfacial layers can be of great importance in determining the overall adhesion; adsorbed water, cohesively weak oxide layers, grease and other contaminants, generally have a negative effect on adhesion. The removal of such weak boundary layers through surface treatment or an effective displacement of the boundary layer by interface engineering, can significantly improve the adhesion properties.

Chemical adhesion (Figure 5.3-d) occurs when the surface atoms of two separate surfaces form ionic, covalent, or hydrogen bonds. A network of these bonds effectively links the surfaces together. A most general model of molecular bonding, in addition to the chemical bonds, includes relatively weak intermolecular forces such as dipole-dipole interactions, van der Waals forces, London forces, etc. These attractive forces are effective over only very small distances (less than few nanometers), this means that, even if strong, these bonds are fairly brittle, since the surfaces need to be kept close together. One example is the grafting of end-functionalized polymer (silane, phosphonic acids, thiols,...) on metal oxides or oxidized surfaces (SiO_2, TiO_2, ZnO, ITO, Al_2O_3, Fe_2O_3,...), on carbon surfaces (graphene, carbon nanotube, diamond,...), on metals and alloys (Au, Ag, Pt, Cr, Cd, CdSe, CdTe...) [17]. Another example is the case of polymer-metal interfaces. From a structural point of view, the creation of such interfaces involves the passage from a crystalline metal structure to a complex molecular polymer structure. Chemical bonds are formed at the interface, usually as a result of a charge transfer from the metal to the polymer. In the case of aluminum deposited onto oligo- and polythiophene [18], it has been shown that $C(sp^2)$-Al and S-Al charge transfer complexes are formed. The existence of analogous metal complexes by charge transfer from the metal to the polymer has been observed for several other metals (such as Na, Ca, Rb,...) and oligomers and polymers [such as diphenylpolyene, poly(*p*-phenylenevinylene) and its derivatives] seems to be a general characteristic of this type of interface.

In the *diffusion model* (Figure 5.3-e), adhesion of two macromolecules in intimate contact results from the interdiffusion of the molecules of the superficial layers. Diffusive bonding occurs when species from one surface penetrate into the other surface, while remaining bound to the

original phase, forming a transition zone, or interphase, of the two materials. This may occur only when the two materials are mutually soluble and the species have high enough mobility. This mechanism is at the base of sintering of metals and ceramics particles and could also be effective for polymers. Diffusive bonding in polymer-on-polymer surfaces can be obtained when sections of polymer chains from one surface interdigitating with those of an adjacent surface.

The *adsorption model* (Figure 5.3-f) emphasizes the point that once a liquid and substrate come into contact, attraction forces will act between them. As long as the extent of wetting is good, these forces, whether primary bonds, such as covalent, or secondary van der Waals forces, are generally considered sufficient to give a high bond strength. In the case of two solids, different theories have been proposed for the characterization of the contact adhesive interactions. Two bodies in contact deform as a result of either external or surface forces. The original theory of contact of two elastic bodies was proposed by *Hertz*, who solved the contact problems of an elastic sphere versus an elastic half-space, and two elastic spheres [19], assuming that there is no adhesion between two elastic spheres in contact. The *Johnson-Kendall-Roberts (JKR) model* [20] describes the contact between soft materials with short range, strong adhesion forces, and large tip radii. In contrast, the *Derjaguin-Muller-Toporov (DMT)* model [21] applies to adhesion between stiff materials with long range, weak adhesion forces, and small tip radii.

In this regime, the adhesion forces can be estimated by the following two limiting cases: the *Johnson-Kendall-Roberts (JKR) model*, which applies when the adhesion forces are short range compared to the elastic deformation they produce (soft material with strong adhesion), and the *Derjaguin-Muller-Toporov (DMT) model*, which describes the case of long range surface forces with a Hertzian geometry (stiff materials, weak adhesion forces). Intermediate between the *JKR* and *DMT* models, the *Maugis-Dugdale (MD) model* [22] proposes an analytical solution (Figure 5.4).
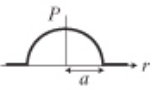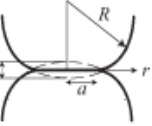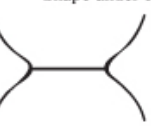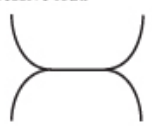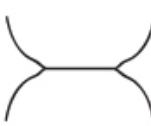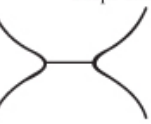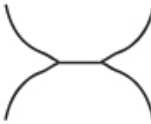
Figure 5.4 Comparison between the different contact mechanics models [23]**.**

5.1.2 Adhesion Testing Techniques

In this sub-section, some of the most diffused techniques used to test the adhesive properties of films will be presented [16] [24]. The peculiarities, advantages, as well as the limits of each technique will be briefly discussed.

5.1.2.1 Peel Test

The *peel test* is the most common test for flexible coatings. The standardization and quantification of the test were achieved by the use of an appropriate tensile test apparatus that allowed to apply the peel load maintaining the required peel angle. The peel test can be performed at any angle between 0 and 180 *degrees*. Unless particular geometric restrictions imposed by the samples or the apparatus, 90 and 180 degrees are the most common angles for testing (Figure 5.5). However, from an analytical point of view, the systematic variation of the peel angle can provide information on the effect of mode mixity on peel strength. During the peel test, the interfacial region is subjected to both tensile and shear strains. The

Figure 5.5 Two different geometries of the Peel Test: a) 90 degrees and b) 180 degrees.

ratio of these two loading types is loosely referred to as the loading mode mixity. The importance of

158

knowing the mode mixity stems from the fact that the apparent adhesion strength of many coatings is sensitive to the mode mixity.

Usually, sample preparation is very simple and straightforward and when used for semi-quantitative measure of the coating adhesion to the substrate, which can be readily used for ranking or quality control purposes. A further advantage of this test is the fact that the rate of delamination and the locus of failure can be controlled fairly precisely. This stems from the fact that a very high stress concentration exists at the point where the coating just lifts off the substrate. This tends to narrowly focus the failure region very close to the geometric interface between coating and substrate, which is the region of most interest in any adhesion test. Since the rate of delamination can be precisely controlled by the test equipment, studies of the rate dependence of adhesion strength can be easily carried out.

However, when trying to ascertain whether the coating will survive a given set of end-use conditions, several problems arise. The main issue is the fact that the peel test subjects the coating to very high strain levels near the peel bend, which most coatings never undergo under common end-use conditions. Thus, it is clear that peel test results can present highly misleading estimates of the actual adhesion strength of a coating when subjected to realistic end-use conditions. Further limitations of the peel test stem from the fact that it is applicable only to tough flexible coatings. A number of other drawbacks and limitations apply to the peel test, including difficulty in initiating a peel strip for coatings with strong adhesion and controlling sample-to-sample variability.

5.1.2.2 Tape Peel Test

The *tape peel test* is a rough-and-ready version of the standard peel test. Its main advantage is the ease of sample preparation. In a typical application, a strip of special tape is applied to the coating to be tested in a predefined manner. The main issue is to be as consistent as possible to achieve reproducible results. The tape is subsequently peeled off in a prescribed fashion, and the test surface is then inspected to check the resulting damages. At the purely qualitative level, the experiment gives an indication whether the adhesion of the coating is acceptable or not. A number of techniques have been introduced to give a semi-quantitative result by quantifying the level of partial damage of the surface.

5.1.2.3 Pull-off Test

Similarly to the *peel test*, the *pull test* is a general method to evaluate the adhesion of coatings to a variety of substrates, in a qualitative or semi-quantitative way. It is applicable to both brittle and flexible coatings and substrates and the sample preparation is relatively easy. As a drawback, the data analysis is difficult, especially for quantitative measurements. This is due to the rapid and uncontrollable failure mode that cause a wide scatter in data. It has been speculated that, in most cases, the failure mode in a given pull test experiment is determined by a preexisting distribution of flaws in the sample. The applied stress field finds the largest, weakest defect in the sample and the failure initiates at this point. It then rapidly propagates to complete separation of the pull stud from the sample surface.

As for the peel test, the pull test involves two additional materials besides the specimen under investigation. The test stud itself is usually made of a high-modulus metal or ceramic material and in the case of flexible coatings can be considered perfectly rigid. An adhesive, often an epoxy glue, is then required to attach the stud to the specimen surface. The adhesive properties should always be considered into the analysis. Once the stud is properly linked to the surface, it is pulled-off under controlled conditions (Figure 5.6-a).
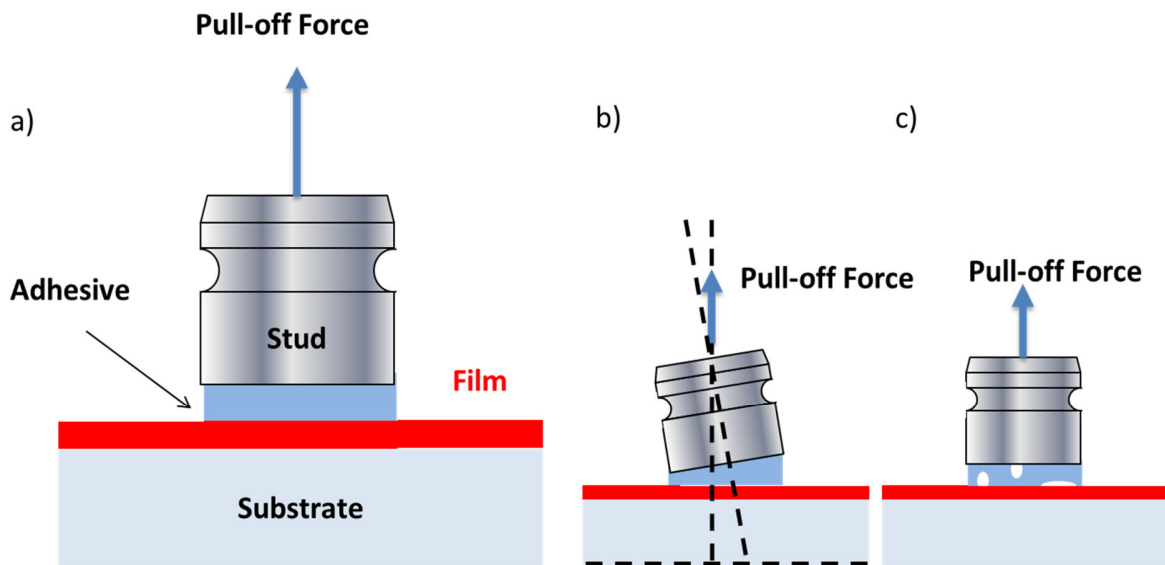
Figure 5.6 a) Schematic representation of the Pull-Off Test; b) development of a bending moment during testing and c) adhesive inhomogeneity that leads to voids.

During the pulling, a series of experimental issues may occur. Unless the stud and the load are orthogonal to the surface, there can be an off-axis component that can impose a *bending moment* to

160

the sample, in addition to the tensile load (Figure 5.6-b). Moreover, any real sample will not be uniformly bonded (Figure 5.6-c), and the applied stress field will be influenced by any defects or bonding weaknesses. The failure starts at the weakest point in the structure and then propagates at acoustic velocities to complete separation. It can occur either adhesively at any of the three sample interfaces or cohesively inside any of the bulk materials. The most common failure is a mixed-mode interfacial and cohesive fracture.

Given these complexities, typical pull test data show a wide scattering. Multiple tests must be run at any given condition, and data censoring techniques have to be applied to eliminate unwanted failure modes.

5.1.2.4 Beam-Bending Test

There are many different tests for measuring adhesion based on the relatively simple mechanics of the *elastic beam*. This geometry enables simplify the analysis for the stress intensity factors and the strain energy release rates that drive the delamination process. The key advantage of having a simple geometry, also leads to the main disadvantage of these tests, which is the very limited sample geometries that can be investigated. The second issue is if and when this test represents the stress/strain loading environment experienced by the sample. In particular, when the main mode of failure is through internal stresses, the delamination process is driven mainly by the elastic energy generated by the stresses. In these cases delamination process occurs under near-infinitesimal strain conditions, while, in all of the beam-bending tests, the delamination process is driven by external loading at important levels of deformation and strain. Even if the level of deformation is far from that generated by a peel test, this still calls into

Figure 5.7 Two different Beam Bending Technique: a) Four point bend and b) standard double cantilever beam.

question the relevance of beam-bending data for certain situations.

One example is the *four-point bend test*. In this test, a cut is first made in the coating down to the underlying substrate and a bending load is then gradually applied (Figure 5.7-a). The singular stress field at the edge of the cut eventually drives a delamination, giving rise to a crack that can later

lead to spoiling of the coating. The four-point bend test is favored largely when interested in obtaining fully quantitative information on the adhesion strength of coatings by taking advantage of the relatively simple beam mechanics involved in the fracture analysis of this problem. One of the problems encountered, was the fact that some structural adhesives showed significantly different strength properties in thin layers and in bulk samples. The *cantilevered beam configuration* (Figure 5.7-b) solved this problem, maintaining a relatively simple analysis of the results. The sample is prepared by carefully gluing two identical beams of the substrate material to a thin layer of the material under test. Great care must be taken regarding the surface preparation and cleaning of the beams and controlling the thickness and cure conditions of the adhesive. A spacer is used to set the layer thickness and provide the initial crack from which the fracture propagates. The sample is then mounted in a standard tensile testing apparatus in which the load-displacement behavior can be carefully determined.

It is clear that the main advantage of using any of the beam-bending tests is that they are all valuable to quantitatively assess the fracture mechanics. The mechanics of bending beams was one of the earliest and quite likely the most studied topic in applied mechanics. Thus, it is fairly easy to convert load-displacement data into the corresponding fracture toughness or surface fracture energy, which are relevant to the adhesion failure process under investigation. This type of data is especially important as input to detailed fracture mechanics-based models, which attempts to predict the failure of structures based on geometry, material properties, and loading conditions.

5.1.2.5 *AFM application in Thin-Film Adhesion Measurement*

*Atomic force microscopy (*AFM*)*, together with the *scanning tunneling microscope (*STM*)* and the *scanning near-field optical microscope (*SNOM*)*, belongs to a series of scanning probe microscopes invented in the 1980s. AFM allows the imaging of the topography of surfaces, up to molecular or atomic resolution. In the AFM the sample is scanned by a tip, which is mounted to a cantilever spring. While scanning, the force between the tip and the sample is measured by monitoring the deflection of the cantilever. A topographic image of the sample is obtained by plotting the deflection of the cantilever versus its position on the sample.

Another major application of AFM is force spectroscopy [25], whose main focus is to study surface forces. A vibrational mode normal to the surface is imposed to the AFM tip. Vertical position of the tip and deflection of the cantilever are recorded and converted to force-versus-distance curves,

briefly called ''force curves''. The forces relevant to AFM are ultimately of electromagnetic origin, but distinct intermolecular, surface and macroscopic effects give rise to interactions with different dependencies. Therefore it is fundamental to understand the different components of the force. Various models [26] [25] are commonly used in the literature, such as the Hertz model (elastic deformation without adhesion), *the Derjaguin−Muller−Toporov model* (elastic deformation with adhesion, applicable for small tips and soft samples with small adhesion), the *Johnson−Kendall−Roberts (JKR) model* (elastic deformation with adhesion, applicable for large tips and soft samples with a large adhesion) and the *Maugis model* (can be applied to any system, with both high and low adhesion) (Figure 5.8 and Table 5.1 from [27]).

AFM tips are usually made of brittle crystal materials, such as Si or Si_3N_4. To study the adhesion of two different materials functionalized tips have been introduced [28]. Also for this so-called *Chemical force microscopy*, the same models have been used to understand the force/deflection curves.

Table 5.1 Characteristics and restrictions of the different contact mechanics models applied for AFM adhesion studies.

Model	Assumptions	Restrictions
Hertz	No surface forces	Not applied to small loads in the presence of surface forces
DMT	Long-range surface forces act only outside the contact area. Model geometry is as in the Hertz model	Contact area can be decreased due to the limited geometry.
JKR	Short-range surface forces act only within the contact area	Force magnitude can be decreased due to surface forces.
Maugis	Tip-sample interface is modeled as a ring.	The solution is analytical but equations are parametric.
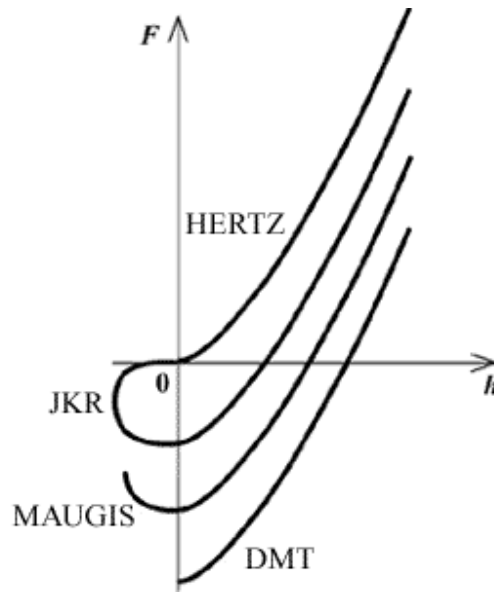
5.1.3 Adhesion of Organic Electronics Materials

Thin film mechanical properties of conjugated polymers and molecules have been studied mainly by AFM *nano-indentation* [29]. Li et al. [30] were also able to correlate photovoltaic and mechanical properties of *P3HT:PC$_{61}$BM* layers processed in different ways, finding that to the layers with lowest *Young's modulus* (20.73 GPa) and hardness (649 MPa) corresponded the devices with the best *PCE*. Another technique utilized to characterize thin film properties is the *buckling method*, which consists on deposing the layer on a compliant **PDMS** substrate and then apply a compressive strain on the thin film-**PDMS** stack resulting in a characteristic buckling pattern [31]. Many materials for organic electronics (such as **rr-P3HT**, **P3HT/PC$_{61}$BM**, **PEDOT**, **PSS** and **PEDOT:PSS** [32]) have been investigated by this method. Awartani *et al.* [33] found that the best photovoltaic properties corresponded to the higher Young's modulus (1.97 GPa).

Concerning adhesive properties of these materials, very few studies have been published. In one of these, Tong *et al.* [34] [35] investigated the adhesive interactions between many organic and inorganic materials for two orders of magnitude higher than any other couple. This difference shows the limits of the technique and of the theoretical model and the need of further investigations and theoretical background.

Very recently, Wood *et al.* [36] reported a new method which allowed them to simultaneously measure electrical space-charge-limited current and material properties, such as Young's modulus

and surface adhesion, all with nanoscale resolution. The force–volume bias spectroscopy (FVBS) combines arrays of force–distance and current–voltage curves acquired simultaneously, allowing the investigation of spatial heterogeneity and statistical analysis of correlations between material properties. In particular, the dependence between Zero Field Mobility and Adhesion force and their dependence on temperature of **P3HT** [36] have been studied. Mobility steadily increases with temperature, while the adhesion force decreases to reach a minimum at 90 °C, it rises again to the initial value and it finally drops dramatically at 140 °C.

5.1.4 Adhesion in OPV Devices

It is well known that the processing yield and the long-term reliability of multilayer electronic devices are strongly influenced by the adhesive and cohesive properties of internal bi-materials and thin films [2]. While the electrical failure mechanisms in OPVs have been thoroughly investigated, little is known about their mechanical stability, which is critical to ensure long term reliability. The intrinsic thin films stresses of each layer present in organic solar cells, in combination with other possible fabrication, handling and operational stresses, provide the mechanical driving force for delamination of weak interfaces or even their decohesion, leading to a loss of device integrity and performance.

Prof. Dauskardt's group at Stanford University recently extended its research interest toward organic photovoltaics. They investigated the dependence of adhesion/cohesion properties in BHJ devices on architecture; processing (deposition as well as post-deposition); materials for the active layer and hole transporting layer; different layer stresses; humidity and so on.

To investigate these properties they used two beam-bending techniques, furtherly developed and adapted inside the group: four-points bending and double cantilevered beam test (Figure 5.9). As aforementioned, these techniques give results which allow to build specific fracture mechanics models, developed based on the material properties. The complete description of these models is out of the scope of this introduction and only the main results will be presented.
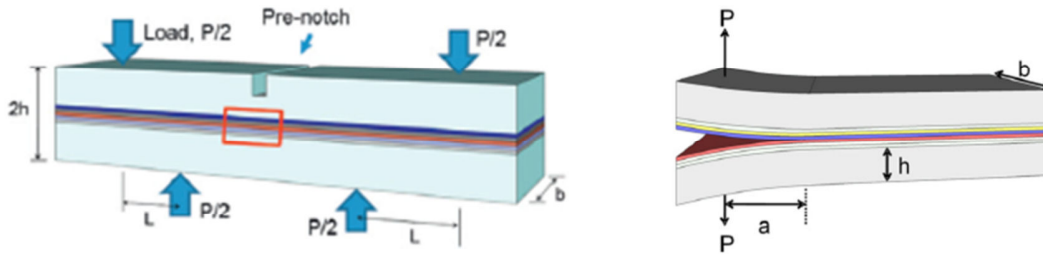
Figure 5.9 Four point bending and double cantilevered beam utilized to measure adhesion energy in OPV.

In one of their first publications [11], Dupont *et al.* investigated interlayer adhesion in inverted polymer solar cells, depending on the deposition technique (*spin, spray or slot-die coating*) of the active layer, on both flexible and non-flexible substrates. They observed the same adhesive failure at the interface between active layer (**P3HT:PCBM**) and hole transporting layer (**PEDOT:PSS**), suggesting a material-dependent mechanism. They also investigated the effect of temperature, solar irradiation and humidity on the adhesive and cohesive properties at this same interface. Annealing increased the adhesion significantly; this was attributed to the thermal induced changing in the active layer morphology and of the chemical properties at the interface. Solar irradiation on fully encapsulated solar cells had again an enhancing effect on the adhesion properties; this was still attributed to the heat generated from IR radiation. Finally, the combined effect of stresses and humidity greatly accelerates the decohesion rate in the hygroscopic **PEDOT:PSS** layer: water easily diffuses through the layer and breaks the hydrogen bonds formed between **PEDOT:PSS** grains.

Subsequently, they investigated the adhesive properties in roll-to-roll processed flexible inverted solar cells [37]. The same results were achieved, the weak point was still the interface between AL (**P3HT:PCBM**) and HTL (**PEDOT:PSS**). Adhesion energy depended on AL composition, with best performance for a 3:1 w/w ratio of **P3HT:PCBM**; post deposition thermal treatment furtherly enhanced adhesion energy. Also, they compared **PEDOT:PSS** to another HTL material: V_2O_5. The adhesion energy was two orders of magnitude higher; this improved adhesion was attributed to the formation of chemical bonds between molecules of the AL and V_2O_5, including possible covalent, ionic and bipolar interactions. In addition, the formation of an intermixed layer also involves an entangled molecular network, that it is known to significantly increase fracture resistance in polymers. Moreover, the adhesion energy was found to be independent of the **PEDOT:PSS** layer thickness (between 10 and 40 nm) and *AL* pre-treatment with O_2 plasma slightly increased it [38]. The adhesive

166

properties of evaporated **MoO₃**, as alternative material for the HTL, were investigated. **MoO₃** adhered less than **PEDOT:PSS**, which was attributed to a reduced interface mixing linked to the different deposition technique.

The positive effect toward adhesion of the annealing on the morphology of these devices has been lately confirmed [39]. Using *near edge X-ray absorption fine structure in Total Electron Yield (*NEXAFS-TEY*), UV-VIS absorption and X-ray photo spectroscopies (*XPS*)*, Dupont *et al.* were able to precisely quantify the atomic fraction of **P3HT**, **PCBM** and **PEDOT:PSS** and the **P3HT** chain orientation at the delaminated surfaces for different annealing conditions. They found that the adhesive failure happened between the AL and an intermixed layer of **P3HT:PCBM** and **PEDOT:PSS**. The size and the strength of this intermixed layer increases with annealing time and temperature, resulting in an increased adhesion.

In another study they investigated the same properties in normal devices, prepared by spin coating deposition [40]. In this case the fracture occured inside the AL and, indeed, it was a cohesive failure. It resulted to be independent from the layer thickness and enhanced after thermal treatment, but only in the case of the annealing being conducted after electrode deposition. This was attributed to a different evolution of the AL morphology: in the absence of the **Al** electrode, **PCBM** diffuses to the surface of the AL [41], forming a weak path for crack propagation during debonding. On the other hand, when annealing is performed after metal electrode deposition, **PCBM** diffusion is limited by the AL/**Ca** interface itself [42]. The same composition/adhesion behavior reported before was observed and substituting **PCBM** with **C₆₀** increased the cohesive properties. This was due to a different interaction between the donor and acceptor and to a different vertical phase segregation, in which there is a **P3HT** reach phase on the **Ca** side [43]. The same observation was reported for inverted devices [44], with the additional indication that the cold crystallization temperature of **PCBM** ($T_C \approx 120$ °C) is a key parameter. Pre-electrode deposition annealing has to be performed below T_C to improve the adhesion at the AL/HTL interface.

The stresses present in the different layers have been measured and associated to decohesion [45]. Compressive biaxial stresses were measured in the **PEDOT:PSS** while tensile stresses were measured in the AL layer. The cracking of the AL is unlikely to happen without any additional stress contributions from other layers or external forces. Brand *et al.* also measured compressive stresses in the **Al** electrode, increasing electrode deposition rate eventually led to a buckling instability, which

resulted in undulating electrode surface topography. The AL was found to have the lowest cohesion among the layers of the solar cell and dependent on the **Al** electrode deposition rate. The cohesive failure path in the AL exhibited the same periodicity and orientation of the **Al** electrode buckling topography.

Also the Mw of **rr-P3HT** influenced the decohesion energy [46] in spin casted normal devices. Increasing the Mw enhanced intermolecular bonding and raised the probability for chain entanglement. This led to an improved cohesion, due to a greater degree of plastic deformation before cohesive failure occurrence. The role of the Mw was then considered when investigating the temperature-dependent decohesion mechanism [47]. It was found that at temperatures below the AL glass transition temperature ($T_g \approx 41$–45 °C, regardless of **P3HT** Mw), decohesion was characterized by brittle failure via molecular bond rupture. The analysis of surface topography revealed an increased roughness for decohesion surfaces tested above T_g, revealing significant plastic deformation. Above the T_g, decohesion growth was driven via viscoelastic relaxation processes in the AL, leading to reduced cohesion energies.

The effects on cohesion energy of different acceptor materials (**PC$_{61}$BM** and **indene-C$_{60}$**) combined with **P3HT** [48] and of different donor materials (poly(3,3'''-didodecyl quaterthiophene), **PQT-12**, and poly(2,5-bis(3-hexadecylthiophen-2-yl)thieno[3,2-*b*]thiophene, **pBTTT**) with **PC$_{71}$BM** and **bis-PC$_{71}$BM** [49] were investigated. In the first study Bruner *et al.* found how, under identical conditions, cohesion significantly changes due to minor variations in the fullerene adduct functionality. **Indene-C$_{60}$** significantly improved the AL cohesion, mainly when combined with high Mw **P3HT**. This was attributed to the different intermolecular interactions in the bulk and at the **P3HT:fullerene** interfaces, induced by the different substituents, leading to different fracture processes inside the AL. In the second case, the best acceptor for all the donors resulted to be **PC$_{71}$BM**. This was attributed to the different polymer:fullerene interaction: **PC$_{71}$BM** is able to intercalate the polymer side chains allowing the formation of a bimolecular crystal phase that enhances the AL cohesion.

An important observation in terms of device long term stability was made by Dupont *et al.* [50]. They explored the decohesion kinetics in the **PEDOT:PSS** layer of inverted devices, varying systematically relative humidity and temperature. They found a time dependent debonding, which occurred at lower mechanical stresses than those usually measured to fracture a polymer layer. They

demonstrated that this debonding happened through a moisture-assisted mechanism, enabled by a stress dependent chemical reaction between the water molecules and strained hydrogen bonds at the debond tip. Using an atomistic kinetic model, they were also able to elucidate a deceleration in debond propagation at intermediate decohesion rates. When the crack spread, the absorption of water causes the development of a local compressive stress field, which opposes the propagation itself.

5.2 Results and Discussions

In this sub-section the development of an experimental set-up and his dependence upon experimental parameters is described in details. The technique was utilized in the testing of new materials introduced with the aim of improving device mechanical stability. The two different strategies, developed in the framework of the ESTABLIS project, are briefly introduced and then the experimental results are presented.

5.2.1 Pull-off Set Up Development

As aforementioned in the *pull-off test* general description, some experimental complications could affect the test sensitivity and reproducibility. Two of the main issues are: i) the presence of a bending moment due to a non-perfect alignment or to a non-homogeneous stress field due to coating defects and ii) bonding weaknesses, eventually leading to a mixed adhesive/cohesive failure mode. Multiple tests have to be performed to have a statistic dataset and some data have to be excluded for unwanted failure modes.

The new set-up allowed a better control on the orthogonality of the sample-stud system and a better homogeneity of the adhesive layer. Most notably the alignment of the stud is insured by the fact that it is linked to a fixed arm leaving only one degree of freedom (z axis). The curing of the epoxy adhesive occurs *in situ* while the stud applies a constant pressure, assuring a more uniform and reproducible adhesive layer. Moreover, when manually applied the stud can slide or twist on the glue.
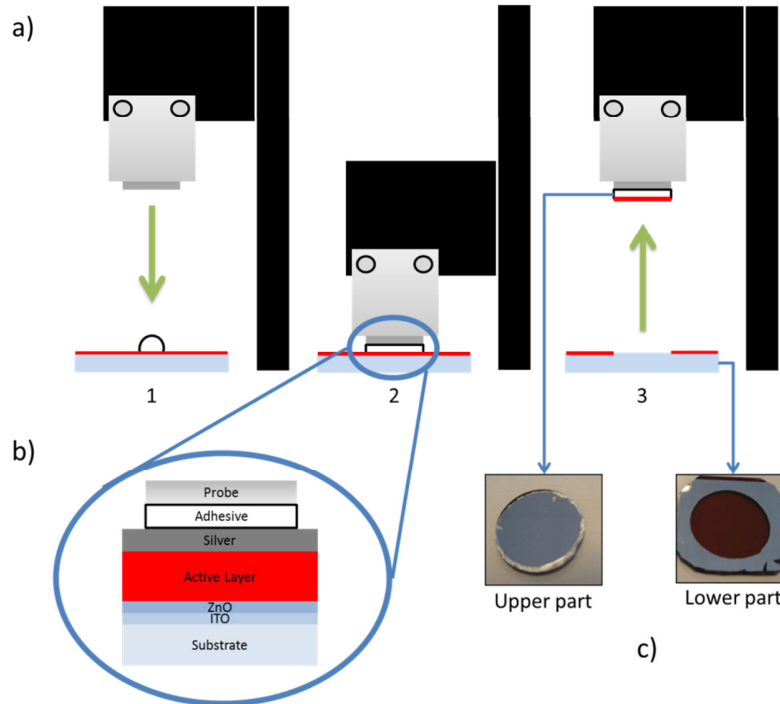
Figure 5.10 a) Schematic representation of the experimental apparatus; b) Layer stack of the inverted devices used in these studies; c) half-cell produced as out-put of the destructive pull-off test.

A schematic representation of the test apparatus (Figure 5.10-a), the specimen structure (Figure 5.10-b) and a picture of the devices after the test (Figure 5.10-c) are shown in Figure 5.10. The sample to test is locked into the sample holder, to ensure the best orthogonality between probe and sample. A drop of adhesive is then deposited at the center of the sample and the probe is approached to the surface at fixed speed (Figure 5.10-a1). The probe touches the adhesive drop and spreads it evenly in the space between sample and probe surfaces. The approach stops when the sensor measures a threshold value and it maintains a constant pressure during the curing process (Figure 5.10-a2). The pulling (Figure 5.10-a3) is conducted at fixed speed to complete detachment of the probe. Probe and sample are photographed and the pictures analyzed with software to extract the value of the area actually removed.
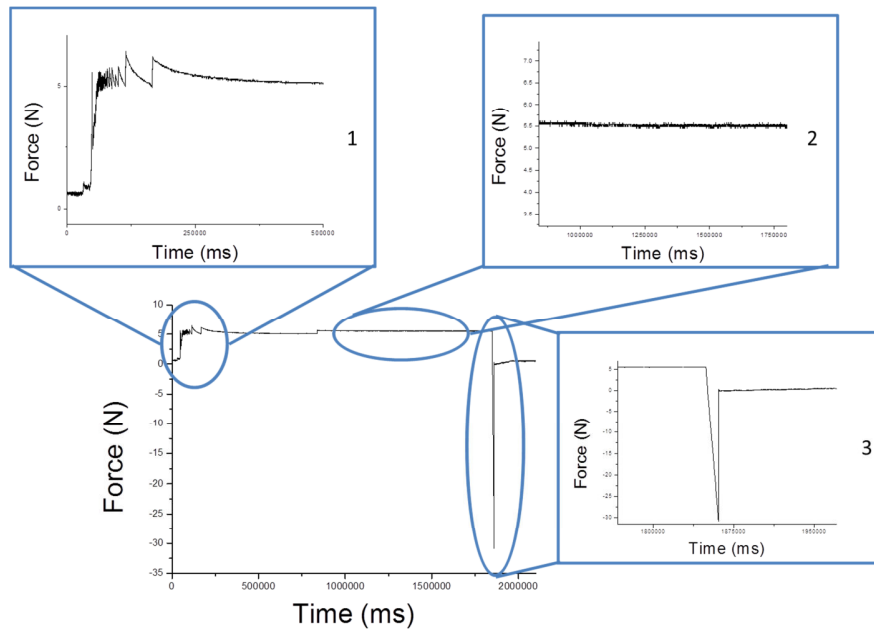
Figure 5.11 Typical Force vs Time curve and the three main phases of the test: 1. approaching and contact; 2. adhesive curing at constant pressure; 3. pull-off at constant speed.

An example of the typical corresponding force vs time graphic is shown in Figure 5.11. When the probe touches the adhesive drop (Figure 5.11-1), a force starts to be measured and, after few oscillations, the preset constant value is imposed (Figure 5.11-2) and maintained for 30 min. Maintaining the pressure is important because, as seen before, it has a strengthening effect and, moreover, it is necessary to keep the contact between the probe and the adhesive while it dries. The adhesive layer thickness just after being spread is around 30 μm, while once cured the thickness is reduced to only one tenth of the initial value. In the third and final segment (Figure 5.11-3), a tensional strain is applied at a constant pulling rate. The maximum stress measured represents the maximal adhesive strength of the system or the characteristic stress at the crack onset. Simply dividing this value by the removed surface gives the Stress at Break (N·m^{-2} or Pa).

The influence of some parameters which usually affect the measurement has been investigated (Figure 5.14-a to d) in order to determine the best experimental conditions. The parameters considered in our study were: *contact area*, *contact pressure* during adhesive curing, *pulling speed* (strain rate) and adhesive *curing time*.

The effect of the *contact area* has been studied using three different *Stamps* (Figure 5.12) and the results are showed in Figure 5.14-a. The *Stress at Break* values are constant and do not depend

upon the Stamp size: *Stamp 1* (0.42±0.05 MPa, 1.1·10^{-4} m^2), *Stamp 2* (0.47±0.17 MPa, 0.4·10^{-4} m^2) and *Stamp 3* (0.39±0.15 MPa, 0.2·10^{-4} m^2).
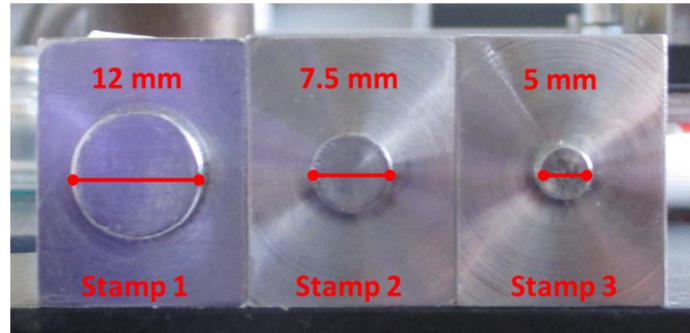
Figure 5.12 Different Stamps used in the study.

The small variation between the values is attributed to the viscoelasticity of the adhesive layer. Upon separation, the *epoxy adhesive* is subjected to both a *tension* (in the center) and a *shear stress* (at the edges) (Figure 5.13). The relative importance of these two stresses can be quantified by the *a/h* aspect ratio (or confinement) of the adhesive, where *a* is the lateral size of contact between the adhesive and the probe and *h* is the adhesive thickness. When the film is not confined (*a/h* very small), studies [51] have shown that the shear components is maximized. Conversely, when the material is very confined (*a/h* very large) the orthogonal tension is the fundamental contribution. In the present case the aspect ratio is always quite large, since *a* and *h* are of the same order of magnitude, respectively millimeters and micrometers, for all the different probes. The difference is most probably due to the presence of a ring of adhesive around the two smaller probes (*Stamp 2* and *Stamp 3*, Figure 5.12), which arise from experimental difficulties in deposing the adhesive layer onto smaller surfaces. This makes the effective area different from that of the probe and also increases the standard deviation, making it harder to correctly measure the surface and increasing the shear strain contribution in an uncontrollable and irreproducible way.
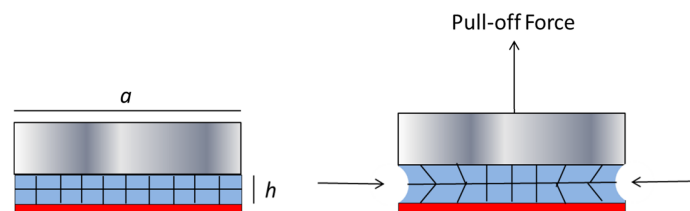
Figure 5.13 Load in a viscoelastic material which undergoes a traction.

The *epoxy adhesive* is a viscoelastic material and its properties depend on the strain rate (pulling speed) and the curing time. In elastic materials the stress is a function of the strain, while in viscoelastic materials, the stress also depends on the *strain rate*. In pristine and cured epoxy resins, it has been shown that the maximum stress is sensitive to the strain rate, in particular it increases for higher strain rates [52], [53]. In the presented case (Figure 5.14-c), the *stress at break* increases with *pulling speed*, following the behavior reported in the literature. In a similar way, *curing time* has an effect on the viscoelastic properties, the degree of elasticity increases with reticulation and the component of tensile stress is reinforced against the shear component, giving a slightly lower *stress at break* with narrower scattering (Figure 5.14-d).
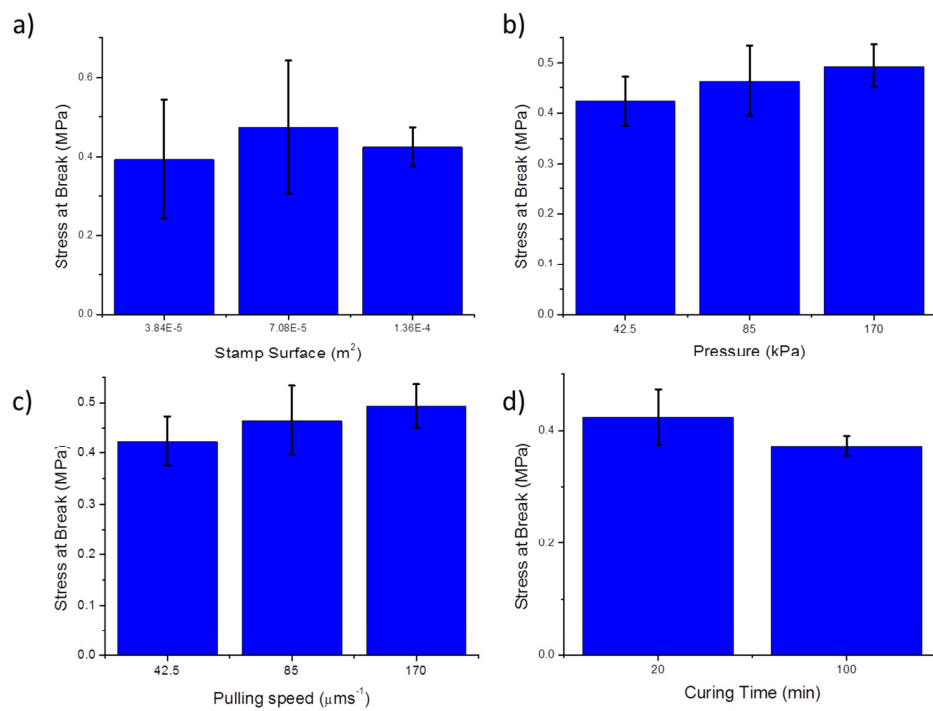
Figure 5.14 Stress at Break (MPa) variation according to: a) contact area; b) pressure during adhesive curing; c) pulling speed (strain rate); d) adhesive curing time.

The *stress at break* values appear to increase with higher *pressures* applied during the adhesive curing (Figure 5.14-b). A similar behavior has been observed in pressure sensitive adhesives [54], where the adhesive energy increases with pressure (or *contact time*) up to a maximum constant level. This was attributed to the relaxation state of the chains which influences the deformation mechanisms during rupture. In a similar way, the relaxation of the chain influences the adhesive reticulation and its final viscoelastic and adhesive properties [52].

From the above discussion, it appears that to compare different measures it is of capital importance to choose a set of parameters and to respect an experimental protocol to further reduce operational variations. For the series of experiments presented in the following sections, a circular probe with a diameter of 12 mm (*Stamp 1*, Figure 5.12) has been used. The adhesive of choice was an epoxy adhesive under the commercial name of *SADER®* from *Bostik S. A.* (5 min hardening, maximum load 130 kg/cm2). The mixture of epoxy resin and hardener was prepared before each measurement and the time between the deposition of the adhesive drop and the probe contact was always kept around 30 s. The *approaching speed* of the probe was 50 µm/s, with a sampling frequency of 100 Hz, and the force sensor used was a TME F108TC, with an operating range of 1-100 N and a sensitivity of 0.05 N. Its calibration was performed at the beginning of every day of measurement. The contact threshold force was of 5 N (42.5 kPa) and it was kept constant during the curing of the adhesive (30 min), with a sampling frequency of 0.1 Hz. The pulling speed was 10 µm /s with a sampling frequency of 100 Hz. The pictures were taken with a *Canon IXUS 132* and the software utilized to treat the images was *ImageJ* (National Institutes of Health, Open source under Title 17, Section 105 of USA code).

5.2.2 New PEDOT:PSS Formulation

Various poly(3,4-ethylenedioxythiophene):poly(styrenesulfonic acid) (**PEDOT:PSS**) dispersions have been widely used in antistatic layers, touch sensors, transparent electrodes, OLED applications and organic solar cells [55]. Water is the most widely used solvent for PEDOT/PSS dispersions. It is a good solvent for most reagents, compatible with the PEDOT/PSS dispersion, low cost and environmentally friendly. However, in some cases water requires long drying times and excludes the use of highly non-polar components. As a consequence PEDOT dispersions in non-polar solvents have recently been developed (*Clevios^{TM} P SB 1* and *Clevios^{TM} P SB 2*, available in solvents such as heptane and toluene), but these dispersions require specific polysulfonic acid copolymers, that can be dispersed in non-polar solvents. Components such as polymeric binders, surfactants, UV stabilizers and solvents were also added to improve the coating properties of the resulting formulation such as surface hardness, better wetting and environmental stability.

In the field of OPV, **PEDOT:PSS** is a well-established hole-transport layer (HTL), due to its good processability and the chance to tailor its electronic properties, such as its work-function and conductivity [56]. Recently, it has been shown how inverted device architecture offers several

advantages over regular architecture, including improved operational lifetime, ease of device fabrication and also the potential of low cost manufacturing. However, when applied in inverted architectures the **PEDOT:PSS** layer itself represents one of the weak points for the device long-term stability, due to its phase separation that induces a deterioration of its interface with the *AL* [57]. Also, as discussed before, this same interface was identified as the weakest point in term of adhesion (Paragraph 5.1.4).

Strategies to increase adhesion at this critical interface include surface treatment by solvents or O_2 plasma, wettability improving surfactants or adhesion promoting interlayers, however, with limited success so far. The chosen strategy to improve the adhesion properties and the overall device lifetime, was to use a new **PEDOT:PSS** dispersion to favor the physical intermixing of the polymer layers. The Clevios^{TM} HTL Solar 2, was successfully developed in the framework of the ESTABLIS project by Dr. Stefan Schumann (ER4) at Heraeus Deutschland GmbH & Co. KG. Its synthesis, characterization of the material and after integration in devices have been already presented in front of the scientific community [58].

The non-aqueous **PEDOT:PSS** dispersion was prepared by a solvent exchange process. The solvent system used includes a mix of higher alcohols such as diethylene glycol and propanediol which was then diluted with ethanol. Surfactants were added to improve wettability and film formation. Moreover, non-polar solvent additives were added in low quantities. The non-polar solvent was selected in order to partially solubilize the photoactive material and, hopefully, to act as a potent adhesion promoter.

5.2.2.1 Aim of the Study

The objective of this part of the work was the characterization of the effect on the adhesion properties of different **PEDOT:PSS** formulations, utilizing the new implemented set-up for the pull-off test. Two standard, commercially available, aqueous **PEDOT:PSS** formulations specifically developed for OPV applications, Clevios™ HTL Solar and Clevios™ HTL Solar N (Heraeus Deutschland GmbH & Co. KG) were used for comparison to the new Clevios^{TM} HTL Solar 2. Their characteristics are reported in Table 5.2.

Table 5.2 Composition and characteristics of Clevios™ HTL Solar, HTL Solar N and HTL Solar 2 [58]**.**

PEDOT	Solvent	pH[a]	ϑ [°][b]	σ [S cm^{-1}][c]
HTL Solar	Aqueous	2	28	0.2
HTL Solar N	Aqueous	7	34	0.1
HTL Solar 2	Organic	2	34	90
a)pH=-$\log_{10}$[H$_3$O$^+$]; b) contact angle ϑ on the photo-active layer P3HT:PC$_{61}$BM; c) σ=conductivity				

The newly created surfaces were characterized by contact angle, optical microscopy, AFM and XPS to exactly identify the fracture path and being able to explain the difference in the adhesive properties. XPS analyses were performed by Aurélien Tournebize (*ESR10*) at the *Institut für Physikalische und Theoretische Chemie of the Eberhard Karls Universität Tübingen*, in the framework of the *ESTABLIS* project. Detailed procedures, data analysis and their discussion are reported in his thesis.

5.2.2.2 Adhesive Properties

The inverted OPV devices used in this study were fabricated by Dr. Stefan Schumann at Heraeus Deutschland GmbH & Co. KG, in the framework of the ESTABLIS project. The layer stack was based on the model system **ITO/ZnO/P3HT:PC$_{61}$BM, 1:1/PEDOT:PSS/Ag** with the following layer thicknesses: **ITO** (120 nm), **ZnO** (30 nm), **P3HT:PC$_{61}$BM** (170-200 nm) and **PEDOT:PSS** with either HTL Solar (50 nm), HTL Solar N (50 nm) or HTL Solar 2 (150 nm), **Ag** (200 nm). Layers were deposited either by spin coating or by Doctor Blading. After each step thermal annealing of 15 minutes at 130 °C was performed.

A preliminary series of tests was performed by Dr. Stefan Schumann at Heraeus Deutschland GmbH & Co. KG. A semi-quantitative standard tape test method, the cross-cut tape test (Test Method B from ASTM D 3359-08 [59], Figure 5.15-a), was used on the half-cell **glass/ITO/ZnO/P3HT:PC$_{61}$BM/PEDOT:PSS**. In this case, all layers were deposited by spin coating.
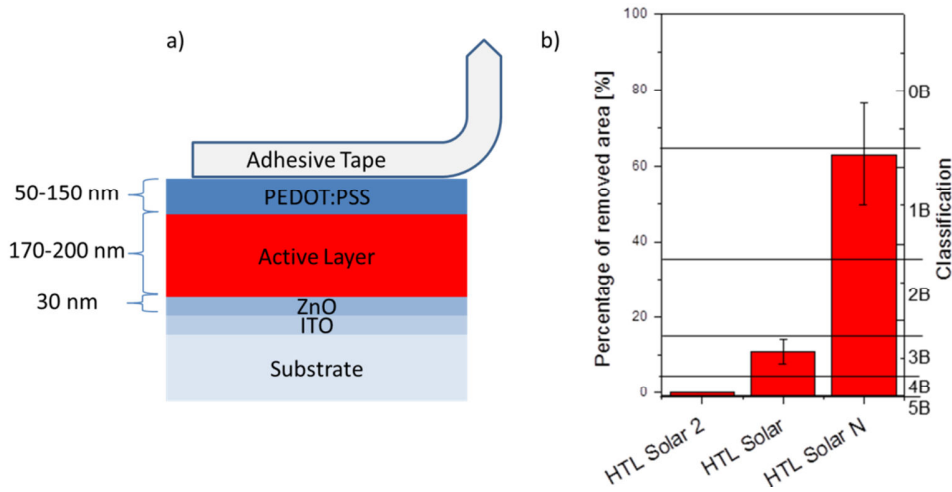
Figure 5.15 a) Layer stack and thicknesses of the samples used for the Cross-Cut Tape Test and b) percentage of removed area for three different PEDOT:PSS formulations with relative adhesion classes, according to [59].

As shown in Figure 5.15-b, upon tape removal the **PEDOT:PSS** top layer was removed from 11% and 63% of the tested area for, respectively, *HTL Solar* and *HTL Solar N* (adhesion classes of 3B and 1B, respectively). *HTL Solar 2* showed an adhesion improvement over the aqueous types with no area removal at all (class 5B), demonstrating superior adhesive properties.

The following step was to test inverted devices with the same layer stack, using the new developed technique. Complete devices, with the *AL* deposited by *Doctor Blading* and the *HTL* by *Spin Coating*, were prepared by Dr. Stefan Schumann.

The *Stress at Break* results (Figure 5.16-a) confirmed the superior adhesive properties of *HTL Solar 2* (0.44±0.07 MPa) on *HTL Solar* (0.38±0.05 MPa). Surprisingly, *HTL Solar N* (0.43±0.09 MPa) resulted to be almost as strong as *HTL Solar 2*, while in the *cross-cut tape test* it was the weakest by far. It is not uncommon that different adhesion tests, and thus different experimental conditions, lead to such different results.
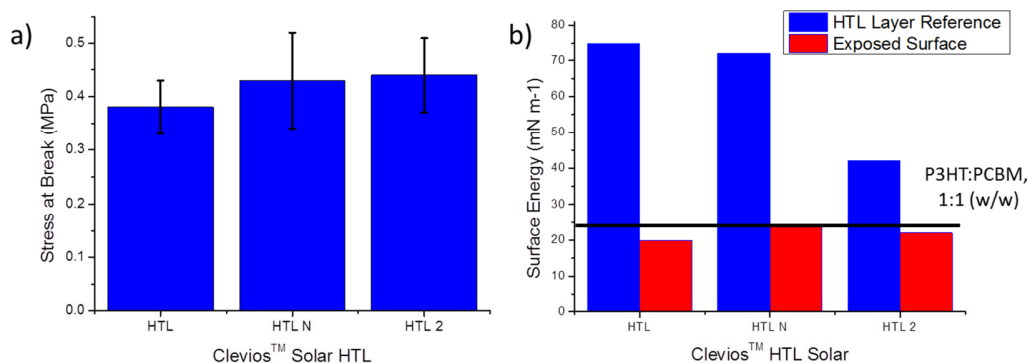
Figure 5.16 a) Stress at Break (MPa) for three different Clevios^TM HTL formulations and b) corresponding Surface Energy of the Lower half-cell.

In this case, it may be due to two different aspects that differentiate the *cross-cut tape* from the *pull-off test*. In the former, a very high strain is concentrated near the peel bend, while, in the latter, the strain concentrates where the structure is weaker. Secondly, in the *pull-off test* the adhesive is in contact with the same **Ag** electrode surface, while in the *cross-cut tape test*, the different interactions of the tape adhesive with the **PEDOT:PSS** layers can play a role.

The exposed surfaces, on top of created half-device, were analyzed by *contact angle* and their *surface energies* (Figure 5.16-b) were calculated, according to the Owen-Wendt Method (see Annex 3). The surface energy values of lower half-devices, showed that the *HTL* was completely removed in all cases. From AFM topography images (Figure 5.17) of the lower part of the three samples it was possible to see how differently the three **PEDOT:PSS** formulations interact with the active layer. The HTL sample surface is quite smooth with some shallow depression. HTL N presented no depression but the surface was 2.5 times rougher (Rq=4) than the HTL sample (Rq=1.6). HTL 2 showed deep and diffused depressions and its surface is 4 times rougher (Rq=6.5) than the HTL sample. The increased roughness can be associated to different interactions between the two layers. For the HTL sample the surface is similar to the pristine **P3HT:PC$_{61}$BM** layer, indicating poor interactions with the HTL and a brittle fracture. In the case of HTL N and HTL 2, the increased roughness and surface modifications are evidence of stronger interactions that lead to a fracture with a certain degree of plasticity, which dissipate more energy and thus a higher adhesive force.
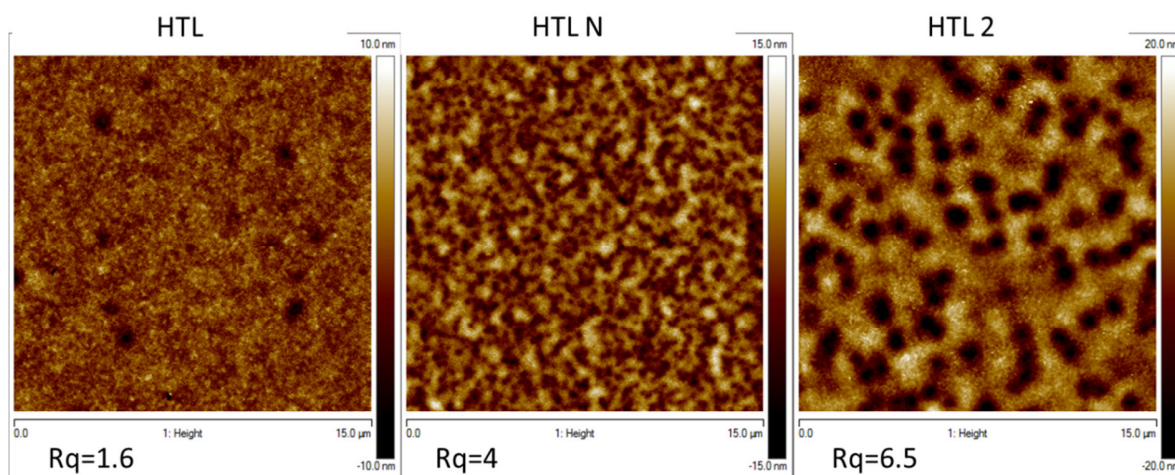
Figure 5.17 AFM-Peak Force QNM Height images of the lower half cells for three different Clevios^{TM} HTL formulations.

5.2.2.3 *Effect of the HTL Deposition Technique*

The **P3HT:PC$_{61}$BM** blend is the most studied system as active layer material in BHJ. The effect on blend morphology of several deposition [60]–[65] and post-deposition [41], [65]–[68] conditions have been investigated with the aim to understand the relationship between nanoscale phase-separation and device photovoltaic characteristics [69]. Achieving the optimal active layer morphology is essential to improve the device efficiency [70]–[72]. Vertical phase separation, as well as the better known lateral phase separation, is a critical aspect that deserves attention. Vertical phase separation is a well-known characteristic of many polymer blend systems [73], as well as in conjugated polymer [74]–[76] and **polymer:PC$_{61}$BM** [41], [61], [77]–[81] blends.

For a device's mechanical stability, as well as for its photovoltaic properties [72], [82], the nature of the layer composition and the interfaces in the layer stack are of capital importance [38]. The effect of two different deposition technique of the **PEDOT:PSS** suspension, spin-coating and doctor blading, on the adhesive strength of inverted devices has been studied. To do so, *Stress at Break* and surface energy of the corresponding half devices were once again measured (Figure 5.18).
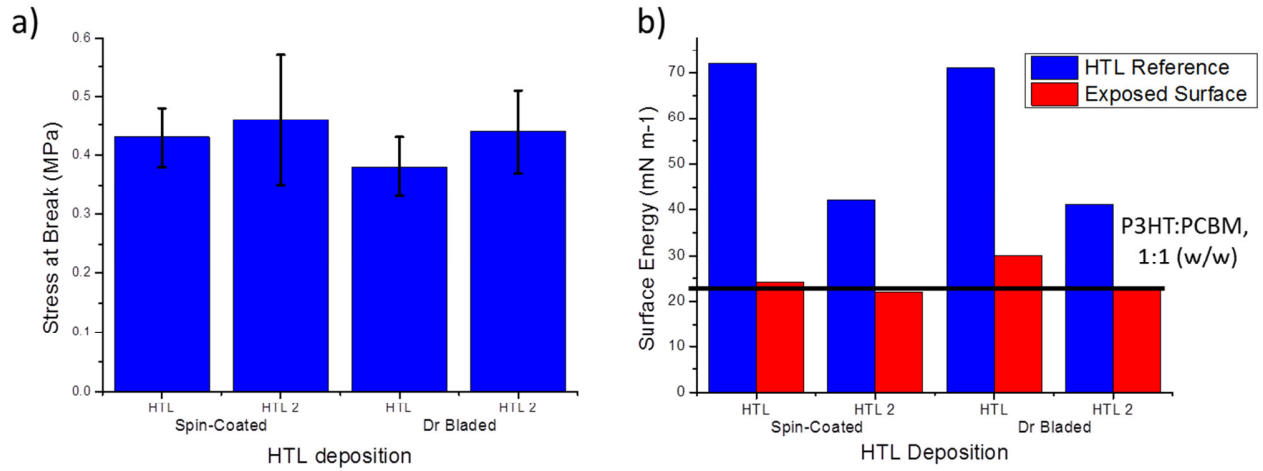
Figure 5.18 a) Stress at Break (MPa) for two Clevios[TM] HTL formulations deposed with different techniques and b) corresponding Surface Energy of the Lower half-cell.

For both HTL Solar and HTL Solar 2, the adhesive strength is improved when the **PEDOT:PSS** formulation is spin-coated rather than doctor bladed (Figure 5.18-a). Surface energy analysis indicate that the exposed surface of the lower half device (red bars) corresponds to the AL (black line) rather than to the HTL (blue bars) (Figure 5.18-b). The AFM surface topography (Figure 5.19) shows a different surface structuration, characterized by depressions, and a higher roughness in case of doctor bladed layers (Figure 5.19-bottom). As aforementioned, this higher roughness can be attributed to a plastic deformation during the fracture, expression of stronger interactions. In the case of HTL Solar, the strongest adhesion corresponded to the flatter samples (spin-coated) and not to the roughest (doctor bladed), while for HTL Solar 2 the values are comparable between them and higher than HTL Solar.
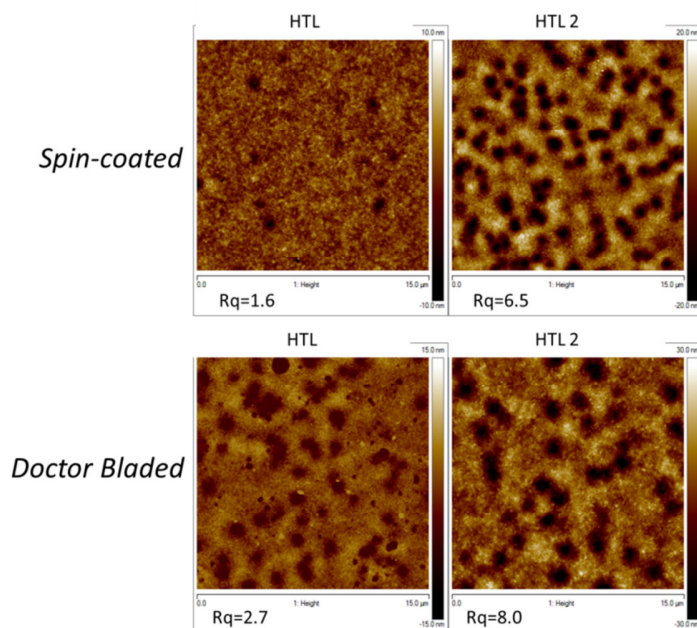
Figure 5.19 AFM-Peak Force QNM Height images of the lower half cells for two Clevios[TM] HTL formulations deposed by *Spin-coating* or *Dr Blading.*

Unfortunately, it has not been possible to investigate the morphology and phase segregation of the AL or HTL. Nonetheless, it is possible to speculate that these variations are related to a different composition at the interface (as better discussed in paragraph 5.2.2.4). These differences can be due to the different solvent systems and to the presence of additives that can drive the phase segregation in different directions [83], [84]. Also, the different layer drying can contribute in differentiating the lateral and vertical segregation [63], [67].

5.2.2.4 Application to Different HTL/AL Combination

After testing the three different **PEDOT:PSS** formulations (Clevios[TM] HTL Solar, HTL Solar N and HTL Solar 2), the study of two of these, HTL Solar and HTL Solar 2, have been extended by changing the donor polymer in the active layer. Besides **P3HT**, we selected two Low BandGap (LBG) polymers from the ESTABLIS polymer library: **PSBTBT** and **PDTSTzTz** (Figure 5.20). The **PSBTBT** was synthesized by myself, while the **PDTSTzTz** was synthesized by Dr. Graham Morse at Merck Chemicals Ltd.
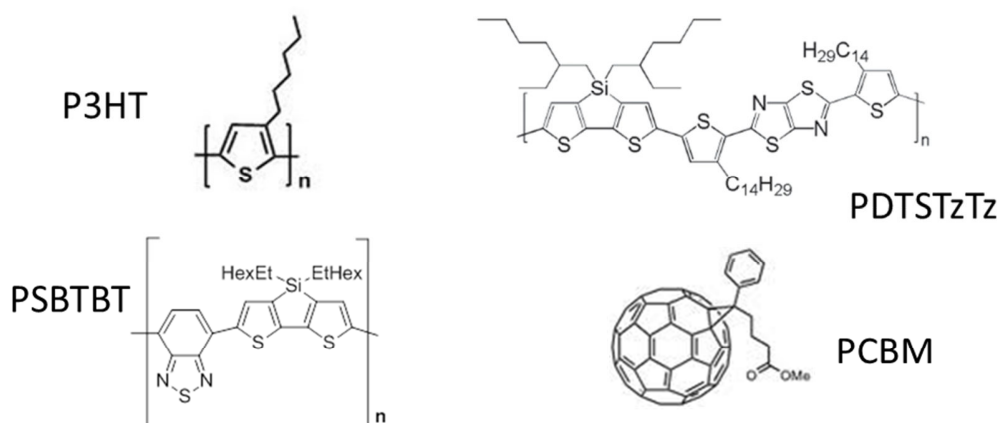
Inverted geometry devices with the layer stack: **ITO/ZnO/Active Layer/PEDOT:PSS/Ag** with the following layer thicknesses: **ITO** (120 nm), **ZnO** (30 nm), active layer with either **P3HT:PC$_{61}$BM**, 1:1 (170-200 nm), **PSBTBT:PC$_{61}$BM**, 1:2 (120 nm) or **PDTSTzTz**, 1:2 (100 nm) and **PEDOT:PSS** with either HTL Solar (50 nm) or HTL Solar 2 (150 nm), **Ag** (200 nm) were fabricated by Dr. Stefan Schumann at Heraeus Deutschland GmbH & Co. KG. Moreover, devices with all the layers listed in the previous stack, except the HTL, were prepared. The elimination of the HTL had as objective to obtain a comparative measure of the cohesion strength of the **polymer:PC$_{61}$BM** blend.

In the case of **P3HT:PC$_{61}$BM** as active layer (Figure 5.21-a), the adhesion force significantly varies between devices with HTL Solar or HTL Solar 2, as previously seen. In the other cases (Figure 5.21-b and c), the adhesion properties do not seem to be influenced by the **PEDOT:PSS** formulation. This can be due to many factors, such as polymer solubility, active layer morphology, etc. In particular, looking at the expected surface engineering behind HTL Solar 2, the polymer solubility can be the determining factor. It is worth mentioning that active layer cohesion is always higher than AL/HTL adhesion. Coherently the fracture in complete devices happens at the weakest point, which is the AL/**PEDOT:PSS** interface.
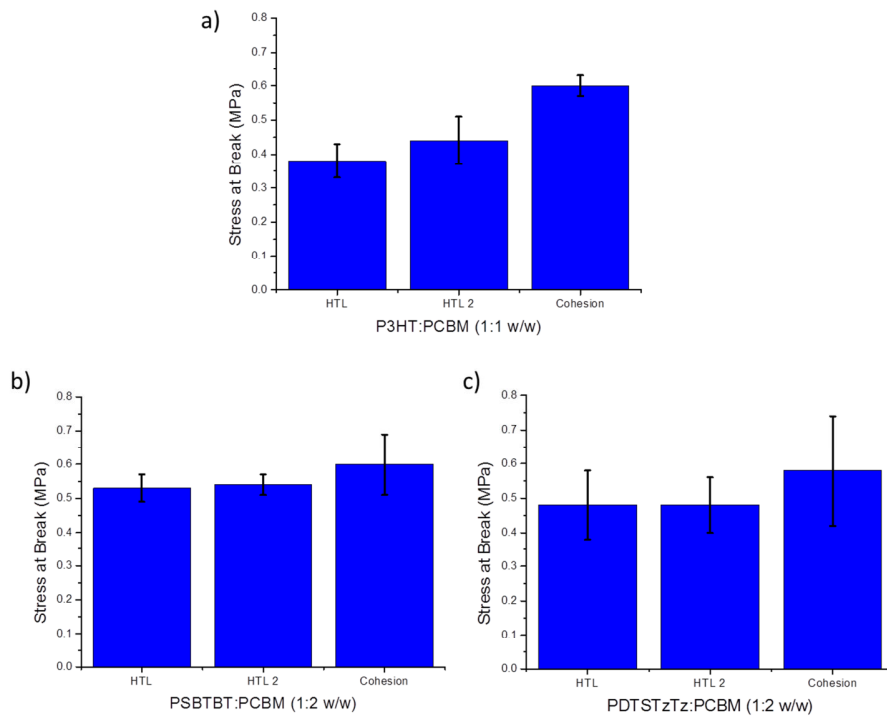
Figure 5.21 Stress at Break for the different AL/HTL combination and cohesion of the AL.

The surface energy values of the lower half devices, calculated according to the Owen-Wendt theory through contact angle measurements, are reported in Figure 5.22. For both HTL (black bar) and HTL 2 (red bar) half-devices, the fracture exposes the AL (reference values reported as blue bars) rather than the HTL (black and red lines), but the technique does not allow to precisely determine if there is any difference between the surfaces with HTL Solar or HTL Solar 2.
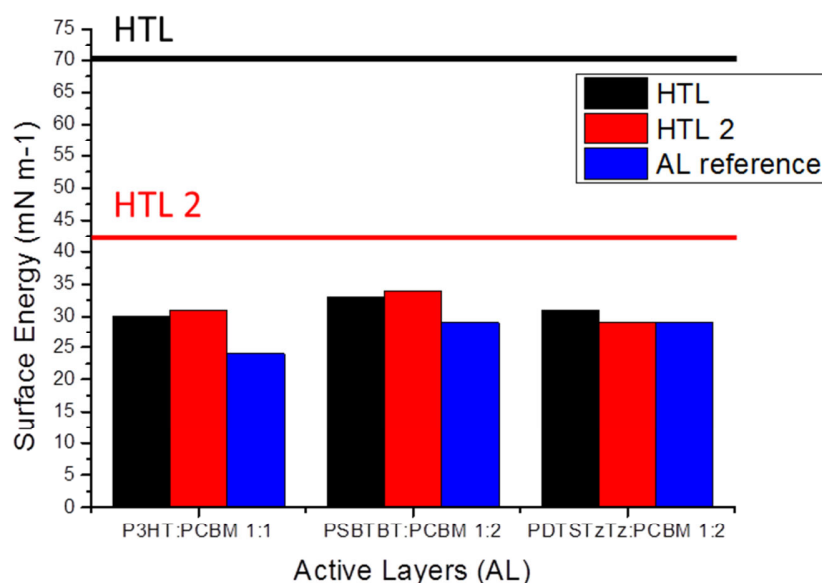
The ratio of carbon on sulfur atomic species was taken as experimental factor to identify the surface composition, since these elements are present in both the considered layers (theoretical and experimental values, for polymers and blends, are reported in Table 5.3).

Table 5.3 Theoretical and experimental C/S ratio for utilized donor materials and blends (data provided by Aurélien Tournebize).

	Theo. C/S (Polymer)	Exp. C/S (Polymer)	Exp. C/S (Polymer:PC$_{61}$BM)
P3HT	10.1	10.5	13.2
PSBTBT	11.0	11.6	16.0
PCDTSTzTz	10.4	10.5	18.0

The surface analysis of the sample with different AL (**P3HT:PC$_{61}$BM**, **PSBTBT:PC$_{61}$BM** and **PDTSTzTz:PC$_{61}$BM**), has been completed only for P3HT:PC$_{61}$BM devices. Therefore, only the case of **P3HT:PC$_{61}$BM** will be thoroughly discussed here and a comparison with the other AL materials are presented at the end of the paragraph, based on first results.

With this aim, the C1s and S2p core levels were chosen as markers since they were very different in the neat materials, allowing an easy identification. In Figure 5.23, the spectra of these core levels for the upper half-devices of **P3HT:PC$_{61}$BM** devices are shown; for comparison the spectra

for neat **P3HT:PC$_{61}$BM** and **PEDOT:PSS** reference layers are reported. From these spectra it is possible to establish that the fracture happens at the interface between AL and HTL, but with some differences. For the **HTL Solar** sample, both core levels strongly correspond to the reference **HTL Solar** layer, indicating that the fracture really happens at the interface and only traces of the opposite layer are present. On the other hand, the C1s and S2p core levels of **HTL Solar 2** samples have a more mixed character, indicating larger amounts of AL on the upper part. Thus, the fracture plane slightly moved inside the AL.
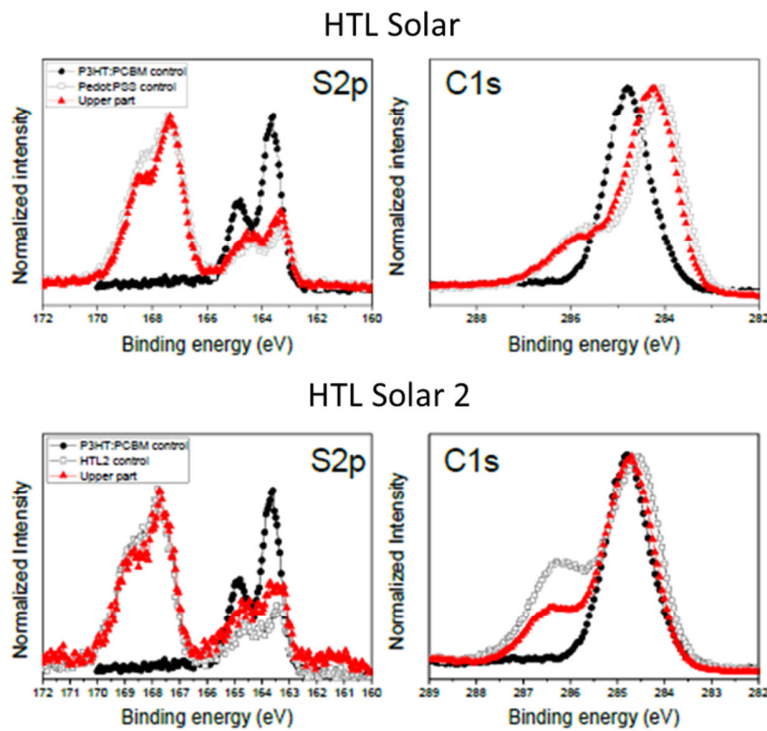
Figure 5.23 Normalized intensity of S2p and C1s core levels of upper half-devices (red) with P3HT:PC$_{61}$BM (1:1 w/w) as active layer and corresponding bare blend (black) and HTL (white) layers for comparison (data provided by Aurélien Tournebize).

Glass/ITO/ZnO/**P3HT:PC$_{61}$BM**/**HTL**/Ag			
C/S **HTL Solar** *Control*	*C/S* **Blend** *Control*	*C/S Upper part*	*C/S Lower part*
7.4	13.2	8.3	12.7
		0.17**Blend**+0.83**HTL Solar**	0.91**Blend**+0.09**HTL Solar**
C/S **HTL Solar 2** *Control*		*C/S Upper part*	*C/S Lower part*
16.4		20.3	11.7
		>	<

From the C/S ratio reported in Table 5.4, it is possible to see that **HTL Solar 2** is reacher in carbon than **HTL Solar**. The corresponding **HTL 2** upper part is even richer in carbon, suggesting the presence of a **PC$_{61}$BM** rich layer. Conversely, the lower part shows a C/S value closer to neat **P3HT** compared to HTL samples. In Figure 5.24 a schematic representation of the fracture path for the two specimen is shown (a and b), together with the upper half devices (c and d). The fracture moves into the active layer passing from HTL to HTL 2: the exposed surface is mainly **PEDOT:PSS** with traces of AL for HTL half-devices (Figure 5.24-c), while it is AL rich in **PC$_{61}$BM** (Figure 5.24-d, grey circles) for HTL 2.

These results showed that the better wettability and the partial swelling of the AL surface, due to the organic solvents formulation and to the presence of compatibilizers, contribute to the enhanced adhesion force. The improved wettability allows a better contact between the molecules of the two systems, promoting the occurrence of long range molecular forces. Moreover the partial swelling of the surface can promote the interdiffusion of the polymer chain, to form an intermixed layer of entangled chains that enhance the overall adhesion (Figure 5.25-a). Another possible effect, which need further investigation, is the reorganization of the top of the AL surface, which results enriched in **PC$_{61}$BM**, as seen by XPS analysis (Figure 5.25-b).
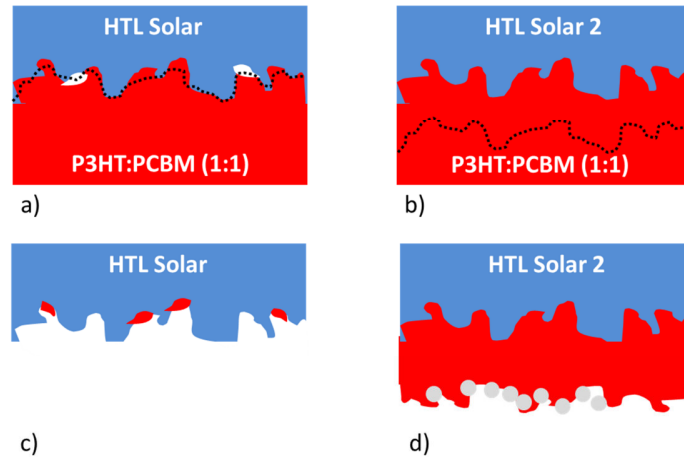
Figure 5.24 Schematic representations of AL/HTL interface and supposed fracture path in case of P3HT:PC$_{61}$BM as Al and HTL Solar (a) and HTL solar 2 (b) devices; c) and d) represents schematically the surface of the upper half-devices with d) reacher in PC$_{61}$BM.

For **PSBTBT** and **PDTSTzTz** based devices, the surface characterization showed an analogous picture, with the fracture that moves inside the AL changing HTL Solar with HTL Solar 2. The reason why in these two cases there is no improvement in adhesive strength is still not clear. It can be speculated that the change in the w/w ratio of the **Polymer:PC$_{61}$BM** blend, i.e., 1:2 and not 1:1 as for **P3HT:PC$_{61}$BM**, plays a fundamental role in the diffusion of **PC$_{61}$BM** upon surface reconstruction. Further experiments, varying systematically the blend composition would be necessary to have a complete and clear base for discussion.
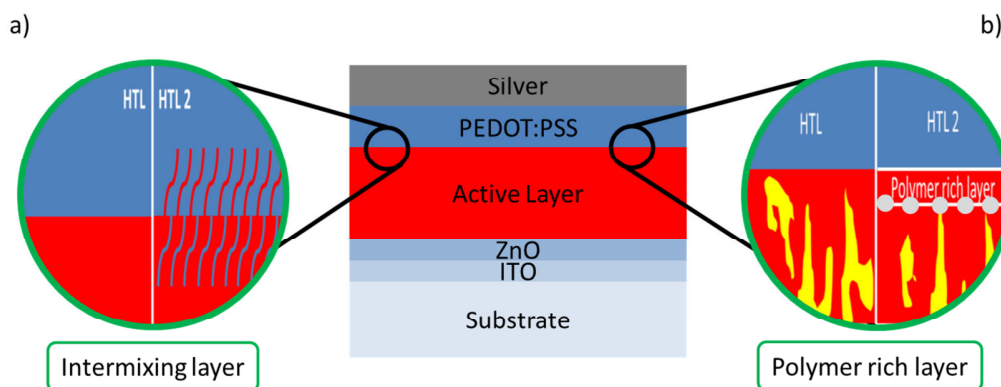
Figure 5.25 Schematic representation of the two speculated effects of the different PEDOT:PSS formulations.

5.2.3 Block Copolymers as Adhesion-Enhancing Interlayers

Adhesion strength can be increased when block (or graft) polymers are added to the interface, working like a molecular bridge between the two homopolymers [85], [86]. The idea behind this surface engineering is to replace the entanglement network, that is present in the homopolymers

layers (or as if the same polymer was on both sides of the interface), with some sort of molecular connections. This effect can be obtained by block copolymers that reside at the interface and entangle with both polymers, or by chemical reaction at the interface. Examples of connector chains are presented in Figure 5.26: di- or tri-block copolymers (Figure 5.26-a and b), random copolymers (Figure 5.26-c), or polymers with reactive functional groups (Figure 5.26-d and e), which can graft at the interface. In practice these connector molecules must satisfy three requirements to be effective: i) a thermodynamic driving force must exist for their segregation to, or reaction across, the interface between the two phases of the blend, ii) the kinetics of this segregation or reaction must ensure a relatively high connectors density and iii) they must be mechanically effective in reinforcing the interface. While the first two of these conditions are controlled by thermodynamics and kinetics, respectively, the latter is related to the mechanical properties of the interfaces.
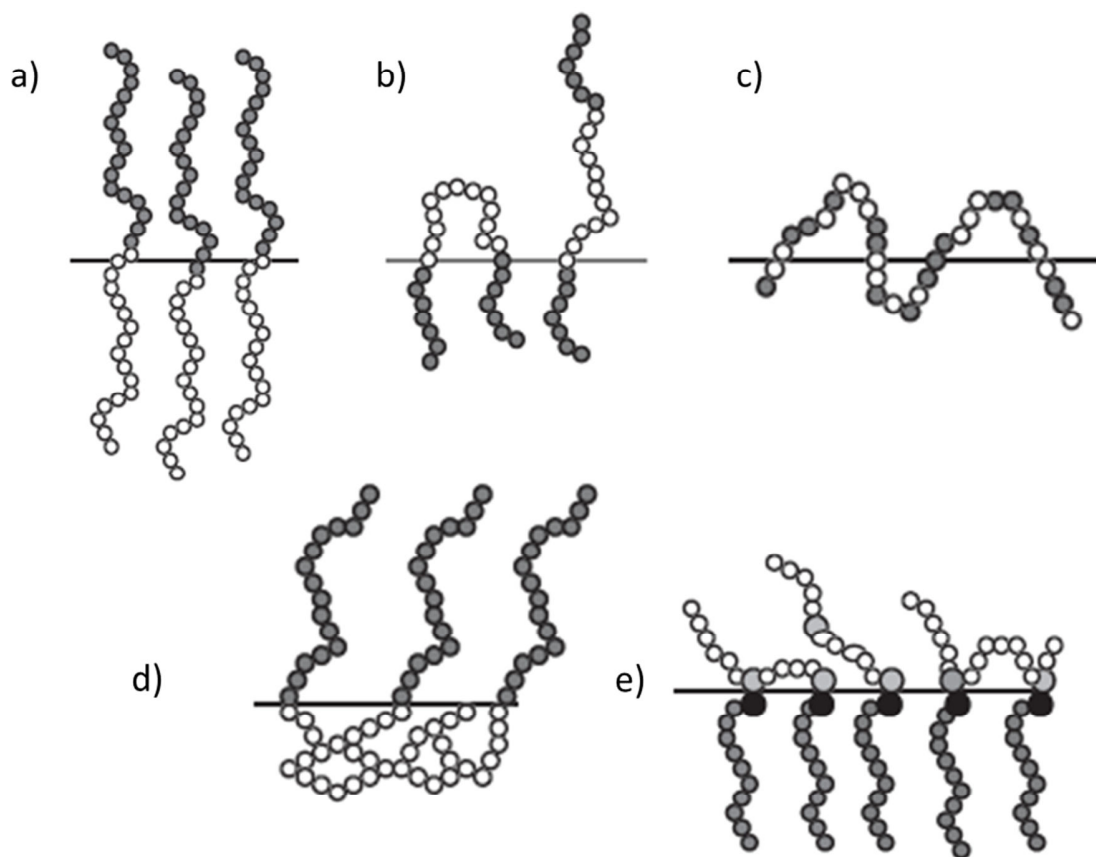
Figure 5.26 Schematic of connecting chains at an interface: a) diblock copolymers; b) triblock copolymers; c) random copolymers; d) end-grafted chains; e) multiply grafted chains [85]**.**

An example of reactive end-chain polymers is given by the introduction of grafted copolymers at the PP/poly(vinylidene fluoride) (**PVDF**) interface, which increased adhesion strength by a factor of

15 [87]. Styrene maleic anhydride random copolymer (**SMA-8wt.% MA**) and poly[methylene (phenylene isocyanate)] (**PMPI**), dual compatibilizers, were demonstrated to bridge the interface of **PET** forming **PET-co-PMPI-co-SMA** allowing for improved mechanical properties [88]. Fracture toughness also increased at the interface between nylon 6 (**Ny6**) and **PP** with the introduction of maleic anhydride grafted polypropylene (**MAPP**); fracture toughness increased as the intermolecular reactions between **MAPP** and **Ny6** increased [89]. Creton et al. [85] investigated three polymer/diblock copolymer interfacial systems: polystyrene (**PS**) and poly(2-vinylpyridine) (**PVP**) reinforced with diblock copolymers of **PS-PVP**; poly(methyl methacrylate) (**PMMA**) and **PS** reinforced with diblock copolymers of **PMMA-PS** and the **PMMA** and poly(phenylene oxide) (**PPO**) reinforced by diblock copolymers of **PMMA-PS**. All of these systems showed an improved adhesion toughness.

In OPV, a very limited amount of examples of interlayer materials placed between a photoactive layer and a hole/electron transporting layer (HTL/ETL) is reported in the literature [90]–[92]. Hau *et al.* [91] introduced a **PC$_{61}$BM** self assembled monolayer (**C$_{60}$-SAM**) in inverted geometry devices, between the ETL (**ZnO**) and the AL (**P3HT:PC$_{61}$BM**). The improved performance was attributed to an enhanced electronic coupling at the inorganic and organic interface from the **C60-SAM** through photoinduced charge transfer. The SAM helped to improve charge selectivity and reduced the charge recombination losses at the interface leading to improved FFs and photocurrent. In 2011, Su Kang et al. [90] introduced a cross linkable polymer in a normal geometry device, between the HTL (**PEDOT:PSS**) and the AL. A photo-curable precursor was deposed on the **PEDOT:PSS** layer and then photo-polymerized, before AL deposition. The device was completed with a **LiF** layer as ETL and a **Al** electrode. The introduction of UV cross linkable layer reduced the leakage current and improved charge extraction due to effective electron blocking. Furthermore, the interlayer was found to be more hydrophobic than the **PEDOT:PSS** layer, which enhances the wetting of the photoactive layer. Deschler et al. [92] showed the influence of a thin donor interlayer, sandwiched between the HTL (PEDOT:PSS) and the AL, on the performance of normal geometry device. The donor interlayer (**P3HT**, **PSBTBT** and **PTB7**) was deposited on top of the **PEDOT:PSS** layer and its thickness was around 30 nm. Importantly, the thickness of the photoactive layer was reduced by approximately 30 nm compared to control devices. For all of the bi-layer devices, an increase in V_{oc}, J_{sc} and *FF* was observed, improving the overall efficiency. This was attributed to an increase in absorption, due to an additional amount of

photo-absorbing material. Moreover, a decrease in recombination, probably due to a limitation of **PEDOT:PSS** layer imperfections by polymer filling, was observed.

5.2.3.1 Aim of the Study

In order to improve adhesion on the weakest **PEDOT:PSS**/photoactive layer interface, a new interlayer copolymer poly(isobutyl p-styrene sulfonate)-block-poly(dodecyl p-styrene sulfonate) (**PiBSS-b-PDDSS**) was designed and synthesized by Joanna Kolomanska (ESR7) in the framework of ESTABLIS project.

In this case, the strategy comprised a production of a sandwich structure with a very thin layer of hydrophobic **PiBSS-b-PDDSS** (Figure 5.27-a) and then its thermal transformation into amphiphilic **PSS-b-PDDSS** through removal of isobutyl protecting group (Figure 5.27-b). Such a copolymer could interact with **PEDOT:PSS** layer through hydrophilic **PSS** block as well as reach the photoactive layer via **PDDSS** hydrophobic block. To better evaluate the effect of the block copolymers, complete devices with both **PiBSS-b-PDDSS** (Figure 5.27-c) and **PSS-b-PDDSS** (Figure 5.27-d) were fabricated and characterized by Joanna Kolomanska and Dr. Stefan Schumann at Heraeus Deutschland GmbH & Co. KG. At the same time the effect of the chain length of the poly(dodecyl-p-styrene sulfonate) block (10, 20 and 31 units) has been investigated (Table 5.5), maintaining the poly(isobutyl p-styrene sulfonate) block (16 units) constant. The detailed synthesis and characterization of the block copolymers and the device fabrication are described in Joanna Kolomanska's PhD thesis, Aston University, UK.
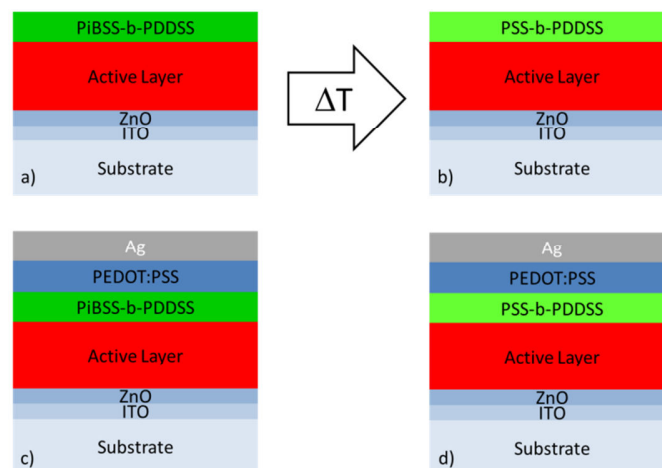
Figure 5.27 Interfacial layer position in the layer stack, a) before and b) after thermal deprotection; c) and d) layer stack of devices used in this study.

Table 5.5 Chemical characteristics of block-copolymers used in the interlayer (data from Joanna Kolomanska).

Poly(isobutyl p-styrene sulfonate)$_n$-block-poly(dodecyl p-styrene sulfonate)$_m$				
Polymer	m	n	M$_n$ (g/mol)	Đ
JK189	16	10	7600	1.2
JK190	16	20	11300	1.2
JK195	16	31	15000	1.3

5.2.3.2 Adhesive Properties of PiBSS-b-PDDSS vs PSS-b-PDDSS Interlayers

In Figure 5.28-a, the *Stress at Break* values for devices which include the new layer, before and after deprotection, in their layer stack are shown. For ease of presentation, these devices will be indicated with respect to the block copolymer used, i.e., JK189, JK190 and JK195 (Table 5.5), with the corresponding deprotected copolymer interlayers assessed as JK189T, 190T and 195T. The **PiBSS-b-PDDSS** layer strongly reduces the adhesive strength in the devices (Figure 5.28-a). After deprotection the adhesion is improved (Figure 5.28-a), but it is still lower than the one of the reference devices, where the interlayer is not integrated. The fact that the **PiBSS-b-PDSS** interlayer reduces adhesion was somehow expected, since it does not contribute to compatibilize the active layer and the **PEDOT:PSS** layer (Clevios[TM] HTL Solar), due to its hydrophobic nature. Moreover, in inverted devices, the formation of an intermixed **P3HT/PSS** layer is limited due to vertical phase segregation [93]. This layer is considered of primary importance in determining the different adhesive/cohesive failure mechanism in normal and inverted devices [38]. The interlayer could completely prevent the formation, not only of this mixed layer, but also of any interfacial complex resulting in the observed adhesion.

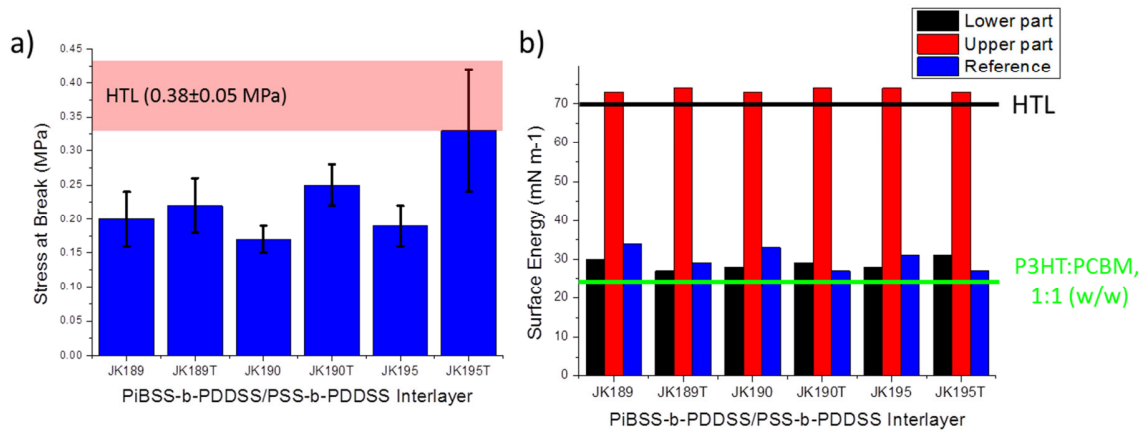**Figure 5.28 a) Stress at Break of devices including the new interlayer before (JKxxx) and after (JKxxxT) deprotection and corresponding value for devices without interlayer; b) surface energy of lowere and upper half-devices with HTL and al references for comparison.**

The devices with deprotected **PSS-b-PDDSS** interlayer, showed improved adhesive properties when compared to the pristine layer (Figure 5.28-a). This can be attributed to an entanglement of the deprotected chain (**PSS**) within the **PEDOT:PSS** layer and not to an improved compatibility of the two layers. In fact, surface energy values for layers of these deprotected polymers were surprisingly lower than the corresponding pristine materials (Figure 5.28-b, blue bars). This reduced wettability of the **PEDOT:PSS** suspension contributes in reducing the contact and thus the establishing of long-range molecular forces. Surface energy values also show that, in all cases, the fracture happens at the interfaces between the interlayer and the **PEDOT:PSS** layer. From Figure 5.28-b, one can see that the surface energy of the upper half-device (red bars) is comparable to the HTL Solar reference (black line), while the lower half-device (black bars) with the interlayer one (blue bars).

This is confirmed by optical micrograph images (Figure 5.29, Figure 5.30 and Figure 5.31), showing how the lower part corresponds to the reference layer. Moreover, for **JK189** and **JK190** (Figure 5.29 and Figure 5.30), it is possible to see a phase segregation of the block copolymer after deprotection. This phase segregation, concurrently with the low wettability, could cause the presence of voids or flaws between the two layers. These defects could strongly reduce the efficiency and the lifetime of the devices. Light-Beam Induced-Current Microscopy (LBIC) images could easily show if the phase segregation has a negative effect on the formation of an effective interface.

Figure 5.29 Optical micrograph, before and after deprotection, of upper and lower half-devices containing JK189 and corresponding bare layer as reference.
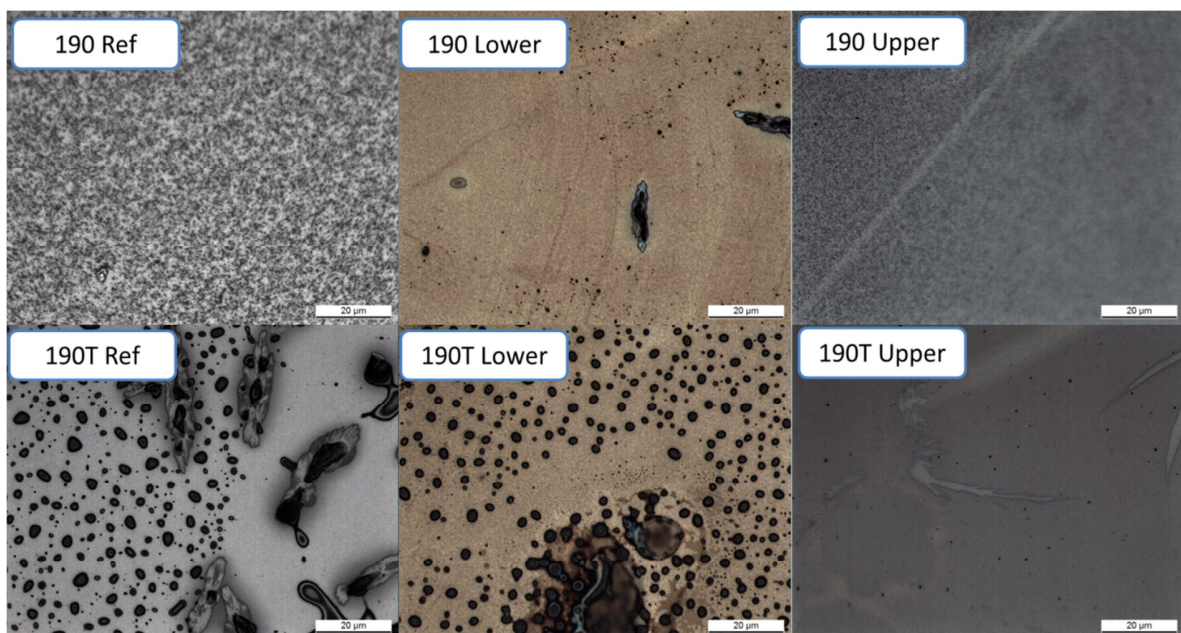
Figure 5.30 Optical micrograph, before and after deprotection, of upper and lower half-devices containing JK190 and corresponding bare layer as reference.

For **JK195** (Figure 5.31), a certain degree of phase segregation is visible, but the main feature is the strong phase segregation of **PC$_{61}$BM**, that forms crystals all over the surface reference and at the interface. This is due to the longer time required to thermally deprotected the **PiBSS** block of the

copolymer, that allows the diffusion and the aggregation of **PC$_{61}$BM** at the interface. It has been shown that a micrometer size the growth of mm-size **PC$_{61}$BM** crystallites size was found to improved the cohesion of the **P3HT:PC$_{61}$BM**, due to a pull-out toughening mechanism. For such large crystals, the cohesive energy or energy required to propagate the debond might be significantly increased due to the energy dissipated by stretching the crystallites. A larger cluster height and fraction of clusters allows for a greater degree of resistance to pull- out as the BHJ is being debonded.

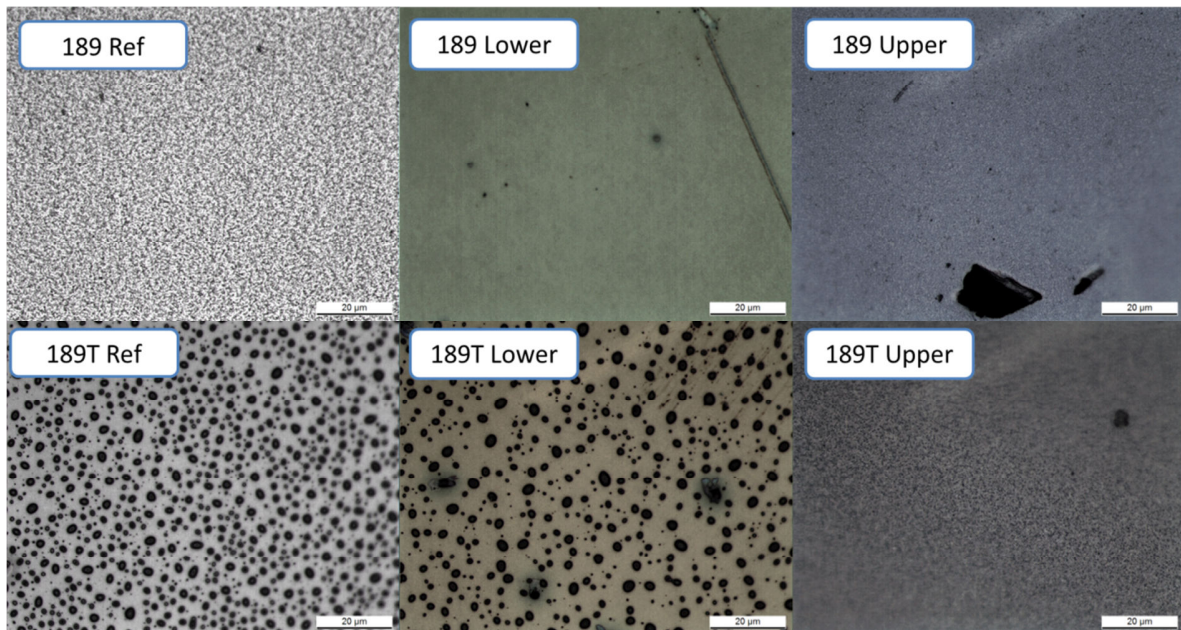**Figure 5.31 Optical micrograph, before and after deprotection, of upper and lower half-devices containing JK195 and corresponding bare layer as reference.**

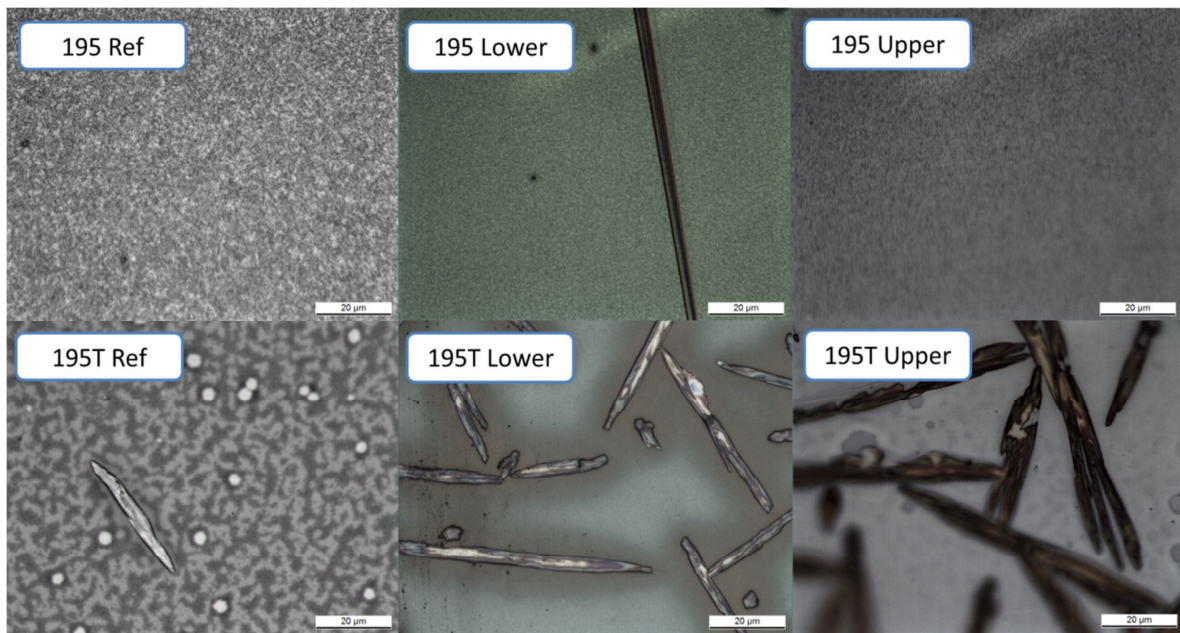XPS analyses on these samples are currently ongoing. The first results, taking the C/S ratio as parameters, do not show any clear picture. A complete discussion of these partial results, is reported in Aurélien Tournebize thesis, Tubingen University, Germany.

5.3 Conclusion

In this chapter one of the long-term durability issues of OPV have been assessed. An experimental set-up to investigate the mechanical integrity of multilayered structures was developed and applied to inverted geometry OPV devices. Several materials for the AL and HTL have been tested and the fracture path have been identified. In particular, new materials developed with the aim of improving the weaknesses within the layer stack have been tested. The physical and chemical characterization of the half-devices produced upon destructive testing allowed us to identify and influence some of the involved parameters.

The phase segregation of each layer influences its mechanical properties, while the vertical phase separation determines the nature of the interface with the following layer. The chemical composition of the two layers at the interface is fundamental for the establishment of physical and chemical bonding. It has been demonstrated that the use of a better solvent system and additives is a viable route to improve the otherwise weak adhesion between two uncompatible layers. The use of an additional layer was explored too, but with little success. The design of the compatibilizer and its processing need to need to be further developed, before being able to discard this route.

The manipulation of the nanoscale morphology and phase separation (both lateral and vertical) of polymer blends is not an easy task. Tuning them with the double objective of improving both photovoltaic properties and chemical/mechanical stability is an Herculean task. To achieve a deeper understanding of such a complex, cross-field and cutting-edge research field more efforts from the whole scientific community are needed.

5.4   References

[1]   T. J. McMahon, "Accelerated testing and failure of thin-film PV modules," *Prog. Photovoltaics Res. Appl.*, vol. 12, no. 23, pp. 235–248, 2004.

[2]   R. H. Dauskardt, M. Lane, Q. Ma, and N. Krishna, "Adhesion and debonding of multi-layer thin film structures," *Eng. Fract. Mech.*, vol. 61, pp. 141–162, Aug. 1998.

[3]   A. A. Abdallah, "Mechanical integrity of multi-layered structures for flexibles displays," 7AD.

[4]   M. Jørgensen, K. Norrman, and F. C. Krebs, "Stability/degradation of polymer solar cells," *Sol. Energy Mater. Sol. Cells*, vol. 92, no. 7, pp. 686–714, Jul. 2008.

[5]   M. O. Reese, M. S. White, G. Rumbles, D. S. Ginley, and S. E. Shaheen, "Optimal negative electrodes for poly(3-hexylthiophene): [6,6]-phenyl C61-butyric acid methyl ester bulk heterojunction photovoltaic devices," *Appl. Phys. Lett.*, vol. 92, no. 5, 2008.

[6]   M. T. Lloyd, C. H. Peters, A. Garcia, I. V. Kauvar, J. J. Berry, M. O. Reese, M. D. McGehee, D. S. Ginley, and D. C. Olson, "Influence of the hole-transport layer on the initial behavior and lifetime of inverted organic photovoltaics," *Sol. Energy Mater. Sol. Cells*, vol. 95, no. 5, pp. 1382–1388, 2011.

[7]   B. Paci, a. Generosi, V. R. Albertini, P. Perfetti, R. De Bettignies, M. Firon, J. Leroy, and C. Sentein, "In situ energy dispersive x-ray reflectometry measurements on organic solar cells upon working," *Appl. Phys. Lett.*, vol. 87, no. 19, pp. 1–3, 2005.

[8]   B. Paci, A. Generosi, V. R. Albertini, P. Perfetti, R. De Bettignies, J. Leroy, M. Firon, and C. Sentein, "Controlling photoinduced degradation in plastic photovoltaic cells: A time-resolved energy dispersive x-ray reflectometry study," *Appl. Phys. Lett.*, vol. 89, no. 4, pp. 7–10, 2006.

[9]   K. Kawano, R. Pacios, D. Poplavskyy, J. Nelson, D. D. C. Bradley, and J. R. Durrant, "Degradation of organic solar cells due to air exposure," *Sol. Energy Mater. Sol. Cells*, vol. 90, no. 20, pp. 3520–3530, 2006.

[10]   M. O. Reese, A. J. Morfa, M. S. White, N. Kopidakis, S. E. Shaheen, G. Rumbles, and D. S. Ginley, "Pathways for the degradation of organic photovoltaic P3HT:PCBM based devices," *Sol. Energy Mater. Sol. Cells*, vol. 92, no. 7, pp. 746–752, 2008.

[11]   S. R. Dupont, E. Voroshazi, P. Heremans, and R. H. Dauskardt, "The effect of anneal, solar irradiation and humidity on the adhesion/cohesion properties of P3HT:PCBM based inverted polymer solar cells," 2012, pp. 003259–003262.

[12]   S. I. Na, S. S. Kim, J. Jo, and D. Y. Kim, "Efficient and Flexible ITO-Free Organic Solar Cells Using Highly Conductive Polymer Anodes," *Adv. Mater.*, vol. 20, p. 4061–+, 2008.

[13]   G. Fourche, "An overview of the basic aspects of polymer adhesion . Part I: Fundamentals," *Polym. Eng. Sci.*, vol. 35, no. 12, pp. 957–967, 1995.

[14]   K. Kendal, *Molecular Adhesion and its Applications*. 2001.

[15]   F. M. Fowkes, B. L. Butler, P. Schissel, G. B. Butler, N. J. DeLollis, J. S. Hartman, R. W. Hoffman, O. T. Inal, W. G. Miller, and H. G. Tompkins, "Basic research needs and opportunities at the solid-solid interface: adhesion, abrasion and polymer coatings," *Mater. Sci. Eng.*, vol. 53, no. 1, pp. 125–136, 1982.

[16]   F. Awaja, M. Gilbert, G. Kelly, B. Fox, and P. J. Pigram, "Adhesion of polymers," *Prog. Polym. Sci.*, vol. 34, no. 9, pp. 948–968, 2009.

[17]   A. Bousquet, H. Awada, R. C. Hiorns, C. Dagron-Lartigau, and L. Billon, "Conjugated-polymer grafting on inorganic and organic substrates: A new trend in organic electronic materials," *Prog. Polym. Sci.*, vol. 39, no. 11, pp. 1847–1877, 2014.

[18]   S. S. and J.-L. B. W. R. Salaneck, "Conjugated polymer surfaces and interfaces. Electronic and chemical structure of interfaces for polymer light emitting diode devices," *Polym. Int.*, vol. 43, no. 1, 1996.

[19]   H. Hertz, "Über die Berührung fester elastischer Körper," *J. für die reine und Angew. Math.*, vol. 171, pp. 156–171, 1881.

[20]   K. L. Johnson, K. Kendall, and a. D. Roberts, "Surface Energy and the Contact of Elastic Solids," *Proc. R. Soc. A Math. Phys. Eng. Sci.*, vol. 324, no. 1558, pp. 301–313, 1971.

[21]   B. V. Derjaguin, V. M. Muller, and Y. P. Toporov, "Effect of contact deformations on the adhesion of particles," *Prog. Surf. Sci.*, vol. 53, no. 2, pp. 314–326, 1975.

[22]   D. Maugis, "Adhesion of spheres: The JKR-DMT transition using a dugdale model," *J. Colloid Interface Sci.*, vol. 150, no. 1, pp. 243–269, 1992.

[23]   H. ZENG, *Polymer Adhesion, Friction and Lubrication*. Wiley, 2013.

[24]   R. Lacombe, *Adhesion Measurement Methods*. 2005.
[25]   H.-J. Butt, B. Cappella, and M. Kappl, "Force measurements with the atomic force microscope: Technique, interpretation and applications," *Surf. Sci. Rep.*, vol. 59, pp. 1–152, Oct. 2005.
[26]   F. L. Leite, C. C. Bueno, A. L. Da Róz, E. C. Ziemath, and O. N. Oliveira, *Theoretical models for surface forces and adhesion and their measurement using atomic force microscopy*, vol. 13, no. 10. 2012.
[27]   "Adhesion forces. AFM-probes, atomic force microscope (AFM, STM, SPM, RAMAN, SNOM)." [Online]. Available: http://www.ntmdt.com/spm-basics/view/adhesion-forces. [Accessed: 28-Aug-2015].
[28]   A. Noy, C. D. Frisbie, L. F. Rozsnyai, M. S. Wrighton, and C. M. Lieber, "Chemical Force Microscopy: Exploiting Chemically-Modified Tips To Quantify Adhesion, Friction, and Functional Group Distributions in Molecular Assemblies," *J. Am. Chem. Soc.*, vol. 117, no. 30, pp. 7943–7951, Aug. 1995.
[29]   K. Zeng, Z.-K. Chen, L. Shen, and B. Liu, "Study of mechanical properties of light-emitting polymer films by nano-indentation technique," *Thin Solid Films*, vol. 477, no. 1–2, pp. 111–118, Apr. 2005.
[30]   H.-C. Li, K. Koteswara Rao, J.-Y. Jeng, Y.-J. Hsiao, T.-F. Guo, Y.-R. Jeng, and T.-C. Wen, "Nano-scale mechanical properties of polymer/fullerene bulk hetero-junction films and their influence on photovoltaic cells," *Sol. Energy Mater. Sol. Cells*, vol. 95, no. 11, pp. 2976–2980, Nov. 2011.
[31]   J. Andersons, S. Tarasovs, and Y. Leterrier, "Evaluation of thin film adhesion to a compliant substrate by the analysis of progressive buckling in the fragmentation test," *Thin Solid Films*, vol. 517, pp. 2007–2011, Jan. 2009.
[32]   D. Tahk, H. H. Lee, and D.-Y. Khang, "Elastic Moduli of Organic Electronic Materials by the Buckling Method," *Macromolecules*, vol. 42, no. 18, pp. 7079–7083, Sep. 2009.
[33]   O. Awartani, B. I. Lemanski, H. W. Ro, L. J. Richter, D. M. DeLongchamp, and B. T. O'Connor, "Correlating Stiffness, Ductility, and Morphology of Polymer:Fullerene Films for Solar Cell Applications," *Adv. Energy Mater.*, vol. 3, pp. 399–406, 2013.
[34]   B. Babatope, A. Onobu, O. O. Adewoye, and W. O. Soboyejo, "Effect of Switching on Metal-Organic Interface Adhesion Relevant to Organic Electronic Devices," vol. 2013, no. November, pp. 299–306, 2013.
[35]   T. Tong, B. Babatope, S. Admassie, J. Meng, O. Akwogu, W. Akande, and W. O. Soboyejo, "Adhesion in organic electronic structures," *J. Appl. Phys.*, vol. 106, no. 8, p. 083708, 2009.
[36]   D. Wood, I. Hancox, T. S. Jones, and N. R. Wilson, "Quantitative Nanoscale Mapping with Temperature Dependence of the Mechanical and Electrical Properties of Poly(3-Hexythiophene) by Conductive Atomic Force Microscopy," *J. Phys. Chem. C*, p. 150427142253007, 2015.
[37]   S. R. Dupont, M. Oliver, F. C. Krebs, and R. H. Dauskardt, "Interlayer adhesion in roll-to-roll processed flexible inverted polymer solar cells," *Sol. Energy Mater. Sol. Cells*, vol. 97, pp. 171–175, Feb. 2012.
[38]   S. R. Dupont, E. Voroshazi, P. Heremans, and R. H. Dauskardt, "Adhesion properties of inverted polymer solarcells: Processing and film structure parameters," *Org. Electron. physics, Mater. Appl.*, vol. 14, no. 5, pp. 1262–1270, 2013.
[39]   S. R. Dupont, E. Voroshazi, D. Nordlund, K. Vandewal, and R. H. Dauskardt, "Controlling Interdiffusion, Interfacial Composition, and Adhesion in Polymer Solar Cells," *Adv. Mater. Interfaces*, p. n/a–n/a, 2014.
[40]   V. Brand, C. Bruner, and R. H. Dauskardt, "Cohesion and device reliability in organic bulk heterojunction photovoltaic cells," *Sol. Energy Mater. Sol. Cells*, vol. 99, pp. 182–189, Apr. 2012.
[41]   J. Jo, S. S. Kim, S. I. Na, B. K. Yu, and D. Y. Kim, "Time-dependent morphology ewolution by annealing processes on polymer:Fullerene blend solar cells," *Adv. Funct. Mater.*, vol. 19, no. 6, pp. 866–874, 2009.
[42]   X. Yang, A. Alexeev, M. a J. Michels, and J. Loos, "Effect of Spatial Confinement on the Morphology Evolution of Thin Poly (p -phenylenevinylene)/ Methanofullerene Composite Films," *Macromolecules*, vol. 38, no. 10, pp. 4289–4295, 2005.
[43]   B. T. de Villers, C. J. Tassone, S. H. Tolbert, and B. J. Schwartz, "Improving the Reproducibility of P3HT: PCBM Solar Cells by Controlling the PCBM/Cathode Interface," *J. Phys. Chem. C*, pp. 28–33, 2009.
[44]   S. R. Dupont, E. Voroshazi, D. Nordlund, and R. H. Dauskardt, "Morphology and interdiffusion control to improve adhesion and cohesion properties in inverted polymer solar cells," *Sol. Energy Mater. Sol. Cells*, vol. 132, pp. 443–449, 2015.
[45]   V. Brand, K. Levi, M. D. McGehee, and R. H. Dauskardt, "Film stresses and electrode buckling in organic solar cells," *Sol. Energy Mater. Sol. Cells*, vol. 103, pp. 80–85, Aug. 2012.
[46]   C. Bruner and R. Dauskardt, "Role of Molecular Weight on the Mechanical Device Properties of Organic Polymer Solar Cells," 2013.
[47]   C. Bruner, F. Novoa, S. Dupont, and R. Dauskardt, "Decohesion Kinetics in Polymer Organic Solar Cells," 2014.

[48]   N. R. Tummala, C. Bruner, C. Risko, J.-L. Bredas, and R. H. Dauskardt, "A Molecular-Scale Understanding of Cohesion and Fracture in P3HT:Fullerene Blends," *ACS Appl. Mater. Interfaces*, p. 150421065231008, 2015.

[49]   C. Bruner, N. C. Miller, M. D. McGehee, and R. H. Dauskardt, "Molecular Intercalation and Cohesion of Organic Bulk Heterojunction Photovoltaic Devices," *Adv. Funct. Mater.*, vol. 23, pp. 2863–2871, 2013.

[50]   S. R. Dupont, F. Novoa, E. Voroshazi, and R. H. Dauskardt, "Decohesion kinetics of PEDOT:PSS conducting polymer films," *Adv. Funct. Mater.*, vol. 24, no. 9, pp. 1325–1332, 2014.

[51]   K. Kendall, "The adhesion and surface energy of elastic solids," *J. Phys. D Appl. Phys*, vol. 4, pp. 1186–1195, 1971.

[52]   B. Ellis, *Chemistry and Technology of Epoxy Resins*. .

[53]   R. K. Goldberg, G. D. Roberts, and A. Gilat, "Strain Rate Sensitivity of Epoxy Resin in Tensile and Shear Loading," *J. Aerosp. Eng.*, vol. 18, no. 1, pp. 18–27, 2005.

[54]   C. Creton and H. Lakrout, "Micromechanics of flat-probe adhesion tests of soft viscoelastic polymer films," *J. Polym. Sci. Part B Polym. Phys.*, vol. 38, no. 7, pp. 965–979, 2000.

[55]   W. Lövenich, "PEDOT-properties and applications," *Polym. Sci. Ser. C*, vol. 56, no. 1, pp. 135–143, 2014.

[56]   T. T. Larsen-Olsen, F. Machui, B. Lechene, S. Berny, D. Angmo, R. Søndergaard, N. Blouin, W. Mitchell, S. Tierney, T. Cull, P. Tiwana, F. Meyer, M. Carrasco-Orozco, A. Scheel, W. Lövenich, R. De Bettignies, C. J. Brabec, and F. C. Krebs, "Round-Robin studies as a method for testing and validating high-effi ciency ito-free polymer solar cells based on roll-to-roll-coated highly conductive and transparent flexible substrates," *Adv. Energy Mater.*, vol. 2, no. 9, pp. 1091–1094, 2012.

[57]   N. Grossiord, J. M. Kroon, R. Andriessen, and P. W. M. Blom, "Degradation mechanisms in organic photovoltaic devices," *Org. Electron.*, vol. 13, no. 3, pp. 432–456, 2012.

[58]   S. Schumann, A. Elschner, D. Gaiser, and W. Lövenich, "Non-aqueous PEDOT:PSS dispersion for improved inverted organic solar cells," *MRS Proc.*, vol. 1771, pp. mrss15–2136576, May 2015.

[59]   ASTM International, "ASTM D3359 - Standard Test Methods for Measuring Adhesion by Tape Test." [Online]. Available: http://www.astm.org/Standards/D3359.htm. [Accessed: 02-Sep-2015].

[60]   G. Li, V. Shrotriya, J. Huang, Y. Yao, T. Moriarty, K. Emery, and Y. Yang, "High-efficiency solution processable polymer photovoltaic cells by self-organization of polymer blends," *Nat. Mater.*, vol. 4, no. 11, pp. 864–868, 2005.

[61]   G. Li, V. Shrotriya, Y. Yao, J. Huang, and Y. Yang, "Manipulating regioregular poly(3-hexylthiophene) : [6,6]-phenyl-C61-butyric acid methyl ester blends—route towards high efficiency polymer solar cells," *J. Mater. Chem.*, vol. 17, no. 30, p. 3126, 2007.

[62]   S. E. Shaheen, C. J. Brabec, N. S. Sariciftci, F. Padinger, T. Fromherz, and J. C. Hummelen, "2.5% Efficient Organic Plastic Solar Cells," *Appl. Phys. Lett.*, vol. 78, no. 6, pp. 841–843, 2001.

[63]   J. Jaczewska, a. Budkowski, a. Bernasik, E. Moons, and J. Rysz, "Polymer vs solvent diagram of film structures formed in spin-cast poly(3-alkylthiophene) blends," *Macromolecules*, vol. 41, no. 13, pp. 4802–4810, 2008.

[64]   H. W. Ro, B. Akgun, B. T. O'Connor, M. Hammond, R. J. Kline, C. R. Snyder, S. K. Satija, A. L. Ayzner, M. F. Toney, C. L. Soles, and D. M. DeLongchamp, "Poly(3-hexylthiophene) and [6,6]-Phenyl-C61-butyric Acid Methyl Ester Mixing in Organic Solar Cells," *Macromolecules*, vol. 45, no. 16, pp. 6587–6599, Aug. 2012.

[65]   B. Schmidt-Hansberg, M. Sanyal, M. F. G. Klein, M. Pfaff, N. Schnabel, S. Jaiser, A. Vorobiev, E. Müller, A. Colsmann, P. Scharfer, D. Gerthsen, U. Lemmer, E. Barrena, and W. Schabel, "Moving through the phase diagram: Morphology formation in solution cast polymer-fullerene blend films for organic solar cells," *ACS Nano*, vol. 5, no. 11, pp. 8579–8590, 2011.

[66]   K. Kim, S. Park, H. Yu, H. Kang, I. H. Song, J. H. Oh, and B. J. Kim, "Determining Optimal Crystallinity of Diketopyrrolopyrrole-based Terpolymers for Highly Efficient Polymer Solar Cells and Transistors Determining Optimal Crystallinity of Diketopyrrolopyrrole-based Terpolymers for Highly Efficient Polymer Solar Cells and T," *Chem. Mater.*, 2014.

[67]   B. Schmidt-Hansberg, M. F. G. Klein, K. Peters, F. Buss, J. Pfeifer, S. Walheim, a. Colsmann, U. Lemmer, P. Scharfer, and W. Schabel, "In situ monitoring the drying kinetics of knife coated polymer-fullerene films for organic solar cells," *J. Appl. Phys.*, vol. 106, no. 12, pp. 1–8, 2009.

[68]   G. Li, Y. Yao, H. Yang, V. Shrotriya, G. Yang, and Y. Yang, "'Solvent annealing' effect in polymer solar cells based on poly(3-hexylthiophene) and methanofullerenes," *Adv. Funct. Mater.*, vol. 17, no. 10, pp. 1636–1644, 2007.

[69]   Y. Huang, E. J. Kramer, A. J. Heeger, and G. C. Bazan, "Bulk Heterojunction Solar Cells : Morphology and Performance Relationships," *Chem. Rev.*, vol. 114, pp. 7006–7043, 2014.

[70]   P. Westacott, J. R. Tumbleston, S. Shoaee, S. Fearn, J. H. Bannock, J. B. Gilchrist, S. Heutz, J. DeMello, M. Heeney, H. Ade, J. R. Durrant, D. S. McPhail, and N. Stingelin, "On the role of intermixed phases in organic photovoltaic blends," *Energy Environ. Sci.*, vol. 6, no. 9, p. 2756, 2013.

[71] N. Stingelin, "On the phase behaviour of organic semiconductors," *Polym. Int.*, vol. 61, no. 6, pp. 866–873, 2012.

[72] E. Buchaca-Domingo, a. J. Ferguson, F. C. Jamieson, T. McCarthy-Ward, S. Shoaee, J. R. Tumbleston, O. G. Reid, L. Yu, M.-B. Madec, M. Pfannmöller, F. Hermerschmidt, R. R. Schröder, S. E. Watkins, N. Kopidakis, G. Portale, a. Amassian, M. Heeney, H. Ade, G. Rumbles, J. R. Durrant, and N. Stingelin, "Additive-assisted supramolecular manipulation of polymer:fullerene blend phase morphologies and its influence on photophysical processes," *Mater. Horizons*, vol. 1, no. 2, p. 270, 2014.

[73] S. Coveney, *Fundamentals of Phase Separation in Polymer Blend Thin Films*. 2015.

[74] A. Claudia Arias, "Vertically Segregated Polymer Blends: Their Use in Organic Electronics," *J. Macromol. Sci. Part C Polym. Rev.*, vol. 46, no. 1, pp. 103–125, 2006.

[75] a. C. Arias, J. D. MacKenzie, R. Stevenson, J. J. M. Halls, M. Inbasekaran, E. P. Woo, D. Richards, and R. H. Friend, "Photovoltaic performance and morphology of polyfluorene blends: A combined microscopic and photovoltaic investigation," *Macromolecules*, vol. 34, no. 17, pp. 6005–6013, 2001.

[76] W. Lee and Y. Park, "Organic Semiconductor/Insulator Polymer Blends for High-Performance Organic Transistors," *Polymers (Basel).*, vol. 6, no. 4, pp. 1057–1073, 2014.

[77] C. M. Björström, S. Nilsson, A. Bernasik, A. Budkowski, M. Andersson, K. O. Magnusson, and E. Moons, "Vertical phase separation in spin-coated films of a low bandgap polyfluorene/PCBM blend-Effects of specific substrate interaction," *Appl. Surf. Sci.*, vol. 253, no. 8, pp. 3906–3912, 2007.

[78] C. M. Björström, A. Bernasik, J. Rysz, A. Budkowski, S. Nilsson, M. Svensson, M. R. Andersson, K. O. Magnusson, and E. Moons, "Multilayer formation in spin-coated thin films of low-bandgap polyfluorene:PCBM blends," *J. Phys. Condens. Matter*, vol. 17, no. 50, pp. L529–L534, 2005.

[79] C. He, D. S. Germack, R. Joseph Kline, D. M. Delongchamp, D. A. Fischer, C. R. Snyder, M. F. Toney, J. G. Kushmerick, and L. J. Richter, "Influence of substrate on crystallization in polythiophene/fullerene blends," *Sol. Energy Mater. Sol. Cells*, vol. 95, no. 5, pp. 1375–1381, May 2011.

[80] L. Zhang, X. Xing, L. Zheng, Z. Chen, L. Xiao, B. Qu, and Q. Gong, "Vertical phase separation in bulk heterojunction solar cells formed by in situ polymerization of fulleride.," *Sci. Rep.*, vol. 4, p. 5071, 2014.

[81] Z. Xu, L. M. Chen, G. Yang, C. H. Huang, J. Hou, Y. Wu, G. Li, C. S. Hsu, and Y. Yang, "Vertical phase separation in poly(3-hexylthiophene): Fullerene derivative blends and its advantage for inverted structure solar cells," *Adv. Funct. Mater.*, vol. 19, no. 8, pp. 1227–1234, 2009.

[82] N. Koch, "Organic electronic devices and their functional interfaces," *ChemPhysChem*, vol. 8, no. 10, pp. 1438–1455, 2007.

[83] Y. H. Kim, C. Sachse, M. L. MacHala, C. May, L. Müller-Meskamp, and K. Leo, "Highly conductive PEDOT:PSS electrode with optimized solvent and thermal post-treatment for ITO-free organic solar cells," *Adv. Funct. Mater.*, vol. 21, no. 6, pp. 1076–1081, 2011.

[84] S. Timpanaro, M. Kemerink, F. J. Touwslager, M. M. De Kok, and S. Schrader, "Morphology and conductivity of PEDOT/PSS films studied by scanning-tunneling microscopy," *Chem. Phys. Lett.*, vol. 394, no. 4–6, pp. 339–343, 2004.

[85] C. Creton, E. J. Kramer, H. R. Brown, and C.-Y. Hui, *Adhesion and Fracture of Interfaces Between Immiscible Polymers: from the Molecular to the Continuum Scale*. 2002.

[86] H. J. Kim, J. Kim, J. Ryu, Y. Kim, H. Kang, W. B. Lee, T. Kim, and B. J. Kim, "Architectural Engineering of Rod À Coil Compatibilizers for Producing Mechanically and Thermally Stable Polymer Solar Cells," *ACS Nano*, vol. 8, no. 10, pp. 10461–10470, 2014.

[87] C. Boyer, B. Boutevin, and J. J. Robin, "Study of the synthesis of graft copolymers by a reactive process. Influence of the copolymer structure on the adhesion of polypropylene onto poly(vinylidene fluoride)," *Polym. Degrad. Stab.*, vol. 90, no. 2 SPEC. ISS., pp. 326–339, 2005.

[88] M. Y. Ju and F. C. Chang, "Compatibilization of PET/PS blends through SMA and PMPI dual compatibilizers," *Polymer (Guildf).*, vol. 41, no. 5, pp. 1719–1730, 2000.

[89] Y. Seo and T. H. Ninh, "Enhanced interfacial adhesion between polypropylene and nylon 6 by in situ reactive compatibilization," *Polymer (Guildf).*, vol. 45, no. 25, pp. 8573–8581, 2004.

[90] N. Su Kang, B. K. Ju, T. Wan Lee, D. H. Choi, J. M. Hong, and J. W. Yu, "Organic photovoltaic devices with a crosslinkable polymer interlayer," *Sol. Energy Mater. Sol. Cells*, vol. 95, no. 10, pp. 2831–2836, 2011.

[91] S. K. Hau, H. L. Yip, H. Ma, and A. K. Y. Jen, "High performance ambient processed inverted polymer solar cells through interfacial modification with a fullerene self-assembled monolayer," *Appl. Phys. Lett.*, vol. 93, no. 23, pp. 111–114, 2008.

[92]   F. Deschler, D. Riedel, B. Ecker, E. von Hauff, E. Da Como, and R. C. I. MacKenzie, "Increasing organic solar cell efficiency with polymer interlayers," *Phys. Chem. Chem. Phys.*, vol. 15, no. 3, pp. 764–769, Dec. 2012.

[93]   D. M. Huang, S. A. Mauger, S. Friedrich, S. J. George, D. Dumitriu-LaGrange, S. Yoon, and A. J. Moulé, "The Consequences of Interface Mixing on Organic Photovoltaic Device Characteristics," *Adv. Funct. Mater.*, vol. 21, no. 9, pp. 1657–1665, 2011.

[94]   R. J. Good and L. A. Girifalco, "A THEORY FOR ESTIMATION OF SURFACE AND INTERFACIAL ENERGIES. III. ESTIMATION OF SURFACE ENERGIES OF SOLIDS FROM CONTACT ANGLE DATA," no. 1924, 1960.

[95]   D. K. Owens and R. C. Wendt, "Estimation of the surface free energy of polymers," *J. Appl. Polym. Sci.*, vol. 13, no. 8, pp. 1741–1747, 1969.

[96]   F. M. Fowkes, "Attractive forces at interfaces," *Ind. Eng. Chem.*, vol. 56, no. 12, pp. 40–52, 1964.

[97]   "Surface Tension Components and Molecular Weight of Selected Liquids." [Online]. Available: http://www.accudynetest.com/surface_tension_table.html?sortby=sort_st_disp.

[98]   Bruker, "Introduction to Brukers Scan Asyst and Peak Force Tapping Atomic Force Microscopy Technology." pp. 1–12.

6 Conclusions

Literature review of the most recent works on conjugated polymers, as efficient donors in BHJ solar cells, reveals that the majority of them has been synthesized with a push-pull strategy. This strategy requires the alternation of donor and acceptor units, in order to obtain low band gap polymers (LBGs). The LBGs increase the efficiency of the OPV device due to a better overlap with the solar spectrum leading to a better absorption of photon flux. The LUMO energy level of the D–A conjugated polymers is mainly localized on the acceptor unit, so a proper selection of the electron withdrawing block influences the LUMO level of these polymers. Also, to avoid charge recombination of the free carriers after exciton separation, the electron-withdrawing ability of the acceptor needs to be carefully tuned. Substituents on the main conjugated backbone influences both polymer electronic level and morphology of the active layer blend.

Two series of LBGs based on dithienosilole (**DTS**) as donor unit and either diketopyrrolopyrrole (**DPP**) or dithienyl-thienopyrazine (**DTP**) as acceptor units have been synthetized. The synthesis of **DTS-DTPs** polymers has not been successful due to not optimized synthesis procedure. Nonetheless, the wide absorption and the electronic properties of the obtained oligomers make them promising materials for application in organic electronics. On the other hand, **DTS-DPPs** polymers have been successfully synthesized and exhibit good solubility, NIR-absorption and favorable optoelectronic properties.

Two of the synthesized polymers, **PSBDPP_C12** and **PSBDPP_C10C6**, were used in inverted architecture devices fabricated by doctor blading under different processing conditions. Opposing behavior was observed for the two polymers with respect to the coating temperature. **PSBDPP_C12** is best performing when coated at room temperature (J_{SC}=2.6 mA cm^{-2}; V_{OC}=0.50 V; *FF*= 0.47; *PCE*=0.61%), while with **PSBDPP_C10C6** best performances (J_{SC}=0.64 mA cm^{-2}; V_{OC}=0.61 V; *FF*= 0.50; *PCE*=0.20%) were achieved for high temperature deposition. The use of additives for the coating of **PSBDPP_C10C6** lead to even lower performances. **PSBDPP_C12** based devices were prepared under inert atmosphere with the active layer deposited by spin-coating. These new conditions led to a further improvement of the photovoltaic characteristics (J_{SC}= 5.9 mA cm^{-2}; V_{OC}= 0.54 V; *FF*= 0.58; *PCE*= 1.7 %), nonetheless, low photocurrent was still observed. To understand the reason behind it, charge

carrier mobility, morphology and phase segregation and charge carrier behavior were investigated. The results showed how, despite favorable energy levels and good charge carrier mobility, unfavorable morphology and charge recombination limit the photocurrent and thus device efficiency.

From a chemical standpoint, the requirements for highly efficient solar cells are therefore not limited to the design of conjugated backbone with its electronic properties; crystallinity of polymer phase, miscibility with **PC$_{61}$BM**, morphology control and stability of the blend at the nanoscale are also critical factors.

In parallel, one of the long-term durability issues of OPV have been assessed. An experimental set-up to investigate the mechanical integrity of multilayered structures was developed and applied to inverted geometry OPV devices. The results on **P3HT:PCBM** devices confirmed the AL/HTL interface as the weak point in the layer stack. Several materials for the AL and HTL have then been tested and the fracture path identified. In particular, these new materials were developed with the aim of improving the weaknesses within the layer stack. The physical and chemical characterization of the half-devices produced upon destructive testing allowed us to identify and influence some of the fundamental parameters involved in establishing of physical and chemical bonding. We demonstrated how the use of a better solvent system and additives for the **PEDOT:PSS** material used as HTL is a viable route to improve the adhesion between the two uncompatible layers. Moreover, the use of an additional layer acting as compatibilizer was explored, but this time with little success. The design of the compatibilizing block copolymer and its processing need further development, before being able to discard this route.

The manipulation of nanoscale morphology and phase separation (both lateral and vertical) of polymer blends is fundamental not only for improving the photovoltaic characteristics of the device, but also for its chemical/mechanical stability.

6   Conclusions

L'état de l'art des travaux récents sur les polymères conjugués utilisés comme matériaux donneur efficaces dans les cellules solaires BHJ, révèle que la majorité d'entre eux a été synthétisée avec une stratégie push-pull. Cette stratégie nécessite l'alternance d'unités de donneur (D) et accepteur (A), afin d'obtenir des polymères à faible bande interdite (LBG). Les LBGs permettent d'accroître le rendement du dispositif OPV grâce à un meilleur recouvrement avec le spectre solaire conduisant à une meilleure absorption du flux de photons. Le niveau LUMO de ces polymères conjugués (D-A) étant principalement localisé sur l'unité acceptrice, le choix de celle-ci conditionne le niveau LUMO de ces polymères. Aussi, pour éviter la recombinaison des porteurs de charges après la séparation de l'exciton, la force de l'accepteur d'électrons doit être soigneusement ajustée. Les substituants nécessaires à la solubilité influencent les niveaux électroniques du polymère mais aussi la morphologie de la couche active.

Deux séries de LBGs basés sur le dithiénosilole (**DTS**) comme unité donneuse et sur le dicétopyrrolopyrrole (**DPP**) et le dithiényl-thiénopyrazine (**DTP**) comme unités acceptrices ont été synthétisées. La synthèse de polymères **DTS-DTP** n'a pas abouti, en raison du protocol de synthèse non optimisé. Néanmoins, les propriétés opto-électroniques des oligomères obtenus rendent ces matériaux prometteurs pour l'application en électronique organique. Par ailleurs, les polymères **DTS-DPP** ont être synthétisés avec et présentent une bonne solubilité, une bonne absorption dans le proche IR et des propriétés optoélectroniques favorables.

Deux des polymères synthétisés, **PSBDPP_C12** et **PSBDPP_C10C6**, ont été utilisés dans des dispositifs d'architecture inverses fabriqués par «doctor blading» sous différentes conditions de traitement. Des comportements opposés ont été observés pour les deux polymères relativement à leur température de dépôt. Le **PSBDPP_C12** est plus performant lorsqu'il est déposé à température ambiante (J_{SC}=2,6 mA cm^{-2}; V_{OC}=0,50 V; FF=0,47; PCE=0,61%), tandis que pour le **PSBDPP_C10C6,** les meilleures performances (J_{SC}=0,64 mA cm^{-2}; V_{OC}=0,61 V; FF=0,50; PCE=0,20%) ont été atteintes pour un dépôt à haute température. L'utilisation d'additifs pour le dépôt du **PSBDPP_C10C6** a diminué les performances. Les cellules basées sur le **PSBDPP_C12** ont été préparées sous atmosphère inerte avec la couche active déposée par «spin-coating». Ces nouvelles conditions ont conduit à une amélioration des caractéristiques photovoltaïques (J_{SC}=5,9 mA cm^{-2}; V_{OC}=0,54 V; FF=0,58; PCE=1,7%). Néanmoins, les photocourant reste inférieur à celui calculé pour ce polymère. Pour en comprendre la raison, la

mobilité de porteurs de charge, la morphologie et la ségrégation de phases ont été étudiées. Les résultats ont montré comment, en dépit des niveaux d'énergie favorables et d'une bonne mobilité de porteurs de charge, une morphologie et une forte recombinaison de charges limitent le photocourant et donc l'efficacité du dispositif.

La versatilité des structures chimiques ne limite pas la conception de polymères conjugués avec des propriétés électroniques adaptées pour viser des hautes rendements. Par contre, la cristallinité de la phase polymère, sa miscibilité avec le **PC$_{61}$BM**, le contrôle de la morphologie et de la stabilité du mélange à l'échelle nanométrique, sont des facteurs critiques.

En parallèle, l'une des questions à long terme pour la durabilité des OPV a été abordée. Un dispositif expérimental pour étudier l'intégrité mécanique des structures multicouches a été développé et appliqué à des dispositifs d'architectures inverses. Les résultats sur les dispositifs **P3HT:PCBM** ont confirmé l'interface HTL/AL comme un point faible de l'empilement des couches. Plusieurs matériaux pour l'AL et HTL ont ensuite été testés et le chemin de fracture identifié. En particulier, ces nouveaux matériaux ont été développés dans le but d'améliorer l'adhésion par enter-diffusion de ces couches. La caractérisation physique et chimique des demi-cellules obtenues après ces tests destructifs, nous a permis d'identifier et d'influencer certains des paramètres fondamentaux impliqués dans l'adhésion des couches. Nous avons démontré comment l'utilisation d'un meilleur solvant et des additifs pour le PEDOT:PSS utilisé comme HTL est une voie viable pour améliorer l'adhésion entre HTL et AL. En outre, l'utilisation d'une couche supplémentaire comme compatibilisant a été explorée, mais sans grand succès. Néanmoins, nous pensons que la conception du copolymère à blocs compatibilisant et sa mise en oeuvre doivent être poursuivies.

Le control de la morphologie à l'échelle nanométrique et de la séparation de phases (latérale et verticale à la fois) de mélanges à base de polymères sont essentielles, pour non seulement améliorer les caractéristiques photovoltaïques du dispositif, mais aussi la stabilité mécanique/chimique.

1 Experimental Section of Synthesis and Characterization of LBGs

1.1 Materials

4,4'-Bis(2-ethylhexyl)-5,5'-bis(trimethyltin)-dithieno[3,2-*b*:2,3-*d*]silole was purchased from 1-Material and used without further purification. 3,6-Bis(5-bromo-2-thienyl)-2,5-bis(2-hexyldecyl)-2,5-dihydropyrrolo[3,4-*c*]pyrrole-1,4-dione was purchased by Solarmer Materials Inc. and used without further purification. Di-isopropylsuccinate, iron(III) chloride anhydrous and K_2CO_3 anhydrous were purchased from ABCR and used without further purification. All other reagents and solvents were purchased from Sigma Aldrich and used without further purification, unless otherwise stated. All reactions using dry solvents were carried out with oven-dried glassware and under inert atmosphere (N_2), unless otherwise stated.

1.2 Instrument

^{1}H-NMR spectra were recorded on a Bruker (400 MHz) spectrometer; chemical shifts are given relative to tetramethylsilane (TMS).

UV–visible absorption spectra were recorded on a Shimadzu UV-2450 spectrophotometer and on a Perkin Elmer Lambda 35 at room temperature.

Gel permeation chromatrography (GPC) was performed with an Agilent Technologies 1260 infinity eluted at 1mL/min with HPLC grade chlorobenzene (Sigma-Aldrich) at 50°C through a PLgel 10 μm Mixed-B (300×7.5 mm) GPC column. The polymers were analysed with a refractive index detector calibrated with narrow polystyrene standards. Samples were dissolved in HPLC grade chlorobenzene at a concentration of 1-4 mg/mL and filtered. The measurement and the calculation of molecular weights (M_n, M_w and M_p) and dispersities (M_w/M_n) were performed by Dr Graham Morse at Merck Chemicals Ltd in the framework of ESTABLIS project.

Cyclic voltammetry was performed using a Princeton Applied Research VersaSTAT 4 potentiostat. Films of the polymers were cast from a concentrated chloroform solution onto a platinum wire working electrode. These solid films were measured in an anhydrous acetonitrile solution containing 0.1 M tetrabutyl ammonium tetrafluoroborate electrolyte with a platinum wire counter electrode and 0.1 M Ag/AgNO$_3$ in acetonitrile reference electrode. The solutions were purged with N_2 gas prior to use. The samples were referenced to an external ferrocene solution which was

also used to calculate the LUMO position. The cyclic voltammetry measurements and HOMO/LUMO calculations were performed by Dr. Graham Morse at Merck Chemicals Ltd in the framework of the ESTABLIS project.

Thermogravimetric analyzes (TGA) were performed with a TA-Q50, with a weighing precision of ± 0.01%, a sensitivity of 0.1 µg, isothermal temperature accuracy of ± 1 °C, isothermal temperature precision of ± 0.1 °C and a controlled heating rate ranging from 0.1 to 100 °C/min. Aluminum pan were used. Unless specified otherwise, the typical sample weight was ≈3 mg and the typical procedure included a stabilization at 40 °C for 30 minutes and a heating ramp of 10°C/min up to 600°C.

Differential scanning calorimetry (DSC) measurements were performed with a TA-Q100, in hermetic aluminum pan. Nitrogen flux was 50 ml s^{-1}. Typical sample weight was ≈5 mg, unless otherwise specified. Typical procedure included a first heating/cooling cycle performed at 10 °C/min to erase the thermal history of the sample.

The morphologies of the polymer and blend films were analyzed using a Bruker Multimode-8 atomic force microscope operated in peak-force mode in ambient conditions at room temperature and SCANASYST-AIR silicon tip on nitride lever (T: 600 nm; L: 115 µm; W: 25 µm; f_o: 70 kHz; k: 0.4 N/m). Few images were taken at Belectric OPV GmbH utilizing Nanosurf Easy Scan 2 AFM in contact mode.

Photoluminescence measurements were performed on active layers which were excited at 796 nm by a Stellarnet Halogen lamp RG850 and IF495 filters, slit 0.5 mm. The PL emission was detected by a Germanium (Ge) detector (ADC 403L) through lockin technique. The fluorescence spectrum was corrected for the optical density of the sample at the excitation wavelength, and for the detection sensitivity of the Ge detector.

1.3 DPP series

1.3.1 Monomer synthesis

#### 1.3.1.1 3,6-Dithiophene-2-yl-2,5-dihydropyrrolo[3,4-*c*]pyrrole-1,4-dione (DPP, 1)
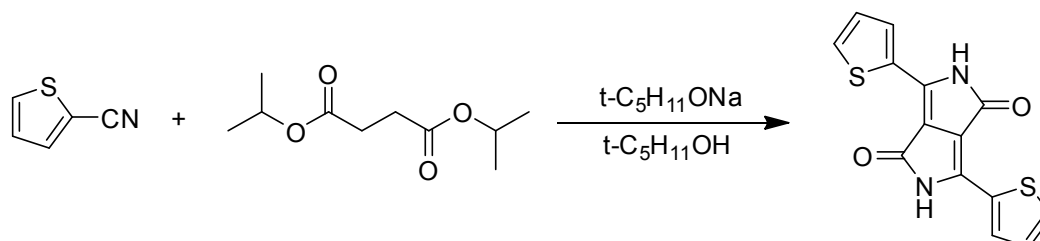
In a 250 ml double necked round bottom flask with a magnetic stirring bar, sodium (3.5 g, 0.15 mol) was added to 60 ml of *t*-amyl alcohol with a small amount of iron(III) chloride anhydrous (50 mg, 0.3 mmol). The mixture was stirred under inert atmosphere (N_2) for 1 h at 110 °C, until complete sodium dissolution. The mixture was then cooled to 80 °C and 2-thiophene-carbonitryle (9.5 g, 0.87 mol) was added in one shot; then a solution of di-isopropylsuccinate (7.092 g, 0.35 mol) in t-amyl alcohol was added drop-wise using a 100 ml dropping funnel. When the addition was completed, the reaction was left at 85 °C for 5 h. The brown-red mixture was cooled at room temperature and filtered on a Buchner funnel. The brown-red solid filtrate was washed several times with warm deionized water and methanol. The final product (8.9 g, 85% yield) was dried under vacuum until complete solvent removal.

Yield: 9.010 g, 0.30 mol, 85%

^{1}H-NMR (d_6-DMSO): 11.24 (s, 2H), 8.21 (d, *J*=4.0 Hz, 2H), 7.96 (*d*, *J*=4.0 Hz, 2H), 7.31 (dd, J_1=4.0 Hz, J_2=4.0 Hz, 2H)
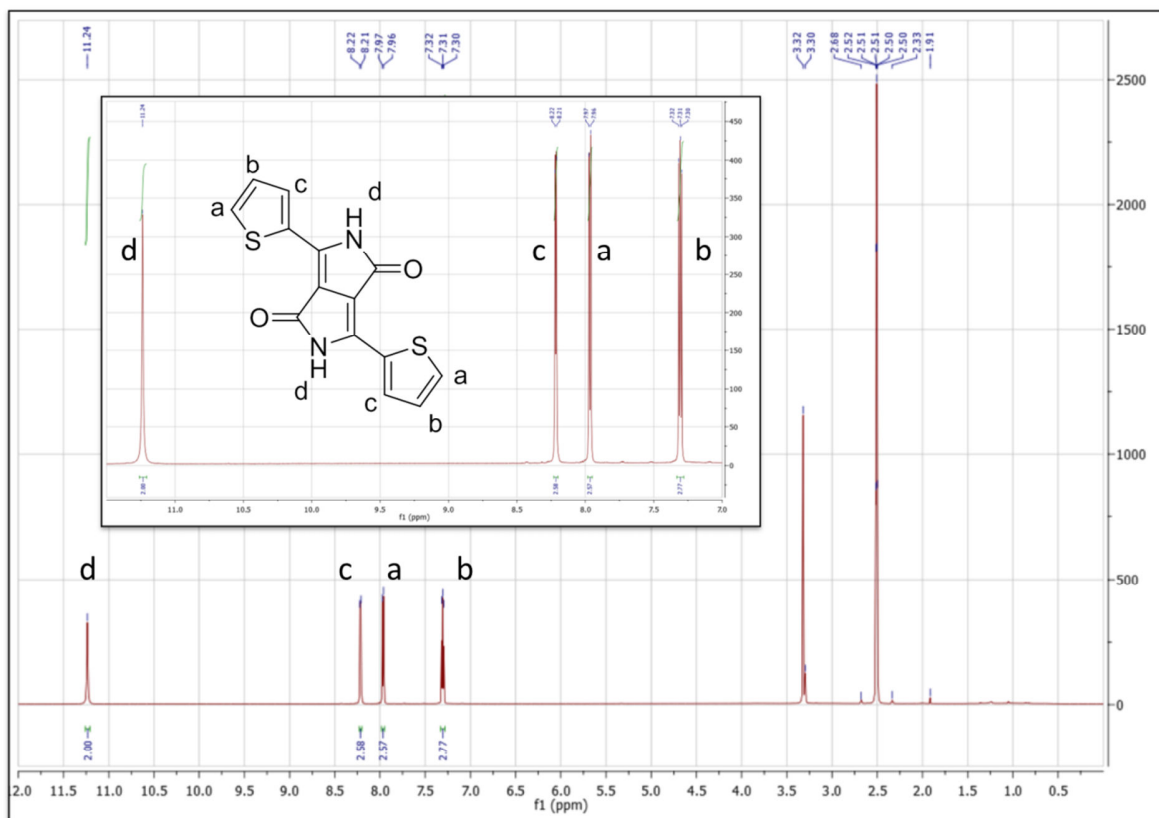
1.3.1.2 General *N*-alkylation procedure (DPP_Cn, 2)
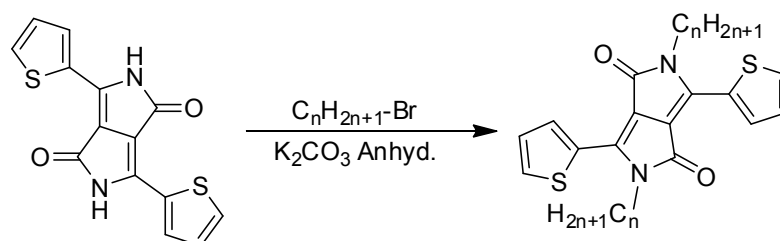
A two necked 100 ml round bottom flask with a magnetic stirring bar, was charged with 1 eq of (1) in anhydrous DMF and stirred under inert atmosphere (N_2) for 1h. 3.5 eq of anhydrous potassium carbonate (K_2CO_3) was added, together with 3 eq of C_nH_{2n+1}-Br and 0.01 eq of 18-crown-6. The mixture was stirred over night at 120 °C. The mixture was filtered on a Buchner funnel and the filtrate washed several times with warm deionized water and methanol. The final product was dried under vacuum until complete solvent removal.

1.3.1.2.1 2,5-Didodecyl-3,6-dithiophene-2-yl-2,5-dihydropyrrolo[3,4-*c*]pyrrole-1,4-dione (DPP_C12, 2a)
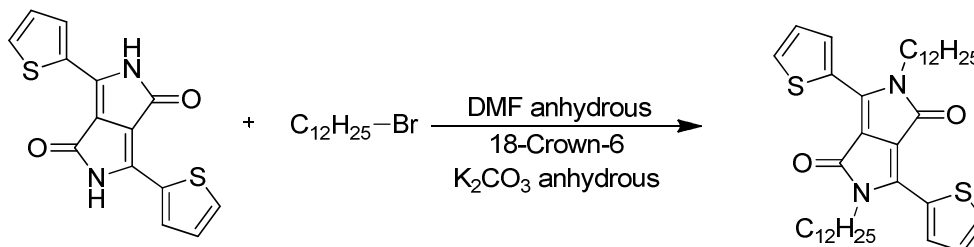
(1): 2.010 g, 6.66 mmol

K_2CO_3 anhydrous: 3.200 g, 23.31 mmol

$C_{12}H_{25}Br$: 5.022 g, 20.15 mmol

18-Crown-6: 30 mg, 0.11 mmol

DMF anhydrous: 50 ml

Yield: 2.680 g, 4.21 mmol, 63%

^{1}H-NMR (CDCl$_3$, 400 Hz): 8.85 (d, J=4.0 Hz, 2H), 7.57 (d, J=8 Hz, 2H), 7.22 (t, J$_1$=4.0 Hz, J$_2$=8.0 Hz, 2H), 4.00 (t, J$_1$=8.0 Hz, J$_2$=16.0 Hz, 4H), 1.61-1.73 (m, 4H), 1.10-1.35 (m, 36 H), 0.75-0.85 (t, J$_1$=4.0 Hz, J$_2$=12.0 Hz 6H)
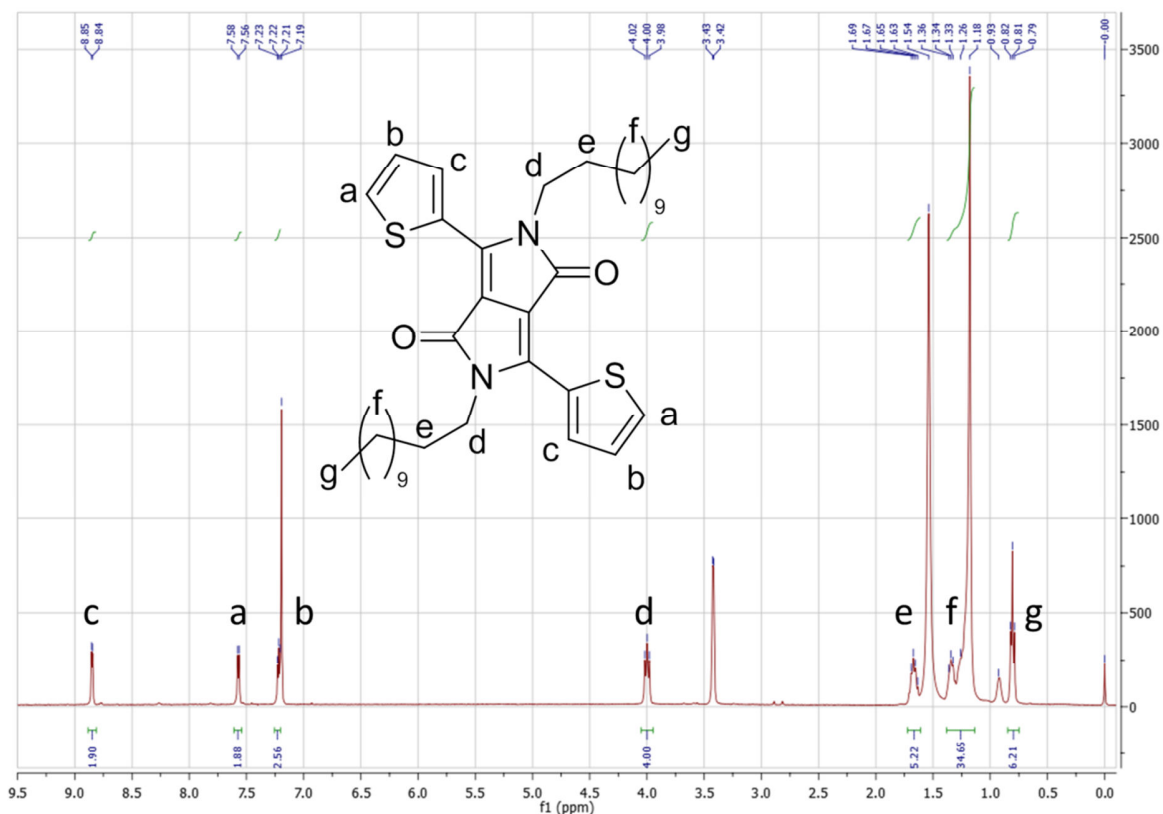
1.3.1.2.2 2,5-hexadecyl-3,6-dithiophene-2-yl-2,5-dihydropyrrolo[3,4-*c*]pyrrole-1,4-dione (DPP_C16, 2b)
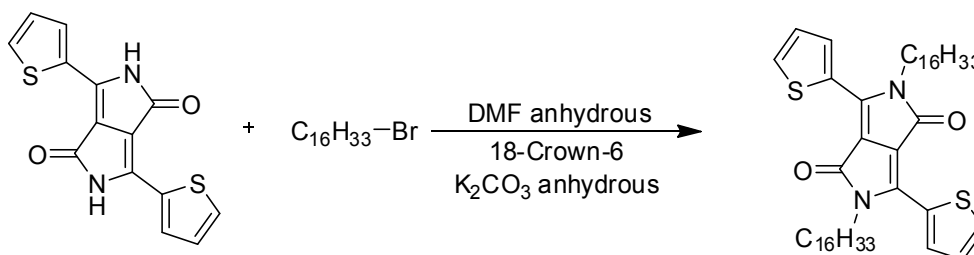
(1): 2.023 g, 6.66 mmol

K_2CO_3 anhydrous: 3.250 mg, 23.31 mmol

$C_{16}H_{33}$Br: 6.115 g, 20 mmol

18-Crown-6: 40 mg, 0.08 mmol

Yield: 4.251 g, 5.67 mmol, 86%

^{1}H-NMR (CDCl$_3$, 400 Hz): 8.86 (d, J=4.0 Hz, 2H), 7.58 (d, J=4 Hz, 2H), 7.22 (t, J$_1$=4.0 Hz, J$_2$=8.0 Hz, 2H), 4.00 (t, J$_1$=8.0 Hz, J$_2$=16.0 Hz, 4H), 1.61-1.73 (m, 4H), 1.10-1.40 (m, 52 H), 0.77-0.85 (t, J$_1$=4.0 Hz, J$_2$=12.0 Hz 6H)
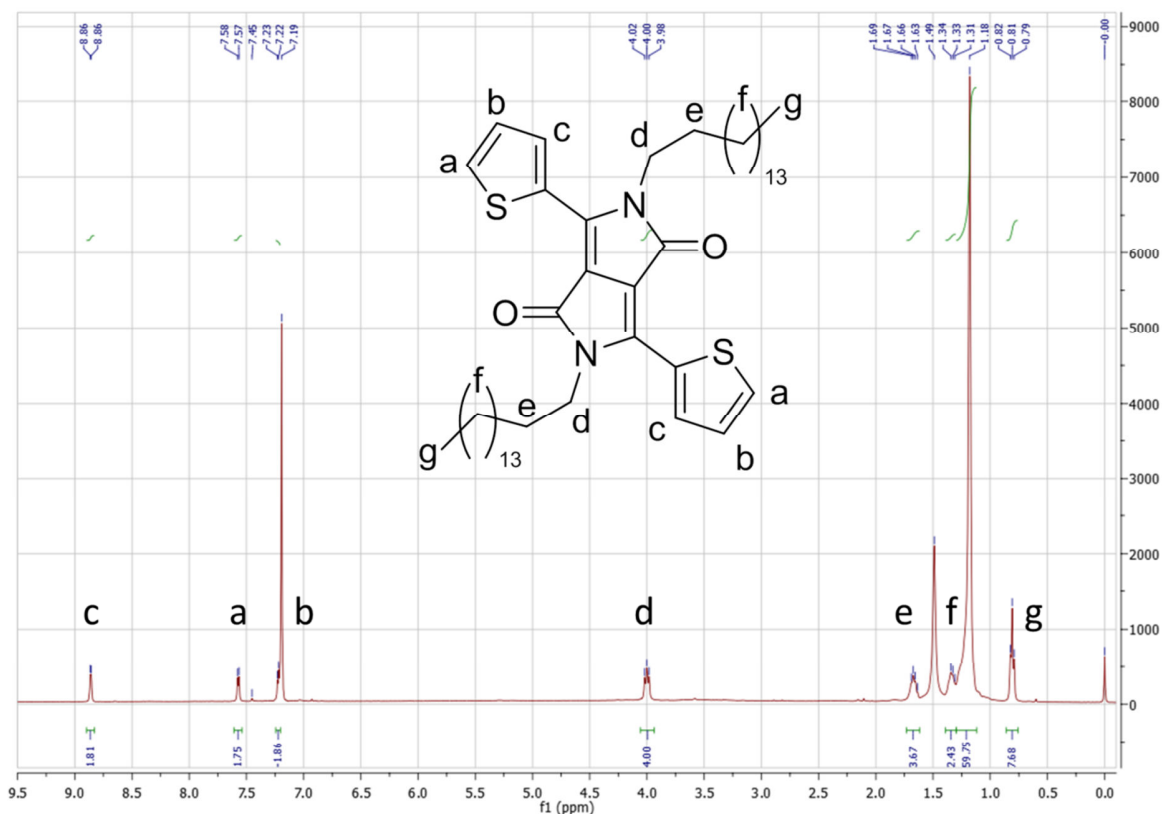
1.3.1.3 General bromination procedure (DPP_Cn-Br$_2$, 3)
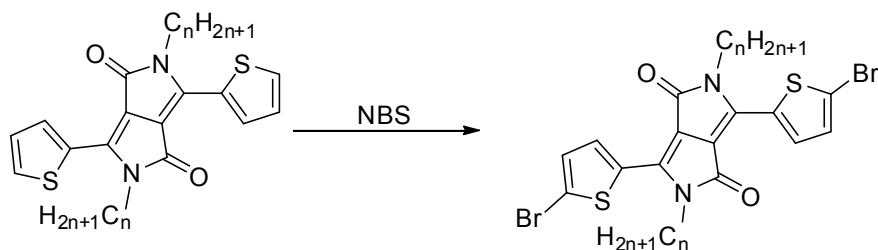
A one neck 100 ml round bottom flask with magnetic stirring bar, was charged with 1 eq of (2) in 50 ml of chloroform. After 30 min of stirring at room temperature, 2.2 eq of NBS were added in small portion. The mixture was stirred at 60°C for 3 h in the dark. The mixture was filtered on Buchner funnel and the crude product washed several times with MeOH. The final product was dried under vacuum until complete solvent removal.

1.3.1.3.1 2,5-Dodecyl-3,6-bis(5-bromothiopen-2-yl)pyrrolo[3,4-*c*]-pyrrole-1,4-dione (DPP_C12-Br$_2$, M-2)

(2a): 1.5 g, 2.35 mmol

NBS: 1.045 g, 5.88 mmol

CHCl$_3$: 30 ml

Yield: 1.178 g, 1.63 mmol, 69%

^{1}H-NMR (C$_2$D$_2$Cl$_2$, 400 Hz): 8.45 (d, J=4.0 Hz, 2H), 7.15 (d, J=4.0 Hz, 2H), 3.87 (t, J$_1$=8.0 Hz, J$_2$=16.0 Hz, 4H), 1-57-1.72 (m, 4H), 1.12-1.42 (m, 36 H), 0.77-0.86 (t, J$_1$=4.0 Hz, J$_2$=12.0 Hz 6H)
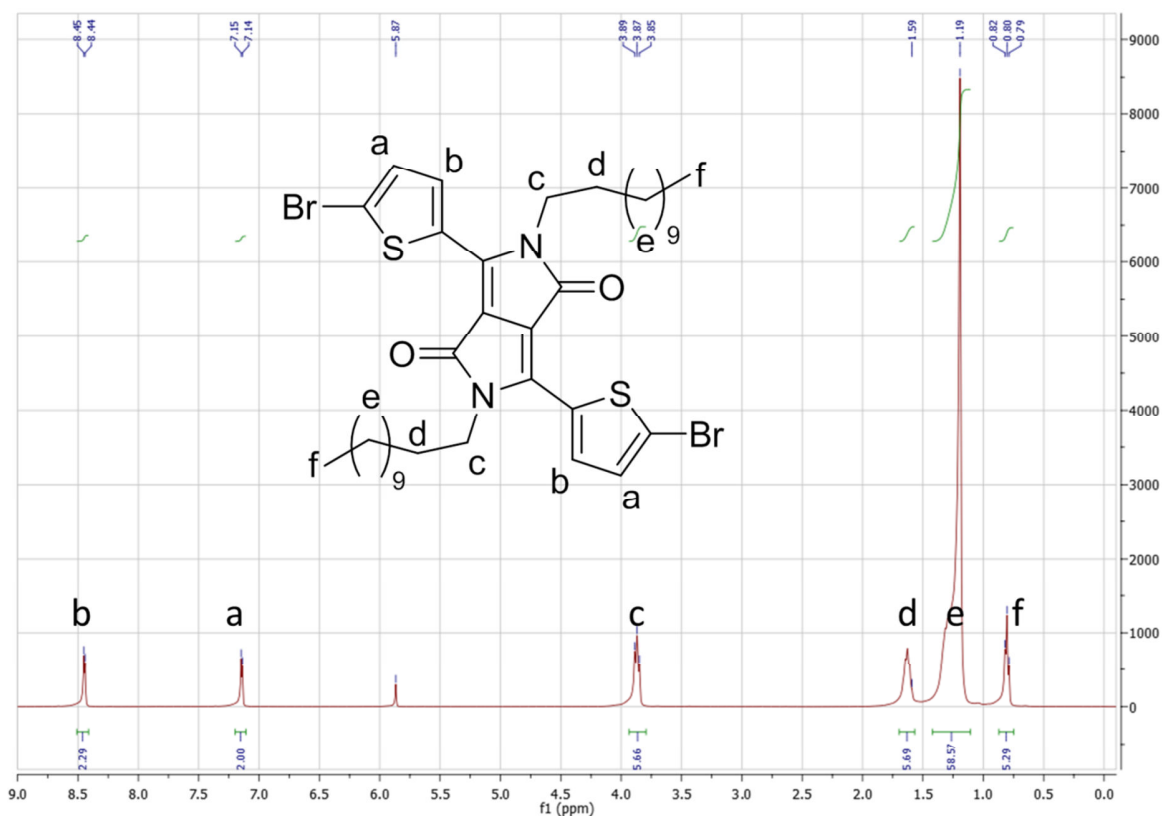
1.3.1.3.2 2,5-Hexadecyl-3,6-bis(5-bromothiopen-2-yl)pyrrolo[3,4-c]-pyrrole-1,4-dione (DPP_C16-Br$_2$, M-3)
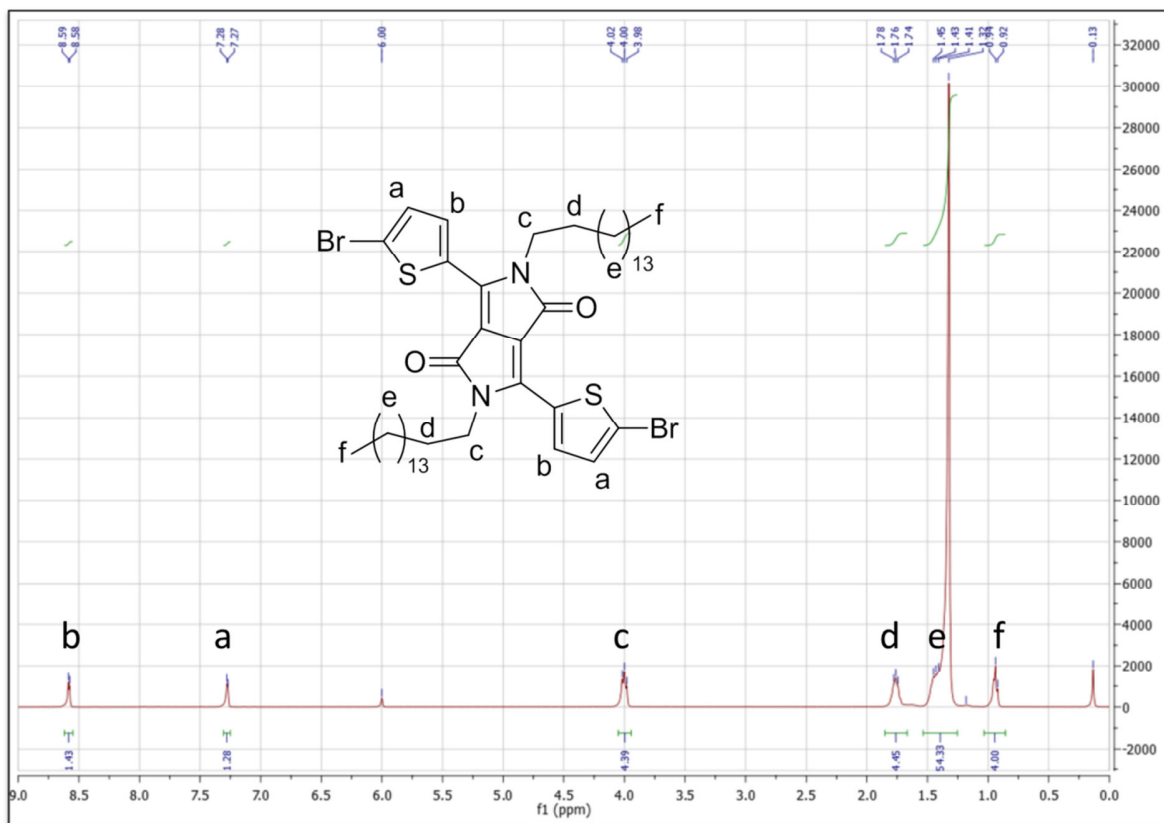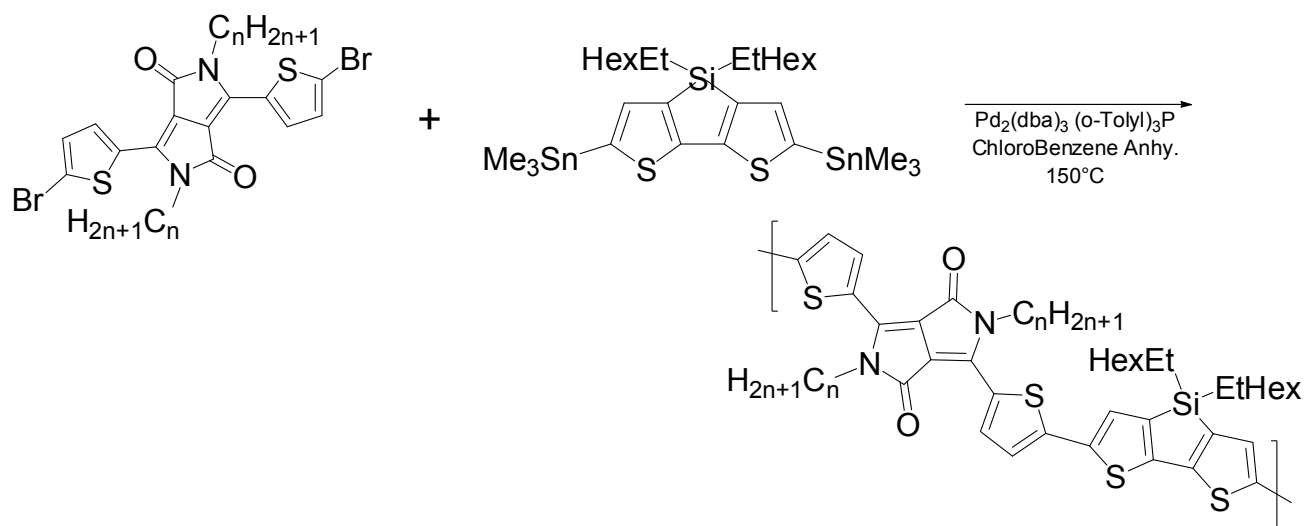
(2b): 1.054 g, 1.34 mmol

NBS: 580 mg, 3.26 mmol

CHCl$_3$: 20 ml

Yield: 0.521, 0.57 mmol, 43%

^{1}H-NMR (C$_2$D$_2$Cl$_2$, 400 Hz): 8.45 (d, J=4.0 Hz, 2H), 7.15 (d, J=4.0 Hz, 2H), 3.87 (t, J$_1$=8.0 Hz, J$_2$=16.0 Hz, 4H), 1-54-1.72 (m, 4H), 1.12-1.42 (m, 52 H), 0.75-0.90 (t, J$_1$=4.0 Hz, J$_2$=12.0 Hz 6H)

1.3.1.4 Polymer synthesis

1.3.1.4.1 General Stille polycondensation procedure

A Schlenk tube with screw cap and a magnetic stirring bar, was charged with 1 equivalent of 4,4'-bis(2-ethylhexyl)-5,5'-bis(trimethyltin)-dithieno[3,2-*b*:2,3-*d*]silole (M-1), 1 equivalent of dithieno-

DPP (M-2 to -4), 2% molar of Pd$_2$(dba)$_3$ and 10% molar of (o-tolyl)$_3$P respect to the catalyst. Then few milliliters of anhydrous chlorobenzene, previously purged with dry nitrogen, were added to the reactor and 3 purge flow cycles are performed to eliminate the remaining oxygen and moisture. The reaction was performed at 150°C for 2-3 hours in the dark. The product was precipitated in MeOH and purified by Soxhlet extractor using a series of solvents (acetone, petroleum ether, cyclohexane, toluene, chloroform and chlorobenzene) to remove residual catalyst and to fractionate the polymer into different molecular weight fractions.

1.3.1.4.2 [(4,4'-Bis(2-ethylhexyl)dithieno[3,2-*b*:2',3'-*d*]silole)-2,6-diyl-*alt*-2,5-dodecyl-3,6-bis(thiopen-2-yl)pyrrolo[3,4-*c*]-pyrrole-1,4-dione] – PSBDPP_C12

M-1: 596 mg, 0.80 mmol

M-2: 637 mg, 0.80 mmol
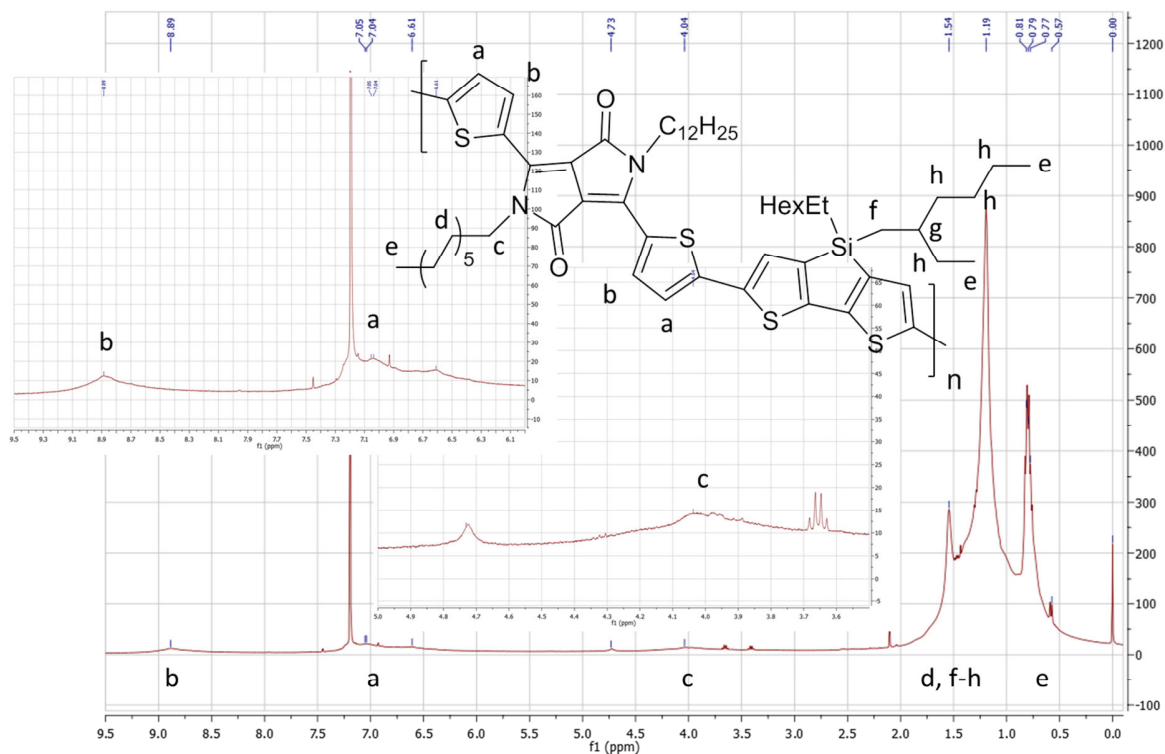
Pd$_2$(dba)$_3$: 15 mg, 0.016 mmol, 2% molar

(o-tolyl)$_3$P: 24 mg, 0.08 mmol

Chlorobenzene anhydrous: 8 ml

Fraction	Yield (%)		
Cyclohexane	71 mg	0.07 mmol	9%
Toluene	632 mg	0.600 mmol	75%
Chlorobenzene	42 mg	0.04 mmol	5%
	745 mg	0.611 mmol	89%

^{1}H-NMR (CDCl$_3$): 8.89 (2H), 7.00-6.60 (2H), 4.73 (4H), 2.00-0.90 (62 H), 0.90-0.50 (18H)

1.3.1.4.3 [(4,4'-Bis(2-ethylhexyl)dithieno[3,2-*b*:2',3'-*d*]silole)-2,6-diyl-*alt*-2,5-hexadecyl-3,6-bis(thiopen-2-yl)pyrrolo[3,4-*c*]-pyrrole-1,4-dione] – PSBDPP_C16

M-1: 328 mg, 0.44 mmol, 1 eq

M-3: 400 mg, 0.44 mmol, 1 eq
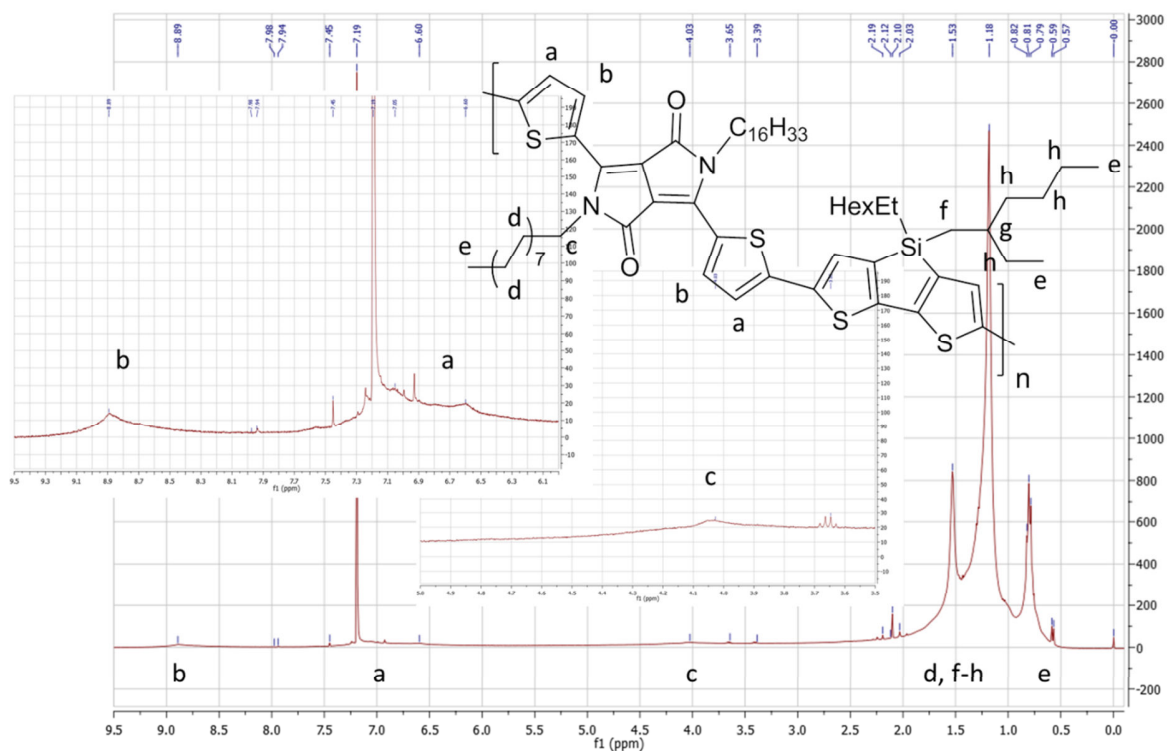
Pd$_2$(dba)$_3$: 10 mg, 0.01 mmol, 0.025 eq

(o-tolyl)$_3$P: 16 mg, 0.05 mmol, 0.11 eq

Chlorobenzene anhydrous: 5 ml

Fraction	Yield (%)		
Cyclohexane	53 mg	0.05 mmol	11%
Toluene	447 mg	0.38 mmol	86%
	600 mg	0.43 mmol	97%

^{1}H-NMR (CDCl$_3$): 8.89 (2H), 7.00-6.60 (2H), 4.73 (4H), 2.00-0.90 (62 H), 0.90-0.50 (18H)

1.3.1.4.4 [(4,4'-bis(2-ethylhexyl)dithieno[3,2-*b*:2',3'-*d*]silole)-2,6-diyl-*alt*-2,5-hexyldecyl-3,6-bis(thiopen-2-yl)pyrrolo[3,4-*c*]-pyrrole-1,4-dione] – PSBDPP_C6C10

M-1: 616 mg, 0.83 mmol
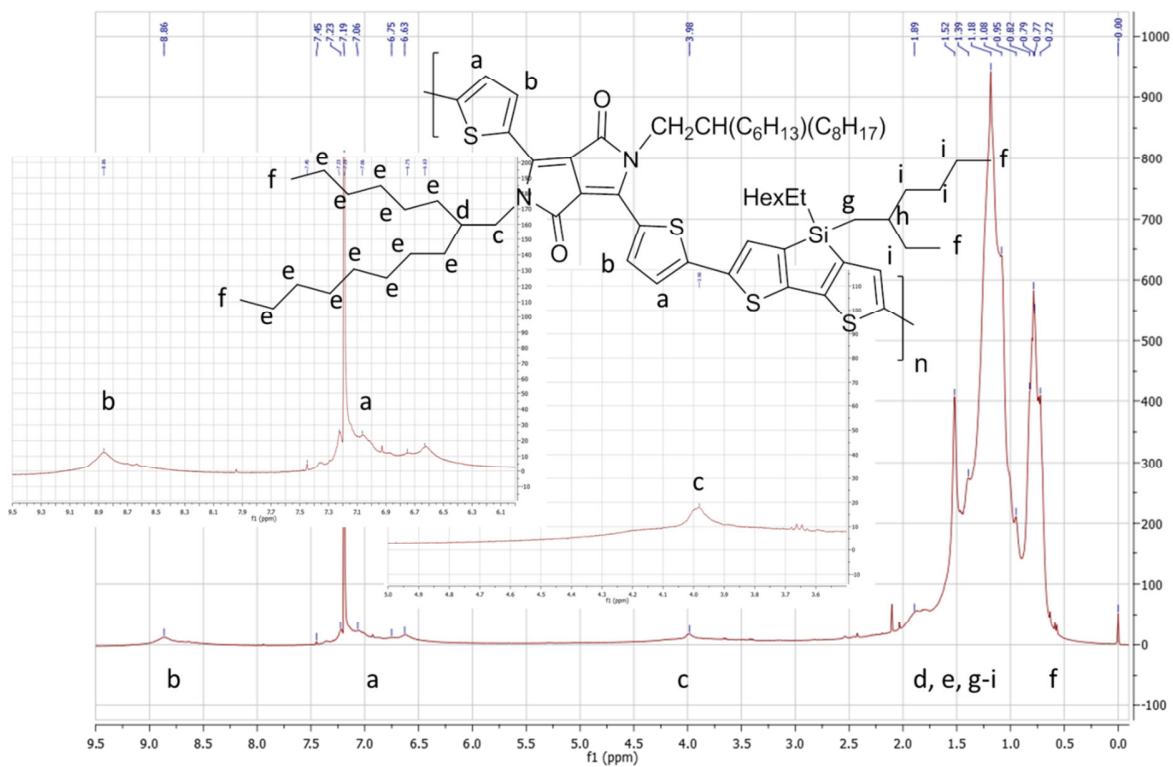
M-4: 753 mg, 0.83

Pd$_2$(dba)$_3$: 17 mg, 0.019 mmol

(o-tolyl)$_3$P: 26 mg, 0.08 mmol

Chlorobenzene anhydrous: 8 ml

Fraction	Yield (%)		
Petroleum ether	5 mg	0.004 mmol	0.5%
Cyclohexane	500 mg	0.43 mmol	52%
	505 mg	0.43 mmol	52.5%

^{1}H-NMR (CDCl$_3$): 8.89 (2H), 7.00-6.60 (2H), 4.73 (4H), 2.00-0.90 (62 H), 0.90-0.50 (18H)

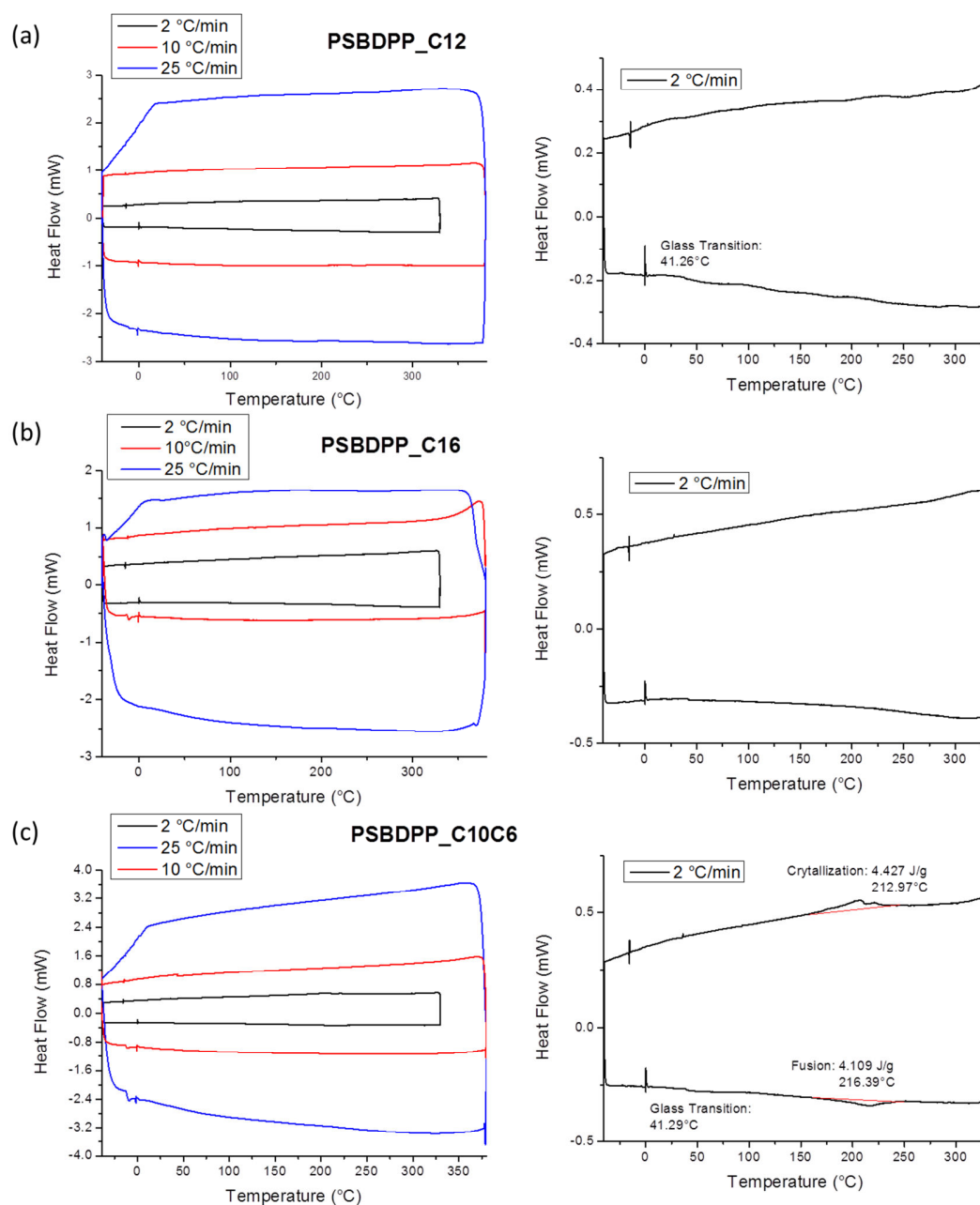## 1.3.1.5 Thermal properties

Figure 1 DSC thermograms of a) PSBDPP_C12, b) PSBDPP_C16 and c) PSBDPP_C110C6. Different temperature rates (2°C/min, black; 10°C/min red; 25°C/min blue) were used to investigate the polymer phase transition. The glass transition at ≈40°C in a) and b) has been attributed to side-chain mobility, while the fusion/crystallization peak at ≈214°C concern all the polymer.

1.4 DTP Series

1.4.1 Monomer synthesis

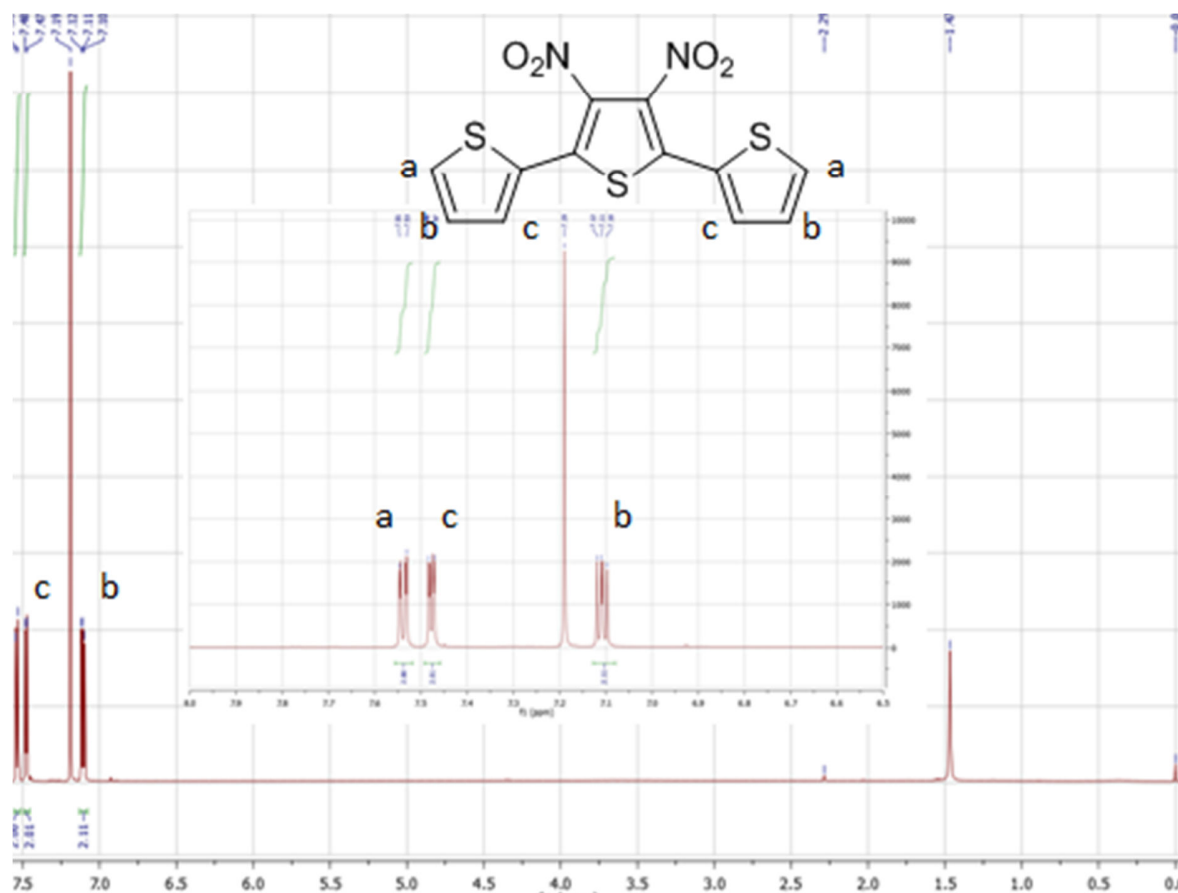#### 1.4.1.1 3',4'-Dinitro-2,2':5',2''-terthiophene (1)
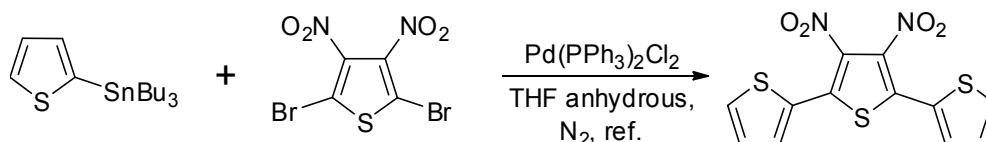
In a 100 ml one neck round bottom Schlenk flask with a magnetic stirring bar, was charged with 2-tributylstannylthiophene (6.9 g, 21.7 mmol), 2,5-dibromo-3,4-dinitrothiophene (3.0 g, 9.0 mmol) and Pd(PPh$_3$)$_2$Cl$_2$ (63 mg, 0.09 mmol). Anhydrous tetrahydrofuran (50 mL, THF) was added and the mixture was stirred for 1 h at room temperature under inert atmosphere and then refluxed overnight. The light brown solution was cooled at room temperature and precipitated in n-hexane. The suspension was filtered on Buchner funnel under reduced pressure and a dark gold precipitate was collected on the filter. The filtrate was washed several times with warm n-hexane and finally dried under vacuum until complete solvent removal.
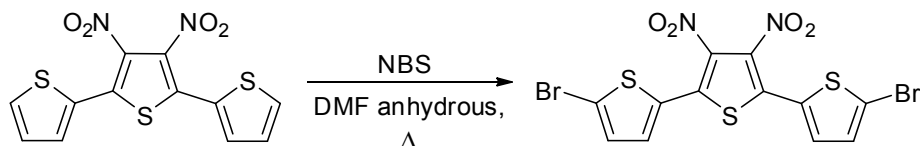
Yield: 2.5 g, 7.4 mmol, 82%

^{1}H-NMR (CDCl$_3$, 400 Hz): 7.54 (d, J=8.0 Hz, 2H), 7.48 (d, J=4.0 Hz, 2H), 7.11 (t, J$_1$=4.0 Hz, J$_2$=8.0 Hz, 2H)

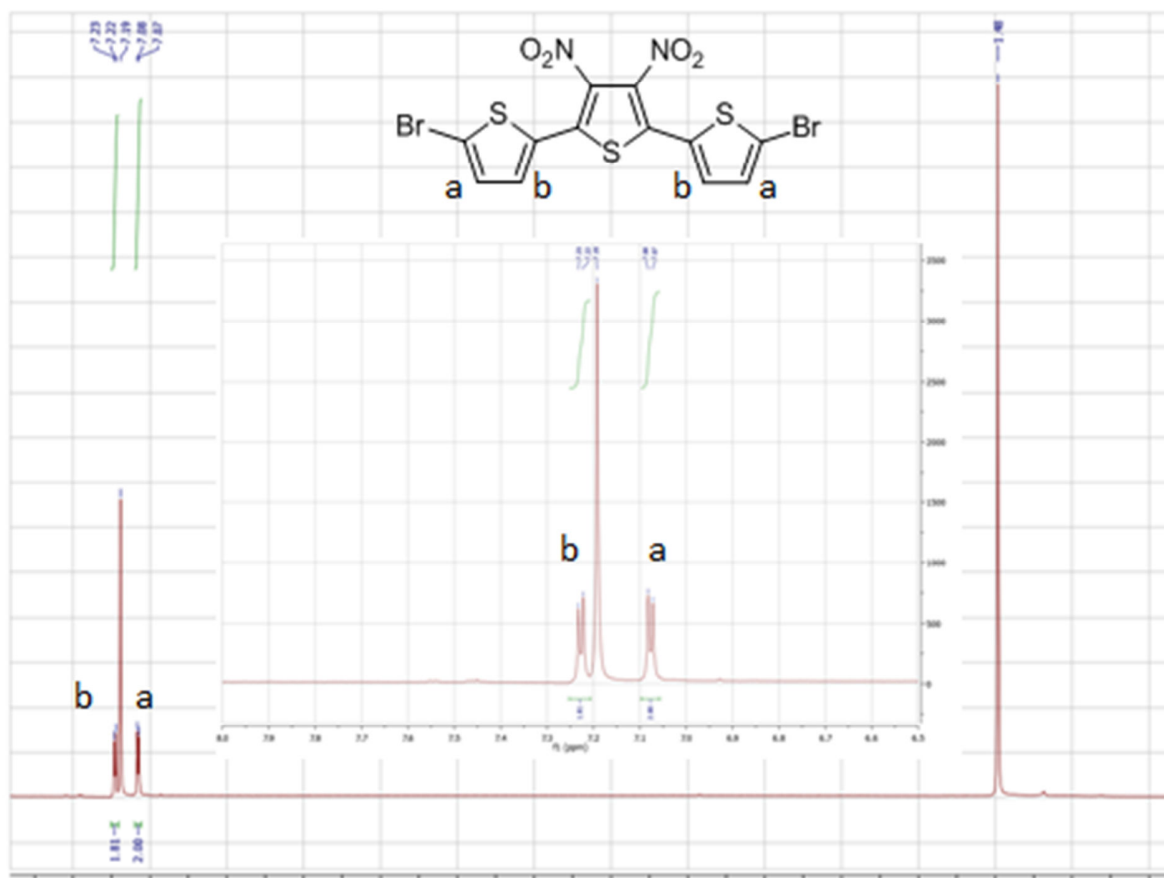## 1.4.1.2 5,5''-dibromo-3',4'-dinitro-2,2':5',2''-terthiophene (2)

A one neck 100 ml round bottom Schlenk flask with a magnetic stirring bar, was charged with (1) (2.5 g, 7.4 mmol) and 50 ml of anhydrous *N,N*-dimethylformamide (DMF) and stirred at room temperature until complete dissolution of the solid. NBS (3.3 g, 18.5 mmol) was added in small portions. The mixture was stirred at 50 °C overnight in the dark. The orange mixture was filtered on a Buchner funnel and the filtrate washed several times with warm deionized water and methanol. The final product, a bright orange powder, was dried under vacuum until complete solvent removal.
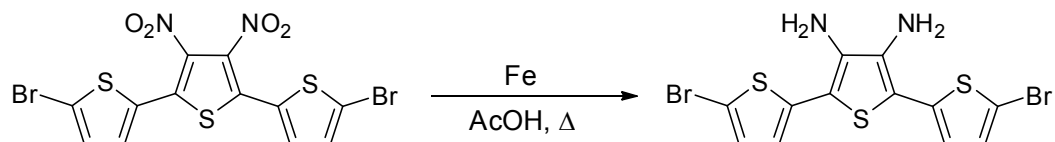
Yield: 2.9 g, 5.8 mmol, 79%

^{1}H-NMR (CDCl$_3$, 400 Hz): 7.23 (d, J=4.0 Hz, 2H), 7.07 (d, J=4.0 Hz, 2H)

1.4.1.3 5,5''-dibromo-3',4'-diamino-2,2':5',2''-terthiophene (3)

A one neck 100 ml round bottom flask with a magnetic stirring bar, was charged with 1 equivalent of (2) and 10 equivalent of iron powder. Acetic acid was added (50 ml) and the mixture was heated at 60°C for 1h. The final brown mixture was filtered on Buchner funnel under reduced pressure to separate the iron powder from the product. The product (3) was directly utilized in the next synthesis step without any purification, accounting for a 100% yield in stoichiometric consideration.

1.4.1.4 **Di-6-(1,4-benzodioxane)ethanedione (4b)**
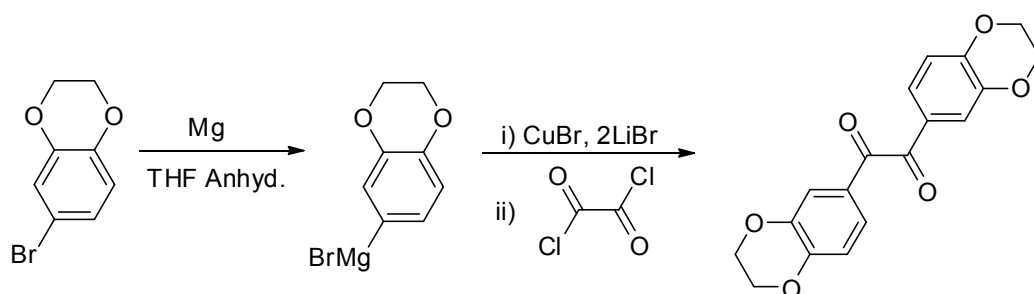
In a one neck 250 ml round bottom Schlenk flask with a magnetic stirring bar, a solution of LiBr (1.61 g, 18.6 mmol) in anhydrous THF (15 ml) to a suspension of CuBr (1.33 g, 9.3 mmol) in anhydrous THF (20 ml). The mixture was stirred at room temperature until it became homogeneous and then cooled at 0°C. To this mixture a solution of 6-(1,4-benzodioxane)magnesium bromide in anhydrous THF, freshly prepared from 6-bromo-1,4-benzodioxane (2.00 g, 9.3 mmol) and Mg (0.23 g, 9.3 mmol), was added dropwise. After 15 minutes 0.31 ml of oxalyl chloride (471 mg, 3.7 mmol) was quickly added to the stirring mixture. The solution was stirred for 30 minutes at 0°C and then let it warm to room temperature. The mixture was then quenched with a saturated aqueous NH_4Cl solution and extraxted with ethyl acetate. The organic phase was dried over Na_2SO_4 and concentrated under vacuum.

Yield: 1.5 g, 3.06 mmol, 83%

^{1}H-NMR (CDCl$_3$, 400 Hz): 7.43 (s, 2H), 7.39 (d, J=8.0 Hz, 2H), 6.86 (d, J= 8.0 Hz, 2H), 4.20 (m, 8H)

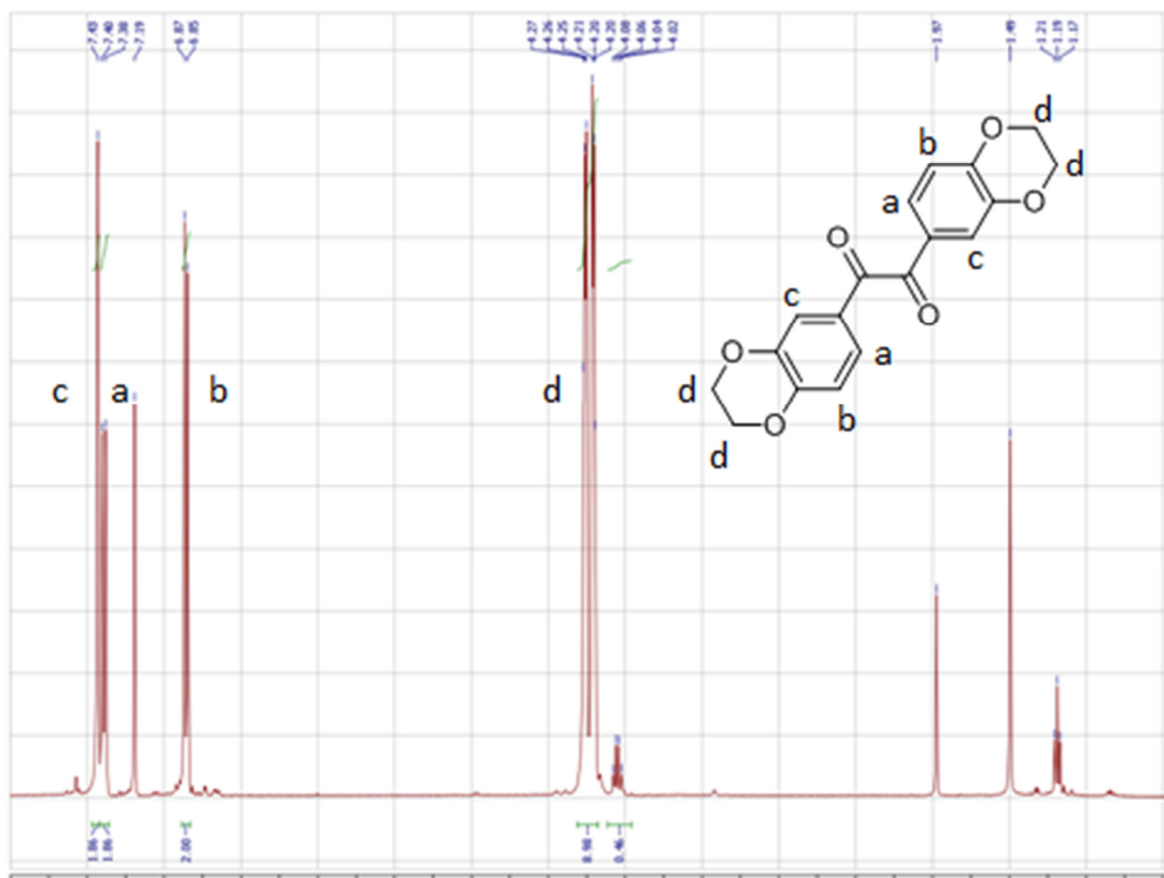### 1.4.1.5 General procedure for the nucleophilic attack of the 5,5''-dibromo-3',4'-diamino-2,2':5',2''-terthiophene (3) to the α–dione (4a and 4b)
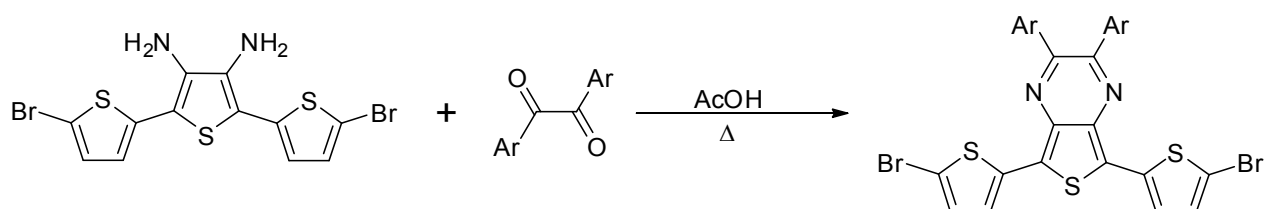
A one neck 100 ml round bottom flask with magnetic stirring bar, was charged with 1 eq of (3) in AcOH. After 30 min of stirring at room temperature, 3 eq of 4 were added in small portion. The mixture was stirred at 60 °C overnight. The mixture was filtered on Buchner funnel and the crude product washed several times with H_2O and MeOH. The final product was dried under vacuum until complete solvent removal.

1.4.1.6 **5,7-Bis(3-bromothiophen-2-yl)-2,3-di(thiophen-2-yl)thieno[3,4-*b*]pyrazine (M-5, DTP_Th)**
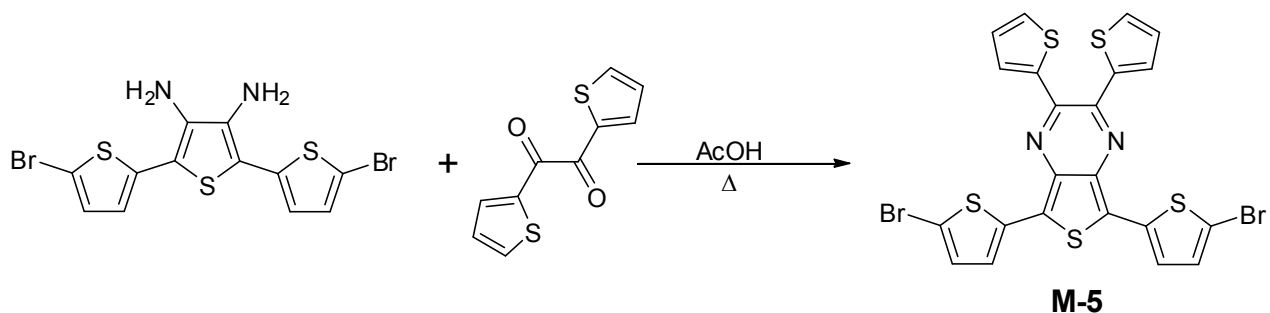
(3): 1.23 g, 2.8 mmol

(4a): 2,00 g, 9.00 mmol

AcOH: 60 ml

Yield: 0.96 g, 1.5 mmol, 54%

^{1}H-NMR (CDCl$_3$, 400 Hz): 7.48 (d, J=8.0 Hz, 2H), 7.28 (d, J=4.0 Hz, 2H), 7.20 (d, J=4.0 Hz, 2H), 6.97 (m, 2H+2H)
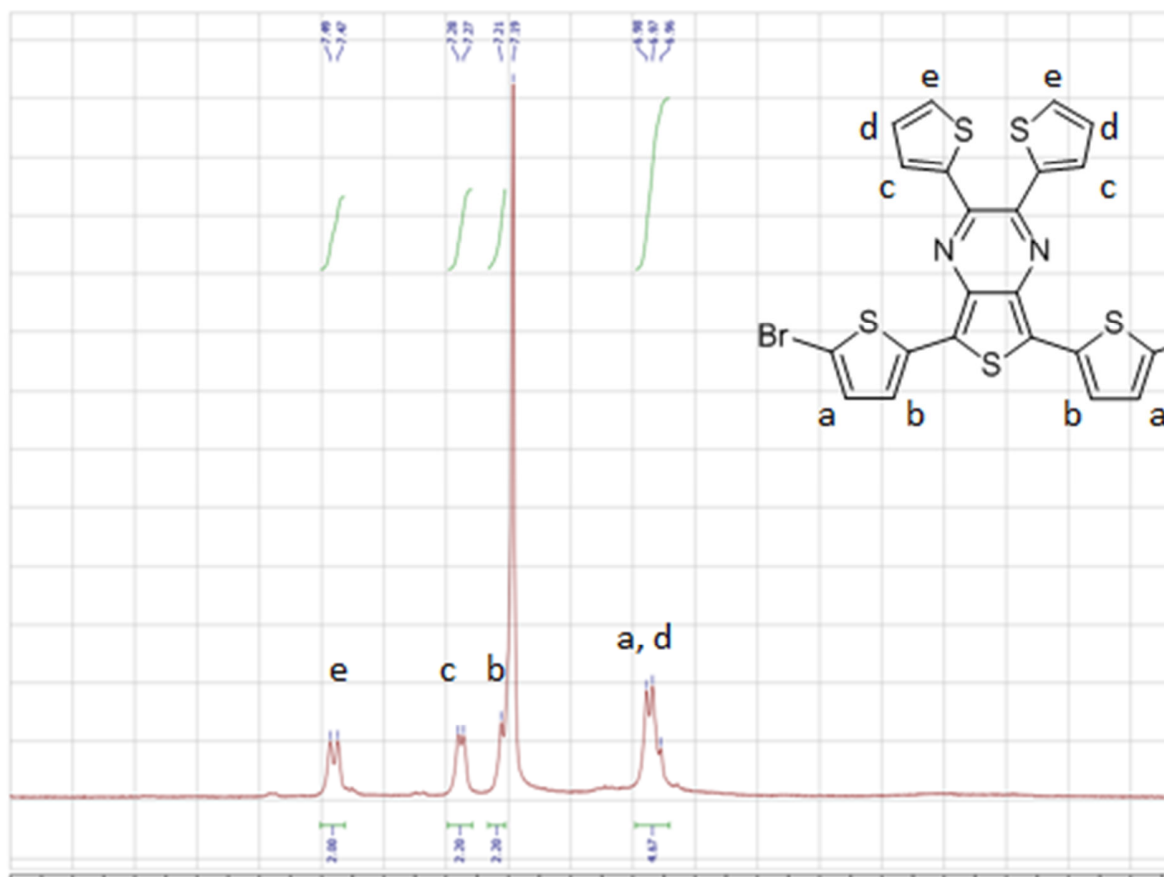
1.4.1.7 5,7-bis(3-bromothiophen-2-yl)-2-(2,3-dihydrobenzo[*b*][1,4]dioxin-6-yl)-3-(2,3-dihydrobenzo[*b*][1,4]dioxin-7-yl)thieno[3,4-*b*]pyrazine (DTP_EDOPh, M-6)
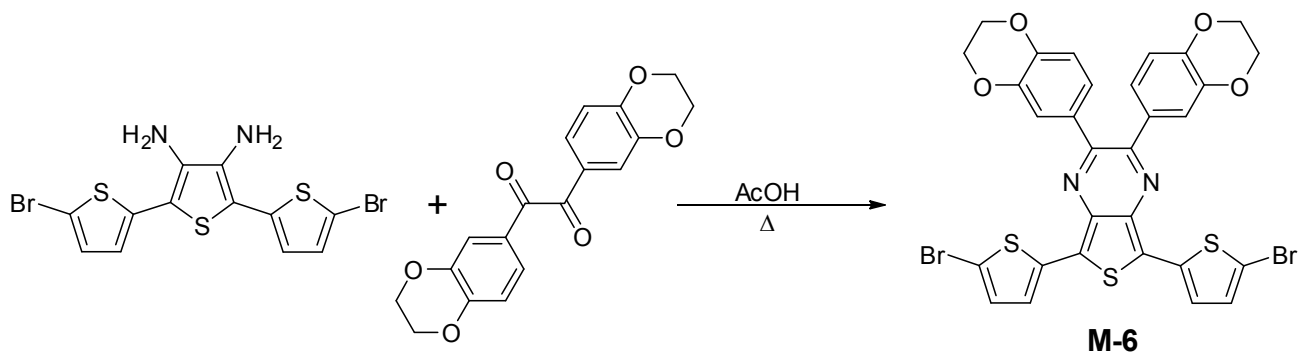
(3):0.69 g, 1.59 mmol

(4b): 1.3 g, 3.98 mmol

AcOH: 40 ml

Yield: 0.61 g, 0.84 mmol, 53%

^{1}H-NMR (CDCl$_3$, 400 Hz): 7.44 (s, 2H), 7.39 (d, J=8.0 Hz, 2H), 7.22 (d, J=4.0 Hz, 2H), 6.86 (d, J=8.0 Hz, 2H), 6.74 (d, J=8.0 Hz, 2H), 4.20 (m, 8H)
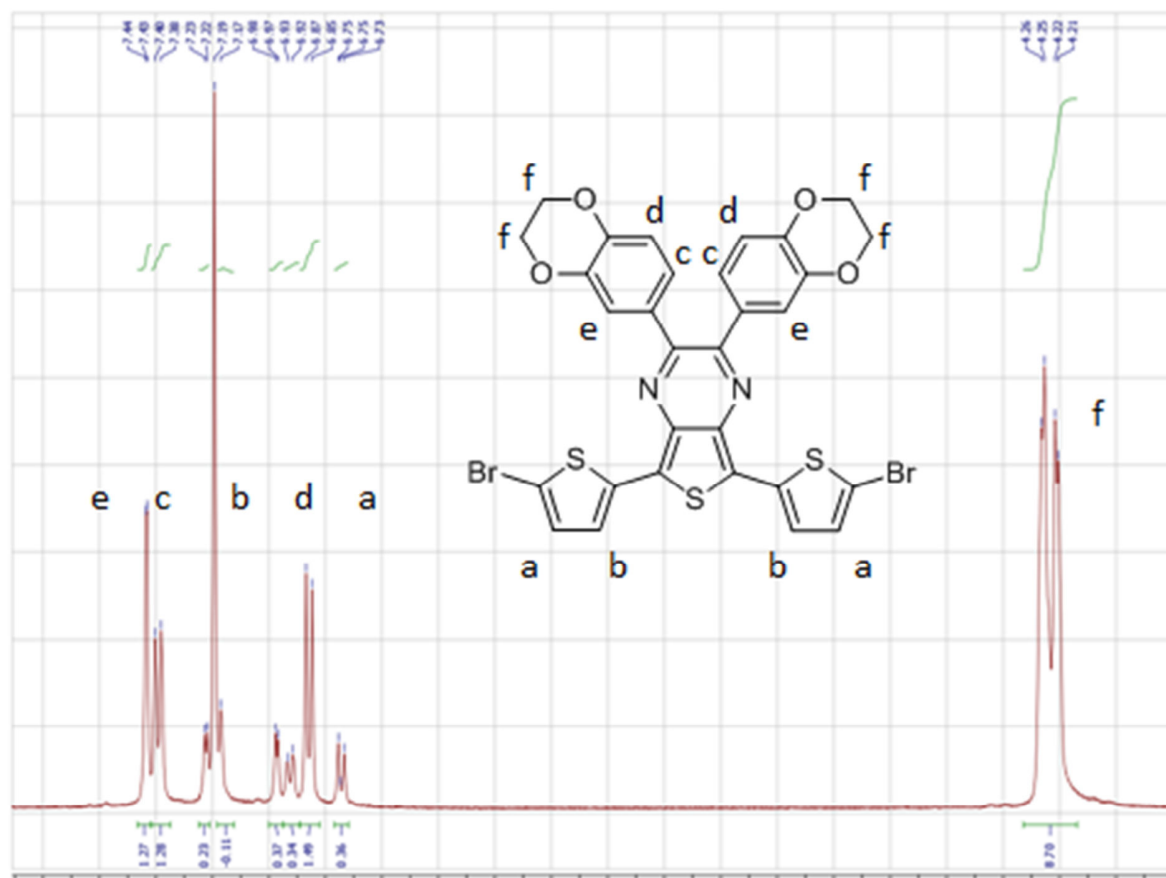
1.4.2 Polymer synthesis

1.4.2.1 General Stille polycondensation procedure

A Schlenk tube with screw cap and a magnetic stirring bar, was charged with 1 equivalent of 4,4'-bis(2-ethylhexyl)-5,5'-bis(trimethyltin)-dithieno[3,2-b:2,3-d]silole (M-1), 1 equivalent of dithieno-DTP (M-5 or M-6), 2% molar of $Pd_2(dba)_3$ and 10% molar of (o-Tolyl)$_3$P respect to the catalyst. Then few milliliters of anhydrous chlorobenzene, previously purged with dry nitrogen, were added to the reactor and 3 purge flow cycles were performed to eliminate the remaining oxygen and moisture. The reaction was performed at 150 °C for few hours in the dark. The product was precipitated in MeOH and purified by Soxhlet extractor using a series of solvents (acetone, petroleum ether, cyclohexane, toluene, chloroform and chlorobenzene) to remove residual catalyst and to fractionate the different molecular weight molecules.

1.4.2.2 [(4,4'-bis(2-ethylhexyl)dithieno[3,2-*b*:2',3'-*d*]silole)-2,6-diyl-*alt*-5,7-bisthiophen-2-yl)-2,3-di(thiophen-2-yl)thieno[3,4-*b*]pyrazine] – PSBDPP_Th

M-1: 0.60 g, 0.81 mmol

M-5: 0.50 g, 0.81 mmol

Pd$_2$(dba)$_3$: 14.8 mg, 0.016 mmol

(o-Tolyl)$_3$P: 24.5 mg, 0.081 mmol

Chlorobenzene anhydrous: 5 ml

Fraction	Yield (%)		
Cyclohexane	43 mg	0.05 mmol	6%
Toluene	125 mg	0.14 mmol	17%
Chlorobenzene	270 mg	0.31 mmol	38%
Soxhlet residual	92 mg	0.10 mmol	12%
	530 mg	0.60 mmol	73%
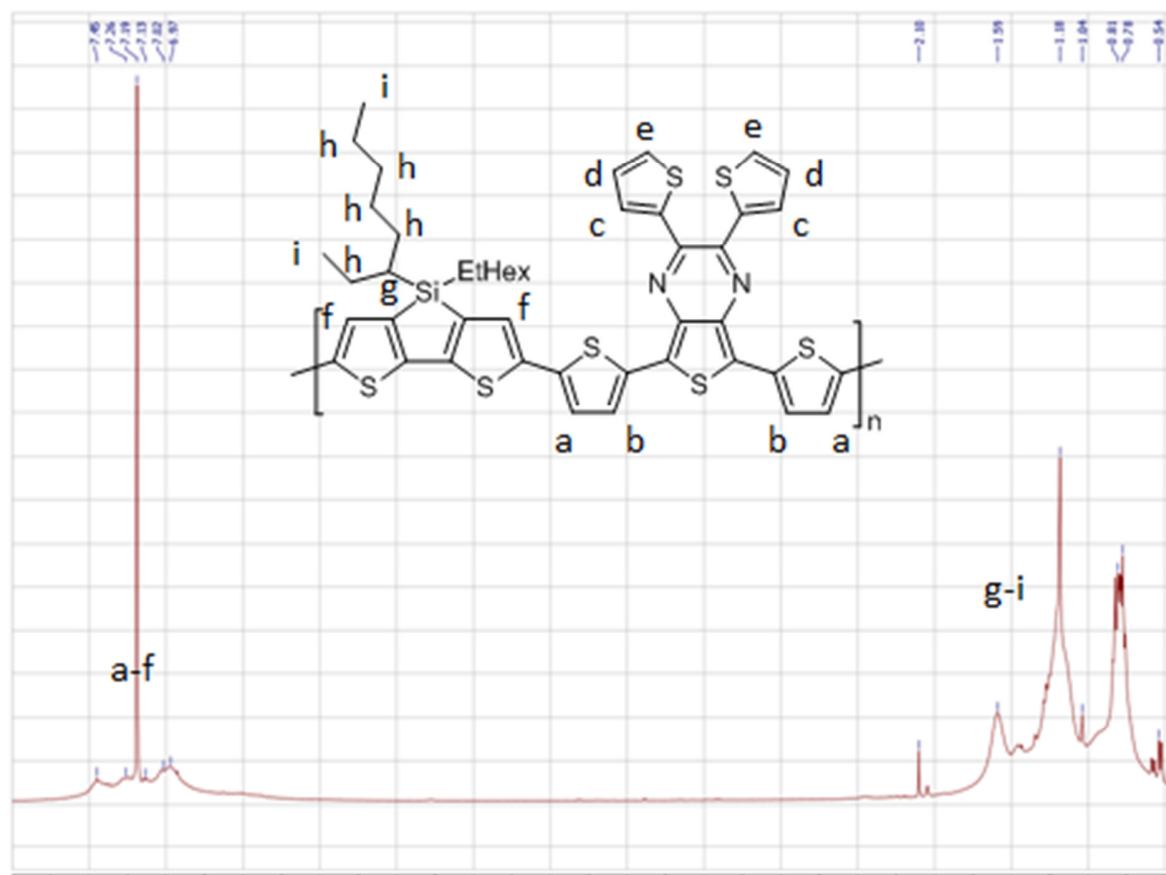
1.4.2.3 [(4,4'-bis(2-ethylhexyl)dithieno[3,2-*b*:2',3'-*d*]silole)-2,6-diyl]-*alt*-[5,7-bithiophen-2-(2,3-dihydrobenzo[*b*][1,4]dioxin-6-yl)-3-(2,3-dihydrobenzo[*b*][1,4]dioxin-7-yl)thieno[3,4-*b*]pyrazine] – PSBDTP_EDOPh
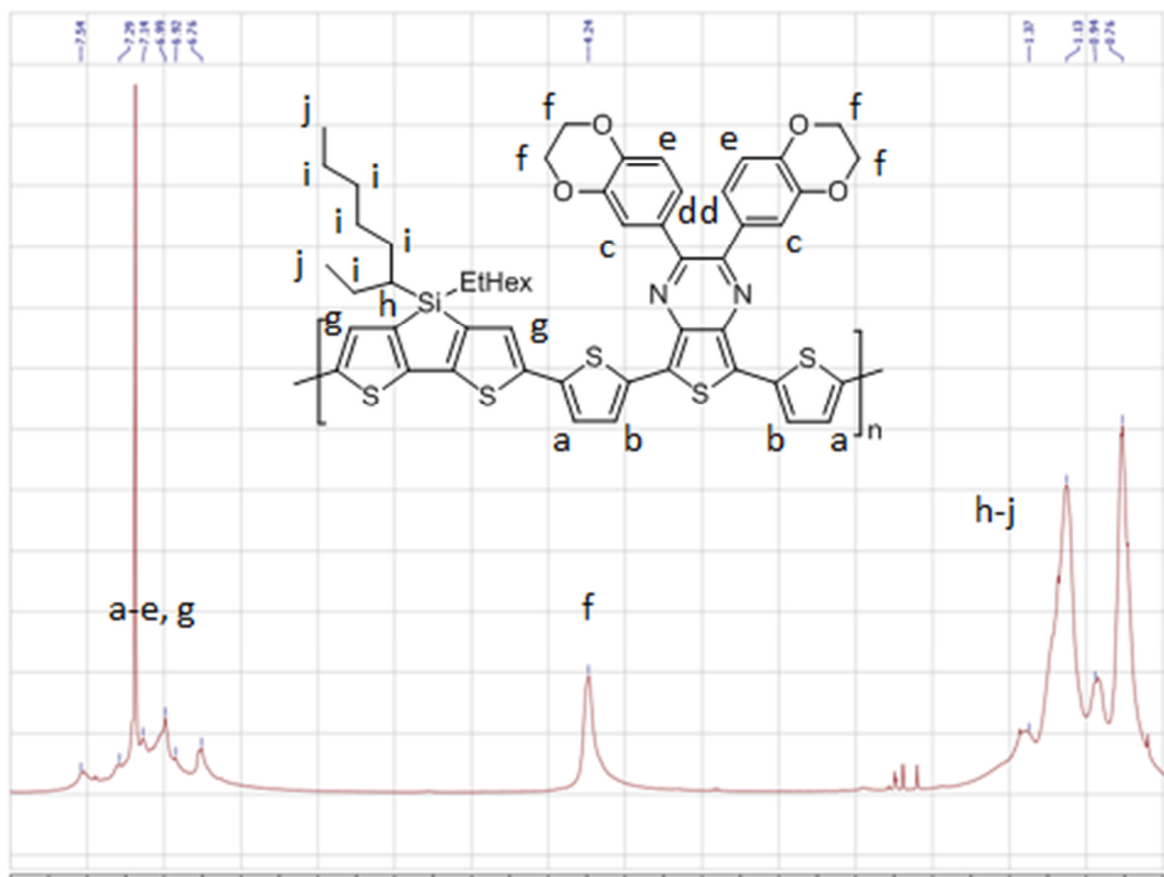
M-1: 0.57 g, 0.76 mmol

M-6: 0.55 g, 0.76 mmol

Pd$_2$(dba)$_3$: 13.7 mg, 0.015 mmol

(o-Tolyl)$_3$P: 23.1 mg, 0.076 mmol

Chlorobenzene anhydrous: 5 ml

Fraction	Yield (%)		
Cyclohexane	26 mg	0.03 mmol	4%
Toluene	210 mg	0.21 mmol	28%
	236 mg	0.24 mmol	32%

2   Application in Inverted Devices

2.1.1   OPV device preparation and characterizations at Belectric OPV GmbH

To fabricate the cells ITO coated glass substrates were used. ITO substrates were wiped with a soft isopropyl alcohol (IPA) soaked tissue before being sonicated in IPA for 15 mins. A thin layer of ZnO nanoparticles was deposited by doctor blading from isopropanol solution onto ITO-substrate and annealed at 140 °C for 10 min. Afterwards, a solution of PSBDPP and $PC_{61}BM$ 10:20 mg/mL in the solvent of choice was doctor bladed on top of the ZnO layer. PEDOT: PSS solution was doctor bladed onto the active layer without any following thermal treatment. A silver electrode (150 nm) was vacuum deposited on top to complete the device (27 mm^2).

Absorption spectra were recorded with a Perkin Elmer Lambda 35 UV-vis spectrometer outside the glove box during device fabrication. J-V curves were measured in the glove box with a Xenon arc lamp (AM 1.5, 100 mW cm^{-2}) and a custom software. EQE curves were measured outside the glove box

2.1.2   OPV device preparation and characterizations at i-MEET

ZnO nanoparticles suspension in isopropanol was spin coated at 3000 rpm on previously cleaned (15 minutes of sonicating bath in isopraponol) 2.5x2.5 cm glass/ITO slides and then annealed at 140 °C for 10 minutes. A solution of PSBDPP_C12:$PC_{61}BM$ 1:2 (m/m) in o-xylene (or chlorobenzene) with 10 mg/ml of polymers was prepared inside the glove box and stirred at 80 °C for few hours before coating. The active layer was spin-coated on top of the ZnO layer at 500, 1000, 2000 and 4000 rpm for 60 s by dynamic deposition.

J–V curves of all the devices were recorded using a source measurement unit from BoTest. Illumination was provided by a solar simulator (Oriel Sol 1 A from Newport) with AM1.5G spectrum and light intensity of 100 mW cm−2, which was calibrated by a certified silicon solar cell.

The EQE spectra were recorded with an EQE measurement system (QE-R) from Enli Technology (Taiwan). The light intensity at each wavelength was calibrated with a standard single-crystal Si solar cell.

2.1.3 EQE
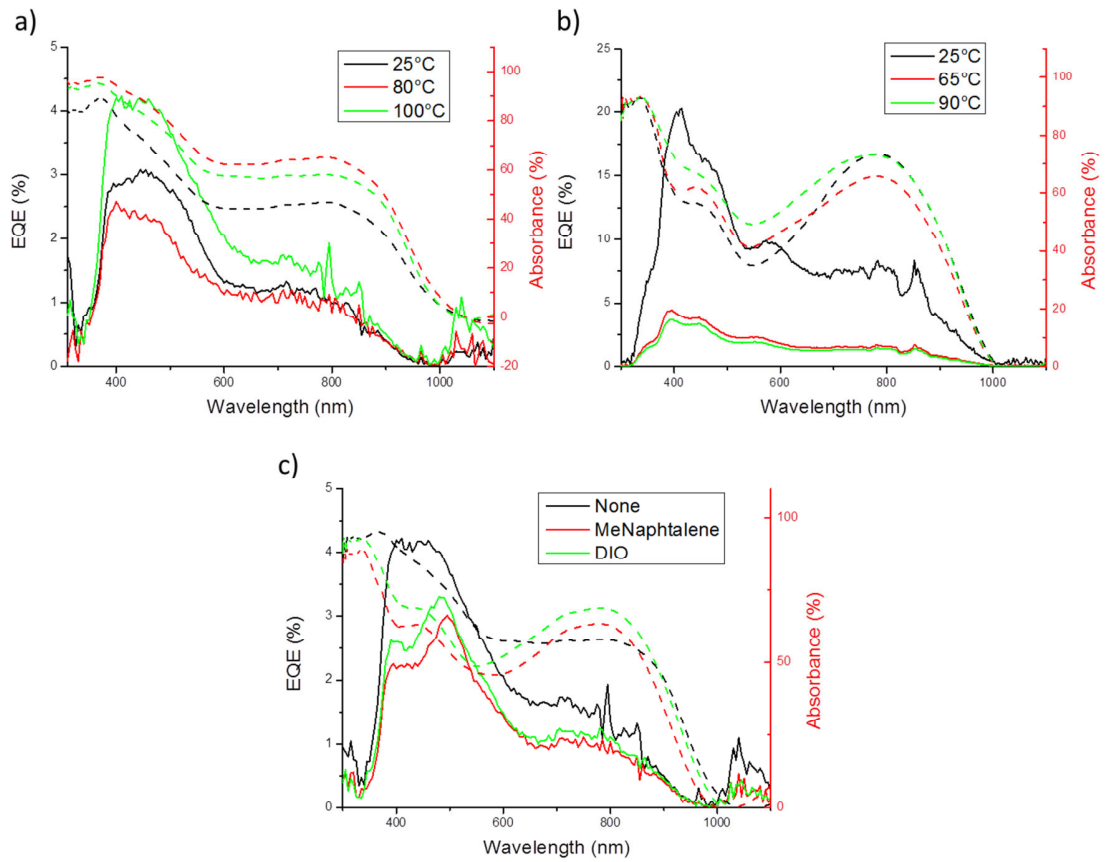
Figure 2.1 EQE curves (left axis) and absorption (%) (right axis) for a) PSBDPP_C10C6 based devices where the AL was coated at different temperature; b) PSBDPP_C12 based devices where the AL was coated at different temperature; c) PSBDPP_C10C6 based devices where the AL was coated from different solvent systems.
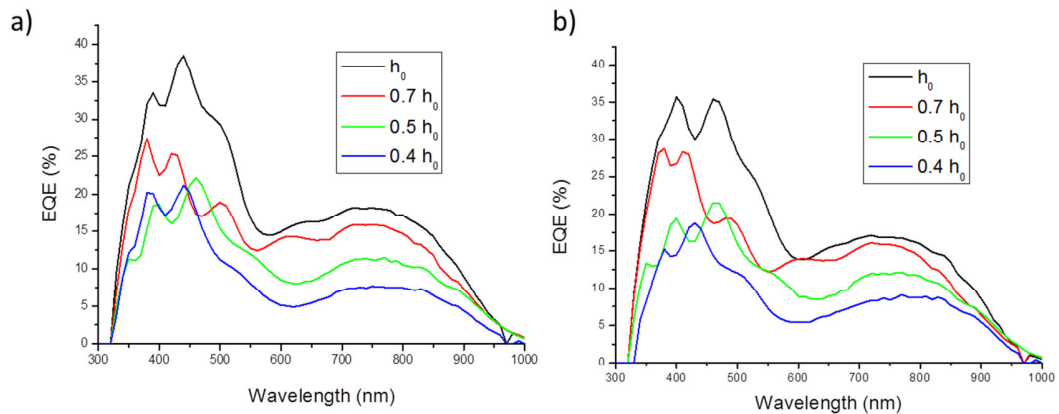
Figure 2.2 EQE curves of devices prepared at i-MEET (spin-coated under inert atmosphere) with AL deposited from o-xylene (a) and chlorobenzene (b) solutions.

2.1.4 OFET preparation and characterization

Bottom-gate bottom-contact transistors featuring 230 nm thermally grown oxide on n++-doped silicon (*Fraunhofer Institute, capacitance 1.5 × 10^{-8} F/cm^2*) were used. For these devices with interdigitated Au source drain electrodes, the channel width was 10 mm and the channel length was 20 μm. The silicon surface was treated with ozone (5 min ozone generation and 25 min incubation). The semiconducting layer consisting of **PSBDPP_C12** (8 mg/mL dissolved in a mixture of 97.5% chloroform and 2.5% *o*-dichlorobenzene) was deposited by *spin-coating* at 1500 rpm for 60 sec with thermal annealing at 80°C for 30 min before characterization. Devices were characterized at room temperature in a N$_2$ atmosphere inside a *glove-box*, using a *Cascade Microtech M150* probe station and *Keithley*.

Details about mobility calculation of field-effect transistors can be found in Ref [43]

2.1.5 AFM images

Figure 2.3 AFM contact micrographs (height and phase) of PSBDPP_C10C6:PC$_{61}$BM 1:2 doctor bladed from a 95:5 (V/V) o-xylene:methylnaphtalene solution at 25°C (top) and 80°C (bottom). These micrographs were taken with a Nanosurf EasyScan 2 AFM.

2.1.6 Femtosecond transient absorption spectroscopy

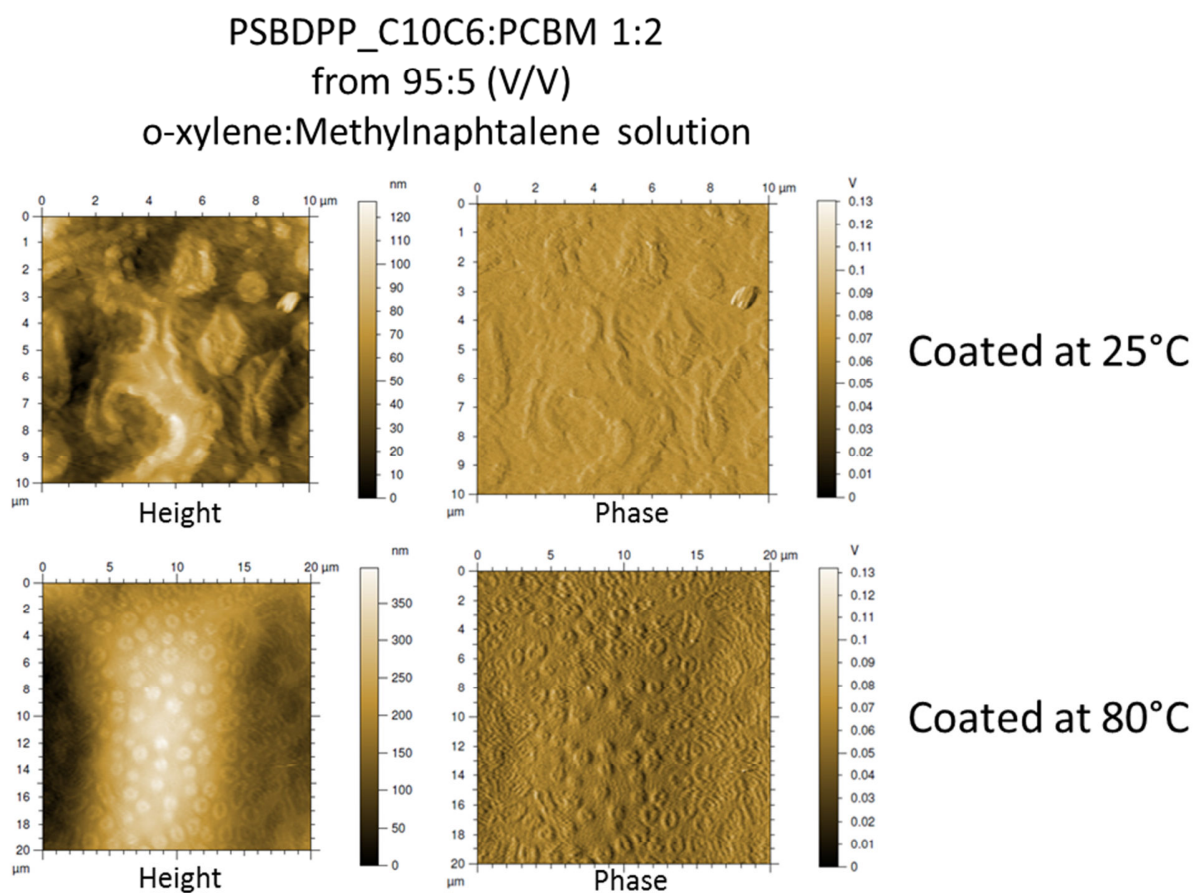Ultrafast spectroscopy (typically 10^{-14}-10^{-12} s) enables us to understand functional, structural and electronic properties of materials. Femtosecond transient absorption spectra yield important device parameters like yield of immediate charge carrier formation (from interfacial charge transfer states), yield of delayed charge carrier formation (due to exciton diffusion to interface), picosecond recombination losses and the reason for them (CT states, triplet states, etc). A detailed schematic of femtosecond pump-probe spectroscopy setup used to investigate organic solar cells in this thesis is shown in Figure 2.4.

BS: Beam Splitter
M: Mirror
SHG: Second Harmonic Generator
CC: Corner Cube
TS: Translation stage
P: Polarizer

C: Chopper
VA: Variable Attenuator
L: Lens
S: Sapphire Crystal
NF: Notch Filter
CF: Colour Filter
SH: Sample Holder
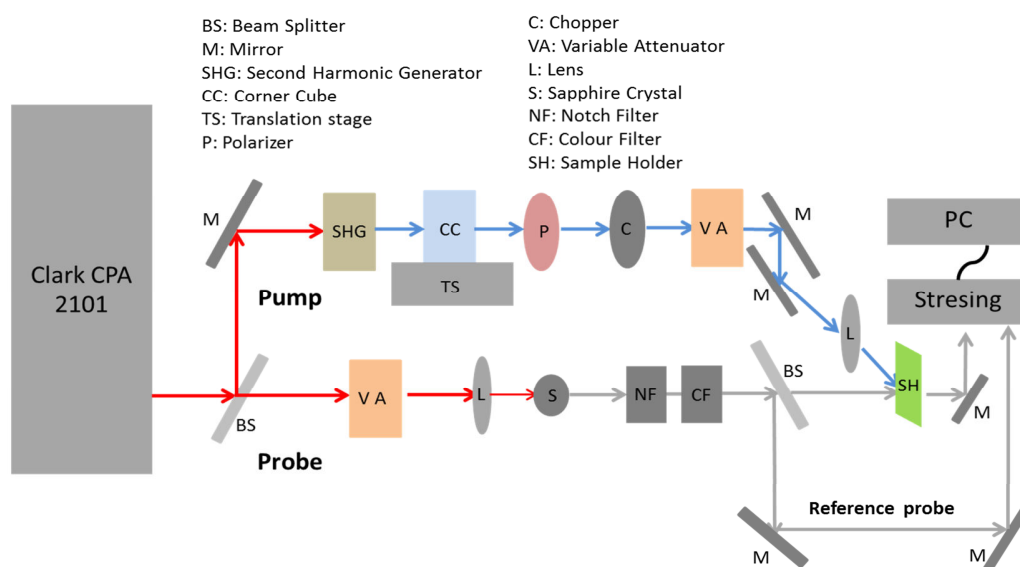
Figure 2.4 Schematics of femtosecond pump probe spectroscopy experimental setup.

A regeneratively amplified laser system was used for producing femtosecond pulses (150 fs) at 1 kHz repetition rate (Clark-MXR CPA2101). The 775 nm pulses were split into two parts: one part was frequency doubled using an LBO crystal (pump pulses), the other part was focused onto a 2 mm Sapphire plate, producing a femtosecond white light super continuum from 420-1600 nm (probe pulses). The probe pulses were focused onto the sample (about 150 µm diameter), and overlapped with the pump pulse (about 300 µm diameter), the delay time of which was controlled via a mechanical translation stage and a corner cube reflector. After transmission through the sample the probe pulses were sent to a prism spectrometer (Entwicklungsbüro Stresing GmbH) with a CCD array (256 pixels, VIS-enhanced InGaAs, Hamamatsu Photonics Inc.). Data acquisition and modelling was

done by custom built Python software, using open source packages *Matplotlib, PyQt4, SciPy, Pyserial*, among others. All measurements were done in a cryostat having dynamic vacuum about 10^{-4} mbar.

Sample details:

Sample: Films of neat polymer (PSBDPP_C12) and active layer blend (PSBDPP_C12:PC$_{61}$BM)

Excitation wavelength: 387 nm and 775 nm with 150 fs, 500 Hz, pulses

Probing: 0.9 eV to 2.5 eV (with white light)

3 Experimental Section of Mechanical Integrity of OPV Devices

3.1 Pull-Off Apparatus and Materials

The instrument used for the *pull-off test* apparatus is an in-house built machine, originally used for the *flat-probe tack test* [54]. It consists of two rigid surfaces, flat and parallel: a cylindrical indenter with a flat surface and a sample holder on which the specimen can be secured. An engine allows the vertical displacement of the indenter, which is connected to a force sensor (TME F108TC, with an operating range of 1-100 N and a sensitivity of 0.05 N) attached to a moving crosshead. The force sensor and a position sensor provide access to every moment *t* the force *F(t)* and the crosshead position *z(t).*

Sampling frequence	10-1000 Hz
Pulling speed range	10-500 µm s^{-1}
F(t) sensitivity	± 0.05N
z(t) sensitivity	± 1 µm

The adhesive utilized was a two component epoxy adhesive, under the commercial name *SADER® from Bostik S. A.* (5 min hardening, maximum load 130 kg/cm2)

The pictures were taken with a *Canon IXUS 132* and the software utilized to treat the images was *ImageJ* (*National Institutes of Health, Open source under Title 17, Section 105 of USA code*).

Contact Angle measurement were performed with *Digidrop DGD-Fast 60, Contact Angle Meter, GBX* in ambient condition. The images were analyzed utilizing a specific GBX software. The solvents used were purchased by *Sigma Aldrich* and used without any further purification. *Milli-Q water* was freshly poured from a *Millipore Synergy-UV*.

The Optical Microscope Images have been taken with a *LEICA DM LM Composed Optical Microscope* equipped with a *LEICA DFC280 Camera* in transmission and reflection modes.

3.2 Sample preparation

The devices fabricated by Dr. Stefan Schumann on 5x5 cm glass/ITO substrate, where cut in square pieces of approximately 1.4x1.4 cm, using a glass cutter. The squares were cut from the center of the plate, in order to exclude a band of approximately ≈0.5 cm from the edges, where the films

were inhomogeneous. During this phase the silver top electrode did not touch the working table surface and glass particle generated by the cutting were gently removed with an air blower.

3.3 Experimental protocol

The specimen was carefully positioned in the center of the sample holder and fixed in it using the screw ring cap. An aluminum disc (12 mm in diameter) was stuck to the indenter head using the epoxy adhesive, in such a way to be strictly parallel to the indenter. The indenter was then put in place on the crosshead. The epoxy adhesive was prepared mixing together the same volume of epoxy resin and hardener. A drop of the liquid adhesive was deposited at the center of the specimen and the measure is started. All the parameters for each step (contact, curing and pulling) were previously entered in the software: force threshold, sampling frequency, pulling speed, etc. From the F(t) curve is possible to directly extract the strain at break (N), as the maximum force before failure.

Once the experiment ended, the two half devices (Lower and Upper half-cell) are photographed, in order to have a visual evaluation of the area effectively removed. This area will be measured afterwards using the *ImageJ* software. The pictures are taken with a *Canon IXUS 132* from a fixed distance of 10 cm, orthogonally to the disc surface.

The stress at break is calculated simply as the *Strain at Break* per unit area (equation (**3.1**)):

$$Stress\ at\ Break\ (Pa) = \frac{Strain\ at\ Break\ (N)}{Removed\ Surface\ (m^2)} \qquad \textbf{(3.1)}$$

The experiment has been repeated between 4 and 8 times for each different samples.

The half devices are then characterized by Contact Angle, AFM, Optical Microscopy and XPS.

3.4 Contact Angle measurement and Surface Energy Calculation

The study of interactions between a solid and a liquid allows the characterization of the solid surface and the prediction, for instance, of its ability to be joined to other materials. One of the most suitable methods to characterize solid surfaces is the determination, by wettability measurement, of the surface free energy. The equilibrium of a liquid droplet on a solid surface is controlled by the same van der Waals forces, which will determine the adhesive characteristic. When a new surface is generated, the atoms located at the surface do not immediately reach their equilibrium position. A phenomenon of stress and strain relaxation occurs. The elementary work needed to extend a solid surface is $dW = \gamma \cdot dA$.

In the case of liquids, it is possible to experimentally measure γ, while the absence of mobility of atoms and molecules of solids does not allow a direct determination of γ_S. It is therefore necessary to use an indirect method, such as the study of interfacial solid-liquid interactions.

When a droplet of a liquid (l) with its vapor (v) is at rest on a solid surface (s) it takes a configuration which minimizes the energy of the system. This equilibrium state is expressed by the Young's equation (equation (3.2)):

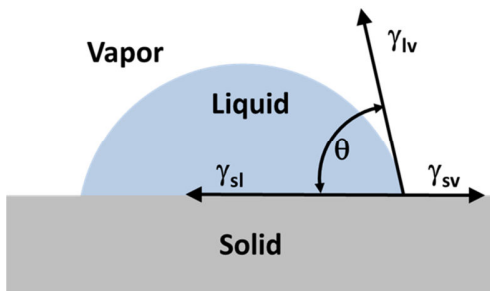$$\gamma_{sv} = \gamma_{sl} + \gamma_{lv} \cos \theta \qquad (3.2)$$

Figure 3.1 Schematic of a liquid drop showing the quantities involved in Young's equation.

where γ_{sv}, γ_{sl} and γ_{lv} are the surface energies of the solid/vapor, solid/liquid and liquid/vapor surfaces and θ is the contact angle between the solid and the liquid (Figure 3.1). The *Young's equation* mathematically relate γ_{sv} and γ_{sl} to two readily measurable properties γ_{lv} and the contact angle θ, however, there is no experimental means to separate them. Good and Girifalco [94] considered the formation of a solid/liquid interface to be similar to the formation of a liquid/liquid interface, with the basic difference that in case of liquid/liquid interfaces all the surface energies can be directly measured. In their study, they noticed the formation of a liquid/liquid interface was promoted when the two liquids were compatible, or capable of similar cohesive interactions. From this observation they developed the two-component surface energy theory. Practically, they defined liquids capable of only van der Waals interaction as dispersive, while all other interactions were described as polar (dipole/dipole, hydrogen bonding, π-π interactions, etc). Thus, it is possible to separate the surface energy of a liquid into these two contributions (equation (3.3)):

$$\gamma_L = \gamma_L^D + \gamma_L^P \qquad (3.3)$$

where γ_L^D and γ_L^P are respectively the dispersive and polar components. According to the same principle the surface energy of a solid, is termed as (equation (3.3)):

$$\gamma_S = \gamma_S^D + \gamma_S^P \qquad (3.4)$$

where γ_S^D and γ_S^P are respectively the dispersive and polar components.

Their observation lead them to develop an empirical equation, able to predict the energy of formation of a liquid/liquid interface (equation (3.5)):

$$\Delta G_{1,2} = -2\left[(\gamma_1^D \gamma_2^D)^{1/2} + (\gamma_1^P \gamma_2^P)^{1/2}\right] \quad\quad\quad \text{(3.5)}$$

where γ_1^D and γ_1^P and γ_2^D and γ_2^P are, respectively, the dispersive and polar components of the surface energy of liquids 1 and 2.

Different theories have been developed based on Good and Girifalco work. The more general and popular of which are the Owens-Wendt [95] and Fowkes [96] method. Owens-Wend assumed that the polar and non-polar components of surface energy could have been combined as a geometric average (equation (3.5)) with Young equation (equation (3.2)), obtaining (equation (3.6)):

$$\left[(\gamma_S^D \gamma_L^D)^{1/2} + (\gamma_S^P \gamma_L^P)^{1/2}\right] = \frac{\gamma_L(\cos\theta + 1)}{2} \quad\quad\quad \text{(3.6)}$$

that can be rearranged in the form of $y = mx + b$:

$$\frac{\gamma_L(\cos\theta + 1)}{2\sqrt{\gamma_L^D}} = \frac{\sqrt{\gamma_S^P}\sqrt{\gamma_L^P}}{\sqrt{\gamma_L^D}} + \sqrt{\gamma_S^D} \quad\quad\quad \text{(3.7)}$$

to give the *Owens-Wendt equation* (3.7). The polar and dispersive components of the solid surface energy can be directed extracted as slope and intercept of the resulting graph. Of course, the problem at this point is that in order to make that graph, knowing the surface energy of the probe liquid is not enough, as it is necessary to know specifically how it breaks down into its polar and dispersive components as well. To do this, one can simply reverse the procedure by testing the probe liquid against a standard reference solid that is not capable of polar interactions, such as PTFE. The values of γ_L^D and γ_L^P of many liquids, are available in publication and open archives and, indeed, it is not necessary to measure them against a standard.

In order to measure the surface energy of the pristine reference samples of active layer (**P3HT/PSBTBT/PDTSTzTz:PC$_{61}$BM**) or hole conductive layers (**Clevios^{TM} HTL Solar, Solar N and Solar 2**), we tested a series of solvents that cover the range of γ_L^D and γ_L^P. The solvents selected for our study, with their surface energy components are reported in Table 3.1.

Annex 3 Experimental Section of Mechanical Integrity of OPV Devices

Table 3.1 Series of solvents used in contact angle measurement and their surface energy, with specified dispersive and polar components values at 20°C [97]**.**

Liquid	Surface Energy (mN/m)		
	γ	γ^D	γ^P
n-Octanol	27.5	25.5	2.0
Water	73	22	51
Di-iodomethane	51	49	2
Formamide	58	40	19
Ethanol	21.4	18.8	2.6

Prior to utilize these solvents, their ability of solubilizing the different layers has been checked. A drop of solvent was deposed on the polymer surface and the evolution of its shape observed for 30 seconds, using the camera of the Contact Angle Meter. If no evolution was observed, the liquid was removed avoiding any contact with the surface. The remaining solvent was allowed to evaporate at ambient condition and the surface was observed by Optical Microscopy to verify any modification of the surface.

The contact angle values were acquired by a sessile drop contact angle system. The droplet is deposited by a syringe pointed vertically down onto the sample surface, and a high resolution camera captures the image, which can then be analyzed using a specific image analysis software. The angle formed between the liquid/solid interface and the liquid/vapor interface is the contact angle. The measure were performed at ambient condition (≈20°C, RH unknown). The size of the drops was varied between 15 and 30 µl and at least three different measure were performed for each sample.

3.5 **AFM analysis**

Peak force tapping AFM [98] has been introduced as an AFM imaging mode that also allows mechanical property mapping. In a peak force tapping experiment the sample is oscillated at a rate well below the resonance frequency of the AFM cantilever. The AFM feedback uses the maximum force load (peak force) as its control signal to maintain a constant imaging force, which reduce sample damage and tip wear. As a result multiple force vs. time curves are being recorded and averaged on each probed sample pixel. From the corresponding force distance curves mechanical parameters like adhesion, deformation and the elastic modulus can be determined.

3.6 **XPS**

XPS measurements were carried out using a multichamber UHV system (base pressure 10−10 mbar), equipped with a *SPECS Phoibos 150* cylindrical hemispherical analyzer and a monochromatic Al Kα source (*Focus 500 monochromator XR50m X-ray source, Al Kα 1486.74 eV*).

All the measurement where carried out by Aurélien Tournebize (ESR10) at the Eberhard Karls Universität Tübingen. The author refers to his Thesis for further experimental details.